ADVANCED NANOMATERIALS FOR LIGHT-EMITTING DIODES AND SOLAR CELLS

EDITED BY: Baiquan Liu, Swee Tiam Tan, Xuyong Yang and Qifan Xue
PUBLISHED IN: Frontiers in Chemistry

frontiers Research Topics

ISSN 1664-8714
ISBN 978-2-88971-401-8
DOI 10.3389/978-2-88971-401-8

About Frontiers

Frontiers is more than just an open-access publisher of scholarly articles: it is a pioneering approach to the world of academia, radically improving the way scholarly research is managed. The grand vision of Frontiers is a world where all people have an equal opportunity to seek, share and generate knowledge. Frontiers provides immediate and permanent online open access to all its publications, but this alone is not enough to realize our grand goals.

Frontiers Journal Series

The Frontiers Journal Series is a multi-tier and interdisciplinary set of open-access, online journals, promising a paradigm shift from the current review, selection and dissemination processes in academic publishing. All Frontiers journals are driven by researchers for researchers; therefore, they constitute a service to the scholarly community. At the same time, the Frontiers Journal Series operates on a revolutionary invention, the tiered publishing system, initially addressing specific communities of scholars, and gradually climbing up to broader public understanding, thus serving the interests of the lay society, too.

Dedication to Quality

Each Frontiers article is a landmark of the highest quality, thanks to genuinely collaborative interactions between authors and review editors, who include some of the world's best academicians. Research must be certified by peers before entering a stream of knowledge that may eventually reach the public - and shape society; therefore, Frontiers only applies the most rigorous and unbiased reviews.
Frontiers revolutionizes research publishing by freely delivering the most outstanding research, evaluated with no bias from both the academic and social point of view. By applying the most advanced information technologies, Frontiers is catapulting scholarly publishing into a new generation.

What are Frontiers Research Topics?

Frontiers Research Topics are very popular trademarks of the Frontiers Journals Series: they are collections of at least ten articles, all centered on a particular subject. With their unique mix of varied contributions from Original Research to Review Articles, Frontiers Research Topics unify the most influential researchers, the latest key findings and historical advances in a hot research area! Find out more on how to host your own Frontiers Research Topic or contribute to one as an author by contacting the Frontiers Editorial Office: frontiersin.org/about/contact

ADVANCED NANOMATERIALS FOR LIGHT-EMITTING DIODES AND SOLAR CELLS

Topic Editors:
Baiquan Liu, Sun Yat-sen University, China
Swee Tiam Tan, Xiamen University, Malaysia
Xuyong Yang, Shanghai University, China
Qifan Xue, South China University of Technology, China

Citation: Liu, B., Tan, S. T., Yang, X., Xue, Q., eds. (2021). Advanced Nanomaterials for Light-Emitting Diodes and Solar Cells. Lausanne: Frontiers Media SA.
doi: 10.3389/978-2-88971-401-8

Table of Contents

frontiers in Chemistry

EDITORIAL
published: 29 July 2021
doi: 10.3389/fchem.2021.741760

Editorial: Advanced Nanomaterials for Light-Emitting Diodes and Solar Cells

Baiquan Liu[1], Qifan Xue[2]*, Xuyong Yang[3]* and Swee Tiam Tan[4]**

[1]School of Electronics and Information Technology, Sun Yat-sen University, Guangzhou, China, [2]Institute of Polymer Optoelectronic Materials and Devices, State Key Laboratory of Luminescent Materials and Devices, South China University of Technology, Guangzhou, China, [3]Key Laboratory of Advanced Display and System Applications of Ministry of Education, Shanghai University, Shanghai, China, [4]School of Energy and Chemical Engineering, Xiamen University Malaysia, Sepang, Malaysia

Keywords: nanomaterial, optoelectronic, interface, morphology, mechanism

Editorial on the Research Topic

Advanced Nanomaterials for Light-Emitting Diodes and Solar Cells

Thanks to the outstanding optoelectronic properties, advanced nanomaterials have received increasing attention from both academia and industry (Liu et al., 2020). In recent years, intensive effort has been devoted to developing high-performance nanomaterials, which enables huge potential in wide optoelectronic applications (Kong et al., 2021; Niu et al., 2021), particularly for light-emitting diodes (LEDs) and solar cells (SCs). It is our great pleasure to introduce this Special Issue entitled "Advanced Nanomaterials for Light-Emitting Diodes and Solar Cells". This Special Issue highlights the major significance of material-device research from different perspectives, combining both the modern experimental approaches and theoretical simulations. We present a collection of 10 featured articles from this exciting field that covers the emerging concepts, strategies and techniques of advanced nanomaterials for the development of LEDs and SCs.

Simplified organic LED (OLED) structure with feasible fabrication process plays a critical role in illumination. Xu et al. incorporated ultrathin non-doped emissive nanolayers (0.3 nm), demonstrating low efficiency roll-off and simple-structure OLEDs. Meanwhile, Xie et al. developed solution-processed blue thermally activated delayed fluorescence OLEDs with a narrow full-width at half-maximum of 32 nm by employing a molecule containing boron and nitrogen atoms as guest emitter, obtaining high color purity OLEDs. On the other hand, it is important to develop novel solution-processed hole injection materials for high-performance OLEDs. Zhu et al. synthesized the molybdenum disulfide quantum dots (MoS_2 QDs) and demonstrated green phosphorescent OLEDs with hybrid poly (3,4-ethylenedioxythiophene)/poly (styrenesulfonate) (PEDOT:PSS)/QDs hole injection layer. The OLED with PEDOT:PSS/MoS_2 hole injection layer exhibited a maximum current efficiency of 72.7 cd A^{-1}, which is 28.2% higher than that of the OLEDs with single PEDOT:PSS, indicating an effective way to achieve the high efficiency OLEDs with sulfide QDs as the hole injection layer.

GaN-based LED is also a promising device for lighting and displays. Zhang et al. systematically investigated the effect of mesa size-reduction in InGaN/GaN LEDs in two lateral dimensions both experimentally and numerically, providing insights on device miniaturization. While Lu et al. fabricated and demonstrated strain-reduced micro-LEDs in various sizes and investigated the size effect on the optical properties and the indium concentration for the quantum wells. Their work provides the rules of thumb to achieve high power performance for micro-LEDs. On the other hand, Liu et al. prepared 2-inch free-standing GaN substrates with a thickness of ~250 μm on double-polished sapphire substrates by employing a combined buffer layer prepared by hydride vapor phase epitaxy and the laser lift-off technique, giving a route for high-power GaN-based devices.

OPEN ACCESS

Edited and reviewed by:
Andreas Rosenkranz, University of Chile, Chile

****Correspondence:***
Baiquan Liu
liubq33@mail.sysu.edu.cn
Qifan Xue
qfxue@scut.edu.cn
Xuyong Yang
yangxy@shu.edu.cn
Swee Tiam Tan
sweetiam.tan@xmu.edu.my

Specialty section:
This article was submitted to Nanoscience, a section of the journal Frontiers in Chemistry

Received: *15 July 2021*
Accepted: *22 July 2021*
Published: *29 July 2021*

Citation:
Liu B, Xue Q, Yang X and Tan ST (2021) Editorial: Advanced Nanomaterials for Light-Emitting Diodes and Solar Cells. Front. Chem. 9:741760. doi: 10.3389/fchem.2021.741760

Global warming and climate change has motivated the community to search for practical sustainable energy sources to replace fossil fuels. SCs provide an effective approach to supply clean and inexhaustible energy. Yu et al. introduced a perylene diimide derivative (PDINO) in organic SCs, passivating the defects between tin oxide (SnO_2) electron transporting layer (ETL) and the active layer. The power conversion efficiency of the PDINO-modified device was 14.9%, demonstrating a strategy of utilizing the organic-inorganic hybrid ETL to realize high-performance SCs. Besides, the thermoelectric effect that enable direct conversion between thermal and electrical energy was incorporated with SCs via heat management and light harvesting. Wang et al. reviewed the interfacial chemistry and electrical feature of various polymer-inorganic thermoelectric hybrid nanomaterials, and discussed the prospect and challenges of polymer-inorganic nanocomposites in the field of thermoelectric energy.

The investigation on luminescence materials and metal nanomaterials is an important complementary field to LEDs and SCs. Xiao et al. investigated the effect of substitution of BaF_2 for BaO to improve spectroscopic properties in Tm^{3+} doped gallium tellurite glasses for efficient 2.0 μm fiber laser, indicating that Tm^{3+} doped gallium tellurite glasses containing BaF_2 was an excellent host material. On the other side, gold nanomaterials can be used not only in optoelectronic fields but also the clinical arena in humans. Jin et al. reviewed the biomedical applications and molecular mechanism of gold nanomaterials in bone and cartilage tissue engineering, and presented the current challenges and future directions.

We would like to take this opportunity to thank all those who have contributed to this Special Issue and all referees for their insightful advice. In addition, we would like to thank *Frontiers in Chemistry* for their excellent editorial support. We hope that this Special Issue will intrigue the researchers worldwide and that future efforts will contribute to the nanomaterials research community.

AUTHOR CONTRIBUTIONS

All authors listed have made a substantial, direct, and intellectual contribution to the work and approved it for publication.

FUNDING

This work was supported by the Open Fund of the State Key Laboratory of Luminescent Materials and Devices (South China University of Technology), the Guangdong Basic and Applied Basic Research Foundation for Distinguished Young Scholar (No. 2021B1515020028), the Natural Science Foundation of China (No 51803060), the Science and Technology Program of Guangdong Province, China (No. 2018A030313045), the Science and Technology Program of Guangzhou, China (No. 201904010147). ST would like to acknowledge the financial support from Collaborative Research in Engineering, Science and Technology Centre (CREST), Malaysia and Xiamen University Malaysia under Grant No. IENG/0039.

REFERENCES

Kong, L., Zhang, X., Li, Y., Wang, H., Jiang, Y., Wang, S., et al. (2021). Smoothing the Energy Transfer Pathway in Quasi-2d Perovskite Films Using Methanesulfonate Leads to Highly Efficient Light-Emitting Devices. *Nat. Commun.* 12, 1246. doi:10.1038/s41467-021-21522-8

Liu, B., Altintas, Y., Wang, L., Shendre, S., Sharma, M., Sun, H., et al. (2020). Record High External Quantum Efficiency of 19.2% Achieved in Light-Emitting Diodes of Colloidal Quantum wells Enabled by Hot-Injection Shell Growth. *Adv. Mater.* 32, e1905824. doi:10.1002/adma.201905824

Niu, T., Zhu, W., Zhang, Y., Xue, Q., Jiao, X., Wang, Z., et al. (2021). D-A-π-A-D-type Dopant-free Hole Transport Material for Low-Cost, Efficient, and Stable Perovskite Solar Cells. *Joule* 5, 249–269. doi:10.1016/j.joule.2020.12.003

Conflict of Interest: The authors declare that the research was conducted in the absence of any commercial or financial relationships that could be construed as a potential conflict of interest.

Publisher's Note: All claims expressed in this article are solely those of the authors and do not necessarily represent those of their affiliated organizations, or those of the publisher, the editors and the reviewers. Any product that may be evaluated in this article, or claim that may be made by its manufacturer, is not guaranteed or endorsed by the publisher.

frontiers in Chemistry

ORIGINAL RESEARCH
published: 08 January 2021
doi: 10.3389/fchem.2020.628273

Effect of BaF_2 Variation on Spectroscopic Properties of Tm^{3+} Doped Gallium Tellurite Glasses for Efficient 2.0 μm Laser

*Jian Yuan[1,2], Weichao Wang[2], Yichen Ye[2], Tingting Deng[1], Deqian Ou[1], Junyang Cheng[1], Shengjin Yuan[1] and Peng Xiao[1]**

[1] Guangdong-Hong Kong-Macao Intelligent Micro-Nano Optoelectronic Technology Joint Laboratory, Foshan University, Foshan, China, [2] State Key Laboratory of Luminescent Materials and Devices, South China University of Technology, Guangzhou, China

The effects of substitution of BaF_2 for BaO on physical properties and 1. 8 μm emission have been systematically investigated to improve spectroscopic properties in Tm^{3+} doped gallium tellurite glasses for efficient 2.0 μm fiber laser. It is found that refractive index and density gradually decrease with increasing BaF_2 content from 0 to 9 mol.%, due to the generation of more non-bridging oxygens. Furthermore, OH^- absorption coefficient (α_{OH}) reduces monotonically from 3.4 to 2.2 cm^{-1} and thus emission intensity near 1.8 μm in gallium tellurite glass with 9 mol.% BaF_2 is 1.6 times as large as that without BaF_2 while the lifetime becomes 1.7 times as long as the one without BaF_2. Relative energy transfer mechanism is proposed. The maximum emission cross section and gain coefficient at around 1.8 μm of gallium tellurite glass containing 9 mol.% BaF_2 are 8.8 × 10^{-21} cm^2 and 3.3 cm^{-1}, respectively. These results indicate that Tm^{3+} doped gallium tellurite glasses containing BaF_2 appear to be an excellent host material for efficient 2.0 μm fiber laser development.

Keywords: gallium tellurite glass, Tm^{3+} doped, OH^-, 1.8 μm emission, BaF_2

OPEN ACCESS

Edited by:
Baiquan Liu,
Sun Yat-sen University, China

Reviewed by:
Fei Chen,
Hangzhou Dianzi University, China
Xueyun Liu,
Ningbo University, China

***Correspondence:**
Peng Xiao
xiaopeng@fosu.edu.cn

Specialty section:
This article was submitted to Nanoscience, a section of the journal Frontiers in Chemistry

Received: *11 November 2020*
Accepted: *10 December 2020*
Published: *08 January 2021*

Citation:
Yuan J, Wang W, Ye Y, Deng T, Ou D, Cheng J, Yuan S and Xiao P (2021) Effect of BaF_2 Variation on Spectroscopic Properties of Tm^{3+} Doped Gallium Tellurite Glasses for Efficient 2.0 μm Laser. Front. Chem. 8:628273. doi: 10.3389/fchem.2020.628273

INTRODUCTION

Over the past few decades, fiber lasers operating in eye-safe 2.0 μm spectral region have attracted a great deal of attention due to strong absorption band of several chemical compounds (H_2O, CO_2, N_2O, etc.) in this region (Chen et al., 2010). Therefore, there are some potential applications in eye-safe laser radar, material processing, laser surgery, remote sensing and effective pump sources as mid-infrared lasers and optical parametric oscillators (Geng et al., 2011; Geng and Jiang, 2014; Slimen et al., 2019; Wang et al., 2019). Up to now, active ions for 2.0 μm laser have been mainly focused on Tm^{3+} and Ho^{3+} ions arising from Tm^{3+} :$^3F_4 \rightarrow {}^3H_6$ and Ho^{3+} :$^5I_7 \rightarrow {}^5I_8$ transition. Compared with Ho^{3+}, Tm^{3+} owns very strong absorption band of $^3H_6 \rightarrow {}^3H_4$ transition and thus can be effectively pumped by commercial high-power 808 nm laser diode. Under the pump scheme, a quantum efficiency of 200% can be expected from "two-for-one" cross relaxation process ($^3H_4 + {}^3H_6 \rightarrow 2{}^3F_4$) (Richards et al., 2010). In addition, broad emission bandwidth of Tm^{3+} :$^3F_4 \rightarrow {}^3H_6$ transition about 300 nm is advantageous to the generation of femtosecond pulse (Agger et al., 2004).

In pursuit of efficient 2.0 μm laser, different glass hosts have been extensively investigated and the laser operation has been demonstrated in silicate, fluoride, germanate and tellurite glasses (Richards et al., 2010; He et al., 2013; Wang et al., 2019). Among these glass hosts, tellurite glasses own a lot of advantage such as broad infrared transmission region, lower phonon energy, high rare-earth ion solubility, high refractive index (∼2) and easy fabrication with low melting temperature(Richards et al., 2010). Recently, our groups have exploited several new tellurite glass systems such as TeO_2-Ga_2O_3-BaO (TGB) and TeO_2-Ga_2O_3-ZnO (TGZ) with excellent glass-forming ability, thermal stability and 2.0 μm spectroscopic properties (Li et al., 2019; Mao et al., 2020). To further improve 2.0 μm emission properties, it is very essential to reduce the hydroxyl content in glasses because OH^- groups are the main energy loss channels for active ions and can result in strong 2.0 μm fluorescence quenching (Terra et al., 2006). We found that the strength of interaction between Tm^{3+} and OH^- (12.9×10^{-19} cm^4/s) was stronger than that between Er^{3+} and OH^- (1.9×10^{-19} cm^4/s) (Yuan et al., 2014).

Herein, based on the composition of TGB glass with good thermal stability, we systematically investigate the effects of substitution of BaF_2 for BaO on physical properties and 1.8 μm emission properties. Density, refractive index, Raman spectra, absorption spectra and emission spectra were measured along with the lifetime of Tm^{3+}:$^3F_4$ energy level. Moreover, energy transfer mechanism is proposed and emission cross section and gain coefficient of Tm^{3+} :$^3F_4 \rightarrow {}^3H_6$ transition in TGB glass with 9 mol.% BaF_2 are determined.

MATERIALS AND METHODS

Tm^{3+} doped gallium tellurite glasses (TGB) with the molar compositions of $80TeO_2$-$10Ga_2O_3$-(9-x)BaO-xBaF_2-$1Tm_2O_3$ (x = 0, 3, 6, and 9) were prepared by the conventional melt-quenching method. TeO_2, Ga_2O_3, BaO, BaF_2 and Tm_2O_3 with 99.99% purity (Aladdin) were used as raw chemicals. Appropriate amounts of these chemicals (∼20 g) were well mixed and then melted in an alumina crucible with an alumina lid at ∼950°C for 30 min. Afterwards, the melts were poured onto a preheated graphite mold and further annealed at 330°C for 2 h, after which they were cooled slowly inside the furnace to room temperature. The annealed samples for the optical property measurements need to be double-sided polishing into $10 \times 10 \times 1.5$ mm^3 cylinders. Densities of glasses were determined by the Archimedes' principle using the distilled water as the medium. The refractive index of all the samples was measured by the prism coupling method (Metricon Model 2010) at 633, 1,309, and 1,533 nm with an error of $\pm 5 \times 10^{-4}$. The infrared transmittance spectra were obtained using Vector 33 Fourier transform infrared (FTIR) spectrophotometer (Bruker, Switzerland). The Raman spectra were measured by Raman spectrometer (Renishawin Via, Gloucestershire, UK) and 532 nm laser as the excitation source. Optical absorption spectra measurements were performed on a Perkin-Elmer Lambda 900/UV/VIS/NIR spectrophotometer. The fluorescence spectra were recorded by a computer-controlled Triax 320 type spectrofluorimeter (Jobin-Yvon Corp.) equipped with an InAs detector upon the excitation of an 808 nm LD. After exciting the samples with an 808 nm LD, InAs detector was used to detect the lifetime of Tm^{3+}:$^3F_4$ energy level (1.8 μm) along with a digital phosphor oscilloscope (TDS3012C, Tektronix, America) and signal generator. All of the measurements were carried out at room temperature.

TABLE 1 | The refractive index and density of TGB glasses with different BaF_2 contents.

Sample	*n* (@633 nm)	*n* (@1,309 nm)	*n* (@1,533 nm)	ρ (g/cm^3)
x = 0	1.9723	1.9324	1.9289	5.265
x = 3	1.9490	1.9097	1.908	5.219
x = 6	1.9281	1.8920	1.8904	5.140
x = 9	1.9132	1.8792	1.8769	5.128

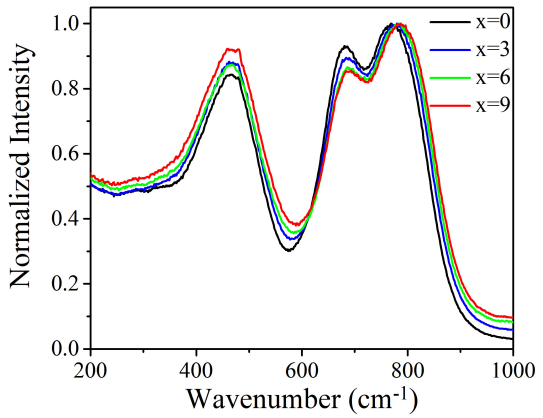

FIGURE 1 | Normalized Raman spectra of TGB glasses with different BaF_2 amounts.

RESULTS AND DISCUSSION

Table 1 presents the refractive index (*n*) and density (ρ) of TGB glasses with different BaF_2 contents. It is found that the refractive index and density monotonously decrease when BaF_2 content increases from 0 to 9 mol.% in step of 3 mol.%. This indicates that the addition of BaF_2 makes glass network looser (Yang et al., 2017), which is demonstrated by the Raman spectra as shown **Figure 1**. It is noted that three major bands appear in TGB glasses with different BaF_2 amounts. The peak A at ∼466 cm^{-1} is assigned to the symmetrical stretching or bending vibrations of Te-O-Te linkages at corner sharing sites (Murugan and Ohishi, 2004; Jose et al., 2007). The peak B at ∼682 cm^{-1} is ascribed to the anti-symmetric stretching vibrations of Te-O-Te linkages constructed by two un-equivalent Te-O bonds containing bridging oxygens (BO) in TeO_4 trigonal bipyramid and the peak C is due to the symmetrical stretching vibrations of Te-O^- and Te=O

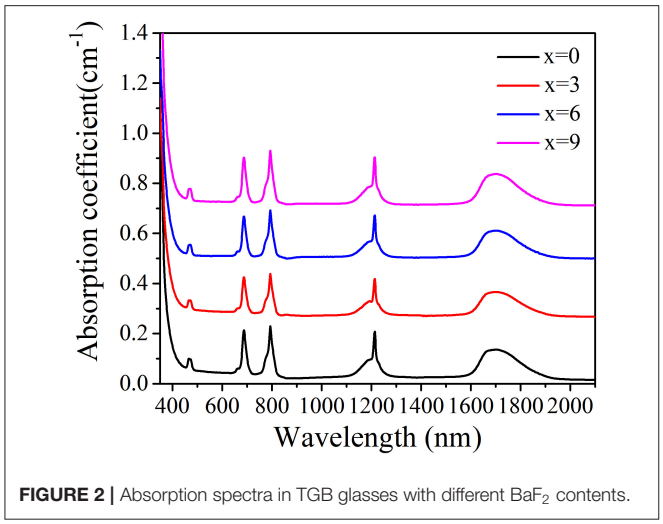

FIGURE 2 | Absorption spectra in TGB glasses with different BaF_2 contents.

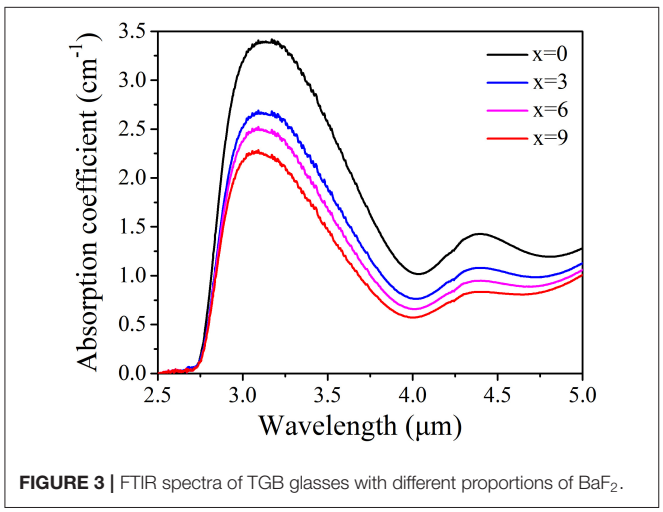

FIGURE 3 | FTIR spectra of TGB glasses with different proportions of BaF_2.

bonds with non-bridging oxygens (NBO) in TeO_3 trigonal pyramid and TeO_{3+1} polyhedra (Murugan and Ohishi, 2004; Jose et al., 2007). It is worth noting that the position of peak C slightly shifts from 769 to 787 cm^{-1} and normalized intensity of peak B declines with the increment of BaF_2 from 0 to 9 mol.%, revealing that glass network structure is broken and more non-bridging oxygens arise. Such low phonon energy of TGB glasses is able to effectively decrease non-radiative relaxation in favor of the enhancement of 2.0 μm emission intensity.

Figure 2 shows the typical absorption spectra of TGB glasses in the wavelength range from 350 to 2,100 nm. The absorption spectrum consists of five absorption bands of Tm^{3+} centered at 473, 687, 794, 1,214, and 1,700 nm, corresponding to respective transitions from the $^3H_6$ ground state to excited states $^1G_4$, $^3F_{2,3}$, $^3H_4$, $^3H_5$, and $^3F_4$. Energy levels above $^1G_4$ energy level are not clearly identified because of strong intrinsic bandgap absorption in the host glass. It is also found that the position and shape of five absorption peaks are almost constant with the addition of BaF_2.

When BaF_2 is added, F^- ions crack O-H bond in glass network and produce HF gas so that OH^- content is reduced. OH^- content is reflected by OH^- absorption coefficient (α_{OH}) (Wang et al., 2013).

$$\alpha_{OH} = \frac{\ln(T_0/T)}{l} \tag{1}$$

where l represents the thickness of glass samples, T_0 and T are the incident and transmitted intensity, respectively. According to FTIR spectra, OH^- absorption coefficient of TGB glasses is determined and presented in **Figure 3**. There are two absorption bands centered at 3.1 and 4.4 μm, corresponding to stretching mode of free Te-OH groups and/or stretching mode of molecular water and stretching mode of strong hydrogen-bonded Te-OH groups, respectively (Wang et al., 2019). α_{OH} at 3.1 μm is obviously higher than the value at 4.4 μm. Moreover, α_{OH} monotonically decreases from 3.4 to 2.2 cm^{-1} with increasing BaF_2 content from 0 to 9 mol.% in step of 3 mol.%, which is beneficial to improve 1.8 μm emission properties of Tm^{3+} ions.

Figure 4 compares the fluorescence spectra and decay curves of Tm^{3+}:$^3F_4 \rightarrow {}^3H_6$ transition in TGB glasses with different BaF_2 amounts pumped by 808 nm LD. From **Figure 4A**, it is clear that the spectra are characterized by two emission peaks located at 1,488 and 1,808 nm, corresponding to $^3H_4 \rightarrow {}^3F_4$ and $^3F_4 \rightarrow {}^3H_6$ transitions, respectively. Emission intensity at 1,488 nm is obviously weaker than that at 1,808 nm, which is attributed to effective cross relaxation process ($^3H_4 + {}^3H_6 \rightarrow 2{}^3F_4$). Moreover, emission intensity at 1,488 nm remains almost unchanged and that near 1.8 μm gradually increases with the increment of BaF_2 concentration. The peak value near 1.8 μm in TGB glasses with 9 mol.% BaF_2 is 1.6 times as high as that without BaF_2 because the reduction of OH^- content weakens the interaction between Tm^{3+} and OH^- and thus enhances radiative transition probability of $^3F_4 \rightarrow {}^3H_6$ transition. **Figure 4B** describes fluorescence decay curves of Tm^{3+}:$^3F_4$ energy level monitored at 1,808 nm in TGB glasses with different proportions of BaF_2. It is clearly noted that the lifetime of $^3F_4$ energy level gradually prolongs from 337.4 to 577.8 μs when BaF_2 content increases from 0 to 9 mol.% in step of 3 mol.%. The lifetime in TGB glass with 9 mol.% BaF_2 is 1.7 times as long as the value without BaF_2. These results mean that the addition of BaF_2 can greatly improve 1.8 μm emission properties.

In general, the total decay rate (W) of Tm^{3+}:$^3F_4$ energy level is defined as the reciprocal of the measured decay lifetime (τ_m) and is described by the following equations (Zhou et al., 2010).

$$W = 1/\tau_m = A_r + W_{OH} + W_{MP} + W_{ET} \tag{2}$$

$$W_{OH} = k_{OH-Tm} N_{Tm} \alpha_{OH} \tag{3}$$

where A_r represents the radiative decay rate, W_{OH} is the energy transfer rate between Tm^{3+} and OH^-, W_{mp} is the multiphonon decay rate, W_{ET} is the energy transfer rate between Tm^{3+} ions, N_{Tm} is the total concentration of Tm^{3+} ions and α_{OH} is OH^- absorption coefficient. k_{OH-Tm} is defined as the strength of interaction between Tm^{3+} and OH^- and doesn't rely on the

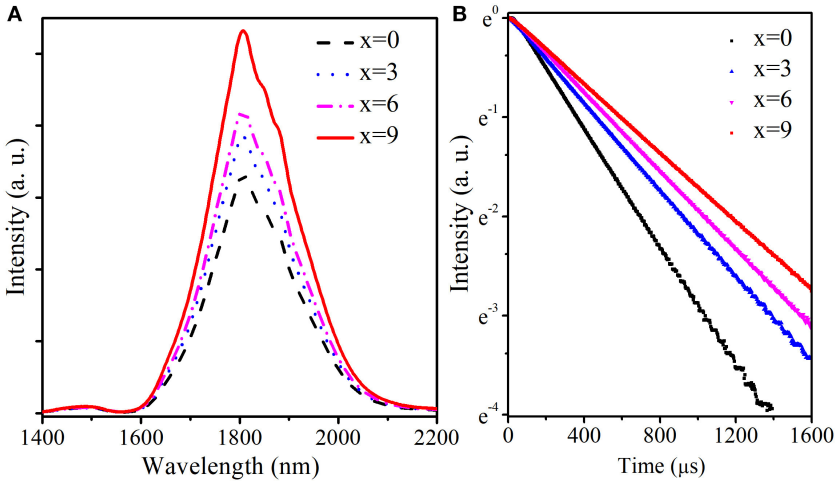

FIGURE 4 | (A) Fluorescence spectra and **(B)** decay curves of Tm^{3+}:$^3F_4$ energy level in TGB glasses with different proportions of BaF_2 pumped by 808 nm LD.

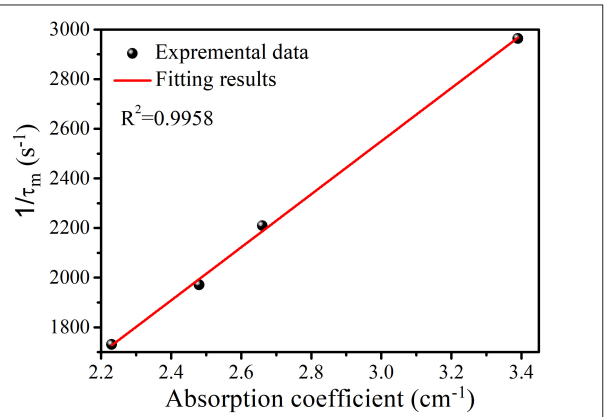

FIGURE 5 | The dependence of the total decay rate on α_{OH} along with the red fitting curve.

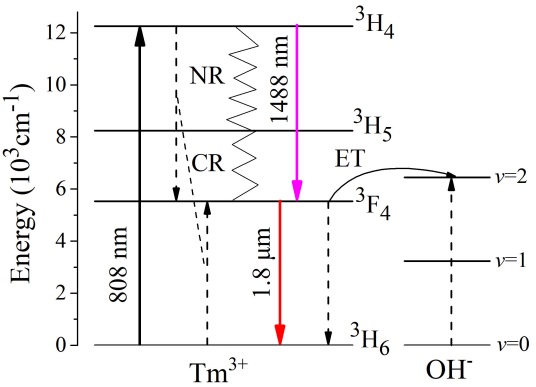

FIGURE 6 | The energy level diagram and energy transfer mechanism of Tm^{3+} ions.

concentrations of Tm^{3+} and OH^-. **Figure 5** represents a good linear relationship between the total decay rate and α_{OH}. From this fit, k_{OH-Tm} is determined and equals to 2.82×10^{-18} cm^4/s, which is larger than k_{OH-Er} (1.9×10^{-19} cm^4/s) (Zhou et al., 2010) and lower than k_{OH-Tm} (7.89×10^{-18} cm^4/s) in germanate glasses (Wang et al., 2014).

Based on above-mentioned results, **Figure 6** shows energy transfer mechanism. Under excitation at 808 nm LD, Tm^{3+} ions are motivated to $^3H_4$ state from the $^3H_6$ ground state. Then, a few Tm^{3+} ions return radiatively to $^3F_4$ state with 1,488 nm photon. However, the majority of ions relax nonradiatively to $^3F_4$ state via muliphonon relaxation process and efficient cross relaxation process (CR) between two adjacent Tm^{3+} ions ($^3H_4 + {}^3H_6 \rightarrow 2{}^3F_4$). Finally, Tm^{3+} ions in the excited $^3F_4$ state return to the $^3H_6$ ground state, emitting fluorescence at 1.8 μm. Significantly, the residual OH^- in TGB glasses can impair 1.8 μm emission via two OH^- ions, indicating that it is essential to decrease the hydroxyl content for improving 1.8 μm emission.

Both absorption and emission cross sections of Tm^{3+} ions are very crucial parameters to evaluate the potential of TGB glasses as 2 μm laser material. Based on the Beer-Lambert equation and Fuchtbauer-Ladenburg equation (Chen et al., 2007), absorption and emission cross sections of Tm^{3+} :$^3H_6 \leftrightarrow {}^3F_4$ transition in TGB glass with 9 mol.% BaF_2 are calculated and presented in **Figure 7A**. The maximum absorption cross section of Tm^{3+} reaches 5.3×10^{-21} cm^2 at 1,706 nm, which is higher than that of silicate glass (1.5×10^{-21} cm^2) (Li et al., 2012), fluorophosphate glass (3.0×10^{-21} cm^2) (Li et al., 2015), tellurium germanate glass (3.2×10^{-21} cm^2) (Gao et al., 2015) and germanate glass (4.1×10^{-21} cm^2) (Yu et al., 2009). Moreover, corresponding maximum emission cross section is 8.8×10^{-21} cm^2 at 1,814 nm, which is higher than that of silicate glass (3.6×10^{-21} cm^2) (Li et al., 2012), fluorophosphate glass (5.5×10^{-21} cm^2) (Li et al., 2015), tellurium germanate glass (6.8×10^{-21} cm^2) (Gao et al., 2015), germanate glass (5.5×10^{-21} cm^2) (Yu et al., 2009) and zinc tellurite glass (7.3×10^{-21} cm^2) (Yuan and Xiao, 2018). The

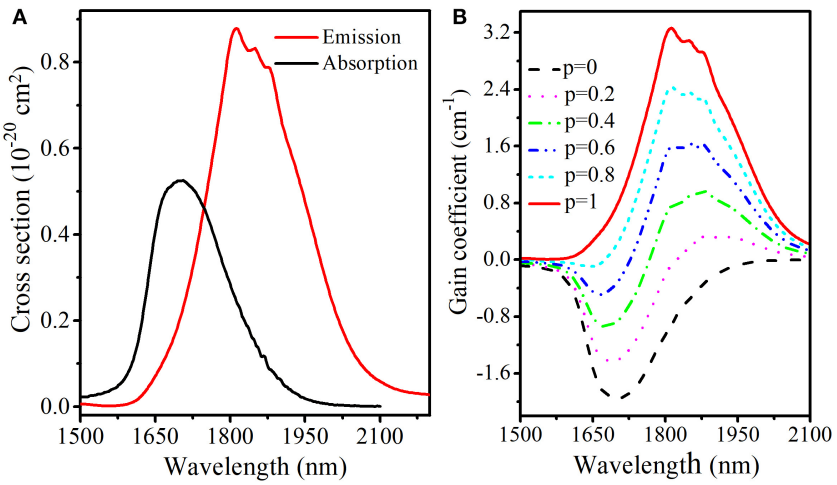

FIGURE 7 | (A) Absorption, emission cross section and **(B)** calculated gain coefficient of TGB glass with 9 mol.% BaF_2.

high emission cross section of TGB glass with 9 mol.% BaF_2 is helpful to provide high laser gain.

Once absorption and emission cross sections are determined and it is supposed that Tm^{3+} ions are only in either the $^3H_6$ or $^3F_4$ state, the gain coefficient $G(\lambda)$ of Tm^{3+} near 1.8 μm can be obtained by the following equation (Zou and Toratani, 1996).

$$G(\lambda) = N[p\sigma_e - (1-p)\sigma_a] \quad (4)$$

where N represents the total concentration of Tm^{3+} ions and p is the inversion factor given by the ratio between the population of lasing upper level ($^3F_4$) and the total concentration that ranges from 0 to 1. **Figure 7B** shows gain coefficient spectrum of TGB glass with 9 mol.% BaF_2. It is found that the gain peak shifts to shorter wavelength with increasing p, which is a typical feature of the quasi-three-level system. Moreover, gain coefficient starts to be greater than zero in the wavelength range from 1,824 to 2,100 nm when $p \geq 0.2$ and the maximum value is 3.3 cm^{-1} at 1,814 nm, which is larger than that of silicate glass (2.57 cm^{-1}) (Tang et al., 2016), germanate glass (2.11 cm^{-1}) (Slimen et al., 2019) and tellurite glass (0.91 cm^{-1}) (Tian et al., 2019). This means that TGB glass with 9 mol.% BaF_2 is a promising host material for efficient 2.0 μm fiber laser development.

CONCLUSIONS

In summary, the effects of BaF_2 contents on density, refractive index, Raman spectra, OH^- absorption coefficient and 1.8 μm spectroscopic properties of Tm^{3+} doped gallium tellurite glasses are studied in detail. When BaF_2 content increases from 0 to 9 mol.% in step of 3 mol.%, refractive index and density gradually reduce. Meanwhile, α_{OH} monotonically decreases from 3.4 to 2.2 cm^{-1}, which makes emission peak value near 1.8 μm in TGB glass with 9 mol.% BaF_2 being 1.6 times as large as that without BaF_2 while the lifetime becomes 1.7 times as long as the value without BaF_2. The maximum emission cross section at around 1.8 μm of TGB glass with 9 mol.% BaF_2 reaches 8.8×10^{-21} cm^2. In addition, positive gain coefficient in the wavelength range from 1,824 to 2,100 nm is achieved when $p \geq 0.2$ and the maximum gain coefficient is 3.3 cm^{-1} at 1,814 nm. As a result, TGB glass with 9 mol.% BaF_2 appears to be a highly promising host material for efficient 2.0 μm fiber laser development.

DATA AVAILABILITY STATEMENT

The raw data supporting the conclusions of this article will be made available by the authors, without undue reservation.

AUTHOR CONTRIBUTIONS

JY, PX, and WW conceived the idea. JY and PX wrote the paper. TD, YY, DO, JC, and SY advised the paper. All authors contributed to the article and approved the submitted version.

FUNDING

The authors gratefully acknowledge the financial support from the National Natural Science Foundation of China (Grant Nos. 51902053 and 61804029), Natural Science Foundation of Guangdong province (Grant Nos. 2019A1515011988 and 2018A030310353), Guangdong Basic and Applied Basic Research Foundation (Grant No. 2019A1515110002), the Foundation for Distinguished Young Talents in Higher Education of Guangdong (Grant No. 2019KQNCX172), the Project of Foshan Education Bureau (Grant No. 2019XJZZ02), Guangdong-Hong Kong-Macao Intelligent Micro-Nano Optoelectronic Technology Joint Laboratory (Grant No. 2020B1212030010), and the Open Fund of the State Key Laboratory of Luminescent Materials and Devices (South China University of Technology, Grant No. 2020-skllmd-13).

REFERENCES

Agger, S., Povlsen, J. H., and Varming, P. (2004). Single-frequency thulium-doped distributed-feedback fiber laser. *Opt. Lett*. 29, 1503–1505. doi: 10.1364/OL.29.001503

Chen, G. X., Zhang, Q. Y., Yang, G. F., and Jiang, Z. H. (2007). Mid-infrared emission characteristic and energy transfer of Ho^{3+}-doped tellurite glass sensitized by Tm^{3+}. *J. Fluoresc*. 17, 301–307. doi: 10.1007/s10895-007-0173-5

Chen, Y. J., Lin, Y. F., Gong, X. H., Zhu, H. M., Luo, Z. D., and Huang, Y. D. (2010). 805-nm diode-pumped continuous-wave 2-μm laser performance of Tm^{3+}:$BaGd_2(MoO_4)_4$ cleavage plate. *Appl. Phys. B*. 98, 55–60. doi: 10.1007/s00340-009-3704-8

Gao, S., Kuan, P. W., Liu, X. Q., Chen, D. P., Liao, M. S., and Hu, L. L. (2015). ∼2-μm single-mode laser output in Tm^{3+}-doped tellurium germanate double-cladding fiber. *IEEE Photon. Technol. Lett*. 27, 1702–1704. doi: 10.1109/LPT.2015.2438077

Geng, J. H., and Jiang, S. B. (2014). Fiber lasers:the 2 μm market heats up. *Opt. Photonics News*. 25, 35–41. doi: 10.1364/OPN.25.7.000034

Geng, J. H., Wang, Q., and Jiang, S. B. (2011). 2 μm fiber laser sources and their applications. *Proc. SPIE*. 8164:816409. doi: 10.1117/12.896259

He, X., Xu, S. H., Li, C., Yang, C. S., Yang, Q., Mo, S. P., et al. (2013). 1.95 μm kHz-linewidth single-frequency fiber laser using self-developed heavily Tm^{3+}-doped germanate glass fiber. *Opt. Exp*. 21, 20800–20805. doi: 10.1364/OE.21.020800

Jose, R., Arai, Y., and Ohishi, Y. (2007). Raman scattering characteristics of the TBSN-based tellurite glass system as a new Raman gain medium. *J. Opt. Soc. Am. B*. 24,1517–1526. doi: 10.1364/JOSAB.24.001517

Li, L. X.;,Wang, W. C., Zhang, C. F., Liu, J. L., Zhang, Q. Y., and Jiang, Z. H. (2019). Exploration of the new tellurite glass system for efficient 2 μm luminescence. *J. Non Cryst. Solids* 508, 15–20. doi: 10.1016/j.jnoncrysol.2018.12.018

Li, M., Bai, G. X., Guo, Y. Y., Hu, L. L., and Zhang, J. J. (2012). Investigation on Tm^{3+}-doped silicate glass for 1.8 μm emission. *J. Lumin*. 132, 1830–1835. doi: 10.1016/j.jlumin.2012.02.022

Li, R. B., Tian, C., Tian, Y., Tao, W., Li, B. P., Jing, X. F., et al. (2015). Mid-infrared emission properties and energy transfer evaluation in Tm^{3+} doped fluorophosphate glasses. *J. Lumin*. 162, 58–62. doi: 10.1016/j.jlumin.2015.02.016

Mao, L. Y., Liu, J. L., Li, L. X., and Wang, W. C. (2020). TeO_2-Ga_2O_3-ZnO ternary tellurite glass doped with Tm^{3+} and Ho^{3+} for 2 μm fiber lasers. *J. Non Cryst. Solids* 531:119855. doi: 10.1016/j.jnoncrysol.2019.119855

Murugan, G. S., and Ohishi, Y. (2004). Raman spectroscopic studies of TeO_2-BaO-SrO-Nb_2O_5 glasses: structure-property correlations. *J. Appl. Phys*. 96, 2437–2442. doi: 10.1063/1.1772890

Richards, B., Jha, A., Tsang, Y., Binks, D., Lousteau, J., Fusari, F., et al. (2010). Tellurite glass lasers operating close to 2 μm. *Laser Phys. Lett*. 7, 177–193. doi: 10.1002/lapl.200910131

Slimen, F. B., Chen, S. X., Lousteau, J., Jung, Y. M., White, N., Alam, S., et al. (2019). Highly efficient Tm^{3+} doped germanate large mode area single mode fiber laser. *Opt. Mater. Exp*. 9, 4115–4125. doi: 10.1364/OME.9.004115

Tang, G. W., Zhu, T. T., Liu, W. W., Qiao, T., Sun, M., Chen, D. D., et al. (2016). Tm^{3+} doped lead silicate glass single mode fibers for 2.0 μm laser applications. *Opt. Mater. Exp*. 6, 2147–2157. doi: 10.1364/OME.6.002147

Terra, I. A.,A; Camargo, A. S. S., Nunes, L. A. O., Carvalho, R. A., and Li, M. S. (2006). Evaluation of the OH^- influence on visible and near-infrared quantum efficiencies of Tm^{3+} and Yb^{3+} codoped sodium aluminophoshate glasses. *J. Appl. Phys*. 100:123103. doi: 10.1063/1.2400510

Tian, Y., Li, B. P., Wang, J. R., Liu, Q. H., Chen, Y. L., Zhang, J. J., et al. (2019). The mid-infrared emission properties and energy transfer of Tm^{3+}/Er^{3+} codoped tellurite glass pumped by 808/980 nm laser diodes. *J. Lumin*. 214:116586. doi: 10.1016/j.jlumin.2019.116586

Wang, R. S., Meng, X. W., Yin, F. X., Feng, Y., Qin, G. S., and Qin, W. P. (2013). Heavily erbium-doped low-hydroxyl fluorotellurite glasses for 2.7 μm laser applications. *Opt. Mater. Exp*. 3, 1127–1136. doi: 10.1364/OME.3.001127

Wang, W. C., Yuan, J., Liu, X. Y., Chen, D. D., Zhang, Q. Y., and Jiang, Z. H. (2014). An efficient 1.8 μm emission in Tm^{3+} and Yb^{3+}/Tm^{3+} doped fluoride modified germanate glasses for a diode-pump mid-infrared laser. *J. Non Cryst. Solids* 404, 19–25. doi: 10.1016/j.jnoncrysol.2014.07.026

Wang, W. C., Zhou, B., Xu, S. H., Yang, Z. M., and Zhang, Q. Y. (2019). Recent advances in soft optical glass fiber and fiber lasers. *Progr. Mater. Sci*. 101, 90–171. doi: 10.1016/j.pmatsci.2018.11.003

Yang, X. L., Wang, W. C., and Zhang, Q. Y. (2017). BaF_2 modified Cr^{3+} /Ho^{3+} co-doped germanate glass for efficient 2.0 μm fiber lasers. *J. Non Cryst. Solids* 482, 147–153. doi: 10.1016/j.jnoncrysol.2017.12.031

Yu, S. L., Yang, Z. M., and Xu, S. H. (2009). Judd–Ofelt and laser parameterization of Tm^{3+}-doped barium gallo-germanate glass fabricated with efficient dehydration methods. *Opt. Mater*. 31, 1723–1728. doi: 10.1016/j.optmat.2009.05.002

Yuan, J., Wang, W. C., Chen, D. D., Peng, M. Y., Zhang, Q. Y., and Jiang, Z. H. (2014). Enhanced 1.8 μm emission in Yb^{3+}/Tm^{3+} codoped tungsten tellurite glasses for a diode-pump 2.0 μm laser. *J. Non Cryst. Solids* 402, 223–230. doi: 10.1016/j.jnoncrysol.2014.06.008

Yuan, J., and Xiao, P. (2018). Compositional effects of Na_2O, GeO_2, and Bi_2O_3 on 1.8 μm spectroscopic properties of Tm^{3+} doped zinc tellurite glasses. *J. Lumin*. 196, 281–284. doi: 10.1016/j.jlumin.2017.12.054

Zhou, Y. X., Gai, N., Chen, F., and Yang, G. B. (2010). Effect of hydroxyl groups in erbium-doped tellurite- and bismuth-based glasses. *Opt. Fiber Technol*. 16, 318–322. doi: 10.1016/j.yofte.2010.08.002

Zou, X. L., and Toratani, H. (1996). Spectroscopic properties and energy transfers in Tm^{3+} singly- and Tm^{3+}/Ho^{3+} doubly-doped glasses. *J. Non Cryst. Solids* 195, 113–124. doi: 10.1016/0022-3093(95)00522-6

Conflict of Interest: The authors declare that the research was conducted in the absence of any commercial or financial relationships that could be construed as a potential conflict of interest.

frontiers in Chemistry

ORIGINAL RESEARCH
published: 26 January 2021
doi: 10.3389/fchem.2020.630050

Experimental and Modeling Investigations of Miniaturization in InGaN/GaN Light-Emitting Diodes and Performance Enhancement by Micro-Wall Architecture

Yiping Zhang[1]†, Shunpeng Lu[1†], Ying Qiu[2], Jing Wu[3], Menglong Zhang[3] and Dongxiang Luo[3]**

[1]School of Electrical and Electronic Engineering, Nanyang Technological University, Singapore, Singapore, [2]Guangdong Research and Design Center for Technological Economy, Guangzhou, China, [3]Institute of Semiconductors, South China Normal University, Guangzhou, China

OPEN ACCESS

Edited by:
Qifan Xue,
South China University of Technology, China

Reviewed by:
Ping Wang,
University of Michigan, United States
Xiaoming Wen,
Swinburne University of Technology, Australia
Liancheng Wang,
Central South University, China

***Correspondence:**
Yiping Zhang
yzhang059@ntu.edu.sg
Dongxiang Luo
luodx@gdut.edu.cn

†These authors have contributed equally to this work

Specialty section:
This article was submitted to Physical Chemistry and Chemical Physics, a section of the journal Frontiers in Chemistry

Received: 17 November 2020
Accepted: 21 December 2020
Published: 26 January 2021

Citation:
Zhang Y, Lu S, Qiu Y, Wu J, Zhang M and Luo D (2021) Experimental and Modeling Investigations of Miniaturization in InGaN/GaN Light-Emitting Diodes and Performance Enhancement by Micro-Wall Architecture. Front. Chem. 8:630050. doi: 10.3389/fchem.2020.630050

The recent technological trends toward miniaturization in lighting and display devices are accelerating the requirement for high-performance and small-scale GaN-based light-emitting diodes (LEDs). In this work, the effect of mesa size-reduction in the InGaN/GaN LEDs is systematically investigated in two lateral dimensions (*x*- and *y*-directions: parallel to and perpendicular to the line where p-n directions are) both experimentally and numerically. The role of the lateral size-reduction in the *x*- and *y*-directions in improving LED performance is separately identified through experimental and modeling investigations. The narrowed dimension in the *x*-direction is found to cause and dominate the alleviated current crowding phenomenon, while the size-reduction in the *y*-direction has a minor influence on that. The size-reduction in the *y*-orientation induces an increased ratio of perimeter-to-area in miniaturized LED devices, which leads to improved thermal dissipation and light extraction through the sidewalls. The grown and fabricated LED devices with varied dimensions further support this explanation. Then the effect of size-reduction on the LED performance is summarized. Moreover, three-micro-walls LED architecture is proposed and demonstrated to further promote light extraction and reduce the generation of the Joule heat. The findings in this work provide instructive guidelines and insights on device miniaturization, especially for micro-LED devices.

Keywords: GaN, light-emitting diode, miniaturization, size effect, micro-LED, current crowding effect, thermal dissipation

INTRODUCTION

Owing to advantages in reliability, long lifetime, vivid colors, and energy efficiency, InGaN/GaN multiple quantum well (MQW) light-emitting diodes (LEDs) are regarded as a promising candidate to replace conventional lighting devices and have been extensively applied in various areas, such as automotive, backlight sources, display screens, electronic equipment, communicating applications, and general lighting (Ponce and Bour, 1997; Pimputkar et al., 2009; Kobayashi et al., 2012; Han et al., 2013). In order to fulfill the requirement of these applications, LEDs with various sizes and geometries are developed and fabricated accordingly (Kim et al., 2013; Cai et al., 2018). The

micro-LED display is an emerging technology in general lighting and displays technology, which has shown its advantages in low power consumption, high dynamic range, short response time, and high contrast ratio (Hwang et al., 2017). The micro-LED display utilizes existing LED technology, which is significantly more efficient at producing light compared to OLED, cathode ray tube (CRT), and other display technologies. The huge opportunity in consumer electronics and the increasing applications in virtual reality, wearable devices, augmented reality, and medical applications become the major driving force behind the recent rapidly growing development in mini- and micro-LEDs (Park et al., 2009; Scharf et al., 2016; Son et al., 2018; Roche, 2019; Tang et al., 2019; Zhang et al., 2020). Extensive efforts of research have been devoted to studying the influence of size-reduction in the GaN-based LEDs (Choi et al., 2003a; Sadaf et al., 2016; Kang et al., 2017; Wu et al., 2018; Huang et al., 2019; Wong et al., 2019; Lin and Jiang, 2020). Francois et al. reported the lower external quantum efficiency (EQE) and maximum EQE when the LED devices went smaller (Olivier et al., 2017). Anis et al. also suggested the stronger Shockley-Read-Hall (SRH) non-radiative recombination was caused when the LED size tended to diminish (Daami et al., 2018). However, Tao et al. pointed out that the strain in QW was relaxed and Auger recombination was suppressed for smaller size LEDs, which lead to improved performance (Tao et al., 2012). Besides, Bourim et al. indicated that the junction temperature of larger LED chips was higher than the smaller ones under the same current densities, which resulted in carrier escapes from quantum wells thus degraded performance was observed (Bourim and Han, 2016). Huang et al. further concluded in the recent work that micro-LED would gradually move toward the central stage of the future display due to its advantages in energy efficiency (Huang et al., 2020).

Despite extensive reports on the effect of size-reduction in the GaN-based LEDs, no conclusive remarks can be drawn. Therefore, a systematical study with complementary theoretical simulation and experimental investigation is strongly required to resolve the discrepancy and uncover the underlying physics. Furthermore, most of the previous works focus on studying the influence of the total size or shape of the lateral mesa on the LED performance without analyzing the individual influence of size-reduction in one certain dimension. Thus, in this work, the size-reduction effect on the performance of InGaN/GaN LEDs is systematically analyzed with both experimental and numerical investigations. The influence of the size-reduction of the lateral mesa in two directions on the performance of the LED chip is separately identified. Then the effect of size-reduction on the GaN-based LEDs is concluded, which offers instructive guidelines in device miniaturization. Finally, a three-micro-walls LED architecture is proposed and demonstrated with the aim of improving the light extraction efficiency and reducing the thermal heat generated.

MATERIALS AND METHODS

The InGaN/GaN MQW LEDs studied in this work were grown on c-plane patterned sapphire substrates by metal-organic chemical vapor deposition (MOCVD) system. The sapphire substrate used is the two-inch patterned-sapphire substrate that has periodic cone patterns with a diameter of 2.4 μm, a height of 1.5 μm, and a pitch of 3 μm. The epitaxial growth was initiated on a 30-nm thick low-temperature GaN nucleation layer followed by a 4 μm unintentionally doped n-type GaN (u-GaN) layer. Subsequently, a 2-μm thick Si-doped GaN layer was grown with a doping concentration of 5×10^{18} cm^{-3}, in which SiH_4 was adopted as the dopant source. Then, eight pairs of $In_{0.15}Ga_{0.85}N$/GaN MQWs with 3-nm thick QW and 12-nm thick QB were grown. In addition, a 20-nm thick p-doped $Al_{0.15}Ga_{0.85}N$ electron blocking layer (EBL) was grown to suppress the excess electron overflow into the p-GaN region. Then a 200-nm thick Mg-doped GaN with a doping concentration of 3×10^{17} cm^{-3} was grown as the hole source layer. The p-type conductivity of the EBL and the hole source layer was realized by Mg doping where Cp_2Mg was used as the Mg precursor. Subsequent to the epitaxial growth, the LED wafers were fabricated into flip-chip LED devices using standard fabrication processes. The mesa area was shaped using reactive ion etching (RIE) for LED devices of different sizes. Ni/Ag (5 nm/5 nm) metal layers were deposited as the current spreading layer using e-beam evaporation, and Ti/Au (30 nm/1,000 nm) metal layers were deposited as p- and n-electrode contact. A schematic diagram of the device structure is shown in **Figure 1A**. The current-voltage characteristics were determined by a LED tester (M2442S-9A Quatek Group) and the optical output power was measured by an integrating sphere attached to an Ocean Optics spectrometer (QE65000).

To study the physical mechanism on how the size-reduction of the lateral mesa influences the LED performance, numerical simulations were conducted by Advanced Physical Models of Semiconductor Devices (APSYS) simulator, which self-consistently solves the Schrödinger equation, continuity equation, and Poisson equation with proper boundary conditions. In the simulations, the Auger recombination coefficient was set to $1 \times 1{,}042\ m^6/s$ and 40% of the polarization charges were assumed such that 60% of the theoretical polarization charges were released because of the crystal strain relaxation by generating dislocations. The other parameters used in the simulation can be found elsewhere (Meneghini et al., 2009; Kim et al., 2010; Kuo et al., 2011; Park et al., 2013; Zhang et al., 2013; Zhang et al., 2017).

RESULTS AND DISCUSSION

Figure 1A presents the schematic diagram of the structure and the current flow paths for the flip-chip InGaN/GaN LEDs, which is extensively used in commercial products and academic research due to its superiority in light extraction. In order to eliminate the influence of the electrode pattern (eg fingers), the p-contact metal layer covers the entire top surface of the p-GaN layer. As shown in **Figure 1A**, there are two lateral orientations to follow when reducing the mesa size of the LED device: *x*- and *y*-directions. In order to identify the individual influence on the LED performance, the effect of size-reduction in these two lateral orientations is separately investigated with the *x*-direction as the

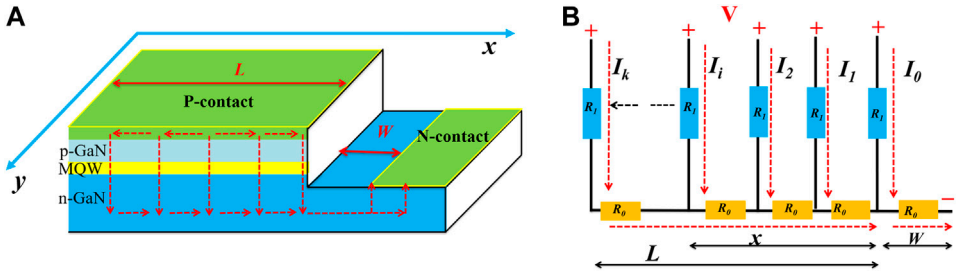

FIGURE 1 | (A) The schematic diagram of the structure and the current flow paths from the p-GaN layer to the n-GaN layer, and **(B)** equivalent circuit of current path model for the flip-chip InGaN/GaN LEDs.

beginning. As we can see from the equivalent circuit shown in **Figure 1B**, there are plenty of current paths from the p-GaN layer to the n-GaN layer and according to Ohm's law we will have:

$$I_i = \frac{V}{R_1 + x_i R_0 + W R_0}, \tag{1}$$

where I_i is current corresponding to each path where $i = 1, 2, \ldots, k-1$, and k, in which k is infinity, x_i denotes its corresponding length, V is the bias voltage applied to the LED, R_1 denotes the resistance along the vertical direction from the p-contact layer to the active region, L is the mesa size in the x-direction, W is the lateral length from the edge of n-contact to the edge of the p-GaN layer, and R_0 is the resistance per unit length of the n-GaN layer in the lateral direction along x. Then the average current for all current paths is obtained, as shown below:

$$I_{\text{average}} = \frac{1}{L}\int_0^L I_i \mathrm{d}x = \frac{1}{L}\int_0^L \frac{V}{R_1 + x_i R_0 + W R_0}\mathrm{d}x, \tag{2}$$

$$I_{\text{average}} = \frac{V}{R_0 L}\left(\ln\frac{1}{R_1 + L R_0 + W R_0} - \ln\frac{1}{R_1 + W R_0}\right). \tag{3}$$

As we can see from the above equation, the average current for all the current paths is increased with the reduction of mesa size in the x-direction, which means the current becomes more uniform in the lateral direction and thus the current crowding effect is alleviated. As the p-GaN layer is entirely covered by the p-contact metal, the reduction of the mesa size in the y-direction has a minor contribution in alleviating the current crowding effect. Therefore, the alleviated current crowding as a consequence of the narrowing in the mesa size mainly originates from the uniform current spreading in the lateral x-direction. It is worth noting that if the finger shape or other types of electrode pattern is adopted in the p-contact metal layer, the electrode distribution along the lateral directions (both x- and y-directions) will further affect the current spreading performance. In that case, the current spreading is subjected to the coupling effect of size-reduction in the x-direction and electrode patterns (Guo and Schubert, 2001; Song, 2012).

In order to further support the above conclusion that the size-reduction in the x-direction contributes to alleviated current crowding, the numerical calculations are conducted for the InGaN/GaN MQW LEDs with varied device dimensions of 45 × 200, 90 × 200, 135 × 200, and 180 × 200 μm^2, respectively. Here, the mesa dimension in the x-direction is narrowed from 180 to 45 μm, while the dimension in the y-direction is fixed at 200 μm. **Figure 2A** shows horizontal profiles of electron current densities in the p-GaN layer for the LEDs with different mesa dimensions. Since the LEDs are of different mesa dimensions, the electron distribution along the x-direction in **Figure 2A** is normalized by dividing the corresponding dimension (45, 90, 135, 180 μm). It can be clearly seen that most electrons are located at the edge of the p-electrode for all the LEDs with varied mesa sizes, implying the inhomogeneous distribution of carrier in the x-direction. This is called the current crowding effect, which is always a tough issue for lateral LED geometry. However, the electrons distribute more uniform along the x-direction for smaller LEDs, as presented in **Figure 2A**, which indicates alleviated current crowding. The improved performance in the narrowed LEDs can also be observed in the curves for current density (J) vs. voltage (V) as shown in **Figure 2B**, which is attributed to the uniform current spreading and consistent with the results in the current path model and previous reports (Tian et al., 2012; Yang et al., 2014; Bourim and Han, 2016).

Moreover, owing to the improved current spreading, the electron overflow into the p-GaN layer is suppressed. The simulated electron concentration near the p-GaN layer is depicted in **Figure 2C** for the LED devices with varied dimensions under the current injection level of 300 A/cm^2, which demonstrates that the electron concentration in EBL and the p-GaN region is reduced when the mesa dimension decreases from 180 to 45 μm. The reduction of the electron concentration in the p-doped region indicates the effective suppression of the electron leakage. These results suggest that with a narrowed mesa dimension in the x-direction, the current crowding phenomenon is alleviated and the electrons will spread more homogeneously.

Based on the above analysis, the conclusion can be drawn that the mesa size-reduction of the InGaN/GaN LEDs in the lateral x-orientation leads to alleviated current crowding thus improved performance is obtained, while the reduction in the y-direction makes a minor contribution to the current spreading performance. However, the diminished dimension in the y-direction increases the ratio of perimeter-to-area. The increased ratio of perimeter-to-area in the smaller LEDs leads to improved heat dissipation and reduced self-heating, hence the

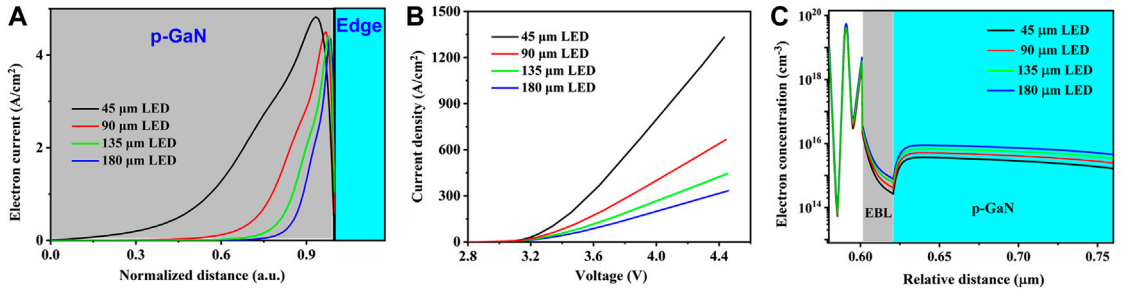

FIGURE 2 | (A) The simulated horizontal profiles of electron current density along the *x*-direction in the p-GaN layer as a function of normalized distance, **(B)** calculated *J-V* curves, and **(C)** computed electron concentration in the EBL and the p-GaN region at the current density of 300 A/cm^2 for LEDs with varied mesa dimensions of 45 × 200, 90 × 200, 135 × 200, and 180 × 200 μm^2, respectively.

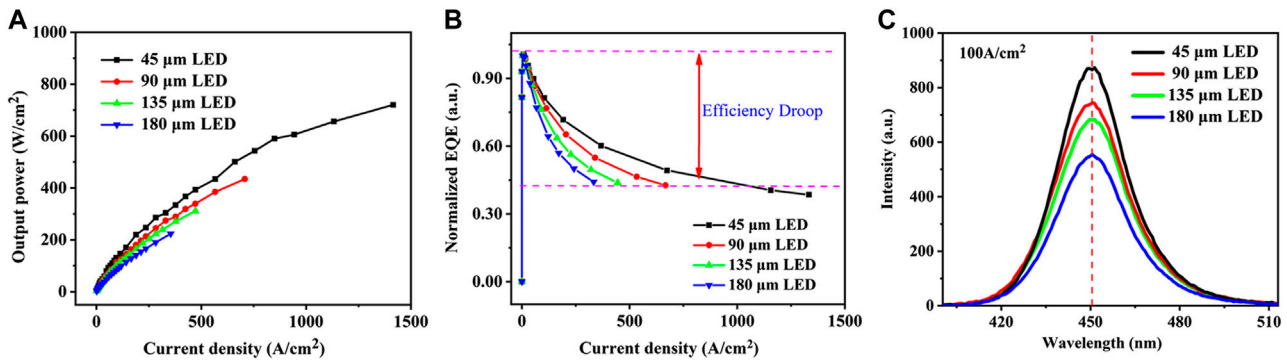

FIGURE 3 | (A) Experimentally measured optical output power as a function of forward current density, **(B)** normalized EQE as a function of forward current density, and **(C)** electroluminescent spectral curves under the current density of 100 A/cm^2 for LEDs with different dimensions of the mesa.

temperature in the LED device is decreased (Kim et al., 2012; Horng et al., 2015). Moreover, the light extraction through the sidewalls is improved with diminished LED size, which contributes to the improvement of the LED performance (Stark et al., 2011).

In order to confirm the above conclusion, InGaN/GaN LED chips with different sizes are fabricated for investigation with the dimensions of 200 × 45, 200 × 90, 200 × 135, and 200 × 180 μm^2, respectively, which have the perimeter-to-area ratio of 0.54, 0.32, 0.25, and 0.21, respectively. Here, the mesa dimension in the *y*-direction is narrowed from 180 to 45 μm, while the dimension in the *x*-direction is fixed at 200 μm. All LED chips are fabricated within a 2 mm × 2 mm region on the same epitaxial wafer to avoid the spatial inhomogeneity in the wafer with standard fabrication procedures in order to eliminate the influence by crystalline quality, epitaxial growth, and fabrication processes, which is the possible reason for the discrepancy in the conclusion of the size-reduction effect among the previous reports (Tao et al., 2012; Olivier et al., 2017; Singh et al., 2017; Daami et al., 2018). The p-contact metal totally covers the top surface of the p-GaN layer to avoid the influence of the electrode pattern, which is different from the previous works (Song, 2012; Singh et al., 2017). The experimentally measured optical output power as a function of current density for LEDs with different mesa dimensions are illustrated in **Figure 3A**, from which we can see that the optical output power increases consistently with the mesa size narrowed from 180 to 45 μm in the *y*-direction. The efficiency droop indicated in **Figure 3B** is also reduced for the narrowed LED devices, which is consistent with the observation in the previous report (Tao et al., 2012). The variation in the ending point of data shown in **Figures 3A,B** is because the optical output power and current are measured under the same biased voltage for LEDs with varied sizes. The enhancement in the performance observed in the smaller LED devices is attributed to the improved light extraction in the sidewall and improved heat dissipation due to the higher perimeter-to-area ratio and reduced device temperature (Choi et al., 2003a; Choi et al., 2003b). **Figure 3C** presents the electroluminescence (EL) spectra curves for the studied LEDs with different mesa dimensions, where the emission density is the strongest for the 45-μm LED. Meanwhile, the EL intensity for LEDs with larger mesa size is reduced as the increase of mesa dimension. The peak wavelength is about 450 nm and is not shifted when the size is reduced from 180 to 45 μm, as indicated in **Figure 3C**. However, it is worth noting that when the LED size is further reduced to the nanoscale, the blue shift in the EL curve can be anticipated due to reduced energy band tilting caused by the

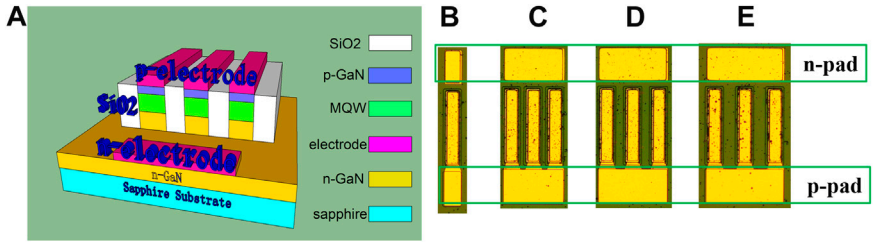

FIGURE 4 | (A) Schematic diagram of the proposed LED architecture with three-micro-walls, and the fabricated LED devices of **(B)** single-micro-wall as controlled group, **(C)** three-micro-walls with wall spacing of 11 μm, **(D)** three-micro-walls with wall spacing of 22 μm, and **(E)** three-micro-walls with wall spacing of 33 μm.

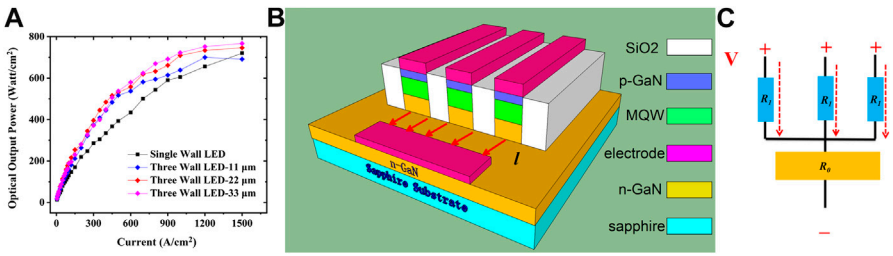

FIGURE 5 | (A) Experimentally measured optical output power for proposed three-micro-walls LED devices and single-wall device, **(B)** illustration of the current path for proposed LED device, and **(C)** corresponding simplified current path model.

strain relaxation in the smaller LED device (Demangeot et al., 2002; Wu et al., 2008; Stark et al., 2011).

Thereafter, we can conclude the effect of size-reduction (E) for InGaN/GaN LEDs as following:

$$E = C(x) + P(x, y) + T(x, y) + S(x, y) - N(x, y) \quad (4)$$

where $C(x)$ is the alleviated current crowding effect (Ge et al., 2019), $P(x, y)$ is the improvement achieved by the increased perimeter-to-area ratio, including improved thermal dissipation and light extraction (Choi et al., 2003a; Choi et al., 2003b), $T(x, y)$ is the reduced self-heating and improved heat distribution (Gong et al., 2010; Ploch et al., 2013), $S(x, y)$ is the enhancement owing to the strain relaxation (Demangeot et al., 2002; Tao et al., 2012; Ge et al., 2019), and $N(x,y)$ is the possible negative effect due to the increased nonradiative recombination (Gong et al., 2010; Stark et al., 2011), surface recombination (Jin et al., 2001), and current leakage induced by etching damage and impurities during fabrications (Jin et al., 2000; Stark et al., 2011). A more detailed quantitative analysis of the above factors is needed to determine the dominant ones and great precautions must be undertaken to avoid degradation in devices during the growth and fabrication processes for smaller LEDs.

In order to further improve the light extraction in the smaller InGaN/GaN LEDs, we design a three-micro-walls LED architecture by incorporating three micro-LEDs into a device. The schematic diagram of the proposed LED structure is shown in **Figure 4A**, in which the micro-walls are defined with the wall dimensions of 200 × 45 μm^2. In order to reduce the current leakage and increase the light extraction efficiency, the wall gap is filled up with SiO_2 by chemical vapor deposition (CVD), which has a refractive index of 1.47. For the proposed LEDs with three-micro-walls geometry, the wall spacing is designed to be varied as 11, 22, and 33 μm, and the corresponding fabricated LED devices are presented in **Figures 4C–E**, respectively. The single-micro-wall LED device is also introduced and fabricated as the controlled group, as shown in **Figure 4B**.

As the three-micro-walls LED device is three times the size of the single-wall LED, the optical power of the former is divided by three for comparison. The experimentally measured optical output power of the devices is shown in **Figure 5A**, in which all the proposed three-micro-walls LED devices perform better than the controlled group due to the improved light extraction through sidewalls achieved by the filling up of SiO_2 in the gap. Meanwhile, the proposed architecture with the wall spacing of 33 μm has the best performance because more light escapes from the sidewall with a larger gap between the micro-walls. More importantly, there is less thermal heat generation for the LED device with wider wall spacing due to the reduced series resistance when current horizontally passes the n-GaN layer. **Figures 5B,C** depict the current paths and the corresponding simplified current paths model for the LEDs with three-micro-walls geometry. As indicated in **Figure 5C**, the Joule heat (J_{heat}) generated in the LED can be expressed as:

$$J_{\text{heat}} = I^2(R_1 + R_0) = I^2\left(R_1 + p\frac{l}{S}\right), \quad (5)$$

where R_1 is the total resistance from top contact layer to active region in the vertical direction, R_0 denotes the resistance of n-GaN

layer, I is current, p denotes the resistivity of n-GaN layer, l is the lateral distance from n-electrode to mesa edge, and S is the cross-sectional area of the n-GaN layer perpendicular to the direction of l. According to **Eq. 5**, with the increasing spacing of the micro-walls, the resistance of R_0 increases due to the enlarged area S. Hence, the total heat generation in the LED device is reduced, which contributes to improved LED performance. It is worth noting that with a larger gap, the thermal heat dissipation is improved accordingly. Thus, the proposed LED architecture has superior performance due to improved light extraction, less thermal heat generation, and better heat dissipation.

CONCLUSION

The InGaN/GaN LEDs with different mesa dimensions are investigated both experimentally and numerically to explore the size-reduction effect on the LED performance. The individual role of the size-reduction in the lateral x- and y-directions is identified separately. The physical mechanism of performance enhancement by mesa size-reduction is revealed by using a model of current paths, which suggests that the current crowding effect is alleviated when the lateral mesa size is narrowed in the x-direction. The calculated results indicate that the LED devices with narrowed dimensions in the x-direction have reduced electron leakage and a better current-voltage characteristic under the same current density, which is attributed to the effectively improved current spreading. Backed by the experiments, the decrease of the mesa size in the y-direction is found to improve the LED performance, which is owing to a higher ratio of perimeter-to-area, better thermal dissipation, and improved light extraction. Then the effect of size-reduction on the LED performance is concluded. Finally, a new LED architecture with three-micro-walls is proposed and demonstrated. The proposed three-micro-walls LEDs are observed to have improved optical performance compared to the controlled group and with the increase of wall spacing, the improvement becomes conspicuous, which is owing to the increased light extraction and less Joule heat generation resulting from the reduced series resistance when current horizontally passes the n-GaN layer.

DATA AVAILABILITY STATEMENT

The original contributions presented in the study are included in the article/Supplementary Material, further inquiries can be directed to the corresponding authors.

AUTHOR CONTRIBUTIONS

All authors have made a substantial, direct, and intellectual contribution to the work and approved it for publication.

ACKNOWLEDGMENTS

We gratefully acknowledge that this work is supported by the Guangdong Basic and Applied Basic Research Foundation (Grant No. 2020B1515020032), the National Natural Science Foundation of China (Grant No. 62074060), the Science and Technology Program of Guangzhou (Grant No. 2019050001), the Guangdong Science and Technology Plan (Grant No. 2019B040403003) and the Pearl River S&T Nova Program of Guangzhou (Grant No. 201906010058).

REFERENCES

Bourim, E.-M., and Han, J. I. (2016). Size effect on negative capacitance at forward bias in InGaN/GaN multiple quantum well-based blue LED. *Electron. Mater. Lett.* 12, 67–75. doi:10.1007/s13391-015-5281-9

Bruchas, Y., Kumakura, K., Akasaka, T., and Makimoto, T. (2012). Layered boron nitride as a release layer for mechanical transfer of GaN-based devices. *Nature* 484, 223–227. doi:10.1038/nature10970

Cai, Y., Zou, X., Liu, C., and Lau, K. M. (2018). Voltage-controlled GaN HEMT-LED devices as fast-switching and dimmable light emitters. *IEEE Electron. Device Lett.* 39, 224–227. doi:10.1109/led.2017.2781247

Chen, M. S., Nakamura, S., and Denbaars, S. P. (2019). Review—progress in high performance III-nitride micro-light-emitting diodes. *ECS Journal of Solid State Science and Technology* 9, 015012. doi:10.1149/2.0302001jss

Choi, H. W., Jeon, C. W., Dawson, M. D., Edwards, P. R., and Martin, R. W. (2003a). Fabrication and performance of parallel-addressed InGaN micro-LED arrays. *IEEE Photon. Technol. Lett.* 15, 510–512. doi:10.1109/lpt.2003.809257

Choi, H. W., Jeon, C. W., Dawson, M. D., Edwards, P. R., Martin, R. W., and Tripathy, S. (2003b). Mechanism of enhanced light output efficiency in InGaN-based microlight emitting diodes. *J. Appl. Phys.* 93, 5978–5982. doi:10.1063/1.1567803

Daami, A., Olivier, F., Dupré, L., Henry, F., and Templier, F. (2018). 59-4: invited Paper: electro-optical size-dependence investigation in GaN micro-LED devices. *SID Symp. Digest Tech. Papers* 49, 790–793. doi:10.1002/sdtp.12325

Demangeot, F., Gleize, J., Frandon, J., Renucci, M. A., Kuball, M., Peyrade, D., et al. (2002). Optical investigation of micrometer and nanometer-size individual GaN pillars fabricated by reactive ion etching. *J. Appl. Phys.* 91, 6520–6523. doi:10.1063/1.1468908

Gong, Z., Jin, S., Chen, Y., Mckendry, J., Massoubre, D., Watson, I. M., et al. (2010). Size-dependent light output, spectral shift, and self-heating of 400 nm InGaN light-emitting diodes. *J. Appl. Phys.* 107, 013103. doi:10.1063/1.3276156

Guo, X., and Schubert, E. F. (2001). Current crowding and optical saturation effects in GaInN/GaN light-emitting diodes grown on insulating substrates. *Appl. Phys. Lett.* 78, 3337–3339. doi:10.1063/1.1372359

Han, N., Cuong, T., Han, M., Ryu, B., Chandramohan, S., Park, J., et al. (2013). Improved heat dissipation in gallium nitride light-emitting diodes with embedded graphene oxide pattern. *Nat. Commun.* 4, 1452. doi:10.1038/ncomms2448

Hong, R.-H., Chen, K.-Y., Tien, C.-H., and Liao, J.-C. (2015). Effects of mesa size on current spreading and light extraction of GaN-based LEDs. *J. Disp. Technol.* 11, 1010–1013. doi:10.1109/jdt.2015.2461015

Huang Chen, Y.-R., Yu, P., Chiu, C., Chang, C.-Y., and Kuo, H. (2008). "*Analysis of strain relaxation and emission spectrum of a free-standing GaN-based nanopillar*," in Eighth International Conference on Solid State Lighting, San Diego, CA (London: SPIE).

Huang, Y., Hsiang, E.-L., Deng, M.-Y., and Wu, S.-T. (2020). Mini-LED, Micro-LED and OLED displays: present status and future perspectives. *Light Sci. Appl.* 9, 105. doi:10.1038/s41377-020-0341-9

Huang, Y., Tan, G., Gou, F., Li, M.-C., Lee, S.-L., and Wu, S.-T. (2019). Prospects and challenges of mini-LED and micro-LED displays. *J. Soc. Inf. Disp.* 27, 387–401. doi:10.1002/jsid.760

Hwang, D., Mughal, A., Pynn, C. D., Nakamura, S., and Denbaars, S. P. (2017). Sustained high external quantum efficiency in ultrasmall blue III–nitride micro-LEDs. *APEX* 10, 032101. doi:10.7567/apex.10.032101

Jin, S. X., Li, J., Li, J. Z., Lin, J. Y., and Jiang, H. X. (2000). GaN microdisk light emitting diodes. *Appl. Phys. Lett.* 76, 631–633. doi:10.1063/1.125841

Jin, S. X., Shakya, J., Lin, J. Y., and Jiang, H. X. (2001). Size dependence of III-nitride microdisk light-emitting diode characteristics. *Appl. Phys. Lett.* 78, 3532–3534. doi:10.1063/1.1376152

Kang, C. M., Kong, D. J., Shim, J. P., Kim, S., Choi, S. B., Lee, J. Y., et al. (2017). Fabrication of a vertically-stacked passive-matrix micro-LED array structure for a dual color display. *Optic Express* 25, 2489–2495. doi:10.1364/OE.25.002489

Kim, T. I., Jung, Y. H., Song, J., Kim, D., Li, Y., Kim, H. S., et al. (2012). High-efficiency, microscale GaN light-emitting diodes and their thermal properties on unusual substrates. *Small* 8, 1643–1649. doi:10.1002/smll.201200382

Kuo, Y.-K., Wang, T.-H., Chang, J.-Y., and Tsai, M.-C. (2011). Advantages of InGaN light-emitting diodes with GaN-InGaN-GaN barriers. *Appl. Phys. Lett.* 99, 091107. doi:10.1063/1.3633268

Lee, K. S., Kim, J. H., Jung, S. J., Park, Y. J., and Cho, S. N. (2010). Stable temperature characteristics of InGaN blue light emitting diodes using AlGaN/GaN/InGaN superlattices as electron blocking layer. *Appl. Phys. Lett.* 96, 091104. doi:10.1063/1.3340939

Lin, J. Y., and Jiang, H. X. (2020). Development of microLED. *Appl. Phys. Lett.* 116, 100502. doi:10.1063/1.5145201

Manin-Ferlazzo, C., Li, J., Wang, G., Su, K., and Lu, X. (2019). Size effect on optical performance of blue light-emitting diodes. *J. Semiconduct.* 40, 102301. doi:10.1088/1674-4926/40/10/102301

Meneghini, M., Trivellin, N., Meneghesso, G., Zanoni, E., Zehnder, U., and Hahn, B. (2009). A combined electro-optical method for the determination of the recombination parameters in InGaN-based light-emitting diodes. *J. Appl. Phys.* 106, 114508. doi:10.1063/1.3266014

Olivier, F., Tirano, S., Dupré, L., Aventurier, B., Largeron, C., and Templier, F. (2017). Influence of size-reduction on the performances of GaN-based micro-LEDs for display application. *J. Lumin.* 191, 112–116. doi:10.1016/j.jlumin.2016.09.052

Park, J. H., Kim, D. Y., Hwang, S., Meyaard, D., Schubert, E. F., Han, Y. D., et al. (2013). Enhanced overall efficiency of GaInN-based light-emitting diodes with reduced efficiency droop by Al-composition-graded AlGaN/GaN superlattice electron blocking layer. *Appl. Phys. Lett.* 103, 061104. doi:10.1063/1.4817800

Park, S. I., Xiong, Y., Kim, R. H., Elvikis, P., Meitl, M., Kim, D. H., et al. (2009). Printed assemblies of inorganic light-emitting diodes for deformable and semitransparent displays. *Science* 325, 977–981. doi:10.1126/science.1175690

Ploch, N. L., Rodriguez, H., Stolmacker, C., Hoppe, M., Lapeyrade, M., Stellmach, J., et al. (2013). Effective thermal management in ultraviolet light-emitting diodes with micro-LED arrays. *IEEE Trans. Electron. Dev.* 60, 782–786. doi:10.1109/ted.2012.2234462

Ponce, F. A., and Bour, D. P. (1997). Nitride-based semiconductors for blue and green light-emitting devices. *Nature* 386, 351–359. doi:10.1038/386351a0

Roche, E. T. (2019). Implanted device enables responsive bladder control. *Nature* 565, 298–300. doi:10.1038/d41586-018-07811-1

Rogers, S., Speck, J. S., Denbaars, S. P., and Nakamura, S. (2009). Prospects for LED lighting. *Nat. Photon.* 3, 180–182. doi:10.1038/nphoton.2009.32

Rogers, T. I., Mccall, J. G., Jung, Y. H., Huang, X., Siuda, E. R., Li, Y., et al. (2013). Injectable, cellular-scale optoelectronics with applications for wireless optogenetics. *Science* 340, 211–216. doi:10.1126/science.1232437

Sadaf, S. M., Ra, Y. H., Szkopek, T., and Mi, Z. (2016). Monolithically integrated metal/semiconductor tunnel junction nanowire light-emitting diodes. *Nano Lett.* 16, 1076–1080. doi:10.1021/acs.nanolett.5b04215

Scharf, R., Tsunematsu, T., Mcalinden, N., Dawson, M. D., Sakata, S., and Mathieson, K. (2016). Depth-specific optogenetic control *in vivo* with a scalable, high-density µLED neural probe. *Sci. Rep.* 6, 28381. doi:10.1038/srep28381

Singh, S., Kumar, S., Pal, S., and Dhanavantri, C. (2017). Performances of p-side down vertical InGaN/GaN blue light-emitting diodes with chip size. *Optic Laser. Technol.* 95, 165–171. doi:10.1016/j.optlastec.2017.05.002

Son, K. R., Lee, T. H., Lee, B. R., Im, H. S., and Kim, T. G. (2018). Nitride-based microlight-emitting diodes using AlN thin-film electrodes with nanoscale indium/tin conducting filaments. *Small* 14, 1801032. doi:10.1002/smll.201801032

Song, X., Zeng, J., Jin, Y., and Meng, X. (2012). Optoelectronic properties of GaN-based light-emitting diodes with different mesa structures. *Mater. Sciences Appl.* 03, 838–842. doi:10.4236/msa.2012.312122

Stark, C. J. M., Detchprohm, T., and Wetzel, C. (2011). The role of mesa size in nano-structured green AlGaInN light-emitting diodes. *Phys. Status Solidi C* 8, 2311–2314. doi:10.1002/pssc.201001190

Tang, B., Miao, J., Liu, Y., Wan, H., Li, N., Zhou, S., et al. (2019). Enhanced light extraction of flip-chip mini-LEDs with prism-structured sidewall. *Nanomaterials* 9, 319. doi:10.3390/nano9030319

Tao, Y. B., Wang, S. Y., Chen, Z. Z., Gong, Z., Xie, E. Y., Chen, Y. J., et al. (2012). Size effect on efficiency droop of blue light emitting diode. *Phys. Status Solidi C* 9, 616–619. doi:10.1002/pssc.201100483

Wu, T., Sher, C.-W., Lin, Y., Lee, C.-F., Liang, S., Lu, Y., et al. (2018). Mini-LED and micro-LED: promising candidates for the next generation display technology. *Appl. Sci.* 8, 1557. doi:10.3390/app8091557

Yang, W., Zhang, S., Mckendry, J. J. D., Herrnsdorf, J., Tian, P., Gong, Z., et al. (2014). Size-dependent capacitance study on InGaN-based micro-light-emitting diodes. *J. Appl. Phys.* 116, 044512. doi:10.1063/1.4891233

Zhang, K., Liu, Y., Kwok, H.-S., and Liu, Z. (2020). Investigation of electrical properties and reliability of GaN-based micro-LEDs. *Nanomaterials* 10, 689. doi:10.3390/nano10040689

Zhang, P., Mckendry, J. J. D., Gong, Z., Guilhabert, B., Watson, I. M., Gu, E., et al. (2012). Size-dependent efficiency and efficiency droop of blue InGaN micro-light emitting diodes. *Appl. Phys. Lett.* 101, 231110. doi:10.1063/1.4769835

Zhang, Y., Zhang, Z.-H., Tan, S. T., Hernandez-Martinez, P. L., Zhu, B., Lu, S., et al. (2017). Investigation of p-type depletion doping for InGaN/GaN-based light-emitting diodes. *Appl. Phys. Lett.* 110, 033506. doi:10.1063/1.4973743

Zhang, Z.-H., Tiam Tan, S., Kyaw, Z., Ji, Y., Liu, W., Ju, Z., et al. (2013). InGaN/GaN light-emitting diode with a polarization tunnel junction. *Appl. Phys. Lett.* 102. doi:10.1063/1.4806978

Conflict of Interest: The authors declare that the research was conducted in the absence of any commercial or financial relationships that could be construed as a potential conflict of interest.

frontiers in Chemistry

ORIGINAL RESEARCH
published: 10 March 2021
doi: 10.3389/fchem.2021.639023

Strain-Reduced Micro-LEDs Grown Directly Using Partitioned Growth

Shunpeng Lu[1]†, Yiping Zhang[1†], Zi-Hui Zhang[1,2], Ping Chieh Tsai[1], Xueliang Zhang[1], Swee Tiam Tan[1,3]* and Hilmi Volkan Demir[1,4,5]**

[1]LUMINOUS! Center of Excellence for Semiconductor Lighting and Displays, The Photonics Institute, School of Electrical and Electronic Engineering, Nanyang Technological University, Singapore, Singapore, [2]Key Laboratory of Electronic Materials and Devices of Tianjin, School of Electronics and Information Engineering, Hebei University of Technology, Tianjin, China, [3]School of Energy and Chemical Engineering, Xiamen University Malaysia, Sepang, Malaysia, [4]School of Physics and Mathematical Sciences, Nanyang Technological University, Singapore, Singapore, [5]Department of Electrical and Electronic Engineering, Department of Physics, UNAM-Institute of Material Science and Nanotechnology, Bilkent University, Ankara, Turkey

Strain-reduced micro-LEDs in 50 μm × 50 μm, 100 μm × 100 μm, 200 μm × 200 μm, 500 μm × 500 μm, and 1,000 μm × 1,000 μm sizes were grown on a patterned c-plane sapphire substrate using partitioned growth with the metal-organic chemical-vapor deposition (MOCVD) technique. The size effect on the optical properties and the indium concentration for the quantum wells were studied experimentally. Here, we revealed that the optical properties can be improved by decreasing the chip size (from 1,000 to 100 μm), which can correspondingly reduce the in-plane compressive stress. However, when the chip size is further reduced to 50 μm × 50 μm, the benefit of strain release is overridden by additional defects induced by the higher indium incorporation in the quantum wells and the efficiency of the device decreases. The underlying mechanisms of the changing output power are uncovered based on different methods of characterization. This work shows the rules of thumb to achieve optimal power performance for strain-reduced micro-LEDs through the proposed partitioned growth process.

Keywords: micro-LED, strain release, partitioned growth model, size effect, QCSE, Raman

OPEN ACCESS

Edited by:
Baiquan Liu,
Sun Yat-Sen University, China

Reviewed by:
Ping Wang,
University of Michigan, United States
Daling Cui,
McGill University, Canada
Yuan Gao,
Shandong University, China

***Correspondence:**
Shunpeng Lu
lush0007@e.ntu.edu.sg
Swee Tiam Tan
sweetiam.tan@xmu.edu.my
Hilmi Volkan Demir
HVDEMIR@ntu.edu.sg

†These authors have contributed equally to this work

Specialty section:
This article was submitted to Physical Chemistry and Chemical Physics, a section of the journal Frontiers in Chemistry

Received: *08 December 2020*
Accepted: *22 January 2021*
Published: *10 March 2021*

Citation:
Lu S, Zhang Y, Zhang Z-H, Tsai PC, Zhang X, Tan ST and Demir HV (2021) Strain-Reduced Micro-LEDs Grown Directly Using Partitioned Growth. Front. Chem. 9:639023. doi: 10.3389/fchem.2021.639023

INTRODUCTION

During the past few decades, InGaN/GaN based light-emitting diodes (LEDs) have been extensively studied to improve the external quantum efficiency (EQE) and optical output power (Shuji et al., 1991; Tan et al., 2012; Ji et al., 2013; Zhang et al., 2013). Owing to the high efficiency, long lifetime, and versatile packaging flexibility, III-nitride based LEDs have been widely used as the backlighting for smartphones and flat-panel displays, and are very promising for applications such as visible light communication and micro-displays (Choi et al., 2004a; McKendry et al., 2010; McKendry et al., 2012). All these applications require small LED chips, which have superior properties including high current density, high power density and high response speed. Thus, small LEDs that hold these properties are imperatively needed. To this end, micro-LEDs have been previously reported (Choi et al., 2003; Choi et al., 2004b; Poher et al., 2008; Lu et al., 2014). Micro-LEDs can deliver much higher current density and power density than general broad-area LEDs due to the reduced thermal mass and Joule heating (Lu et al., 2014). Nevertheless, to reduce the costs and satisfy the outdoor applications of micro-displays and visible light communication, the performance of micro-LEDs needs to be further improved. However, in all of these previous reports, the top-down approach based on dry etching and patterning micro-size mesas was used and the performance of the LED

epitaxial wafers grown on the c-plane sapphire substrates is limited by the quantum confined Stark effect (QCSE) (Ryou et al., 2009). The strain induced large piezoelectric polarization fields contribute to the internal electric field reducing the oscillator strength and emission due to the QCSE (Tetsuya et al., 1997). To overcome this issue, numerous efforts have been made to release the strain. For example, nonpolar tetragonal $LiAlO_2$ substrate was used to reduce the QCSE by Waltereit et al. (Waltereit et al., 2000). InGaN/GaN multiquantum well (MQW) nanorod arrays were implemented to improve the efficiency of LEDs by Kim et al. (Kim et al., 2004). Graphene-assisted growth was carried out to address the strain-induced problems in LEDs (Chen et al., 2018; Wang et al., 2020). Substrates such as semi-polar and non-polar bulk GaN were used to achieve high internal quantum efficiency (IQE) and low droop LEDs by Nakamura et al. (Arpan et al., 2005; Denbaars et al., 2013). However, these proposed methods come at high costs of substrates or nanoimprint lithography technology. On the other hand, it is deemed that if the micro-LEDs could be directly *in situ* grown in the metal-organic chemical-vapor deposition (MOCVD) chamber by adopting the partitioned growth process, the QCSE can be reduced in such partition-grown micro-LEDs (PG micro-LEDs). Furthermore, compared with typically fabricated micro-LEDs using ICP etching, there is no side-wall defects, and the efficiency will be even higher. Therefore, in this work, we propose and show a low-cost and effective way to release the strain for achieving high-efficiency strain-reduced micro-LEDs through partitioned growth.

In this work, strain-reduced micro-LEDs with various sizes of 50 μm × 50 μm, 100 μm × 100 μm, 200 μm × 200 μm, 500 μm × 500 μm, and 1,000 μm × 1,000 μm are demonstrated to be directly grown on patterned c-plane sapphire substrates by using our MOCVD system. To protect these PG micro-LEDs during the dicing process, a margin (10 μm) was included between two individual chip partitions. Here we systematically investigated the size effect on the strain and studied the electrical and optical properties for the proposed PG micro-LEDs which are critical to optimize the size for PG micro-LEDs.

MATERIALS AND METHODS

The LED epitaxial wafers were grown on c-plane single polished sapphire substrates by the MOCVD system. The sapphire substrate was first deposited with SiO_2 (100 nm) by plasma enhanced chemical vapour deposition (PECVD), and the SiO_2 layer was then patterned and etched with reactive-ion etching (RIE) to obtain square opening regions with different sizes. The margin width between two opening regions was set to 10 μm. Trimethylaluminum (TMAl), trimethylindium (TMIn), trimethylgallium (TMGa), and ammonia (NH_3) were used as Al, In, Ga, and N precursors, respectively. The growth was initiated with a 3 μm thick unintentionally doped GaN, followed by a 5.5 μm thick Si-doped N-GaN (doping concentration ≈ $5 \times 10^{18}/cm^3$). Then, six pairs of $In_{0.15}Ga_{0.85}N$/GaN multiple quantum wells (MQWs) (thickness of 3 nm/12 nm) were grown. A Mg-doped $Al_{0.15}Ga_{0.85}N$ electron blocking layer (EBL), with a thickness of 20 nm, was grown to reduce the electron overflow. Finally, a 200 nm thick Mg-doped GaN (with a free hole concentration of $3 \times 10^{17}/cm^3$) was grown as the hole source layer. In both of the EBL and the hole source layers, bis(cyclopentadienyl)magnesium (Cp2Mg) was used as the Mg precursor.

The images of different PG micro-LEDs were taken by a scanning electron microscopy (SEM) (JEOL JSM-5600LV) system. Micro-Raman spectra were also recorded using a spectrometer (Horiba JY-T64000) equipped with an excitation laser of 532 nm wavelength to reveal the strain level. Electroluminescence (EL) spectra and the optical output power were acquired by an Ocean Optics spectrometer (QE65000) attached to an integrating sphere. The micro-LEDs were fabricated into the same size (1 mm × 1 mm) using micro-fabrication technique. A LED tester (M2442S-9A Quatek Group) was used to measure the current-voltage characteristics of the resulting LED chips.

RESULTS AND DISCUSSION

Figure 1 shows the SEM images for the PG micro-LEDs of different sizes and the pattern before growth. Here **Figures 1A,C,E,G,H** show the top-view images for the 50 μm × 50 μm, 100 μm × 100 μm, 200 μm × 200 μm, 500 μm × 500 μm, and 1,000 μm × 1,000 μm PG micro-LEDs, respectively. **Figures 1B,D,F** display the 45°-tilted-view images for the 50 μm × 50 μm, 100 μm × 100 μm, and 200 μm × 200 μm PG micro-LEDs, respectively. **Figure 1I** depicts the patterned sapphire substrate with SiO_2 before the epitaxial layers growth. As the top-view and 45°-tilted-view images for the 500 μm × 500 μm and 1,000 μm × 1,000 μm sizes look similar, here we only show the top-view images for these two sizes. From these images, we can observe that smaller PG micro-LEDs have a larger ratio of opening area. Since the chip dimension for PG micro-LEDs is smaller than the anode, which is made of a 1 mm × 1 mm contact on the P-GaN surface, the active light emission area has to be taken into consideration. To facilitate the analysis, we used the square of the side length over the square of the side length plus half of the margin width (10 μm) as the ratio of active lighting area. For example, the ratio of active lighting area for the 50 μm × 50 μm device is 50 × 50 over (50 + 5) × (50 + 5). After calculation, we find that the ratios of active lighting area are 83, 91, 95, 98, and 99%, respectively, for the 50 μm × 50 μm, 100 μm × 100 μm, 200 μm × 200 μm, 500 μm × 500 μm, and 1,000 μm × 1,000 μm devices. From the calculation results, we can see that 50 μm × 50 μm PG micro-LEDs possess a much smaller ratio of the active light emission area than others.

The optical output power and the external quantum efficiency (EQE) for these PG micro-LEDs of different sizes are presented in **Figures 2A,B**, which show that the optical performance is enhanced as the device size decreases from 1,000 μm × 1,000 μm–100 μm × 100 μm as a general trend. Higher optical output power can be obtained in smaller devices at a given current level. However, the 50 μm × 50 μm device exhibits a smaller optical output power and EQE than others at the lower current

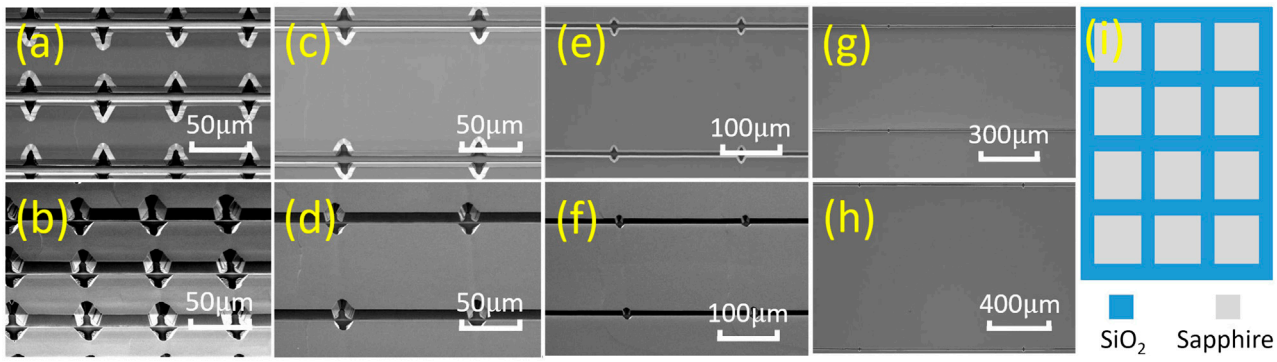

FIGURE 1 | SEM images of the proposed PG micro-LEDs grown in different sizes: top-view images for **(A)** 50 μm × 50 μm, **(C)** 100 μm × 100 μm, **(E)** 200 μm × 200 μm, **(G)** 500 μm × 500 μm, and **(H)** 1,000 μm × 1,000 μm chips; 45°-tilted-view images for **(B)** 50 μm × 50 μm, **(D)** 100 μm × 100 μm, and **(F)** 200 μm × 200 μm chips. **(I)** The schematic diagram of the patterned substrate before growth with SiO_2 on the sapphire substrate.

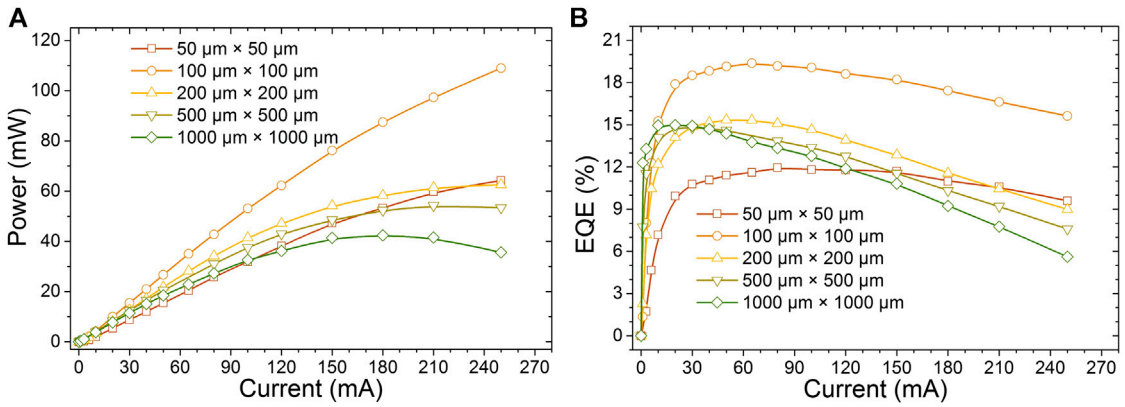

FIGURE 2 | (A) Optical power versus electrical current and **(B)** the EQE as a function of the current of PG micro-LEDs in different sizes.

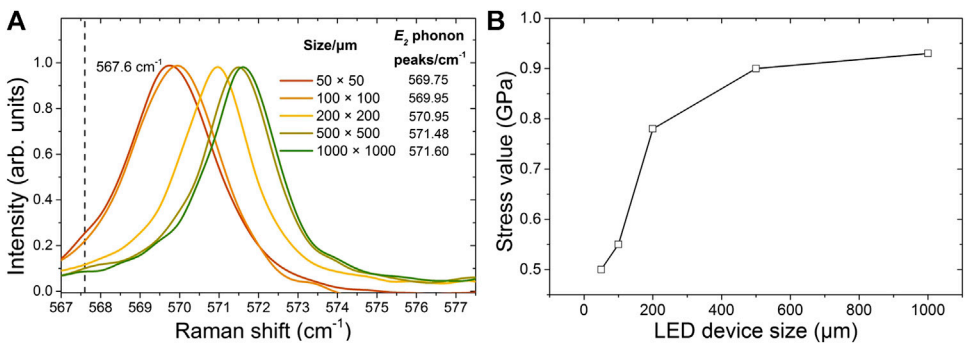

FIGURE 3 | (A) Raman spectra of E_2 (high) phonon peaks for the PG micro-LEDs of different sizes; **(B)** the in-plane compressive stress of different sized PG micro-LEDs.

density. As the 50 μm × 50 μm device has the smallest ratio of active lighting area, which may be one of the underlying reasons. Nevertheless, it seems that the small ratio of active lighting area is not the only reason for such a degradation for the 50 μm × 50 μm device. To figure out the underlying reasons of these observations, a series of characterization methods were performed and the results were analyzed.

Raman scattering is a widely used method to study the strain for III-nitrides (Tian et al., 2015). As the E_2 (high) phonon frequency is sensitive to strain, it has been extensively applied

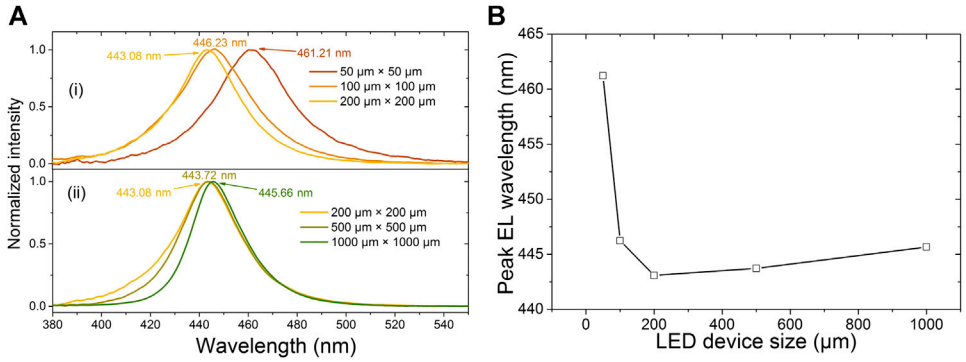

FIGURE 4 | EL spectra of the PG micro-LEDs of different sizes at 20 mA: **(A)** 1,000 μm × 1,000 μm, 500 μm × 500 μm, and 200 μm × 200 μm devices; and **(B)** 200 μm × 200 μm, 100 μm × 100 μm, and 50 μm × 50 μm devices. **(C)** Peak EL wavelength of different sized PG micro-LEDs.

to quantify the in-plane stress in GaN (Davydov et al., 1997; Tripathy et al., 1999). It is accepted that the peak of E_2 phonon in the unstrained GaN layer is 567.6 cm^{-1} (Davydov et al., 1998), and the blueshift for this phonon frequency indicates the in-plane compressive stress, whereas a redshift indicates the in-plane tensile stress. As depicted in **Figure 3A**, Raman spectra of E_2 phonon peaks for different PG micro-LEDs show that all the measured phonon frequencies of the PG micro-LEDs are blueshifted, which accounts for the in-plane compressive stress. From **Figure 3A**, we can also see that with the size decreasing from 1,000 μm × 1,000 μm–50 μm × 50 μm, the E_2 phonon peaks move toward to the unstrained 567.6 cm^{-1}, which indicates that the in-plane compressive stress is released with the size decreasing. To facilitate the analysis, the in-plane compressive stress was further calculated according to $\sigma = (\Delta\omega/4.3)\,cm \cdot GPa$ (Tripathy et al., 2002), where σ is the biaxial stress and $\Delta\omega$ is the E_2 phonon peak difference between the strained GaN and unstrained GaN (567.6 cm^{-1}). The calculated in-plane compressive stress values of different sized PG micro-LEDs are presented in **Figure 3B**. From **Figure 3B**, it is clear that the in-plane stress reduces as the size decreases. This is because at the edge of micro-LEDs, the growth is free and nearly no in-plane stress. From the edge to the center of the micro-LEDs, the stress becomes large. Smaller sized micro-LEDs have more edge area, so it shows large area ratio for strain relaxation. The reduced in-plane compressive stress for the GaN template layer grown on the sapphire substrate correspondingly suppresses the QCSE level in the InGaN/GaN quantum wells. The reduced QCSE suggests that by decreasing the PG micro-LED size the output power and EQE can be improved. However, as can be observed from **Figure 2**, when the chip size is below 100 μm × 100 μm, the other effects need to be taken into account because the device performance decreases.

As the in-plane stress reduces, the blueshift for the electroluminescence wavelength caused by the reduced QCSE in the quantum wells is expected. The EL spectra and the peak EL wavelength for the studied PG micro-LEDs at 20 mA are depicted in **Figure 4**. As expected, the emission wavelength is blueshifted with the size decreasing from 1,000 μm × 1,000 μm–200 μm × 200 μm, as can be seen from

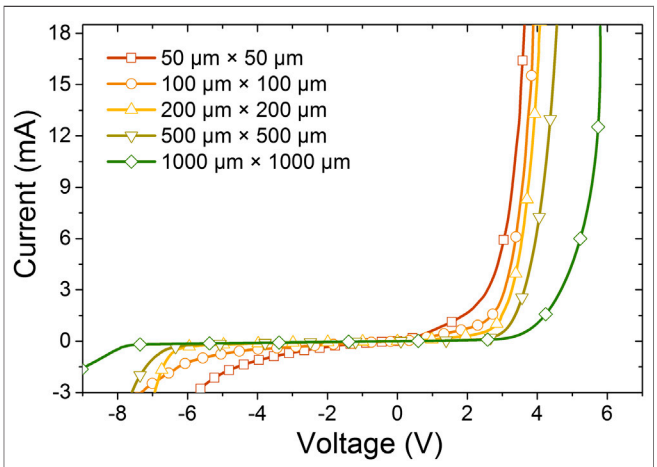

FIGURE 5 | I–V characteristics for PG micro-LEDs of different sizes.

Figures 4Aii,B; however, the blueshift for the wavelength is very small. This phenomenon is because the blueshift for the wavelength caused by the reduced QCSE in the quantum wells can be partially compensated by the redshift, which is due to the more indium incorporation into the quantum wells with decreased stress (Johnson et al., 2004; Ju et al., 2012). On the other hand, the wavelength shows redshift as the size is decreased from 200 μm × 200 μm–50 μm × 50 μm, as can be seen from **Figures 4Ai,B**, which is not expected. For the 50 μm × 50 μm and 100 μm × 100 μm cases, with the in-plane stress further reducing, the effect of the indium incorporation is stronger than that of the QCSE suppression, so we see the wavelength redshift. However, this high concentration of indium not only makes the peak wavelength redshifted, but also introduces more defects (Johnson et al., 2004), which can be proved by the shift of EQE peak toward higher current (Zhang et al., 2015), as shown in **Figure 2B**. It has also been reported that point defects enhance the nonradiative recombination (Cao et al., 2003), which can be another reason for the lower output power and EQE for the 50 μm × 50 μm size when the current is smaller than 120 mA.

We further carried out the current voltage (I–V) characteristics for the PG micro-LEDs of different sizes in **Figure 5**. From **Figure 5** we can see that the reverse leakage current increases when the PG micro-LED size is decreased, indicating more defects in the quantum wells (Cao et al., 2003). It is worth noting that the 50 μm × 50 μm device shows the largest leakage current when the device is reversely biased, which is a signature of the high defect density. In our case, the higher defect density in the quantum wells is ascribed to the higher indium incorporation efficiency for the smaller PG micro-LEDs, and therefore, further epi-growth optimizations are required.

CONCLUSION

In this work, to study the size effect on strain release, strain-reduced micro-LEDs in 50 μm × 50 μm, 100 μm × 100 μm, 200 μm × 200 μm, 500 μm × 500 μm, and 1,000 μm × 1,000 μm sizes were grown on patterned c-plane sapphire substrates by the MOCVD technique. Various characterization methods were performed to study the strain for different sizes. The output power and EQE characteristics show that the optical performance can be enhanced when the PG micro-LED size is reduced from 1,000 μm × 1,000 μm–100 μm × 100 μm. The improved EQE is due to the reduced QCSE in the InGaN/GaN quantum wells for those PG micro-LEDs. However, for the 50 μm × 50 μm size, the optical performance is limited by the smallest effective lighting area and additional defects induced by higher indium incorporation. Therefore, in our case, the 100 μm × 100 μm size delivers the highest output power and EQE. In summary, our experimental results indicate that to obtain high-quality epitaxy based on partitioned growth, a small size is needed provided that the defects density and margin ratio are carefully controlled. Since the partitioned growth method is easy and low-cost to apply to the sapphire substrate LEDs growth process, such directly grown micro-LEDs hold great promise for being adopted in commercial product lines.

DATA AVAILABILITY STATEMENT

The original contributions presented in the study are included in the article/Supplementary Material, further inquiries can be directed to the corresponding authors.

AUTHOR CONTRIBUTIONS

All authors listed have made a substantial, direct, and intellectual contribution to the work and approved it for publication.

FUNDING

This work is supported by the Singapore National Research Foundation under Grant No., NRF-CRP-6-2010-2 and the Singapore Agency for Science, Technology and Research (A*STAR) SERC Pharos Program under Grant No. 1527300025. HD gratefully acknowledges TUBA.

REFERENCES

Arpan, C., Benjamin, A. H., Stacia, K., James, S. S., Steven, P. D., Shuji, N., et al. (2005). Demonstration of nonpolar m-plane InGaN/GaN light-emitting diodes on free-standing m-plane GaN substrates. *Jpn. J. Appl. Phys.* 44, L173. doi:10.1143/JJAP.44.L173

Cao, X. A., Sandvik, P. M., Leboeuf, S. F., and Arthur, S. D. (2003). Defect generation in InGaN/GaN light-emitting diodes under forward and reverse electrical stresses. *Microelectron. Reliab.* 43, 1987–1991. doi:10.1016/j.microrel.2003.06.001

Chen, Z., Zhang, X., Dou, Z., Wei, T., Liu, Z., Qi, Y., et al. (2018). High-brightness blue light-emitting diodes enabled by a directly grown graphene buffer layer. *Adv. Mater.* 30, 1801608. doi:10.1002/adma.201801608

Choi, H. W., Dawson, M. D., Edwards, P. R., and Martin, R. W. (2003). High extraction efficiency InGaN micro-ring light-emitting diodes. *Appl. Phys. Lett.* 83, 4483–4485. doi:10.1063/1.1630352

Choi, H. W., Jeon, C. W., and Dawson, M. D. (2004a). High-resolution 128 x 96 nitride microdisplay. *IEEE Electron. Device Lett.* 25, 277–279. doi:10.1109/LED.2004.826541

Choi, H. W., Jeon, C. W., and Dawson, M. D. (2004b). InGaN microring light-emitting diodes. *IEEE Photon. Technol. Lett.* 16, 33–35. doi:10.1109/LPT.2003.818903

Davydov, V. Y., Averkiev, N., Goncharuk, I., Nelson, D., Nikitina, I., Polkovnikov, A., et al. (1997). Raman and photoluminescence studies of biaxial strain in GaN epitaxial layers grown on 6H–SiC. *J. Appl. Phys.* 82, 5097–5102. doi:10.1063/1.366310

Davydov, V. Y., Kitaev, Y. E., Goncharuk, I., Smirnov, A., Graul, J., Semchinova, O., et al. (1998). Phonon dispersion and Raman scattering in hexagonal GaN and AlN. *Phys. Rev. B* 58, 12899. doi:10.1103/PhysRevB.58.12899

Denbaars, S. P., Feezell, D., Kelchner, K., Pimputkar, S., Pan, C.-C., Yen, C.-C., et al. (2013). Development of gallium-nitride-based light-emitting diodes (LEDs) and laser diodes for energy-efficient lighting and displays. *Acta Mater.* 61, 945–951. doi:10.1016/j.actamat.2012.10.042

Ji, Y., Zhang, Z. H., Tan, S. T., Ju, Z. G., Kyaw, Z., Hasanov, N., et al. (2013). Enhanced hole transport in InGaN/GaN multiple quantum well light-emitting diodes with a p-type doped quantum barrier. *Opt. Lett.* 38, 202–204. doi:10.1364/OL.38.000202

Johnson, M. C., Bourret-Courchesne, E. D., Wu, J., Liliental-Weber, Z., Zakharov, D. N., Jorgenson, R. J., et al. (2004). Effect of gallium nitride template layer strain on the growth of $In_xGa_{1-x}N$/GaN multiple quantum well light emitting diodes. *J. Appl. Phys.* 96, 1381–1386. doi:10.1063/1.1766407

Ju, Z. G., Tan, S. T., Zhang, Z.-H., Ji, Y., Kyaw, Z., Dikme, Y., et al. (2012). On the origin of the redshift in the emission wavelength of InGaN/GaN blue light emitting diodes grown with a higher temperature interlayer. *Appl. Phys. Lett.* 100, 123503. doi:10.1063/1.3694054

Kim, H.-M., Cho, Y.-H., Lee, H., Kim, S. I., Ryu, S. R., Kim, D. Y., et al. (2004). High-brightness light emitting diodes using dislocation-free indium gallium nitride/gallium nitride multiquantum-well nanorod arrays. *Nano Lett.* 4, 1059–1062. doi:10.1021/nl049615a

Lu, S., Liu, W., Zhang, Z.-H., Tan, S. T., Ju, Z., Ji, Y., et al. (2014). Low thermal-mass LEDs: size effect and limits. *Opt. Express* 22, 32200–32207. doi:10.1364/OE.22.032200

Mckendry, J. J. D., Green, R. P., Kelly, A. E., Zheng, G., Guilhabert, B., Massoubre, D., et al. (2010). High-speed visible light communications using individual pixels in a micro light-emitting diode array. *IEEE Photon. Technol. Lett.* 22, 1346–1348. doi:10.1109/LPT.2010.2056360

Mckendry, J. J. D., Massoubre, D., Zhang, S., Rae, B. R., Green, R. P., Gu, E., et al. (2012). Visible-light communications using a CMOS-controlled micro-light- emitting-diode array. *J. Lightwave Technol.* 30, 61–67. doi:10.1109/JLT.2011.2175090

Poher, V., Grossman, N., Kennedy, G. T., Nikolic, K., Zhang, H. X., Gong, Z., et al. (2008). Micro-LED arrays: a tool for two-dimensional neuron stimulation. *J. Phys. D: Appl. Phys.* 41, 094014. doi:10.1088/0022-3727/41/9/094014

Ryou, J. H., Yoder, P. D., Liu, J., Lochner, Z., Kim, H., Choi, S., et al. (2009). Control of quantum-confined Stark effect in InGaN-based quantum wells. *IEEE J. Sel. Top. Quantum Electron.* 15, 1080–1091. doi:10.1109/JSTQE.2009.2014170

Shuji, N., Takashi, M., and Masayuki, S. (1991). High-power GaN P-N junction blue-light-emitting diodes. *Jpn. J. Appl. Phys.* 30, L1998. doi:10.1143/JJAP.30.L1998

Tan, S. T., Sun, X. W., Demir, H. V., and Denbaars, S. P. (2012). Advances in the LED materials and architectures for energy-saving solid-state lighting toward "lighting revolution". *IEEE Photonics J.* 4, 613–619. doi:10.1109/JPHOT.2012.2191276

Tetsuya, T., Shigetoshi, S., Maki, K., Miho, K., Hideo, T., Hiroshi, A., et al. (1997). Quantum-confined Stark effect due to piezoelectric fields in GaInN strained quantum wells. *Jpn. J. Appl. Phys.* 36, L382. doi:10.1143/JJAP.36.L382

Tian, Y., Shao, Y., Wu, Y., Hao, X., Zhang, L., Dai, Y., et al. (2015). Direct growth of freestanding GaN on C-face SiC by HVPE. *Sci. Rep.* 5, 10748. doi:10.1038/srep10748

Tripathy, S., Chua, S., Chen, P., and Miao, Z. (2002). Micro-Raman investigation of strain in GaN and $Al_xGa_{1-x}N$/GaN heterostructures grown on Si (111). *J. Appl. Phys.* 92, 3503–3510. doi:10.1063/1.1502921

Tripathy, S., Soni, R. K., Asahi, H., Iwata, K., Kuroiwa, R., Asami, K., et al. (1999). Optical properties of GaN layers grown on C-, A-, R-, and M-plane sapphire substrates by gas source molecular beam epitaxy. *J. Appl. Phys.* 85, 8386–8399. doi:10.1063/1.370686

Waltereit, P., Brandt, O., Trampert, A., Grahn, H. T., Menniger, J., Ramsteiner, M., et al. (2000). Nitride semiconductors free of electrostatic fields for efficient white light-emitting diodes. *Nature* 406, 865–868. doi:10.1038/35022529

Wang, P., Pandey, A., Gim, J., Shin, W. J., Reid, E. T., Laleyan, D. A., et al. (2020). Graphene-assisted molecular beam epitaxy of AlN for AlGaN deep-ultraviolet light-emitting diodes. *Appl. Phys. Lett.* 116, 171905. doi:10.1063/1.5144906

Zhang, Y. P., Zhang, Z.-H., Liu, W., Tan, S. T., Ju, Z. G., Zhang, X. L., et al. (2015). Nonradiative recombination—critical in choosing quantum well number for InGaN/GaN light-emitting diodes. *Opt. Express* 23, A34–A42. doi:10.1364/OE.23.000A34

Zhang, Z.-H., Tiam Tan, S., Kyaw, Z., Ji, Y., Liu, W., Ju, Z., et al. (2013). InGaN/GaN light-emitting diode with a polarization tunnel junction. *Appl. Phys. Lett.* 102, 193508. doi:10.1063/1.4806978

Conflict of Interest: The authors declare that the research was conducted in the absence of any commercial or financial relationships that could be construed as a potential conflict of interest.

frontiers in Chemistry

ORIGINAL RESEARCH
published: 15 March 2021
doi: 10.3389/fchem.2020.630687

Simple-Structured OLEDs Incorporating Undoped Phosphorescent Emitters Within Non-Exciplex Forming Interfaces: Towards Ultraslow Efficiency Roll-Off and Low Driving Voltage for Indoor R/G/B Illumination

Ting Xu[1,2,3,4], Ruichen Yi[3], Chunqin Zhu[3] and Mingquan Lin[5]*

[1]Shenzhen Key Laboratory of Polymer Science and Technology, College of Materials Science and Engineering, Shenzhen University, Shenzhen. China, [2]Key Laboratory of Optoelectronic Devices and Systems of Ministry of Education and Guangdong Province, College of Physics and Optoelectronic Engineering, Shenzhen University, Shenzhen. China, [3]State Key Laboratory of Surface Physics and Department of Physics, Fudan University, Shanghai, China, [4]Jiangsu Key Laboratory for Carbon-Based Functional Materials and Devices, Soochow University, Suzhou, China, [5]Department of Electrical Engineering, City University of Hong Kong, Hong Kong, China

OPEN ACCESS

Edited by:
Qifan Xue,
South China University of Technology, China

Reviewed by:
Mingjie Li,
Hong Kong Polytechnic University, Hong Kong
Jungui Zhou,
Soochow University, China

***Correspondence:**
Ting Xu
robin@pku.edu.cn

Specialty section:
This article was submitted to Physical Chemistry and Chemical Physics, a section of the journal Frontiers in Chemistry

Received: *19 November 2020*
Accepted: *30 December 2020*
Published: *15 March 2021*

Citation:
Xu T, Yi R, Zhu C and Lin M (2021) Simple-Structured OLEDs Incorporating Undoped Phosphorescent Emitters Within Non-Exciplex Forming Interfaces: Towards Ultraslow Efficiency Roll-Off and Low Driving Voltage for Indoor R/G/B Illumination. Front. Chem. 8:630687. doi: 10.3389/fchem.2020.630687

To meet the requirement of indoor R/G/B monochrome illumination a simplified OLEDs structure and fabrication process must occur. Herein, a design philosophy of low efficiency roll-off and simple-structure OLEDs incorporating R/G/B phosphorescent ultrathin non-doped emissive layers (EMLs) within non-exciplex forming interfaces a luminescent system by a direct charge trapping mechanism has been reported, which uses bis(2-methyldibenzo [f,h]-quinoxaline)(acetylacetonate)iridium(III) $(MDQ)_2Ir(acac)$, bis(3-phenylpyridin-e)iridium(III) $(Ir(ppy)_3)$, and bis(3,5-difluoro-2 -(2-pyridyl)phenyl-(2-carboxypyridyl) iridiumII) (Firpic) as R/G/B luminescent dyes, respectively. Although the recombination zone is narrow in the designed OLEDs, the efficiency roll-off of the designed OLEDs are unexpectedly slow, due to stable charge trapping of the emitters and are refrained from concentration quenching in relatively low current density, but the luminance meets the requirement of indoor lighting. With a low threshold voltage of 2.9/2.9/3.5 V, the designed R/G/B phosphorescent OLEDs show an efficiency roll-off as low as 7.6/3.2/4.3% for indoor luminance from 10 cd/m^2 to 1,000 cd/m^2, respectively. The perspective of R/G/B luminescent dyes on luminous efficiency, chromaticity coordinate drifts, efficiency roll-off, and direct charge trapping has been thoroughly studied. Therefore, our research may help to further develop ideal indoor lighting using a simplified undoped R/G/B OLEDs structure with simultaneous ultraslow efficiency roll-off, low threshold voltage, simplified fabrication process, low reagent consumption, and cost.

Keywords: indoor illumination, OLEDs, efficiency roll-off, simple structure, direct charge trapping

INTRODUCTION

As an energy conserving and environmentally friendly healthy organic semiconductor illumination apparatus, organic light emitting diodes (OLEDs) have been widely applied in health lighting sources and displays due to their excellent properties since being invented by Tang and VanSlyke (1987) and Burroughes et al. (1990) based on small molecule and conjugated polymers, respectively. However, conventional OLED products are still rather expensive for consumers (Thejokalyani and Dhoble, 2014). Hence, it is imminently required to reduce the cost of products by simplifying the OLED structure and fabrication technology. OLEDs with a doping-free ultrathin emissive layer (UEML) have aroused research interest and have been developed rapidly due to their simple structure and easily fabrication which removes the need for doping and needs fewer sensors, which therefore reduces the requirement for equipment and lowers the cost of the OLEDs (Liu et al., 2016b; Xu L. et al., 2016). Two main aspects are promoting this field development. On the one hand, OLEDs with UEML have advanced rapidly with novel UEML materials (e.g., new complexes (Zhang et al., 2012), TADF (Zhang Q. et al., 2014; Hirata et al., 2015; Zhang et al., 2015; Ahn et al., 2019), and AIE (Liu et al., 2016a; Ruan et al., 2016). Simplified doping-free white OLED (Liu et al., 2014a) and yellow-orange OLED (Liu B. et al., 2015) are achieved based on a Pt(II)-based complex emitter that achieves rather low operating voltages and high power efficiencies (Wang et al., 2014). An efficient and concentration-insensitive metal-free thermally activated delayed fluorescence (TADF) material was reported and applied in undoped OLEDs by the Adachi group (Zhang et al., 2015). Aggregation-induced emission (AIE), color tunable, efficient undoped OLEDs and good mechanochromic properties were confirmed (Ruan et al., 2016). On the other hand, a deeper understanding of device physics, photophysics (e.g., exciplex (Park et al., 2013; Seino et al., 2014; Shin et al., 2014), electroplax (Wang et al., 2004; Yang et al., 2009; Luo et al., 2017), excimer (Chen et al., 2016), or TADF (Lin et al., 2018) property), and novel device structure with efficient exciton harvesting (Schwartz et al., 2007; Wang et al., 2009; Cui et al., 2016) also play a key role in the development of OLEDs with UEML. The Cao group fabricated a novel white OLED with a doping-free process (Liu et al., 2014b; Liu et al., 2016b). The He group designed an inverted OLED with UEML (Liu et al., 2014), which was suitable for a display driven by an active matrix transistor backplane (Lee et al., 2008). The Ma group fabricated a highly efficient and simple monochrome OLED based on UEMLs within an exciton confinement energy band structure while a deeper understanding of the exciplex formation of TCTA and TmPyPB was not clearly pointed out (Zhao et al., 2013). The Ma group also designed a novel white OLED applied with an exciplex co-host and UEML in one device (Wang et al., 2016). The Lee group managed excitons distribution in TADF (Liu et al., 2015a) and white OLEDs (Liu et al., 2015b) by an exciplex energy transfer (Cui et al., 2015). We also developed a device design philosophy of OLEDs using mixed bulk (Xu et al., 2017b; Xu et al., 2019) or an interface exciplex forming host (Xu et al., 2017c), UEMLs (Xu et al., 2018b), double UEMLs (Xu et al., 2016b), or a tandem structure (Xu et al., 2018a) as a synergistic strategy (Xu et al., 2017a) toward a simplified OLED structure (Zhang et al., 2018) and fabricated the process without sacrificing device efficiency due to improving the energy transfer process. Nowadays, the indoor conditions of photovoltaic devices under low-illuminance conditions have been extensively researched as a specialized issue (Cui et al., 2017), (Xu et al., 2016a). Meanwhile, researchers rarely pay specialized attention to indoor lighting as the energy source of indoor photovoltaics. According to the international standard of the Commission Internationale de L'Eclairage (CIE): the lighting of indoor work places (ISO 8995:2002 CIE S 008/E:2001) (Rabich et al., 2017), and the corresponding brightness of interior illumination is generally from 10 to 1,000 cd/m^2.

Herein, we designed and fabricated monochrome red, green, and blue phosphorescent OLEDs based on non-doped UEMLs to meet the requirement of indoor R/G/B monochrome illumination. Particularly, it is observed that the non-doped UEML-based OLEDs generally show very slow efficiency roll-off and low threshold voltage, which is fitting for indoor lighting in low current density with a brightness from 10 cd/m^2 to 1,000 cd/m^2. Moreover, the maximum power efficiency reached 5.766 lm/w at 177.8 cd/m^2, 15.74 lm/w at 99.27 cd/m^2, and 2.277 lm/w at 252.2 cd/m^2 for the R/G/B monochrome OLEDs, respectively. The perspective of R/G/B luminescent dyes on luminous efficiency, chromaticity coordinate drifts, efficiency roll-off, and charge trapping mechanism has been thoroughly studied. Therefore, our work helps to develop ideal indoor lighting using a simplified undoped R/G/B OLED structure with simultaneous slow efficiency roll-off, low threshold voltage, simplified fabrication, low reagent consumption, and cost.

EXPERIMENT DETAILS

All OLED devices were fabricated based on the same glass substrate pattern with a conducting indium-tin-oxide (ITO) anode and a sheet resistance lower than 20 Ω/square. The substrate fabrication was followed by a routine cleaning process (Xu et al., 2016a). The basic structure of the devices is a ITO/MoO_3 (1 nm)/4′-bis(carbazol-9-yl) biphenyl (CBP) (35 nm) /Ultrathin emitter (0.3 nm)/1,3,5-Tris(N -phenylbenzimidazol -2-yl)benzene (TPBi) (65 nm)/LiF (1 nm)/Al (100 nm), in which the schematic parameter diagram and energy level diagram of the device structures are shown in **Figures 1A, B**, including MoO_3 and CBP which act as the hole injection layer (HIL) and hole transporting layer (HTL). LiF and TPBi are used as the electron injection layer (EIL) and electron transporting layer (ETL). A 1 nm thick thermally evaporated MoO_3 layer was deposited on top to achieve a high work function for the hole injection into CBP. The phosphorescent dyes in this study were bis(3-phenylpyridine) iridium(III) [Ir(ppy)$_3$] for green in device A, bis(2-methyldibenzo[f,h]-quinoxaline) (acetylacetonate) iridium(III) [(MDQ)$_2$Ir(acac)] for red in device B, and bis(3,5-difluoro-2 -(2-pyridyl)phenyl-(2-carboxypyridyl)iridium III (FIrpic) for

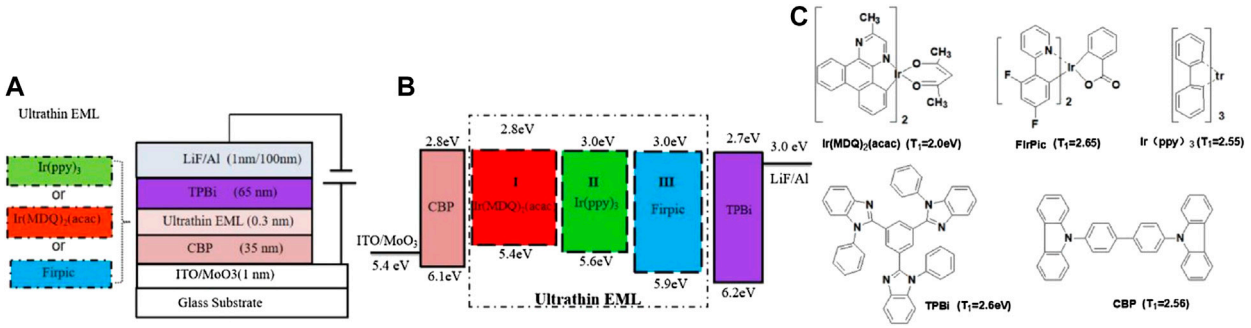

FIGURE 1 | (A) Schematic device structure and **(B)** corresponding energy-level diagram of the devices considered in this work as well as **(C)** the molecular structure and triplet energies (T1) of the materials used.

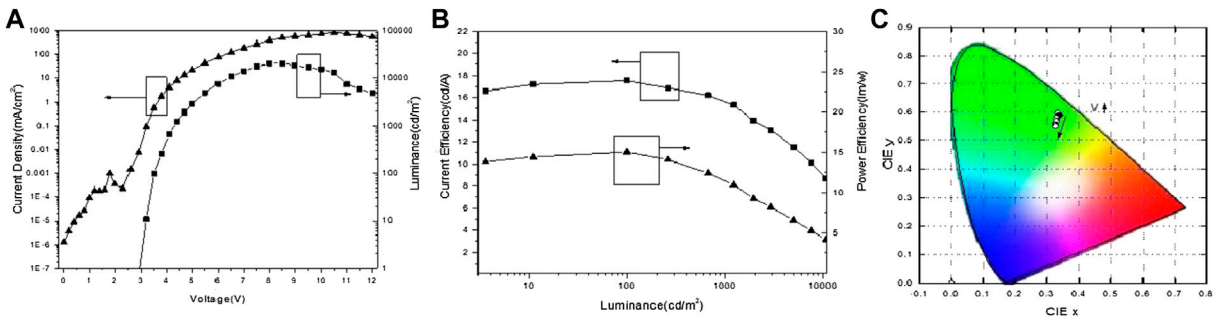

FIGURE 2 | (A) Current density-voltage-luminance characteristics, **(B)** current efficiency-luminance-power efficiency characteristics, and **(C)** chromaticity coordinates of green OLEDs.

blue in device C. **Figure 1C** shows the molecular structures of $Ir(ppy)_3$, $Ir(MDQ)_2(acac)$, Firpic, TPBi, and CBP, respectively.

RESULTS AND DISCUSSION

Lots of researchers have proposed two primary mechanisms for the exciton process in OLEDs: host-guest energy transfer and direct charge trapping of the guest. Exciton formation occurs directly on the guest molecules, which play an important role in balancing charge injection. This direct charge trapping on the guest can be confirmed by the dependence of the drive voltage and electroluminescence spectrum on guest concentration (Holmes et al., 2003). The light emission mechanism of OLEDs with a mixed co-host emitting layer was also studied using an exciplex-type mixed co-host and an exciplex free mixed co-host (Song and Lee, 2015). The light emission process in the interface of exciplex-type OLED devices was dominated by energy transfer while the interface of non-exciplex type devices was dominated by a charge trapping emission mechanism (Wang et al., 2016). In this research, a design philosophy of low efficiency roll-off and simple-structure OLEDs incorporating R/G/B phosphorescent non-doped UEMLs within a non-exciplex forming interface luminescent system by a direct charge trapping mechanism was proposed. The device structures and the energy levels of the designed OLEDs are shown in **Figure 1A,B**.

In working OLEDs, firstly, electrons and holes can be easily injected from the ITO anode and aluminum cathode under driving voltage, respectively. Then, electrons and holes go through ETL/HTL and meet to form excitons. There were some differences between devices A, B, and C. Under voltage from 2.9 to 4.9 V with a corresponding luminance from 10 cd/m^2 to 1,000 cd/m^2, the luminance of device A was linear to the logarithmic coordinate voltage of device A as shown in **Figures 2A,B**, and the current efficiency roll-off of device A was as low as 7.6%. As to the chromaticity coordinate of device A, the $CIE_{(x,y)}$ was nearly unchanged from 2.9 to 4.9 V as shown in **Figure 2C**. This phenomenon is indicative of the direct charge trapping of $Ir(ppy)_3$ as the luminescent dye of device A was quite effective in a low current density. Lastly, as the voltage increased after exceeding 5 V with a corresponding luminance of 1,000 cd/m^2, the luminance of device A showed a gradual invariant with fast efficiency roll-off. There are three main reasons for this phenomenon. Firstly, the values of HOMO and LUMO of TPBi are closed to CBP as shown in **Figure 1B**, the energy level cannot block the leak current in a high current density, and carriers meet to form excitons in wide bandwidth HTL/ETL for

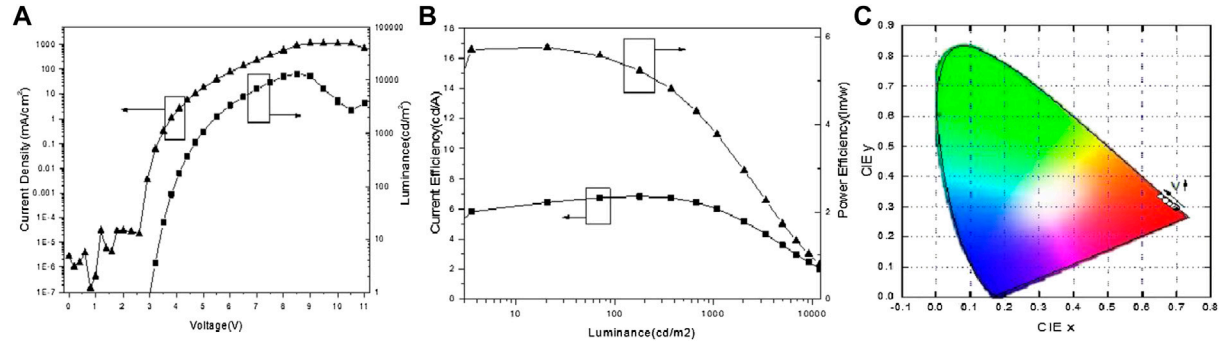

FIGURE 3 | (A) Current density-voltage-luminance characteristics. **(B)** Current efficiency-luminance-power efficiency characteristic. **(C)** Chromaticity coordinate of red OLEDs.

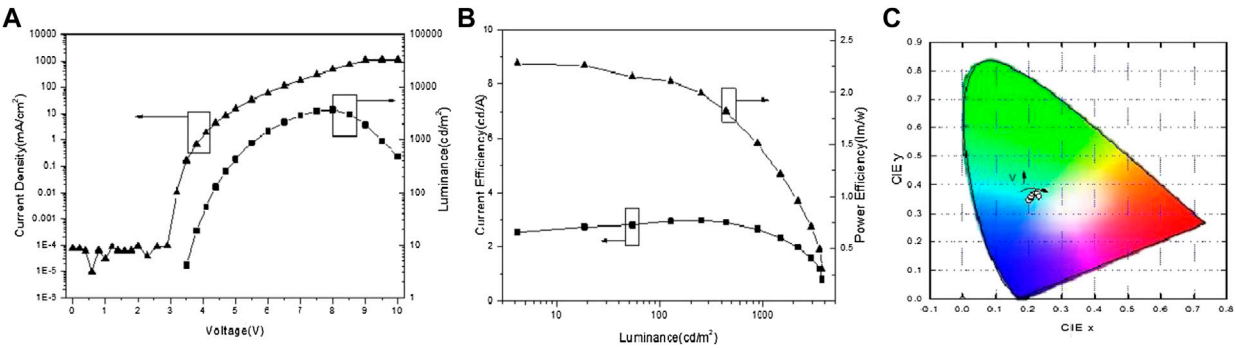

FIGURE 4 | (A) Current density-voltage-luminance characteristics. **(B)** Current efficiency-luminance-power efficiency characteristic. **(C)** Chromaticity coordinate of blue OLEDs.

inefficient lighting. Secondly, the direct charge trapping of $Ir(ppy)_3$ as the luminescent dye of device A is saturated in high current density, while device performance is also saturated without assisting the energy transfer process (Forster energy transfer and Dexter energy transfer) in a non-exciplex system. Thirdly, the triplet state energy levels (T_1) of CBP (2.55 eV) and TPBi (2.67 eV) could not be confirmed for luminescent dye $Ir(ppy)_3$ (2.47 eV) in high voltage leading to drifting of excitons into a wide bandwidth HTL/ETL for inefficient lighting. Therefore, the chromaticity coordinate $CIE_{(x,y)}$ of device A was remarkably changed following the direction as the voltage increased after exceeding 5 V as shown in **Figure 2C**.

As seen in **Figure 3A** and **Figure 4A**, under low voltage with corresponding luminance from 10 to 1,000 cd/m^2, the luminance of devices B and C were linear to the logarithmic coordinate voltage of devices B and C. The current efficiency roll-off of devices B and C were as low as 3.2 and 4.3% in as shown in **Figure 3B** and **Figure 4B**, respectively. The $CIE_{(x,y)}$ of devices B and C were nearly unchanged under low voltage while the $CIE_{(x,y)}$ of devices B and C changed remarkably following the direction as the voltage increased after exceeding 5–6 V as shown in **Figure 3C** and **Figure 4c**.

Thanks to the equal thickness of devices A, B, and C, the J-V-L curves of the phosphorescent dyes were different as shown in **Figures 2A,B**, **Figures 3A,B**, and **Figures 4A,B**. In low working voltage, there was no significant difference for J-V among devices A, B, and C implying that exciton quenching or the nonradiative decay of excitons was greatly suppressed by the direct charge trapping of this simple UEML within the non-exciplex interface TPBi/CPB. However, the efficiencies of the OLEDs with UEML were affected by the phosphorescent dyes with different T_1 levels. The case of CPB or TPBi as the host with exciton formation as the guest should be similar to this OLED with non-doped UEML by direct charge trapping. The utilization of the non-doped UEML structure yields high efficiencies for the green OLED with $Ir(ppy)_3$ as the UEML, while the efficiencies of the red and blue OLEDs with $(MDQ)_2$ Ir(acac) and Firpic were not as high as the green dye on account of relatively low PLQY, which was similar in the host-guest doping system. The non-doped UEML was constructed by introducing a 0.3 nm thin layer of pure phosphorescent dyes between the HTL and ETL layer. The maximum current efficiency reached 15.74 lm/w at 99.27 cd/m^2, 5.77 lm/w at 177.8 cd/m^2, and 2.28 lm/w at 252.2 cd/m^2 for the green, red, and blue monochrome OLEDs, respectively.

TABLE 1 | A summary of OLEDs with non-doped UEML.

Device	$V_{turn\text{-}on}$ (V)	L_{max} (cd/m^2)	$\eta_{c\ max}$ (cd/A)	η_c@500 nit (cd/A)	P_{max} (lm/W)	Roll-off (%) (10~1,000 cd/m^2)
A	2.9	20,700	17.5 (5.1%)	16.2	15.7	7.6%
B	2.9	13,210	6.9 (2.3%)	6.7	5.8	3.2%
C	3.5	3,740	2.98 (1.3%)	2.9	2.3	4.3%

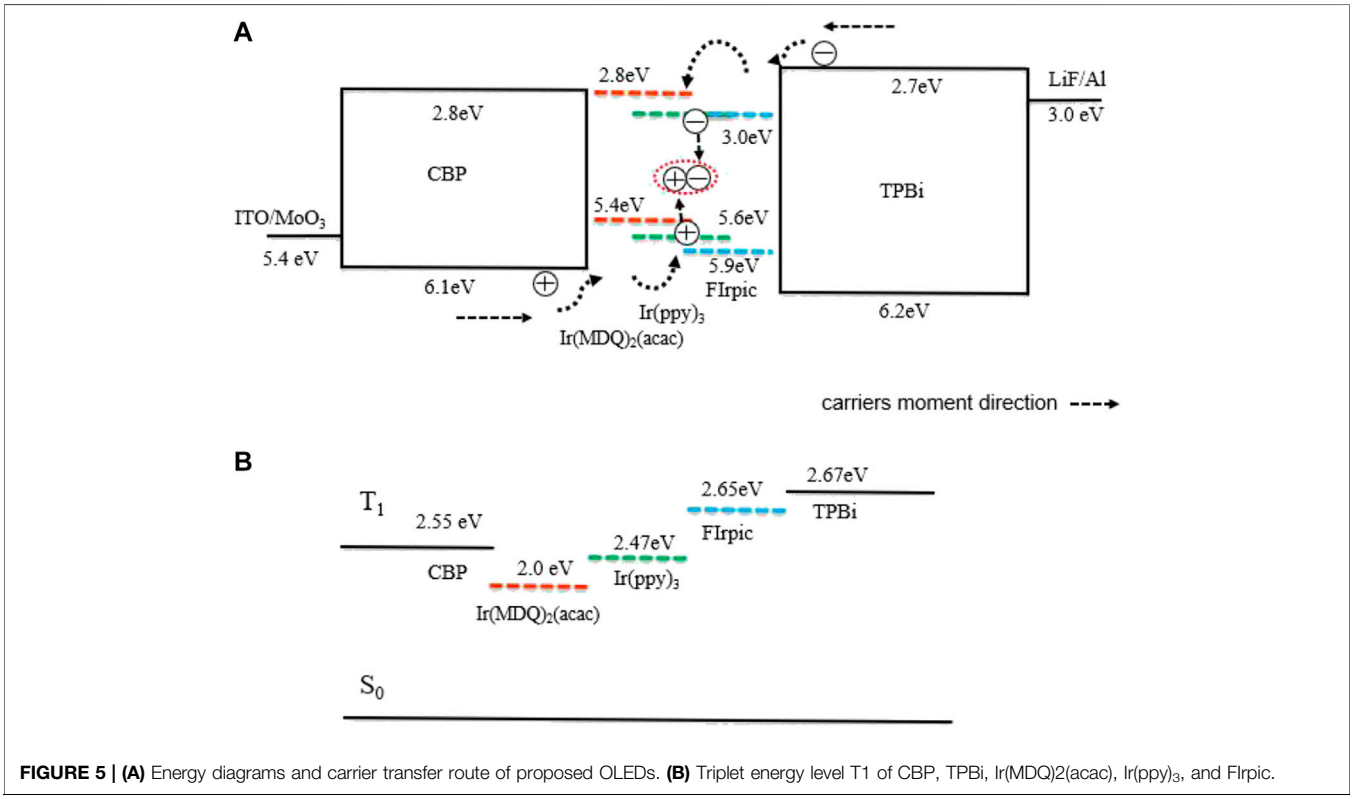

FIGURE 5 | (A) Energy diagrams and carrier transfer route of proposed OLEDs. **(B)** Triplet energy level T1 of CBP, TPBi, Ir(MDQ)2(acac), Ir(ppy)$_3$, and FIrpic.

To further explore the working mechanism of the designed OLEDs with UEML in high current density, **Supplementary Figure S1** shows the electroluminescence (EL) spectra of the non-doped OLEDs with UEML for the R/G/B phosphorescent dyes at the higher voltage of 8 V. It can be seen that device A with Ir(ppy)$_3$ and device B with Ir(MDQ)$_2$ (acac) show pure dye emission due to the high T_1 level of CPB and TPBi confirming direct charge trapping excitation in the relatively lower T_1 level of Ir(ppy)$_3$ or Ir(MDQ)$_2$ (acac) in high current density. In device C with FIrpic, it is interesting that the EL spectra peak around 380 nm showed the characteristics of host materials intramolecular luminescence in TPBi (Zhang T. et al., 2014) rather than in CBP (Park et al., 2011), which indicates exciton diffusion into TPBi. This may have been due to ETL occurring intensely or due to the charge carrier recombination zone in TPBi, and then radiative decay which emitted light into TPBi in a primary way. There was also a secondary peak around 450 showing the dye emission of FIrpic due to direct charge trapping of FIrpic to form exciton, but the EL of FIrpic was much weaker than the emitted light in TPBi due to the relatively low efficient exciton energy transfer from TPBi (Jang et al., 2011) to FIrpic as shown in **Supplementary Figure S1**. Moreover, there was a wide peak around 700 nm which shows the characteristics of inter-molecular overlay of the red-shifted excimer of phosphorescence (Kalinowski et al., 2007). Low direct charge trapping of FIrpic, exciton diffusion to ETL, and low efficient exciton energy transfer from TPBi to FIrpic led to the low efficiency of device C in high current density.

The J-V-L characteristics, the CE-L-PE characteristics, and the chromaticity coordinate of the device A are shown in **Figures 2A–C**, separately. Similarly, **Figure 3** and **Figure 4** show the corresponding performance of device B and device C. The turn-on voltages (V_{on}) (which are defined as a luminance of 1 cd /cm^2) of devices A and B were as low as 2.9 V, and device C was 3.5 V as summarized in **Table 1**. The maximum current and power efficiency ($\eta_{c\ max}$, P_{max}) of (17.5 cd/A, 15.7 lm/W), (6.9 cd/A, 5.8 lm/W), and (2.98 cd/A, 2.3 lm/W) were obtained in devices A, B, and C, respectively. And the maximum brightness of devices A, B, and C were as high as

20,700, 13,210, and 3,740 cd/m^2, respectively. The phosphorescence dyes have different capabilities to trap the charge carriers directly leading to different efficiencies in the OLEDs with UEML.

In low working voltage, the power efficiency of the blue dye OLEDs with non-doped UEML was as high as the red one. The utilization of this kind of non-doped UEML within non-exciplex forming interfaces can be appropriate for R/G/B dyes. All the monochrome R/G/B OLEDs based UEML show relatively high efficiency and ultraslow efficiency roll-off in low driving voltage, the non-doped UEML structure within a non-exciplex forming interface has broad adaptability for most phosphorescent dyes with ultraslow efficiency roll-off in low driving voltage. As there is relatively few reports on non-exciplex forming interfaces as direct charge tapping structures that have such broad adaptability for phosphorescent dyes with ultraslow efficiency roll-off in low driving voltage, our technical route offers a brief scheme to achieve indoor lighting requirements. Further, in order to clearly describe the work mechanism of this device structure, a physical model of exciton dynamics in OLED with non-doped UEML is proposed in **Figure 5**.

The higher turn on voltage for device C suggests that the excitons from direct charge trapping are not efficient comparing with devices A and B. As depicted in **Figure 5A**, some of the carriers would enter into the UEMLs as deep as 3 nm (Zhao et al., 2012), and then would recombine in the organic layers, while the direct charge carrier recombination on phosphorescent dyes would generate dye emission due to the thin nature of non-doped UEML. These excitons may either transport their energy from ETL or HTL to the EML. The efficiency of OLEDs with Ir(MDQ)$_2$ (acac) was lower than that of OLEDs with Ir(ppy)$_3$ since the LUMO energy level of Ir(MDQ)$_2$ (acac) was nearly equal to the LUMO energy level of CBP and TPBi. There was also no doubt that the capability of Ir(MDQ)$_2$ (acac) to direct charge trapping was weaker than that of Ir(ppy)$_3$ in the same thickness. From the OLED-based UEML, the energy transport process from the ETL/HTL to the EML was much more than that of exciton diffusion in device A and device B. Meanwhile, as depicted in **Figure 5B**, thanks to the higher T_1 exciton between the transporting layers of T_1 of CBP and TBPi, the excitons generated were effectively confined in the UEML for the Ir(MDQ)$_2$ (acac) and Ir(ppy)$_3$ dyes. As to the blue OLED with FIrpic, the efficiency of the OLEDs with FIrpic was lower than that of OLEDs with Ir(ppy)$_3$ since the T_1 energy level of FIrpic was higher than that of CBP. Although the recombination zone is narrow in the designed OLEDs, the efficiency roll-off of the designed OLEDs are unexpectedly slow mainly due to the stable charge trapping of the emitter and avoiding concentration quenching in relatively low current density for the requirements of indoor lighting. With a low threshold voltage of 2.9/2.9/3.5 V, the designed R/G/B phosphorescent OLEDs show an efficiency roll-off as low as 7.6/3.2/4.3% in the indoor luminance intensity range from 10 to 1,000 cd/m^2, respectively.

CONCLUSION

In summary, we succeeded in applying a series of R/G/B ultrathin non-doped phosphorescent dye layers into non-exciplex forming interfaces as a cost-effective method to realize OLEDs with ultraslow efficiency roll-off and low driving voltage to satisfy indoor R/G/B illumination requirements in low driving voltage. This device structure shows great superiority in easy fabrication, low-cost, and high-efficiency when compared to compact fluorescent lamps due to the highly simplified ultrathin and undoped emitters. This technical route has high value for the future of indoor solid-state lighting applications.

DATA AVAILABILITY STATEMENT

The original contributions presented in the study are included in the article/**Supplementary Material**, further inquiries can be directed to the corresponding author.

AUTHOR CONTRIBUTIONS

TX conceived of the work. TX, RY, and CZ fabricated and characterized OLED. TX, and ML directed and supervised the project.

FUNDING

This project was funded by the China Postdoctoral Science Foundation (2019M663027). This work was also supported by the Shenzhen Peacock Plan (KQTD20170330110107046), the Science and Technology Innovation Commission of Shenzhen (JCYJ20170818085627721, JCYJ20180507182244027), the Open Project of J Key Laboratory for Carbon-Based Functional Materials & Devices, Soochow University, P. R. China, (KJS1908), and the State Key Laboratory of Surface Physics and Department of Physics, Fudan University, P. R. China (Grant No. KF2019_13). I would like to express my special gratitude to Liang-Sheng Liao and Hong Meng for their guidance in my research.

SUPPLEMENTARY MATERIAL

The Supplementary Material for this article can be found online at: https://www.frontiersin.org/articles/10.3389/fchem.2020.630687/full#supplementary-material.

REFERENCES

Ahn, D. H., Kim, S. W., Lee, H., Ko, I. J., Karthik, D., Lee, J. Y., et al. (2019). Highly efficient blue thermally activated delayed fluorescence emitters based on symmetrical and rigid oxygen-bridged boron acceptors. *Nat. Photon.* 1, 540–546. doi:10.1038/s41566-019-0415-5

Burroughes, J. H., Bradley, D. D. C., Brown, A. R., Marks, R. N., Mackay, K., Friend, R. H., et al. (1990). Light-emitting diodes based on conjugated polymers. *Nature* 347 (6293), 539–541. doi:10.1038/347539a0

Chen, Y.-H., Tang, K.-C., Chen, Y.-T., Shen, J.-Y., Wu, Y.-S., Liu, S.-H., et al. (2016). Insight into the mechanism and outcoupling enhancement of excimer-associated white light generation. *Chem. Sci.* 7 (6), 3556–3563. doi:10.1039/C5SC04902D

Cui, L. S., Kim, J. U., Nomura, H., Nakanotani, H., and Adachi, C. (2016). Benzimidazobenzothiazole-based bipolar hosts to harvest nearly all of the excitons from blue delayed fluorescence and phosphorescent organic light-emitting diodes. *Angew. Chem. Int. Edn.* 55 (24), 6864–6868. doi:10.1002/anie.201601136

Cui, L.-S., Xie, Y.-M., Wang, Y.-K., Zhong, C., Deng, Y.-L., Liu, X.-Y., et al. (2015). Pure hydrocarbon hosts for ≈100% exciton harvesting in both phosphorescent and fluorescent light-emitting devices. *Adv. Mat.* 27 (28), 4213–4217. doi:10.1002/adma.201501376

Cui, Y., Wang, Y., Bergqvist, J., Yao, H., Xu, Y., Gao, B., et al. (2017). Wide-gap non-fullerene acceptor enabling high-performance organic photovoltaic cells for indoor applications. *Nat. Energy* 4 (9), 768–775. doi:10.1038/s41560-019-0448-5

Hirata, S., Sakai, Y., Masui, K., Tanaka, H., Lee, S. Y., Nomura, H., et al. (2015). Highly efficient blue electroluminescence based on thermally activated delayed fluorescence. *Nat. Mater.* 14 (3), 330. doi:10.1038/nmat4154

Holmes, R., D'Andrade, B., Forrest, S., Ren, X., Li, J., and Thompson, M. (2003). Efficient, deep-blue organic electrophosphorescence by guest charge trapping. *Appl. Phys. Lett.* 83 (18), 3818–3820. doi:10.1063/1.1624639

Jang, J. G., Ji, H. J., Kim, H. S., and Jeong, J. C. (2011). TPBI:FIrpic organic light emitting devices with the electron transport layer of Bphen/Alq_3. *Curr. Appl. Phys.* 11 (1), S251–S254. doi:10.1016/j.cap.2010.11.103

Kalinowski, J., Cocchi, M., Virgili, D., Fattori, V., and Williams, J. G. (2007). Mixing of excimer and exciplex emission: a new way to improve white light emitting organic electrophosphorescent diodes. *Adv. Mat.* 19 (22), 4000–4005. doi:10.1002/adma.200700655

Lee, Y., Kim, J., Kwon, S., Min, C.-K., Yi, Y., Kim, J., et al. (2008). Interface studies of aluminum, 8-hydroxyquinolatolithium (Liq) and Alq_3 for inverted OLED application. *Org. Elect.* 9 (3), 407–412. doi:10.1016/j.orgel.2008.01.001

Lin, T.-C., Sarma, M., Chen, Y.-T., Liu, S.-H., Lin, K.-T., Chiang, P.-Y., et al. (2018). Probe exciplex structure of highly efficient thermally activated delayed fluorescence organic light emitting diodes. *Nat. Commun.* 9 (1), 3111. doi:10.1038/s41467-018-05527-4

Liu, B., Luo, D., Gao, D., Wang, X., Xu, M., Zou, J., et al. (2015). An ideal host-guest system to accomplish high-performance greenish yellow and hybrid white organic light-emitting diodes. *Org. Elect.* 27, 29–34. doi:10.1016/j.orgel.2015.08.030

Liu, B., Nie, H., Zhou, X., Hu, S., Luo, D., Gao, D., et al. (2016aa). Manipulation of charge and exciton distribution based on blue aggregation-induced emission fluorophors: a novel concept to achieve high-performance hybrid white organic light-emitting diodes. *Adv. Funct. Mat.* 26 (5), 776–783. doi:10.1002/adfm.201503368

Liu, B., Tao, H., Wang, L., Gao, D., Liu, W., Zou, J., et al. (2016b). High-performance doping-free hybrid white organic light-emitting diodes: the exploitation of ultrathin emitting nanolayers (< 1 nm). *Nan. Ene.* 26, 26–36. doi:10.1016/j.nanoen.2016.04.054

Liu, B., Xu, M., Wang, L., Yan, X., Tao, H., Su, Y., et al. (2014a). Investigation and optimization of each organic layer: a simple but effective approach towards achieving high-efficiency hybrid white organic light-emitting diodes. *Org. Elect.* 15 (4), 926–936. doi:10.1016/j.orgel.2014.02.005

Liu, B., Xu, M., Wang, L., Zou, J., Tao, H., Su, Y., et al. (2014b). Regulating charges and excitons in simplified hybrid white organic light-emitting diodes: the key role of concentration in single dopant host–guest systems. *Org. Elect.* 15 (10), 2616–2623. doi:10.1016/j.orgel.2014.07.033

Liu, J., Shi, X., Wu, X., Wang, J., Min, Z., Wang, Y., et al. (2014). Achieving above 30% external quantum efficiency for inverted phosphorescence organic light-emitting diodes based on ultrathin emitting layer. *Org. Elect.* 15 (10), 2492–2498. doi:10.1016/j.orgel.2014.07.027

Liu, X.-K., Chen, Z., Qing, J., Zhang, W.-J., Wu, B., Tam, H. L., et al. (2015a). Remanagement of singlet and triplet excitons in single-emissive-layer hybrid white organic light-emitting devices using thermally activated delayed fluorescent blue exciplex. *Adv. Mat.* 27 (44), 7079–7085. doi:10.1002/adma.201502897

Liu, X.-K., Chen, Z., Zheng, C.-J., Liu, C.-L., Lee, C.-S., Li, F., et al. (2015b). Prediction and design of efficient exciplex emitters for high-efficiency, thermally activated delayed-fluorescence organic light-emitting diodes. *Adv. Mat.* 27 (14), 2378–2383. doi:10.1002/adma.201405062

Luo, D., Li, X.-L., Zhao, Y., Gao, Y., and Liu, B. (2017). High-performance blue molecular emitter-free and doping-free hybrid white organic light-emitting diodes: an alternative concept to manipulate charges and excitons based on exciplex and electroplex emission. *ACS Photon.* 4 (6), 1566–1575. doi:10.1021/acsphotonics.7b00364

Park, Y.-S., Jeong, W.-I., and Kim, J.-J. (2011). Energy transfer from exciplexes to dopants and its effect on efficiency of organic light-emitting diodes. *J. Appl. Phys.* 110 (12), 124519. doi:10.1063/1.3672836

Park, Y. S., Lee, S., Kim, K. H., Kim, S. Y., Lee, J. H., and Kim, J. J., (2013). Exciplex-forming co-host for organic light-emitting diodes with ultimate efficiency. *Adv. Funct. Mat.* 23 (39), 4914–4920. doi:10.1002/adfm.201300547

Ruan, Z., Li, L., Wang, C., Xie, Y., Hu, Q., Peng, Q., et al. (2016). Tetraphenylcyclopentadiene derivatives: aggregation-induced emission, adjustable luminescence from green to blue, efficient undoped OLED performance and good mechanochromic properties. *Small* 12 (47), 6623–6632. doi:10.1002/smll.201602285

Rabich, O., Chumak, L., Meshcheriakova, I., and Laukhyna, L. (2017). "Possibility and effectiveness of led lighting of the permanent workplaces in modern construction production," in Proceedings in memory of Starodubov, 5. Available at: http://smm.pgasa.dp.ua/article/view/103633.

Schwartz, G., Pfeiffer, M., Reineke, S., Walzer, K., and Leo, K. (2007). Harvesting triplet excitons from fluorescent blue emitters in white organic light-emitting diodes. *Adv. Mat.* 19 (21), 3672–3676. doi:10.1002/adma.200700641

Seino, Y., Sasabe, H., Pu, Y. J., and Kido, J. (2014). High-performance blue phosphorescent OLEDs using energy transfer from exciplex. *Adv. Mat.* 26 (10), 1612–1616. doi:10.1002/adma.201304253

Shin, H., Lee, S., Kim, K. H., Moon, C. K., Yoo, S. J., Lee, J. H., et al. (2014). Blue phosphorescent organic light-emitting diodes using an exciplex forming co-host with the external quantum efficiency of theoretical limit. *Adv. Mat.* 26 (27), 4730–4734. doi:10.1002/adma.201400955

Song, W., and Lee, J. Y. (2015). Light emission mechanism of mixed host organic light-emitting diodes. *Appl. Phys. Lett.* 106 (12), 123306. doi:10.1063/1.4916549

Tang, C. W., and VanSlyke, S. A. (1987). Organic electroluminescent diodes. *Appl. Phys. Lett.* 51 (12), 913–915. doi:10.1063/1.98799

Thejokalyani, N., and Dhoble, S. J. (2014). Importance of eco-friendly OLED lighting. *Defect Diffusion Forum* 357, 1–27. doi:10.4028/www.scientific.net/DDF

Wang, J., Chen, J., Qiao, X., Alshehri, S. M., Ahamad, T., and Ma, D., (2016). Simple-structured phosphorescent warm white organic light-emitting diodes with high power efficiency and low efficiency roll-off. *ACS Appl. Mat. Inter* 8 (16), 10093–10097. doi:10.1021/acsami.6b00861

Wang, Q., Ding, J., Ma, D., Cheng, Y., Wang, L., Jing, X., et al. (2009). Harvesting excitons via two parallel channels for efficient white organic LEDs with nearly 100% internal quantum efficiency: fabrication and emission-mechanism analysis. *Adv. Funct. Mat.* 19 (1), 84–95. doi:10.1002/adfm.200800918

Wang, Q., Oswald, I. W. H., Perez, M. R., Jia, H., Shahub, A. A., Qiao, Q., et al. (2014). Doping-free organic light-emitting diodes with very high power efficiency, simple device structure, and superior spectral performance. *Adv. Funct. Mat.* 24 (30), 4746–4752. doi:10.1002/adfm.201400597

Wang, X., Wang, R., Zhou, D., and Yu, J. (2016). Study of organic light-emitting diodes with exciplex and non-exciplex forming interfaces consisting of an ultrathin rubrene layer. *Synth. Met.* 214, 50–55. doi:10.1016/j.synthmet.2016.01.022

Wang, Y. M., Teng, F., Xu, Z., Hou, Y. B., Yang, S. Y., Qian, L., et al. (2004). White emission via electroplex formation at poly (N-vinylcarbazole)/2, 9-dimethyl-4,

7-diphenyl-1, 10-phenanthroline interface. *Appl. Surf. Sci.* 236 (1–4), 251–255. doi:10.1016/j.apsusc.2004.04.031

Xu, L., Tang, C. W., and Rothberg, L. J., (2016). High efficiency phosphorescent white organic light-emitting diodes with an ultra-thin red and green co-doped layer and dual blue emitting layers. *Org. Elect.* 32, 54–58. doi:10.1016/j.orgel.2016.02.010

Xu, T., Yan, L., Miao, J., Hu, Z., Shao, S., Li, A., et al. (2016a). Unlocking the potential of diketopyrrolopyrrole-based solar cells by a pre-solvent annealing method in all-solution processing. *RSC Adv.* 6 (58), 53587–53595. doi:10.1039/C6RA09770G

Xu, T., Yang, M., Liu, J., Wu, X., Murtaza, I., He, G., et al. (2016b). Wide color-range tunable and low roll-off fluorescent organic light emitting devices based on double undoped ultrathin emitters. *Org. Elect.* 37, 93–99. doi:10.1016/j.orgel.2016.06.014

Xu, T., Zhang, Y. X., Huang, C. C., Zhou, J. G., Fung, M. K., and Meng, H. (2019). Highly simplified blue phosphorescent organic light-emitting diodes incorporating exciplex-forming co-host assisting energy transfer. *J. Lumin.* 206, 554–559. doi:10.1016/j.jlumin.2018.10.007

Xu, T., Zhang, Y.-X., Murtaza, I., and Meng, H. (2017a). P-170: organic light-emitting diodes incorporating a novel exciplex-forming host: a synergistic strategy to design highly simplified OLEDs for application. *SID Symp. Dig. Tech. Pap.* 48 (1), 1915–1918. doi:10.1002/sdtp.12004

Xu, T., Zhang, Y. X., Wang, B., Huang, C. C., Murtaza, I., Meng, H., et al. (2017b). Highly simplified reddish orange phosphorescent organic light-emitting diodes incorporating a novel carrier-and exciton-confining spiro-exciplex-forming host for reduced efficiency roll-off. *ACS Appl. Mater. Inter.* 9 (3), 2701–2710. doi:10.1021/acsami.6b13077

Xu, T., Zhou, J. G., Fung, M. K., and Meng, H. (2018aa). Simplified efficient warm white tandem organic light-emitting devices by ultrathin emitters using energy transfer from exciplexes. *Org. Elect.* 63, 369–375. doi:10.1016/j.orgel.2018.09.026

Xu, T., Zhou, J. G., Huang, C. C., Zhang, L., Fung, M. K., Murtaza, I., et al. (2017c). Highly simplified tandem organic light-emitting devices incorporating a green phosphorescence ultrathin emitter within a novel interface exciplex for high efficiency. *ACS Appl. Materials Inter.* 9 (12), 10955–10962. doi:10.1021/acsami.6b16094

Xu, T., Zhou, J. G., Meng, H., and Fung, M. K. (2018bb). P-164: energy transfer from interface exciplexes to ultrathin emissive layers: a path way to design simplified efficient white tandem organic light-emitting diodes for application. *SID Symp. Dig. Tech. Pap.* 49 (1), 1779–1781. doi:10.1002/sdtp.12394

Yang, C. C., Hsu, C. J., Chou, P. T., Cheng, H. C., Su, Y. O., and Leung, M. k. (2009). Excited state luminescence of multi-(5-phenyl-1, 3, 4-oxadiazo-2-yl) benzenes in an electron-donating matrix: exciplex or electroplex? *The J. Phys. Chem. B* 114 (2), 756–768. doi:10.1021/jp9093063

Zhang, B., Tan, G., Lam, C. S., Yao, B., Ho, C. L., Liu, L., et al. (2012). High-efficiency single emissive layer white organic light-emitting diodes based on solution-processed dendritic host and new orange-emitting iridium complex. *Adv. Mat.* 24 (14), 1873–1877. doi:10.1002/adma.201104758

Zhang, Q., Li, B., Huang, S., Nomura, H., Tanaka, H., and Adachi, C. (2014). Efficient blue organic light-emitting diodes employing thermally activated delayed fluorescence. *Nat. Photon.* 8 (4), 326. doi:10.1038/nphoton.2014.1

Zhang, Q., Tsang, D., Kuwabara, H., Hatae, Y., Li, B., Takahashi, T., et al. (2015). Nearly 100% internal quantum efficiency in undoped electroluminescent devices employing pure organic emitters. *Adv. Mat.* 27 (12), 2096–2100. doi:10.1002/adma.201405474

Zhang, T., Chu, B., Li, W., Su, Z., Peng, Q. M., and Zhao, B., (2014). Efficient triplet application in exciplex delayed-fluorescence oleds using a reverse intersystem crossing mechanism based on a δ es–t of around zero. *ACS Appl. Mater. Inter.* 6 (15), 11907–11914. doi:10.1021/am501164s

Zhang, W., Wang, H., Miao, J., Zhu, Y., Ali, M. U., Xu, T., et al. (2018). Revealing the influence of hole injection material's molecular orientation on OLED's performance. *Org. Elect.* 59, 301–305. doi:10.1016/j.orgel.2018.05.022

Zhao, Y., Chen, J., and Ma, D. (2013). Ultrathin nondoped emissive layers for efficient and simple monochrome and white organic light-emitting diodes. *ACS Appl. Materials Inter.* 5 (3), 965–971. doi:10.1021/am3026097

Zhao, Y., Zhu, L., Chen, J., and Ma, D. (2012). Improving color stability of blue/orange complementary white OLEDs by using single-host double-emissive layer structure: comprehensive experimental investigation into the device working mechanism. *Org. Elect.* 13 (8), 1340–1348. doi:10.1016/j.orgel.2012.04.015

Conflict of Interest: The authors declare that the research was conducted in the absence of any commercial or financial relationships that could be construed as a potential conflict of interest.

frontiers in Chemistry

ORIGINAL RESEARCH
published: 22 April 2021
doi: 10.3389/fchem.2021.671720

Fabrication of 2-Inch Free-Standing GaN Substrate on Sapphire With a Combined Buffer Layer by HVPE

Nanliu Liu[1,2], Yongjing Jiang[2], Jian Xiao[1], Zhiwen Liang[2], Qi Wang[2]* and Guoyi Zhang[2,3]*

[1] School of Physics and Electronics, Qiannan Normal University for Nationalities, Duyun, China, [2] Dongguan Institute of Opto-Electronics, Peking University, Dongguan, China, [3] Research Center for Wide-Gap Semiconductors, State Key Laboratory for Artificial Microstructures and Mesoscopic Physics, School of Physics, Peking University, Beijing, China

Free-standing GaN substrates are urgently needed to fabricate high-power GaN-based devices. In this study, 2-inch free-standing GaN substrates with a thickness of ~250 μm were successfully fabricated on double-polished sapphire substrates, by taking advantage of a combined buffer layer using hydride vapor phase epitaxy (HVPE) and the laser lift-off technique. Such combined buffer layer intentionally introduced a thin AlN layer, using a mix of physical and chemical vapor deposition at a relatively low temperature, a 3-dimensional GaN interlayer grown under excess ambient H_2, and a coalescent GaN layer. It was found that the cracks in the epitaxial GaN layer could be effectively suppressed due to the large size and orderly orientation of the AlN nucleus caused by pre-annealing treatment. With the addition of a 3D GaN interlayer, the crystal quality of the GaN epitaxial films was further improved. The 250-μm thick GaN film showed an improved crystalline quality. The full width at half-maximums for GaN (002) and GaN (102), respectively dropped from 245 and 412 to 123 and 151 arcsec, relative to those without the 3D GaN interlayer. The underlying mechanisms for the improvement of crystal quality were assessed. This method may provide a practical route for fabricating free-standing GaN substrates at low cost with HVPE.

Keywords: free-standing GaN substrate, LT-AlN, pre-annealing, combined buffer layer, 3D GaN interlayer, HVPE

OPEN ACCESS

Edited by:
Baiquan Liu,
Sun Yat-Sen University, China

Reviewed by:
Dongxiang Luo,
South China Normal University, China
Guoshun Pan,
Tsinghua University, China

***Correspondence:**
Jian Xiao
ufo_xiao@sgmtu.edu.cn
Qi Wang
wangq@pku-ioe.cn

Specialty section:
This article was submitted to Physical Chemistry and Chemical Physics, a section of the journal Frontiers in Chemistry

Received: *24 February 2021*
Accepted: *30 March 2021*
Published: *22 April 2021*

Citation:
Liu NL, Jiang YJ, Xiao J, Liang ZW, Wang Q and Zhang GY (2021) Fabrication of 2-Inch Free-Standing GaN Substrate on Sapphire With a Combined Buffer Layer by HVPE. Front. Chem. 9:671720. doi: 10.3389/fchem.2021.671720

INTRODUCTION

GaN-based devices have experienced important development for applications in light-emitting diodes, radio frequency devices, and electronics (Sandvik et al., 2001; Chai et al., 2018; Li et al., 2018). However, these devices are generally constructed on foreign substrates, such as SiC, Si, and patterned sapphire substrates (PSSs). For short-wavelength laser diodes and for high-power and high-frequency devices, native GaN substrates have many advantages, such as their low level of current leakage and long lifetimes due to the high quality of the active epitaxial layer, accompanied by low dislocation densities and a lower level of lattice distortion, derived from homo-epitaxy (Liu et al., 2017; Sumiya et al., 2017; Han et al., 2018).

Generally speaking, hydride vapor-phase epitaxy (HVPE) is the most commonly used technique to obtain free-standing GaN substrates, due to the high growth rate it produces and its low cost (Fujito et al., 2009). Normally, the procedure for fabricating free-standing GaN substrates includes the following steps. First, a GaN template with a low temperature GaN buffer layer (LT-GaN), grown with metal organic chemical vapor deposition (MOCVD) is used for the re-growth of GaN film in HVPE. Following that, a GaN film, with a thickness of several 100 μm, is then separated from its foreign substrate using self-separation (Lee et al., 2009) or the laser lift-off (LLO) technique (Paskova et al., 2006). However, the residual strain and lattice distortion caused by hetero-epitaxy could not be completely suppressed using the LT-GaN buffer layer method. It has recently been reported that the crystal quality of GaN film and related devices were improved when the LT-GaN buffer layer was replaced with a thin AlN buffer layer on both PSS and plain sapphire substrate, due to the improvement of the crystal quality of the GaN nucleation layer (Chen et al., 2015, 2016). The AlN buffer layer can also be used in a cost-effective way because it can be deposited either through a sputter or with physical vapor deposition (PVD), using cheaper appliances than MOCVD.

In this study, GaN thick film was directly grown on a double-polished sapphire substrate with a LT-AlN buffer layer using HVPE. The GaN thick films grown on a pre-annealed LT-AlN layer and a 3-dimensional (3D) GaN interlayer grown under the excess ambient H_2, the variation in the morphology and crystal quality of LT-AlN and GaN films were studied with differential-interference contrast microscopy (DICM), atomic-force microscopy (AFM), and X-ray diffraction (XRD). The behaviors of GaN nucleation were also investigated, and they further testify to the effects of pre-annealing the LT-AlN layer. Two-inch free-standing GaN substrate with a high crystal quality was obtained with LLO.

MATERIALS AND METHODS

A thin AlN buffer layer (labeled LT-AlN) with a thickness of 30 nm was deposited on the surface of commercial double-polished sapphire substrates at a temperature below 200°C using a mix of physical and chemical vapor deposition system (Liu et al., 2018). The LT-AlN can be clearly observed in the SEM image in **Figure 1A**. All of the sapphire substrates that were covered with LT-AlN in the experiment had previously been cleaned and dried using a routine process (Liu et al., 2016).

First, to investigate the effects of the annealing process of LT-AlN on the growth of the GaN film on top of it, comparative

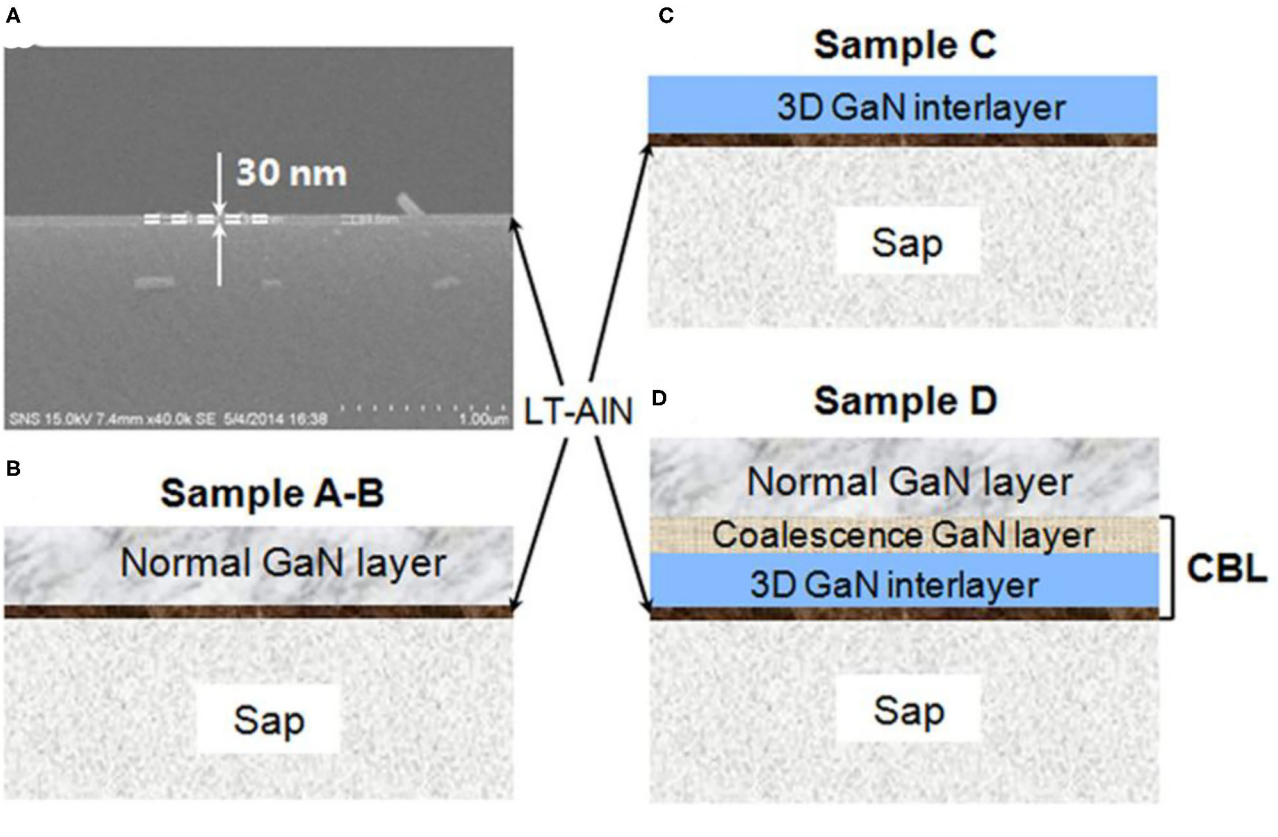

FIGURE 1 | (A) SEM image of a cross-section of a double-polished sapphire covered with LT-AlN. **(B–D)** Schematic diagrams of the processes designed for GaN growth.

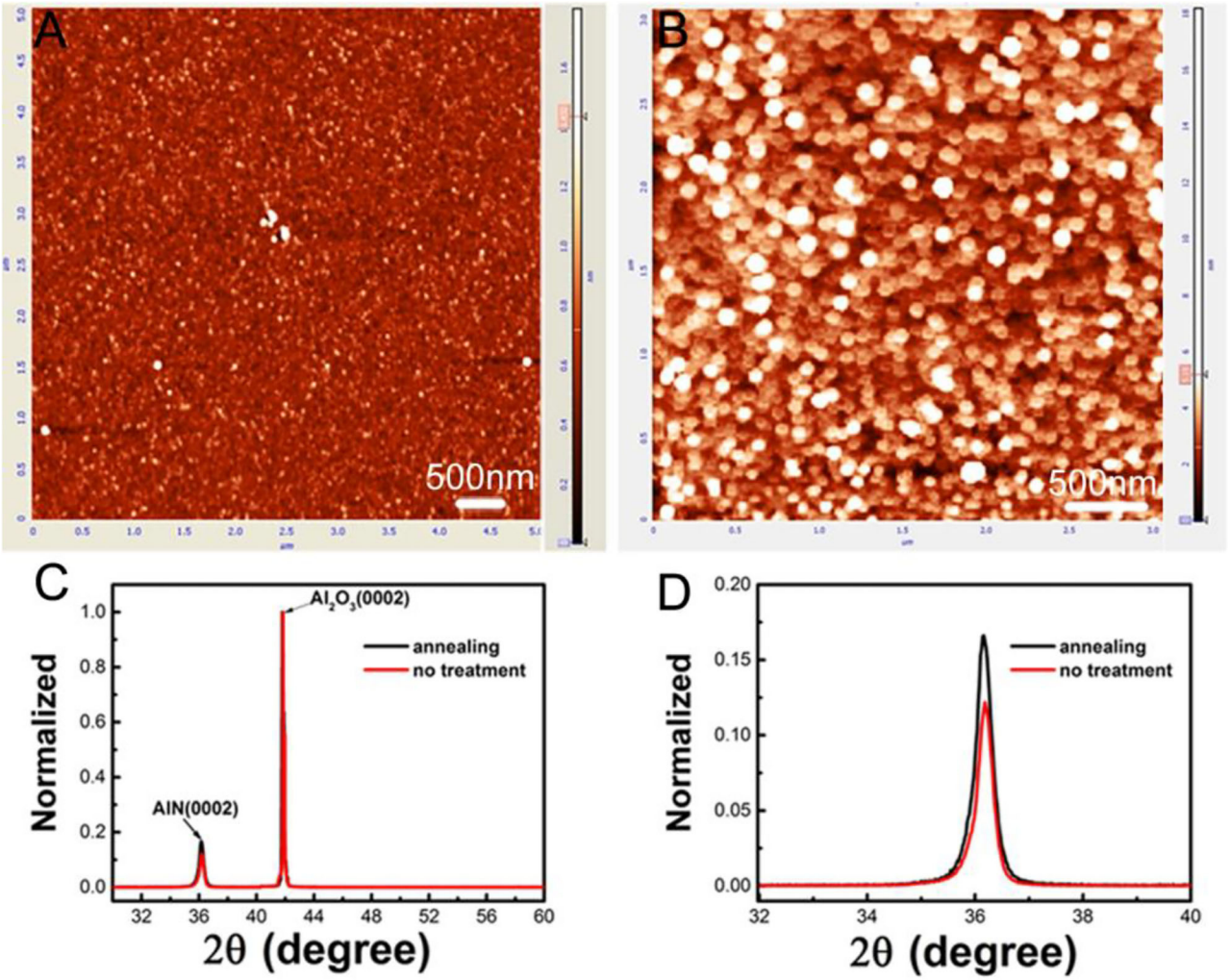

FIGURE 2 | AFM images of LT-AlN without **(A)** and with **(B)** annealing treatment. **(C)** ω-2θ scan patterns of the (002) plane peak of LT-AlN with and without annealing treatment. **(D)** Magnification of **(C)**.

studies were performed under normal growth conditions (NGCs) using HVPE, as shown in **Figure 1B**. Samples that did not undergo pre-annealing treatment were called sample A. Sample B samples were annealed under mixed gases N_2/NH_3 gases at 3/1 and 1070°C for 8 min prior to the GaN epitaxial growth. Then, samples A and B were loaded into our home-made HVPE reactor for thick GaN film growth. During the NGC processing, the carrier gas was a mixture of N_2 and H_2 ($N_2/H_2 = 1/1$). The growth pressure and the V/III ratio of source gases was set to 550 torr and 800/20, respectively. Under these conditions, a thick GaN layer, with thicknesses ranging from 20 to 250 μm, was grown on the LT-AlN at 1070°C.

A modified structure with a 3D GaN interlayer was then proposed, as shown in **Figure 1C**. In this structure, samples (labeled sample C) were first annealed under the same conditions as sample B, and then extra H_2 gas at a flow rate of 10 slm was added into the growth zone during HVPE growth. Here, the V/III ratio of source gases was set to 100/1 for the 3D GaN interlayer growth for about 1000 s. For sample D, shown in **Figure 1D**, the V/III ratio of source gases was changed to 60/1 to initiate the coalescence growth of the GaN layer for another 1000 s (Zhao et al., 2007) after the series of processes for sample C were completed. Then, a normal GaN layer was then programmed for growth for 1–3 h.

The surface and cross-sectional morphologies of the samples were characterized with DICM, AFM, and scanning electron microscope (SEM). The DICM was implemented with a Leica DM 2700 RL, and the AFM tapping mode was performed in Bruker Dimension ICON. The SEM images were obtained using a field-emission scanning electron microscope (Zeiss, SIGMA 300), and energy dispersive spectroscopy (EDS) testing was conducted with a Bruker Quantax 400 system. High-resolution XRD was measured using a Bruker D8 Discovery system.

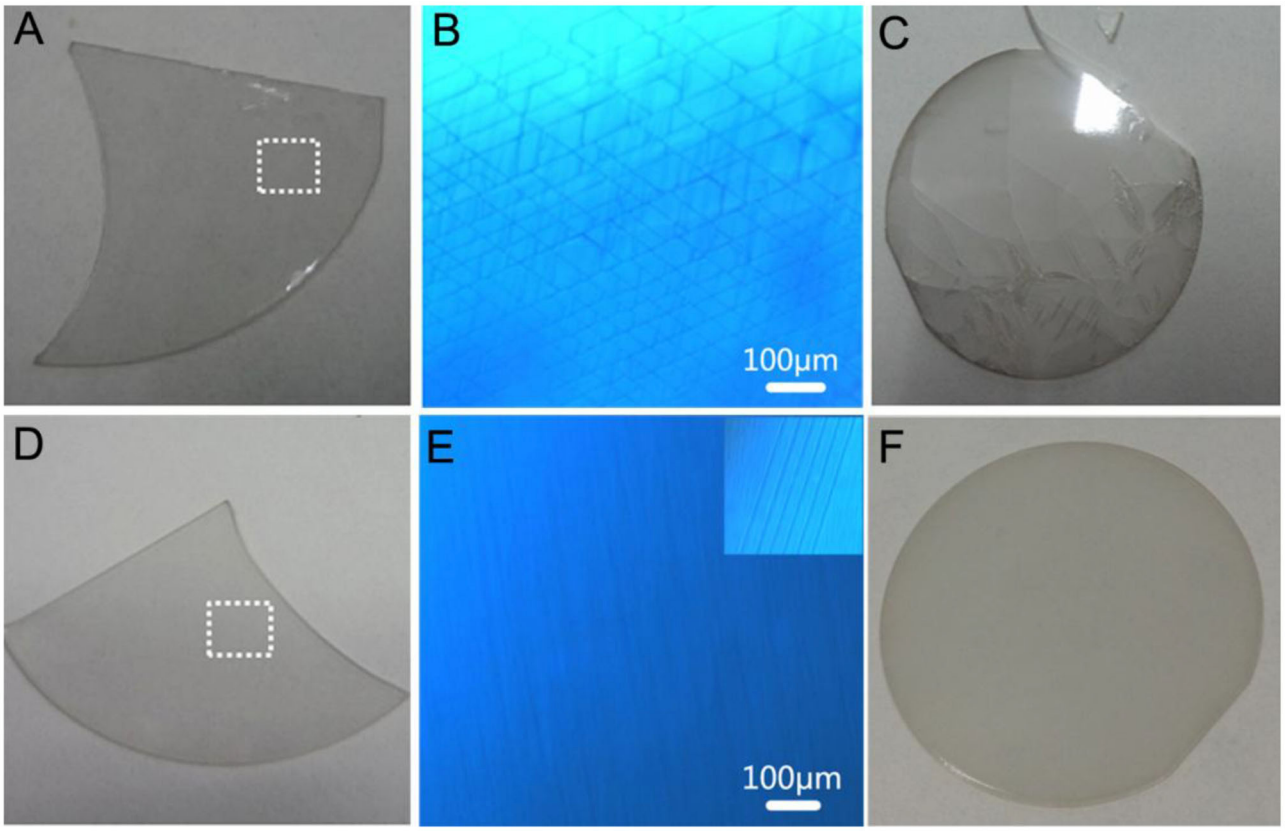

FIGURE 3 | Photographic and optical microscopic images of GaN films grown above LT-AlN with no annealing treatment **(A–C)** (sample A) and with annealing pre-treatment **(D–F)** (sample B) [the thicknesses of GaN for **(A,D,C,F)** are 20 and 100 μm, respectively]. **(B,E)** Microscopic images of the dot white rectangle of **(A,D)**, respectively, where the insert of **(E)** shows the local micro-crack in **(D)**.

RESULTS AND DISCUSSION

Effects of Pre-annealing of LT-AlN on the Crystalline Quality of GaN Film

Figure 2 shows the AFM images and the XRD measurements for LT-AlN with and without annealing treatment. As shown in **Figures 2A,B**, after annealing treatment, the surface roughness of the AlN film increased from 0.27 to 1.20 nm, and the nucleus of AlN exhibited an obvious hexagon columnar structure, indicating a highly oriented and increased crystal quality for the AlN nucleus. In addition, the size of the nucleus of AlN was larger than it was before annealing treatment.

The results of the ω-2θ scan patterns for the (002) peak of LT-AlN with high-resolution XRD characterization also confirmed the improvement of the crystal quality of the AlN nucleus after the annealing process, as shown in **Figures 2C,D**. After the annealing treatment, the intensity of the (002) peak of LT-AlN film showed an obvious increase, which indicates an improvement for the AlN crystal quality, mainly due to obvious grain coarsening and orientation following annealing, as shown in **Figure 2B** (Okuno et al., 2013).

The GaN film was grown on LT-AlN substrates under NGCs with HVPE. **Figure 3** shows photographic and optical microscopic images for samples A and B. When the LT-AlN was not annealed before the GaN growth, in sample A, the GaN layer with a thickness of 20 μm demonstrated a gray color, as shown in **Figure 3A**, and mesh-like sub-surface cracks appeared in the DCIM in **Figure 3B**. Furthermore, as shown in **Figure 3C**, the GaN film and its substrate cracked into pieces when the thickness reached ∼100 μm. However, as shown in **Figures 3D,F**, for sample B with LT-AlN pre-annealed at 1070°C, the GaN film with the same thickness as sample A brightens and becomes transparent. In the more detailed image shown in **Figure 3E**, most of the GaN film showed smooth, stepwise formation with no cracks. This confirms that the majority of cracks in the GaN film were effectively suppressed by pre-annealing of LT-AlN at high temperatures, although local micro-cracks continued to exist, as shown in the insert to **Figure 3E**. Thus, pre-annealing LT-AlN is a main factor for the improvement in the quality of the crystal for the GaN film, which is in accordance with previous reports (Liu et al., 2009; Yoshizawa et al., 2018).

It has been reported that the crystal properties of the GaN layer were mainly determined by the properties of the underlying AlN buffer layer through an influence on the nucleation of GaN (Yoshizawa et al., 2018). To study the underlying growth mechanism, the evolution of the surface morphology of GaN

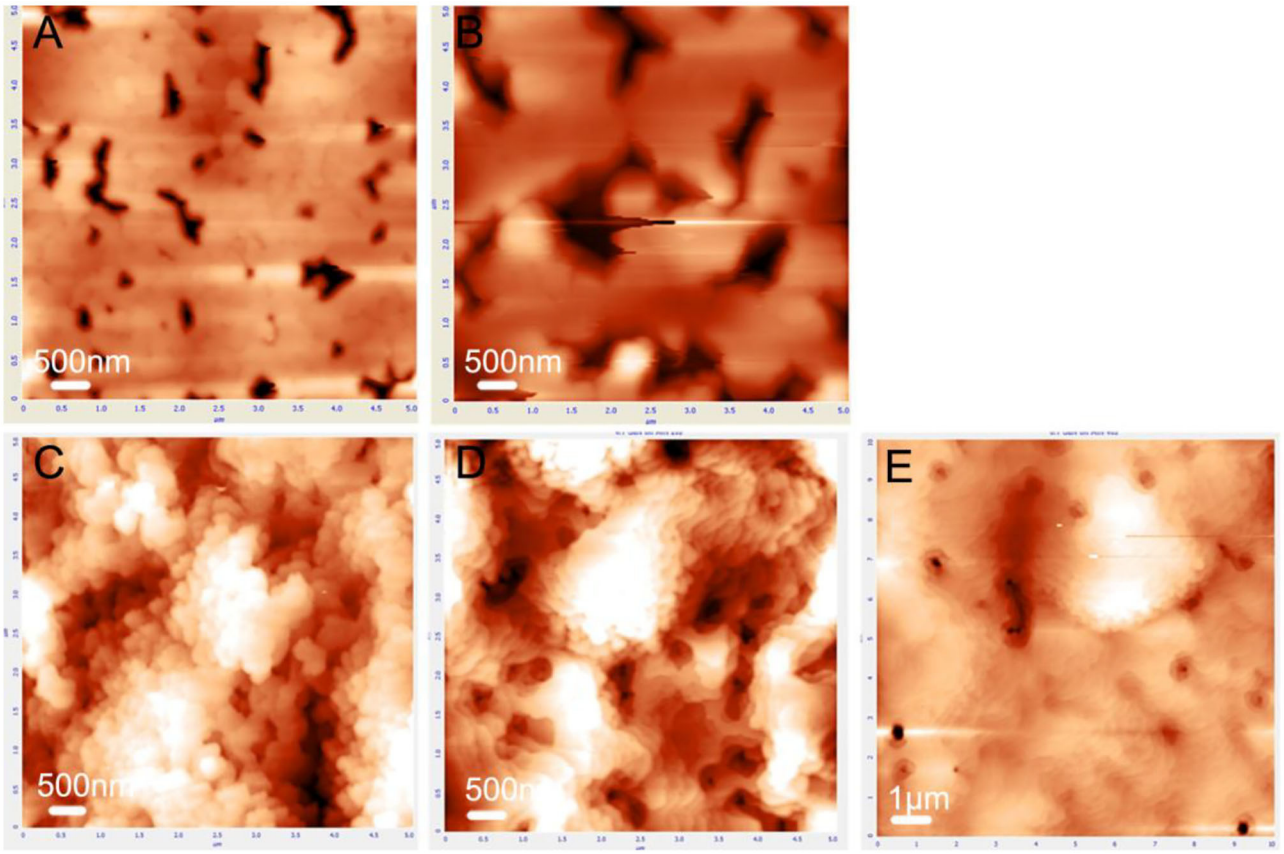

FIGURE 4 | AFM images of GaN nucleation layer of sample A **(A,B)** and sample B **(C–E)**. Nucleation layer growth times were set to 10 s for **(A,C)**, 20 s for **(B,D)**, and 40 s for **(E)**.

nucleation advanced with time was observed (**Figure 4**). First, AFM images of the GaN nucleation layer grown by HVPE for 10 and 20 s on top of LT-AlN without annealing are exhibited in **Figures 4A,B**, respectively. Moreover, **Figures 4C–E** shows a time series of AFM images of the GaN nucleation layer grown by HVPE for 10, 20, and 40 s on LT-AlN with annealing pre-treatment, respectively. From these images, it is clear that the behavior of the GaN nucleation on the pre-annealed LT-AlN was significantly different from that appearing under no annealing treatment. For the no-annealing sample, the GaN nucleation layer began to merge at 10 s, and many deep pits formed as a result, as shown in **Figure 4A**. These pits became larger with time, as shown in **Figure 4B**. These large pits then became the source of cracks and further expanded as the GaN film grew, as shown in **Figures 3A–C**. However, for the annealed sample, nucleation formed 3D GaN islands at 10 s, as shown in **Figure 4C**, and then these islands enlarged in a clear stepwise formation as shown in **Figure 4D**. Finally, the nucleation layer for GaN coalesced with smaller pits until 40 s, as shown in **Figure 4E**. This delayed coalescence behavior for the GaN nucleation layer blocked the propagation of dislocation and of cracks, which led to an improvement in the crystal quality of the GaN film grown on the annealed LT-AlN film (Shang et al., 2015).

Growth of Crack-Free 2-Inch GaN Thick Wafers With High Crystal Quality Using CBL

According to the above analyses, the crystal properties of GaN film grown under NGCs were greatly improved by the use of pre-annealed LT-AlN. However, as shown in **Figure 3E**, sub-surface micro cracks also appeared that would detract from the ability to obtain a thick GaN film and a free-standing GaN substrate. It has been reported that the lateral overgrowth of GaN could be passivated under rich ambient H_2 gas and change the GaN nucleus into 3D islands for the use of both MOCVD (Tadatomo et al., 1999) and the HVPE technique (André et al., 2012; Lekhal et al., 2016). This results in high single-crystal quality for GaN film, due to dislocation bending and termination on the inclined planes (Hiramatsu et al., 2000; Imade et al., 2011). Optical microscopic images for sample C are shown in **Figures 5A–C**. Here, a 3D GaN interlayer grown under an excess large flow of H_2 gas was introduced on top of the annealed LT-AlN, and the growth process was immediately terminated when the GaN 3D interlayer growth was accomplished. In relation to the picture focused on the surface of the GaN 3D interlayer, as shown in **Figure 5A**, multiple surface pits larger than 10 μm were obtained by adding an additional high flow rate for the

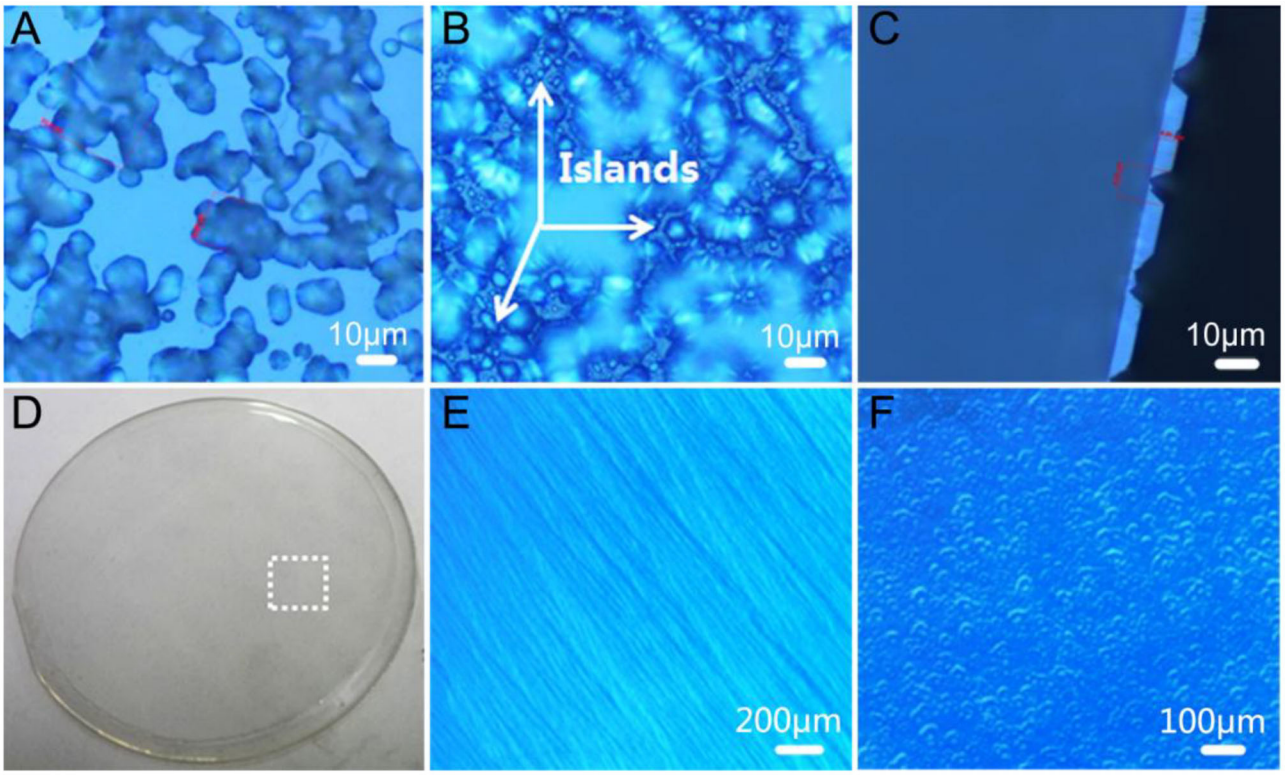

FIGURE 5 | Optical images of the GaN 3D interlayer grown on LT-AlN with annealing pre-treatment focused on the surface **(A)** and near the interface between the GaN epitaxial layer and the LT-AlN-covered sapphire substrate **(B)**. **(C)** Microscopic mage of the cross-section of **(A)**. **(D)** Photographic image of sample D. Microscope images of the dotted white rectangle in **(D)** when focused on surface morphology **(E)** and near the interface between GaN epitaxial layer and the LT-AlN-covered sapphire substrate **(F)**.

H_2 gas. Moreover, as shown in **Figure 5B**, the image showing near interface between the GaN 3D interlayer and the LT-AlN-covered sapphire substrate demonstrates that a large number of islands formed among the pits. The depth of the deepest pits was ∼4.8 μm, as shown in the cross-section in **Figure 5C**.

A 2-inch GaN wafer with a thickness of 250 μm (sample D) was obtained by adding a coalescence GaN layer and a normal GaN layer above the sample C. In the photographic image presented in Figure 5D, it can be seen that sample D is extremely bright and transparent, and the morphology and crystal quality of the GaN film are greatly improved by the perfect stepwise formation seen in Figure 5E. From the XRD rocking curve, measured with a slit width of 0.5 mm, the FWHMs of (002) and (102) for the XRD in sample D decreased from 245 and 412 to 123 and 151 arcsec, respectively, compared to sample B, grown under NGCs. Focusing on the interface between the GaN epitaxial layer and the LT-AlN covered sapphire substrate, shown in Figure 5F, many dense GaN 3D islands can be seen. It can be speculated that the shape of GaN islands could be kept unchanged for longer, and the coalescence could be delayed by adding a mass flow of H_2 gas. In addition, the formation of GaN 3D islands could enhance the crystal quality and relax the stress. On the basis of these analyses, therefore, it can be concluded that combing the pre-annealing of the LT-AlN and adding the extra high flow rate of H_2 gas could effectively improve the properties of the epitaxial GaN film due to the increased size and crystalline quality of the AlN nucleus by annealing, along with the 3D GaN interlayer formed by adjusting the lateral growth by H_2 gas.

Fabrication of a 2-Inch Free-Standing GaN Wafer Using LLO

The sapphire substrate of sample D, shown in **Figure 5D**, was removed with LLO, and a 2-inch free-standing GaN wafer was obtained. As seen in **Figure 6A**, it was found that the black parts existing on the N-face of the free-standing GaN substrate could not be dissolved in hot hydrochloric acid (HCl), as shown in the insert to **Figure 6A**. **Figure 6B** shows the SEM image for the local area of 2-inch free-standing GaN substrate after immersion in hot HCl at 50°C for 30 min, and EDS mapping analyses for the elements N, Ga, Al, and O are shown in **Figures 6C–F**, respectively. A much denser pattern of blue dots denoted as N elements are shown in **Figure 6C**, and red dots denoted as Ga elements are shown in **Figure 6D** confirm that the left part of the picture in **Figure 6B** is GaN film. Moreover, the much brighter and denser violet dots, representing Al, as shown in **Figure 6E**, and yellow dots, representing O, shown in **Figure 6F** illustrate that the bugle on the right part of the picture in **Figure 6B** is really a residual part of an oxidized AlN layer.

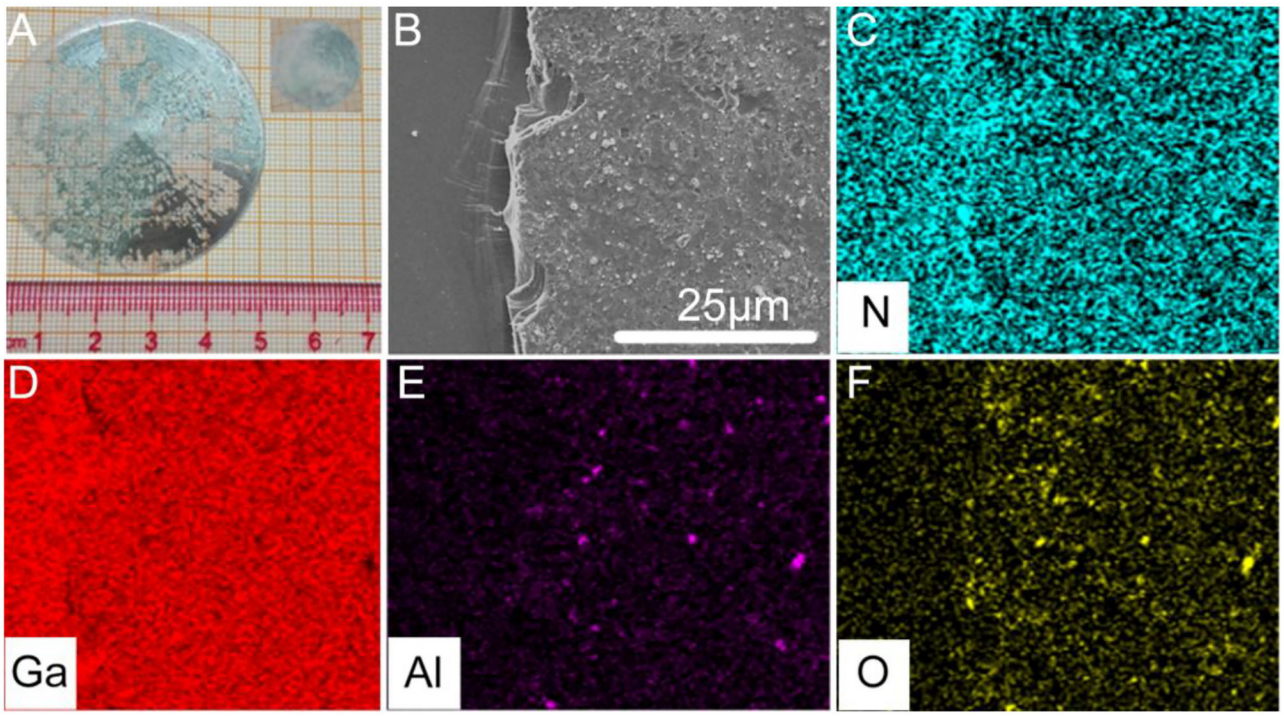

FIGURE 6 | (A) Photographic image of 2-inch free-standing GaN wafer in **Figure 5D** after the sapphire substrate is removed with LLO. **(B)** SEM image for local area of insert of **(A)** after immersion in hot concentrated HCl at 50°C for 30 min. **(C–F)** EDS mapping analyses for the elements N, Ga, Al, and O in **(B)**, respectively.

Thus, it is speculated that part of the LT-AlN layer below the pits might be melted due to giant local heat instantaneously released from the decomposition of the GaN with the laser, which might primarily attack the pits formed within the 3D GaN layer, and the black parts existing on the N-face of a GaN free-standing substrate as the residual parts of the LT-AlN layer, which did not melt during the LLO process. This partly melted LT-AlN layer may act as a protecting buffer layer, blocking the shock-wave during LLO process (Safadi et al., 2005; Su et al., 2013).

CONCLUSION

In summary, 2-inch crack-free free-standing GaN substrates with high crystal quality were obtained using the CBL and LLO techniques. Large AlN nuclei with an orderly orientation were obtained by annealing at high temperature, which led to the improvement of the crystal quality of GaN nuclei grown on it. Moreover, the addition of an excessive large flow of H_2 gas during HVPE growth further increased the size of the GaN nucleus and delayed the coalescent growth as well. Therefore, the combination of LT-AlN and a 3D GaN interlayer plays a critical role in improving the properties of GaN film grown on top of it. In the meantime, LT-AlN buffer layer may have protected GaN film from rupture by partial melting during LLO processing, and thus a crack-free 2-inch free-standing GaN substrate was obtained. This suggests that the CBL method might be useful for the fabrication of free-standing GaN substrates and GaN-based devices.

DATA AVAILABILITY STATEMENT

The original contributions presented in the study are included in the article/supplementary material, further inquiries can be directed to the corresponding authors.

AUTHOR CONTRIBUTIONS

All authors listed have made a substantial, direct and intellectual contribution to the work, and approved it for publication.

FUNDING

This work was supported by the key research and development program of Guangdong Province of China (Nos. 2020B090922001, 2020B010169001), the Project of the National Natural Science Foundation of China (61974005), and the Guangdong Basic and Applied Basic Research Foundation (No. 2019B1515120091).

ACKNOWLEDGMENTS

We acknowledge the help of Yilmaz Dikme for deposition of the LT-AlN film and our former colleague Huang Xiong, who performed some of the tests.

REFERENCES

André, Y., Trassoudaine, A., Gil, E., Lekhal, K., Chelda-Gourmala, O., Castelluci, D., et al. (2012). Demonstration of crystal-vapor equilibrium leading to growth blockade of GaN during selective area growth. *J. Cryst. Growth* 354, 135–141. doi: 10.1016/j.jcrysgro.2012.05.026

Chai, X. Z., Qu, B. Y., Liu, P., Jiao, Y. C., Zhu, Y. S., Fang, X. Q., et al. (2018). Reduction of yellow and blue luminescence in Si-doped GaN by rapid thermal annealing. *J. Opt*. 47, 511–515. doi: 10.1007/s12596-018-0473-y

Chen, S. W., Li, H., and Lu, T.-C. (2016). Improved performance of GaN based light emitting diodes with ex-situ sputtered AlN nucleation layers. *AIP Adv*. 6:045311. doi: 10.1063/1.4947299

Chen, Y. A., Kuo, C. H., Wu, J. P., and Chang, C. W. (2015). Interruption-free growth of 10 μm-thick GaN film prepared on sputtered AlN/PSS template by hydride vapor phase epitaxy. *J. Cryst. Growth* 426, 180–185. doi: 10.1016/j.jcrysgro.2015.05.011

Fujito, K., Kubo, S., Nagaoka, H., Mochizuki, T., Namita, H., Nagao, S., et al. (2009). Bulk GaN crystals grown by HVPE. *J. Cryst. Growth* 311, 3011–3014. doi: 10.1016/j.jcrysgro.2009.01.046

Han, S., Yang, S., and Sheng, K. (2018). High-Voltage and High-ION/IOFF Vertical GaN-on-GaN Schottky barrier diode with nitridation-based termination. *IEEE Electron. Device Lett*. 39, 572–575. doi: 10.1109/LED.2018.2808684

Hiramatsu, K., Nishiyama, K., Onishi, M., Mizutani, H., Narukawa, M., Motogaito, A., et al. (2000). Fabrication and characterization of low defect density GaN using facet-controlled epitaxial lateral overgrowth (FA-CELO). *J. Cryst. Growth* 221, 316–326. doi: 10.1016/S0022-0248(00)00707-7

Imade, M., Hirabayashi, Y., Miyoshi, N., Yoshimura, M., Kitaoka, Y., Sasaki, T., et al. (2011). Control of growth facets and dislocation propagation behavior in the Na-flux growth of GaN. *Cryst. Growth Des*. 11, 2346–2350. doi: 10.1021/cg2000443

Lee, H.-J., Ha, J.-S., Yao, T., Kim, C., Hong, S.-K., Chang, J. H., et al. (2009). Microstructural analysis of void formation due to a NH_4Cl layer for self-separation of GaN thick films. *Cryst. Growth Des*. 9, 2877–2880. doi: 10.1021/cg900193k

Lekhal, K., Bae, S.-Y., Lee, H.-J., Mitsunari, T., Tamura, A., Deki, M., et al. (2016). Controlled morphology of regular GaN microrod arrays by selective area growth with HVPE. *J. Cryst. Growth* 447, 55–61. doi: 10.1016/j.jcrysgro.2016.05.008

Li, X., Wang, Y. J., Hane, K., Shi, Z., and Yan, J. (2018). GaN-based integrated photonics chip with suspended LED and waveguide. *Opt. Commun*. 415, 43–47. doi: 10.1016/j.optcom.2017.12.077

Liu, B., Gao, J., Wu, K. M., and Liu, C. (2009). Preparation and rapid thermal annealing of AlN thin films grown by molecular beam epi-taxy. *Solid State Commun*. 149, 715–717. doi: 10.1016/j.ssc.2009.02.008

Liu, N. L., Cheng, Y. T., Wu, J. J., Li, X. B., Yu, T. J., Xiong, H., et al. (2016). HVPE homoepitaxial growth of high quality bulk GaN using acid wet etching method and its mechanism analysis. *J. Cryst. Growth* 454, 59–63. doi: 10.1016/j.jcrysgro.2016.08.038

Liu, N. L., Wang, Q., Zheng, X. P., Li, S. F., Dikme, Y., Xiong, H., et al. (2018). The influence of V/III ratio on GaN grown on patterned sapphire substrate with low temperature AlN buffer layer by hydride vapor phase epitaxy. *J. Cryst. Growth* 500, 85–90. doi: 10.1016/j.jcrysgro.2018.07.014

Liu, X. K., Liu, Q., Li, C., Wang, J. F., Yu, W. J., Xu, K., et al. (2017). 1.2 kV GaN Schottky barrier diodes on free-standing GaN wafer using a CMOS-compatible contact material. *Jpn. J. Appl. Phys*. 56:026501. doi: 10.7567/JJAP.56.026501

Okuno, K., Oshio, T., Shibata, N., Honda, Y., Yamaguchi, M., Tanaka, S., et al. (2013). Structural evolution of AlN buffer and crystal quality of GaN films on a- and c-sapphire grown by metal organic vapor phase epitaxy. *Phys. Status Solidi C* 10, 369–372. doi: 10.1002/pssc.201200587

Paskova, T., Darakchieva, V., Paskov, P. P., Monemar, B., Bukowski, M., Suski, T., et al. (2006). Bending in HVPE GaN free-standing films: effects of laser lift-off, polishing and high-pressure annealing. *Phys. Status Solidi C* 3, 1475–1478. doi: 10.1002/pssc.200565412

Safadi, M. R., Thakur, J. S., and Auner, G. W. (2005). Laser ablation of AlN films grown on sapphire substrate. *J. Appl. Phys*. 97:084901. doi: 10.1063/1.1863420

Sandvik, P., Mi, K., Shahedipour, F., McClintock, R., Yasan, A., Kung, P., et al. (2001). AlxGa1-xN for solar-blind UV detectors. *J. Cryst. Growth* 231, 366–370. doi: 10.1016/S0022-0248(01)01467-1

Shang, L., Lu, T. P., Zhai, G. M., Jia, Z. G., Zhang, H., Ma, S. F., et al. (2015). The evolution of a GaN/sapphire interface with different nucleation layer thickness during two step growth and its influence on the bulk GaN crystal quality. *RSC Adv*. 5, 51201–51207. doi: 10.1039/C5RA08369A

Su, X. J., Xu, K., Xu, Y., Ren, G. Q., Zhang, J. C., Wamg, J. F., et al. (2013). Shock-induced brittle cracking in HVPE-GaN processed by laser lift-off techniques. *J. Phys. D* 46:205103. doi: 10.1088/0022-3727/46/20/205103

Sumiya, M., Toyomitsu, N., Nakano, Y., Wang, J. Y., Harada, Y., Sang, L. W., et al. (2017). Deep-level defects related to the emissive pits in thick InGaN films on GaN template and bulk substrates. *APL Mater*. 5:016105. doi: 10.1063/1.4974935

Tadatomo, K., Ohuchi, Y., Okagawa, H., Itoh, H., Miyake, H., Hiramatsu, K., et al. (1999). Hydrogen and nitrogen ambient effects on epitaxial lateral overgrowth (ELO) of GaN via metal organic vapor-phase epitaxy (MOVPE). *MRS Int. J. Nitride Semicond. Res.* 4:G3.1. doi: 10.1557/S1092578300002325

Yoshizawa, R., Miyake, H., and Hiramatsu, K. (2018). Effect of thermal annealing on AlN films grown on sputtered AlN templates by metal organic vapor phase epitaxy. *Jpn. J. Appl. Phys*. 57:01AD05. doi: 10.7567/JJAP.57.01AD05

Zhao, D. G., Jiang, D. S., Zhu, J. J., Liu, Z. S., Zhang, S. M., Yang, H., et al. (2007). The influence of V/III ratio in the initial growth stage on the properties of GaN epilayer deposited on low temperature AlN buffer layer. *J. Cryst. Growth* 303, 414–418. doi: 10.1016/j.jcrysgro.2007.01.019

Conflict of Interest: The authors declare that the research was conducted in the absence of any commercial or financial relationships that could be construed as a potential conflict of interest.

frontiers in Chemistry

MINI REVIEW
published: 26 April 2021
doi: 10.3389/fchem.2021.677821

Polymer–Inorganic Thermoelectric Nanomaterials: Electrical Properties, Interfacial Chemistry Engineering, and Devices

Xiaoyan Zhang, Shuang Pan, Huanhuan Song, Wengai Guo, Shiqiang Zhao, Guang Chen, Qingcheng Zhang, Huile Jin, Lijie Zhang, Yihuang Chen* and Shun Wang**

College of Chemistry and Materials Engineering, Institute of New Materials and Industrial Technologies, Key Laboratory of Carbon Materials of Zhejiang Province, Wenzhou University, Wenzhou, China

Though solar cells are one of the promising technologies to address the energy crisis, this technology is still far from commercialization. Thermoelectric materials offer a novel opportunity to convert energy between thermal and electrical aspects, which show the feasibility to improve the performance of solar cells *via* heat management and light harvesting. Polymer–inorganic thermoelectric nanocomposites consisting of inorganic nanomaterials and functional organic polymers represent one kind of advanced hybrid nanomaterials with tunable optical and electrical characteristics and fascinating interfacial and surface chemistry. During the past decades, they have attracted extensive research interest due to their diverse composition, easy synthesis, and large surface area. Such advanced nanomaterials not only inherit low thermal conductivity from polymers and high Seebeck coefficient, and high electrical conductivity from inorganic materials, but also benefit from the additional interface between each component. In this review, we provide an overview of interfacial chemistry engineering and electrical feature of various polymer–inorganic thermoelectric hybrid nanomaterials, including synthetic methods, properties, and applications in thermoelectric devices. In addition, the prospect and challenges of polymer–inorganic nanocomposites are discussed in the field of thermoelectric energy.

Keywords: polymer-inorganic hybrids, nanomaterials, electrical properties, interfacial chemistry, thermoelectric devices

OPEN ACCESS

Edited by:
Qifan Xue,
South China University of Technology, China

Reviewed by:
Xueqin Liu,
China University of Geosciences Wuhan, China
Ruiping Liu,
China University of Mining and Technology, China

****Correspondence:***
Shuang Pan
shuangpan@wzu.edu.cn
Yihuang Chen
yhchen@wzu.edu.cn
Shun Wang
shunwang@wzu.edu.cn

Specialty section:
This article was submitted to Nanoscience, a section of the journal Frontiers in Chemistry

Received: *08 March 2021*
Accepted: *06 April 2021*
Published: *26 April 2021*

Citation:
Zhang X, Pan S, Song H, Guo W, Zhao S, Chen G, Zhang Q, Jin H, Zhang L, Chen Y and Wang S (2021) Polymer–Inorganic Thermoelectric Nanomaterials: Electrical Properties, Interfacial Chemistry Engineering, and Devices. Front. Chem. 9:677821. doi: 10.3389/fchem.2021.677821

INTRODUCTION

Thermoelectric materials represent a functional material capable of direct mutual conversion between heat and electricity. As an alternative strategy for conventional power generation, thermoelectric devices with less size, noise, and pollution have important application prospects (Wang et al., 2010). For instance, thermoelectric devices enable the effective utilization of the previously wasted heat, thus providing promising solutions for optimizing power generation technologies and improving fuel energy efficiency (Sales, 2002; Bell, 2008). Moreover, advanced techniques such as solar cells are also benefited due to the heat management and light harvesting of thermoelectric devices (Jurado et al., 2019; Xu et al., 2019). The corresponding thermoelectric performance is defined as thermoelectric figure of merit ZT: $ZT = S^2T\sigma/\kappa$, where S is thermoelectric power or Seebeck coefficient, T is absolute temperature, σ is electrical conductivity, and κ is thermal conductivity. In order to obtain a large value of ZT, the material should possess

high S, high σ and low κ. However, it remains a grand challenge to achieve all these features in one material as properties are interrelated. For example, based on the Wiedemann–Franz law, an increase in σ usually leads to larger κ (Carrete et al., 2012). To this end, hybrid thermoelectric materials such as polymer–inorganic nanomaterials have shown the feasibility to solve the issues of a single thermoelectric material.

Polymer–inorganic nanomaterials are an emerging and functional hybrid. They not only inherit the advantageous characteristics from each component such as high σ and S of inorganic materials, and low κ of polymeric materials, but they also possess novel interfacial chemistry. Their morphology, electrical features, and interfacial and surface chemistry play a vital role in the related application, which can be rationally designed *via* the well-established synthetic approaches. Due to these outstanding characteristics, polymer–inorganic nanomaterials can promote the value of ZT with enhanced compatibility, which leads to superior activity and stability in thermoelectric devices. In addition, *via* heat management and light harvesting, polymer–inorganic thermoelectric nanomaterials can also improve the efficiency of solar cells (Jurado et al., 2019).

In this review, we will highlight the development of polymer–inorganic thermoelectric nanomaterials, including the synthetic strategies, structures, electrical characteristics (thermoelectric properties), interfacial and surface chemistry, and applications in (solar) thermoelectric devices such as thermoelectric generators (TEGs), thermoelectric coolers (TECs), and thermoelectric sensors. The challenges of polymer–inorganic nanomaterials in thermoelectric devices will be discussed in depth.

INTERFACIAL AND SURFACE CHEMISTRY OF POLYMER–INORGANIC NANOMATERIALS

Surface and interfacial chemistry is of fundamental importance in functional polymer–inorganic nanomaterials, which can be rationally designed and modified during synthetic stage (Marchetti et al., 2017). Benefiting from the development of synthetic strategies and the emerging technologies, polymer–inorganic nanomaterials with controllable dimension, composition and architecture have been designed and prepared. There are mainly four synthetic strategies: (1) assembly of polymer and inorganic material, (2) assembly of polymer and inorganic precursors, (3) assembly of organic precursor and inorganic material, and (4) assembly of organic and inorganic precursor.

These four strategies offer convenient tunability over interfacial and surface chemistry and thus properties. For example, for the polymer–inorganic nanomaterials prepared by the assembly strategy of polymer and inorganic material, the interface between each component is connected *via* relatively weak interfacial force. In contrast, the organic inorganic interface of the polymer–inorganic nanomaterials prepared by the polymer and inorganic precursor assembly strategy is well-defined, leading to better interfacial and surface chemistry and electrical characteristics in the following application.

ELECTRICAL PROPERTIES OF POLYMER–INORGANIC THERMOELECTRIC NANOMATERIALS

The unique electrical properties of thermoelectric materials lie in their thermoelectric feature, which offers a novel opportunity to convert energy between thermal and electrical aspects. Their thermoelectric performance can be expressed *via* evaluating the figure of merit (ZT) (Majumdar, 2004; Jin et al., 2019). Although copious impressive work was devoted to developing thermoelectric materials, the ZT values are usually <1, still lower than the targeted values of 3 or higher. This challenge shows the difficulties to realize high σ, high S, and low κ in one material for high ZT. Inorganic nanomaterials usually exhibit high S and σ (Zhang et al., 2020b). However, increased σ is usually associated with enhanced κ in conventional inorganic materials based on the Wiedemann–Franz law as the density, migration, and scattering of charge carriers are interrelated with heat transfer and thermal energy (Carrete et al., 2012). Meanwhile, inorganic reagents are relatively expensive. On the other hand, polymeric thermoelectric materials have low σ, S, and power factor ($S^2\sigma$). Therefore, thermoelectric materials consisting of polymer exhibit ZT values several orders of magnitude lower than those of inorganic ones. However, polymeric materials possess peculiar features like low density, cost and κ, and capability of large-scale preparation (Zhang et al., 2014). Clearly, it is highly desirable to design and craft polymer–inorganic nanohybrids integrating high σ and S of inorganic materials, and low κ of polymeric materials.

Polyaniline is a typical conducting polymer with a conductivity of up to 10^5 S m^{-1} and good stability. However, its power factor is low. Recently, researchers have added inorganic nanomaterials to improve its power factor. Up to now, there have been several reports on polyaniline-inorganic thermoelectric composite materials. For example, Yao et al. (2010) synthesized *in situ* single wall carbon nanotubes/polyaniline (SWNT/PANI) polymer–inorganic nanohybrids using single wall carbon nanotubes (SWNT) as templates (**Figure 1A**), which directed the polyaniline to grow along the surface of CNT forming an ordered chain structure. Compared with pure PANI, SWNT/PANI nanohybrids displayed higher electrical conductivity and Seebeck coefficient up to 1.25×104 S m^{-1} and 40 μV K^{-1} (**Figure 1B**), respectively, with maximum power factors being as high as 2×10^{-5} W m^{-1}K^{-2} (**Figure 1C**). This performance improvement could be ascribed to the interfacial and surface chemistry (strong π-π interactions) of SWNT/PANI.

Graphene is also one type of preferred nanofillers due to its large surface area and aspect ratio (Hasani et al., 2020). Compared with SWNT, graphene is easier to prepare at lower cost, which facilitates the practicability of the final thermoelectric product (Liu et al., 2019). To this end, Wang et al. (2015) prepared polyaniline/graphene (PANI/GP) polymer–inorganic nanohybrids by *in situ* polymerization and solution method

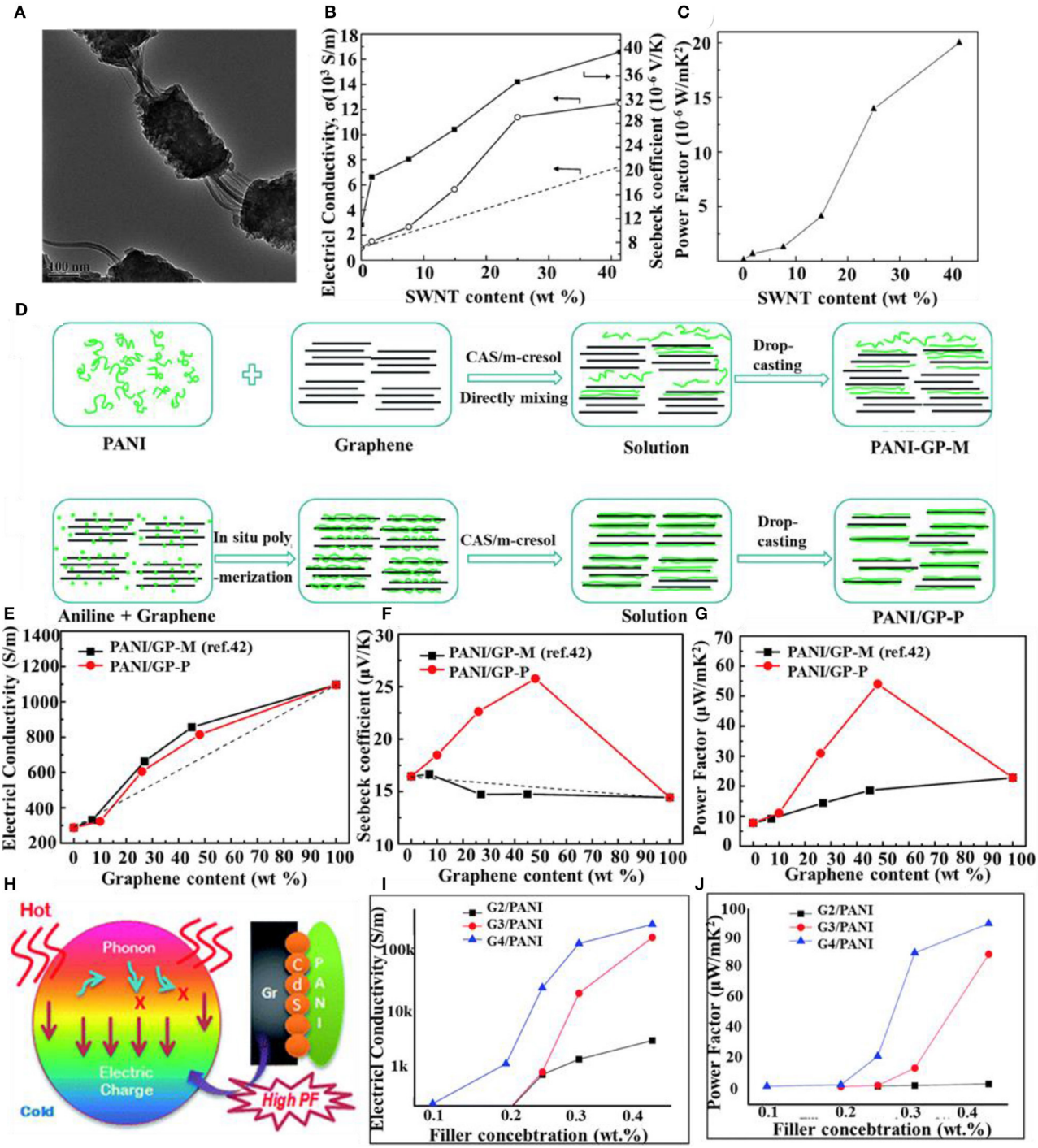

FIGURE 1 | (A) TEM image for SWNT/PANI composites containing 25 wt% SWNT, **(B)** Seebeck coefficient (closed squares), electrical conductivity (open circles), and **(C)** power factor (closed triangles) of SWNT/PANI composites containing different SWNT content. The dashed line is the calculated electrical conductivity based on the particle mixture rule. **(D)** Schematic illustrations of the synthesis procedure of (top) PANI/GP-M and (bottom) PANI/GP-P composite films and their corresponding **(E)** in-plane electrical conductivity, **(F)** Seebeck coefficient, and **(G)** power factor at room temperature with different graphene contents. **(H)** Schematic representation of RGO/CdS/PANI preparation nanocomposites for thermoelectric applications, **(I)** Seebeck coefficient, and **(J)** power factor vs. filler concentration. Reproduced with permission.

(**Figure 1D**). During *in situ* polymerization, polyaniline covered the graphene surface with intense π-π conjugation interactions, resulting in the formation of improved molecular ordering in the nanohybrid. Therefore, the thermoelectric properties of the composite were significantly enhanced with an optimal electrical conductivity of 814 S cm^{-1} (**Figure 1E**) and a Seebeck coefficient of 26 μV K^{-1} (**Figure 1F**), and the maximum power factor was 55 μW m^{-1} K^{-2} (**Figure 1G**). Graphene oxide is another effective material to improve the thermoelectric properties of polyaniline. After hybridization, the electrical conductivity, Seebeck coefficient, and power factor reached around 1,489 S cm^{-1}, 59 μV K^{-1}, and 52.11 × 10^{-7} W K^{-2} cm, with a maximum *ZT* of 0.8 at 363 K (Shalini et al., 2019).

In addition to carbon materials, metal-based inorganic materials have a large Seebeck coefficient, such as Bi_2Te_3 (Li et al., 2011), $Sn_{0.85}Sb_{0.15}O_2$ (Plochmann et al., 2014), PbTe (Wang et al., 2010), Ag_2Te (Wang et al., 2012), Cu_2Te (Zhou et al., 2015), PtTe (Zhang et al., 2020), and Au (Toshima et al., 2012). Therefore, these inorganic materials can be combined with conducting polymers to improve the thermoelectric properties. For example, More et al. (2017). prepared RGO–CdS–polyaniline (PANI) ternary hybrid polymer–inorganic nanohybrids by a simple *in situ* thermoelectric method. As shown in **Figures 1H–J**, the energy band arrangement between reduced graphene oxide (RGO), CdS quantum dots (QDs), and PANI improved the P-type electrical conductivity with reduced thermal conductivity and proved the synergetic energy filtering effect. The electrical conductivity and power factor of RGO/CdS/PANI nanohybrids increased with the increase of filler concentration (RGO–CdS). The nanohybrid (with 0.4 wt% filler; G4) had low thermal conductivity and high electrical conductivity, and its *ZT* value was as high as 1.97.

APPLICATIONS IN THERMOELECTRIC DEVICES

Thermoelectric materials are usually assembled into thermoelectric devices for use in the energy field, which efficiently takes advantage of the low-quality heat that otherwise is dissipated. Thus, thermoelectric devices have received increasing attention from the viewpoints of both scientific research and technological development. The past several decades have witnessed a rapid advance of high-performance thermoelectric devices including TEGs, TECs, and thermoelectric sensors, which will be highlighted in the following sections.

Thermoelectric Generators

A TEG is a kind of device that directly generates electrical energy from heat. Generally (Sales, 2002; Bell, 2008), various thermal energy sources such as natural heat (e.g., solar radiation) and waste heat (e.g., industrial production), which induces a temperature gradient and can be capitalized on for energy generation in a reliable, pollution-free, and eco-friendly way (Mulla et al., 2020). Since many low-quality heat sources display irregular shapes and surfaces, it is vital for TEGs to be flexible for tight contact with the heat sources and thus maximizing heat collection. Such flexible TEGs have also gained increasing interest for advancing the development of many self-powered devices [e.g., smartwatches and smart and flexible wearable electrocardiograms (Dargusch et al., 2020)].

To minimize the cost of energy cost with optimal performance, polymer/inorganic nanohybrids with additional interfacial and surface chemistry have been developed as promising thermoelectric materials. For example, Mulla et al. (2020) successfully fabricated flexible paper-based TEGs using graphite and polyethylenimine (**Figure 2**). Graphite served as both p-type and n-type thermoelectric legs, which did not require additional paste for connection. The thermoelectric voltage and corresponding output power reached 9.2 mV and 1.75 nW, respectively, at a temperature difference of about 60 K. Flexible TEGs with optical transparency exert a crucial impact on novel applications such as smart windows and solar cells (Chowdhury et al., 2009). The key lies in the development of transparent p-type thermoelectric materials. To this end, Yang et al. deposited transparent p-type γ-Cui onto the PET substrate for single-leg thermoelectric device. The corresponding maximum output power at ΔT of 10.8 K was 8.2 nW with a power density of 0.1 mW cm^{-2}, comparable with those of devices based on Bi_2Te_3/Sb_2Te_3 (Yang et al., 2017).

Rational design in architecture can further improve the thermoelectric performance of flexible TEGs. For example, the thermal energy loss generated by commercial substrate (e.g., Si, paper, and polymer film) significantly restricts the energy generation efficiency. To this end, Kim et al. (2014) developed a wearable TEG on a glass fabric without top and bottom substrates. The flexible device possessed a thin thickness of ∼500 μm and a lighter density of ∼.13 g cm^{-2} enabled by screen printing technology. Due to the unique design, the TEG displayed a high output power density, which is one order of magnitude higher than that of the previously reported flexible TEG.

Conducting polymers [e.g., poly(3,4-ethylenedioxythiophene)/poly(styrenesulfonate) (PEDOT:PSS) and poly(3-hexylthiophene) (P3HT)] with high flexibility and low thermal conductivity are ideal materials for fabricating flexible TEGs (Chabinyc, 2014). Song and Cai (2017) *in situ* synthesized PEDOT:PSS functionalized Te nanorod [phenol–formaldehyde–Te (PF–Te)], which were incorporated with PEDOT:PSS forming PEDOT:PSS/PF–Te composite film via vacuum-assisted filtration method. Through the thermoelectric performance test, it was found that the conductivity of the composite material increased to 1,262 S cm^{-1}, and the power factor reached 51.4 μW $m^{-1}K^{-2}$. PEDOT:PSS/PF-Te composite film was then used to fabricate a composite prototype generator consisting of eight single-leg modules pasted onto a polyimide substrate. At a temperature difference of 13.4 K, an output voltage of 2.5 mV was achieved. These investigations have shown promising feasibility for tremendous applications such as wearable devices and smart systems *via* advancing the development of new thermoelectric materials and novel TEG designs.

The relatively small temperature difference from body heat hinders its practical application (Jung et al., 2017). Therefore,

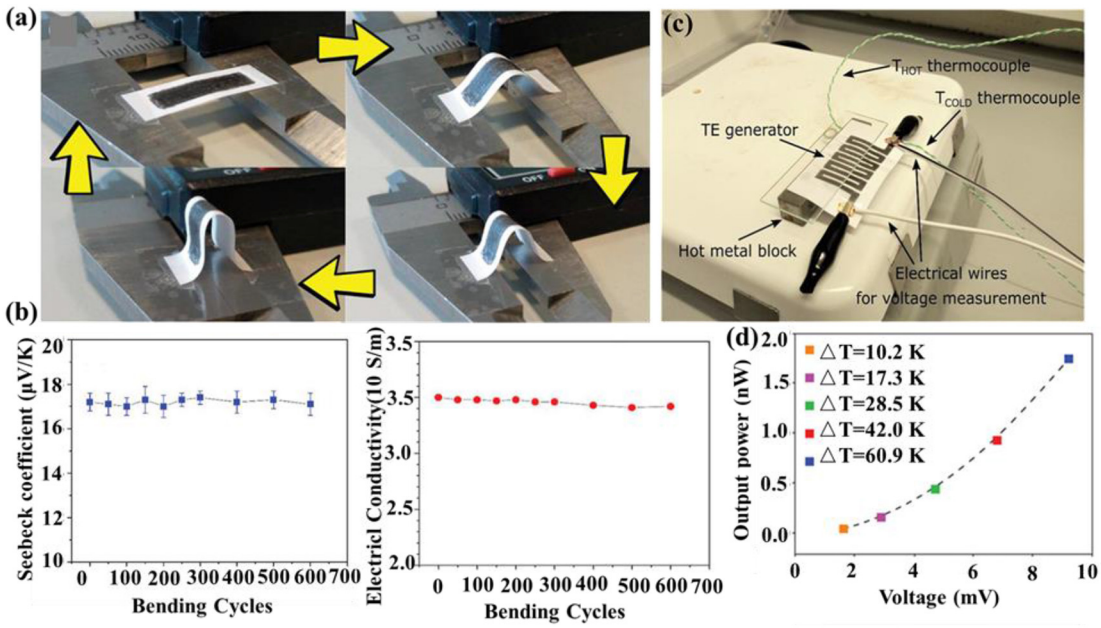

FIGURE 2 | (a) Photographs of the cyclical bending procedure applied to the thermoelectric trace with individual p-type and n-type graphite traces and **(b)** Seebeck coefficient (left) and electrical conductivity (right) over multiple bending cycles. **(c)** Photograph of the setup used for electrical testing of the thermoelectric generator (TEG) module using graphite and polyethylenimine and **(d)** the corresponding power output vs. voltage with respect to ΔT. Reproduced with permission.

TEG with solar energy as a heat source (i.e., solar TEGs and STEGs) has attracted increasing interest. In this regard, the conversion of sunlight to electricity is mainly achieved by photovoltaic and solar thermal power generation (Kraemer et al., 2011; Wang et al., 2019). The solar cell represents a promising technique to solve energy crisis (Jiang et al., 2020; Zhang et al., 2020a). Thermoelectric materials in STEGs have two advantages: (a) TEGs can act as a cooling system to decrease the temperature, which improves the performance of solar cells (Benghanem et al., 2016). (2) TEGs utilize the dissipated heat energy for additional electricity generation (Kil et al., 2017). Based on this, Jurado et al. (2019) studied STEGs using polymer–CNT composites as both solar absorbent and active TE materials. Due to the effect of interfacial chemistry and solar thermoelectric synergy effect, STEG with a power output of 180 nW was obtained.

Thermoelectric Coolers

The basic principle of TECs follows the Peltier effect to generate endothermic or exothermic phenomena between the interfaces of two different materials. During the past few decades, TEC has garnered increasing attention in academia and industries due to its simple construction, reliability, flexibility, noiseless operation, and long life. Localized cooling enabled by wearable TECs can gradually take the place of conventional systems, which decreases climate warming and power cost (Kishore et al., 2019). Hu et al. (2020) prepared polymer–inorganic nanohybrid film consisting of nickel nanowires evenly dispersed in PVDF matrix by solution mixing casting and compression molding. The electrical conductivity of the film raised as a function of Ni NW content while the optimal power factor reached 24.3 $\mu W m^{-1} K^{-2}$. The flexible thermoelectric thin film has enormous potential in the TECS. Sun et al. (2012) fabricated a thermoelectric module containing 35 n-type couples of poly[Na_x(Ni-ett)] and p-type poly[Cu_x(Cu-ett)] (ett: 1,1,2,2-ethenetetrathiolate), which generated output voltage, current, and power of 0.26 V, 10.1 mA, and 2.8 $\mu W\ cm^{-2}$, respectively, with good stability at a temperature difference of 80 K. The single thermocouple exhibited cooling effect with a ΔT of 3.5 K at an external voltage of 0.6 V.

Batteries usually generate a lot of heat during rapid charging and discharging cycles, which causes high temperatures and even battery explosions (Xie et al., 2020). Therefore, temperature control is important for safe battery operation (Kai et al., 2018). In a water-based electrolyte, the water molecules can form extrathermodynamic cycle via evaporation and solidification to realize the heat absorption/release cycle during thermoelectric conversion (Zhang et al., 2017). With this in mind, Chen et al. designed an intelligent hydrogel film consisting of polyacrylamide (PAAm) and $Fe(CN)_6^{3-}$ and $Fe(CN)_6^{4-}$. The results showed that TG hydrogel reduced battery temperature by 6.5, 13.2, 15.7, and 20°C at discharge rates of 1.6, 1.8, 2, and 2.2°C, respectively (Pu et al., 2020).

Thermoelectric Sensors

In addition to TEGs and TECs, the thermoelectric properties have also prompted the development of thermoelectric sensors, which release combustion heat during chemical reaction with gas. Currently, thermoelectric sensors based on a catalyst combustor have realized the monitoring of various chemical gases with a wide range (e.g., 0.5 ppm to 5 vol% for H_2,

1 ppm for CH_4) (Nishibori et al., 2009; Nagai et al., 2015). However, even though these devices are efficient, their cost and weight are relatively high. To address these, polymer–inorganic thermoelectric nanohybrids served as alternative thermoelectric sensors. Slobodian et al. (2016) designed one self-powered thermoelectric sensor consisting of oxidized multi-walled carbon nanotubes and ethylene-octene copolymer (MWCNT/EOC). The thermoelectric power became larger as a function of the generated oxygen-containing functional groups on the MWCNT surface. The resistance of MWCNT/EOC composite material was affected by organic vapor, with average increases of 3.6, 1.1, and 0.05 S upon exposure to heptane, toluene, and ethanol saturated vapor, respectively. Such a device has provided a platform for convenient gas alarm and detection.

SUMMARY AND PERSPECTIVES

In summary, the recent advancement of polymer–inorganic thermoelectric nanomaterials is highlighted. After an introduction of synthetic strategies, interfacial chemistry engineering and electrical properties are presented. The development of thermoelectric devices, namely, TEGs, TECs, and thermoelectric sensors is also summarized. In particular, the burgeoning integration of solar cells with the thermoelectric technique is discussed.

However, despite the copious advances achieved by polymer–inorganic thermoelectric nanomaterials, in-depth explorations are still necessary due to the remaining challenges. For example, the substantial distinctions between inorganic and organic materials regarding intrinsic nature may cause phase and charge separation induced within the interface. In addition, due to the restricted transportation of charge carriers over the interface between phases with dissimilar electrical properties, a local polarization may generate an electric field much larger than the applied one. Thus, the polymer–inorganic thermoelectric nanomaterials may suffer from quicker destruction. To circumvent these issues, delicately balancing the intrinsic distinct properties between organic and inorganic components is needed for an optimized characteristic feature and practical behavior of polymer–inorganic nanohybrids. The following aspects for the development of polymer–inorganic thermoelectric nanomaterials might deserve more attention: (1) Adjusting the architectures and size of inorganic components may lead to additional quantum effects, which is conducive to the charge transport process. (2) Development of synthetic approaches that are capable of generating polymer–inorganic thermoelectric nanomaterials with well-defined interfacial and surface chemistry is of great importance, such as the polymer-enabled nanoreactor strategy (Li et al., 2018). (3) Surface of each component is better to be functionalized with specific ligands to improve the overall compatibility, therefore enhancing the stability and electric properties of nanohybrids. (4) Experimental results are expected to combine with powerful *in situ* characterizations and theoretical modeling (Yu et al., 2020) which facilitates the comprehensive insight of structure–property–performance relationship.

With the significant progress and tremendous effort in this emerging area, we envision that many breakthroughs of polymer–inorganic thermoelectric nanomaterials will promote their use in the near future.

AUTHOR CONTRIBUTIONS

All authors listed have made a substantial, direct and intellectual contribution to the work, and approved it for publication.

FUNDING

The authors would like to thank the financial support from the National Natural Science Foundation of China (52072273, 51872209, and 21905208), the Zhejiang Provincial Natural Science Foundation of China (LQ21B030002), and the Basic Science and Technology Research Project of Wenzhou (G2020007).

REFERENCES

Bell, L. E. (2008). Cooling, heating, generating power, and recovering waste heat with thermoelectric systems. *Science* 321, 1457–1146. doi: 10.1126/science.1158899

Benghanem, M., Al-Mashraqi, A. A., and Daffallah, K. O. (2016). Performance of solar cells using thermoelectric module in hot sites. *Renew. Energy* 89, 51–59. doi: 10.1016/j.renene.2015.12.011

Carrete, J., Mingo, N., Tian, G., Ågren, H., Baev, A., and Prasad, P.N. (2012). Thermoelectric properties of hybrid organic–inorganic superlattices. *J. Phys. Chem. C* 116, 10881–10886. doi: 10.1021/jp30 25039

Chabinyc, M. (2014). Thermoelectric polymers: behind organics' thermopower. *Nat. Mater.* 13, 119–121. doi: 10.1038/nmat3859

Chowdhury, I., Prasher, R., Lofgreen, K., Chrysler, G., Narasimhan, S., Mahajan, R., et al. (2009). On-chip cooling by superlattice-based thin-film thermoelectrics. *Nat. Nanotechnol.* 4, 235–238. doi: 10.1038/nnano.2008.417

Dargusch, M., Liu, W. D., and Chen, Z. G. (2020). Thermoelectric generators: alternative power supply for wearable electrocardiographic systems. *Adv. Sci.* 7:2001362. doi: 10.1002/advs.202001362

Hasani, A., Teklagne, M. A., Do, H. H., Hong, S. H., Van Le, Q., Ahn, S. H., et al. (2020). Graphene-based catalysts for electrochemical carbon dioxide reduction. *Carbon Energy* 2, 158–175. doi: 10.1002/cey2.41

Hu, S., Zeng, S., Li, X., Jiang, J., Yang, W., Chen, Y., et al. (2020). Flexible and high performance of n-type thermoelectric PVDF composite film induced by nickel nanowires. *Mater. Des.* 188:108496. doi: 10.1016/j.matdes.2020.108496

Jiang, K., Wang, J., Wu, F., Xue, Q., Yao, Q., Zhang, J., et al. (2020). Dopant-Free organic hole-transporting material for efficient and stable inverted all-inorganic and hybrid perovskite solar cells. *Adv. Mater.* 32:e1908011. doi: 10.1002/adma.201908011

Jin, H., Li, J., Iocozzia, J., Zeng, X., Wei, P. C., Yang, C., et al. (2019). Hybrid organic-inorganic thermoelectric materials and devices. *Angew. Chem. Int. Ed. Engl.* 58, 15206–15226. doi: 10.1002/anie.201901106

Jung, Y. S., Jeong, D. H., Kang, S. B., Kim, F., Jeong, M. H., Lee, K.-S., et al. (2017). Wearable solar thermoelectric generator driven by unprecedentedly high temperature difference. *Nano Energy* 40, 663–672. doi: 10.1016/j.nanoen.2017.08.061

Jurado, J. P., Dörling, B., Zapata-Arteaga, O., Roig, A., Mihi, A., and Campoy-Quiles, M. (2019). Solar harvesting: a unique opportunity for organic thermoelectrics? *Adv. Energy Mater.* 9:1902385. doi: 10.1002/aenm.201902385

Kai, L., Liu, Y., Lin, D., Pei, A., Cui, Y. (2018). Materials for lithium-ion battery safety. *Science Adv.* 4:eaas9820. doi: 10.1126/sciadv.aas9820

Kil, T.-H., Kim, S., Jeong, D.-H., Geum, D.-M., Lee, S., Jung, S.-J., et al. (2017). A highly-efficient, concentrating-photovoltaic/thermoelectric hybrid generator. *Nano Energy* 37, 242–247. doi: 10.1016/j.nanoen.2017.05.023

Kim, S. J., We, J. H., and Cho, B. J. (2014). A wearable thermoelectric generator fabricated on a glass fabric. *Energy Environ. Sci.* 7, 1959–1965. doi: 10.1039/c4ee00242c

Kishore, R. A., Nozariasbmarz, A., Poudel, B., Sanghadasa, M., and Priya, S. (2019). Ultra-high performance wearable thermoelectric coolers with less materials. *Nat. Commun*. 10:1765. doi: 10.1038/s41467-019-09707-8

Kraemer, D., Poudel, B., Feng, H. P., Caylor, J. C., Yu, B., Yan, X., et al. (2011). High-performance flat-panel solar thermoelectric generators with high thermal concentration. *Nat. Mater*. 10, 532–538. doi: 10.1038/nmat3013

Li, X., Iocozzia, J., Chen, Y., Zhao, S., Cui, X., Wang, W., et al. (2018). From precision synthesis of block copolymers to properties and applications of nanoparticles. *Angew. Chem. Int. Ed. Engl*. 57, 2046–2070. doi: 10.1002/anie.201705019

Li, Y., Zhao, Q., Wang, Y.-,g., and Bi, K. (2011). Synthesis and characterization of Bi2Te3/polyaniline composites. *Mater. Sci. Semiconduct. Process.* 14, 219–222. doi: 10.1016/j.mssp.2011.02.019

Liu, F., Wang, C., Sui, X., Riaz, M. A., Xu, M., Wei, L., et al. (2019). Synthesis of graphene materials by electrochemical exfoliation: recent progress and future potential. *Carbon Energy* 1, 173–199. doi: 10.1002/cey2.14

Majumdar, A. (2004). Thermoelectricity in semiconductor nanostructures. *Science* 303, 777–778. doi: 10.1126/science.1093164

Marchetti, A., Chen, J., Pang, Z., Li, S., Ling, D., Deng, F., et al. (2017). Understanding surface and interfacial chemistry in functional nanomaterials via solid-state NMR. *Adv. Mater.* 29:1605895. doi: 10.1002/adma.201605895

More, P. V., Hiragond, C., Dey, A., and Khanna, P. K. (2017). Band engineered p-type RGO–CdS–PANI ternary nanocomposites for thermoelectric applications. *Sust. Energy Fuels* 1, 1766–1773. doi: 10.1039/C7SE00290D

Mulla, R., Jones, D. R., and Dunnill, C. W. (2020). Thermoelectric paper: graphite pencil traces on paper to fabricate a thermoelectric generator. *Adv. Mater. Technol.* 5:2000227. doi: 10.1002/admt.202000227

Nagai, D., Nishibori, M., Itoh, T., Kawabe, T., Sato, K., and Shin, W. (2015). Ppm level methane detection using micro-thermoelectric gas sensors with Pd/Al2O3 combustion catalyst films. *Sens. Actuat. B Chem.* 206, 488–494. doi: 10.1016/j.snb.2014.09.059

Nishibori, M., Shin, W., Izu, N., Itoh, T., and Matsubara, I. (2009). Sensing performance of thermoelectric hydrogen sensor for breath hydrogen analysis⋆. *Sens. Actuat. B Chem.* 137, 524–528. doi: 10.1016/j.snb.2009.01.029

Plochmann, B., Lang, S., Rüger, R., and Moos, R. (2014). Optimization of thermoelectric properties of metal-oxide-based polymer composites. *J. Appl. Poly. Sci.* 131:40038. doi: 10.1002/app.40038

Pu, S., Liao, Y., Chen, K., Fu, J., Zhang, S., Ge, L., et al. (2020). Thermogalvanic hydrogel for synchronous evaporative cooling and low-grade heat energy harvesting. *Nano Lett*. 20, 3791–3797. doi: 10.1021/acs.nanolett.0c00800

Sales, B. C. (2002). Smaller is cooler. *Science* 295, 1248–1249. doi: 10.1126/science.1069895

Shalini, V., Navaneethan, M., Harish, S., Archana, J., Ponnusamy, S., Ikeda, H., et al. (2019). Design and fabrication of PANI/GO nanocomposite for enhanced room-temperature thermoelectric application. *Appl. Surf. Sci*. 493, 1350–1360. doi: 10.1016/j.apsusc.2019.06.249

Slobodian, P., Riha, P., Olejnik, R., and Benlikaya, R. (2016). Analysis of sensing properties of thermoelectric vapor sensor made of carbon nanotubes/ethylene-octene copolymer composites. *Carbon* 110, 257–266. doi: 10.1016/j.carbon.2016.09.023

Song, H., and Cai, K. (2017). Preparation and properties of PEDOT:PSS/Te nanorod composite films for flexible thermoelectric power generator. *Energy* 125, 519–525. doi: 10.1016/j.energy.2017.01.037

Sun, Y., Sheng, P., Di, C., Jiao, F., Xu, W., Qiu, D., et al. (2012). Organic thermoelectric materials and devices based on p- and n-type poly(metal 1,1,2,2-ethenetetrathiolate)s. *Adv. Mater.* 24, 932–937. doi: 10.1002/adma.201104305

Toshima, N., Jiravanichanun, N., and Marutani, H. (2012). Organic thermoelectric materials composed of conducting polymers and metal nanoparticles. *J. Elec. Mater*. 41, 1735–1742. doi: 10.1007/s11664-012-2041-6

Wang, B., Iocozzia, J., Zhang, M., Ye, M., Yan, S., Jin, H., et al. (2019). The charge carrier dynamics, efficiency and stability of two-dimensional material-based perovskite solar cells. *Chem. Soc. Rev*. 48, 4854–4891. doi: 10.1039/C9CS00254E

Wang, L., Yao, Q., Bi, H., Huang, F., Wang, Q., and Chen, L. (2015). PANI/graphene nanocomposite films with high thermoelectric properties by enhanced molecular ordering. *J. Mater. Chem. A* 3, 7086–7092. doi: 10.1039/C4TA06422D

Wang, Y. Y., Cai, K. F., Yin, J. L., An, B. J., Du, Y., and Yao, X. (2010). In situ fabrication and thermoelectric properties of PbTe–polyaniline composite nanostructures. *J. Nanopart. Res.* 13, 533–539. doi: 10.1007/s11051-010-0043-y

Wang, Y. Y., Cai, K. F., Yin, J. L., Du, Y., and Yao, X. (2012). One-pot fabrication and thermoelectric properties of Ag2Te–polyaniline core–shell nanostructures. *Mater. Chem. Phys*. 133, 808–812. doi: 10.1016/j.matchemphys.2012.01.098

Xie, C., Li, Y., Wang, Q., Sun, D., Tang, Y., and Wang, H. (2020). Issues and solutions toward zinc anode in aqueous zinc-ion batteries: a mini review. *Carbon Energy* 2, 540–560. doi: 10.1002/cey2.67

Xu, R., Zhao, H., Jin, H., Wang, Z., Zhang, Z., Xu, S., et al. (2019). Scalable fabrication of geometry-tunable self-aligned superlattice photonic crystals for spectrum-programmable light trapping. *Nano Energy* 58, 543–551. doi: 10.1016/j.nanoen.2019.01.074

Yang, C., Souchay, D., Kneiss, M., Bogner, M., Wei, H. M., Lorenz, M., et al. (2017). Transparent flexible thermoelectric material based on non-toxic earth-abundant p-type copper iodide thin film. *Nat. Commun*. 8:16076. doi: 10.1038/ncomms16076

Yao, Q., Chen, Y., Zhang, W., Liufu, S., and Chen, X. (2010). Enhanced thermoelectric performance ofsingle-walled carbon nanotubes/polyaniline hybrid nanocomposites. *ACS Nano* 4, 2445–2451. doi: 10.1021/nn1002562

Yu, X., Shao, H., Wang, X., Zhu, Y., Fang, D., and Hong, J. (2020). Anomalous lattice thermal conductivity in layered MNCl (M = Zr, Hf) materials driven by lanthanide contraction. *J. Mater. Chem. A* 8, 3128–3134. doi: 10.1039/C9TA12600G

Zhang, J., Xie, Y., Hu, Y., and Shao, H. (2020). Remarkable intrinsic ZT in the 2D PtX2(X = O, S, Se, Te) monolayers at room temperature. *Appl. Surf. Sci* 532:147387. doi: 10.1016/j.apsusc.2020.147387

Zhang, L., Kim, T., Li, N., Kang, T. J., Chen, J., Pringle, J. M., et al. (2017). High power density electrochemical thermocells for inexpensively harvesting low-grade thermal energy. *Adv. Mater.* 29:1605652. doi: 10.1002/adma.201605652

Zhang, M., Ye, M., Wang, W., Ma, C., Wang, S., Liu, Q., et al. (2020a). Synergistic cascade carrier extraction via dual interfacial positioning of ambipolar black phosphorene for high-efficiency perovskite solar cells. *Adv. Mater.* 32:e2000999. doi: 10.1002/adma.202000999

Zhang, Q., Sun, Y., Xu, W., and Zhu, D. (2014). Organic thermoelectric materials: emerging green energy materials converting heat to electricity directly and efficiently. *Adv. Mater.* 26, 6829–6851. doi: 10.1002/adma.201305371

Zhang, Y., Zhang, Q., and Chen, G. (2020b). Carbon and carbon composites for thermoelectric applications. *Carbon Energy* 2, 408–436. doi: 10.1002/cey2.68

Zhou, C., Dun, C., Wang, Q., Wang, K., Shi, Z., Carroll, D. L., et al. (2015). Nanowires as building blocks to fabricate flexible thermoelectric fabric: the case of copper telluride nanowires. *ACS Appl. Mater. Interfaces* 7, 21015–21020. doi: 10.1021/acsami.5b07144

Conflict of Interest: The authors declare that the research was conducted in the absence of any commercial or financial relationships that could be construed as a potential conflict of interest.

The reviewer XL declared a past co-authorship with one of the authors YC to the handling Editor.

frontiers in Chemistry

ORIGINAL RESEARCH
published: 29 April 2021
doi: 10.3389/fchem.2021.657557

Use of Hybrid PEDOT:PSS/Metal Sulfide Quantum Dots for a Hole Injection Layer in Highly Efficient Green Phosphorescent Organic Light-Emitting Diodes

Wenqing Zhu[1,2], Kuangyu Ding[1,2], Chen Yi[1,2], Ruilin Chen[1,2], Bin Wei[2], Lu Huang[1] and Jun Li[1]*

[1]School of Materials Science and Engineering, Shanghai University, Shanghai, China, [2]School of Mechatronic Engineering and Automation, Key Laboratory of Advanced Display and System Applications, Ministry of Education, Shanghai University, Shanghai, China

In this study, we have synthesized the molybdenum sulfide quantum dots (MoS_2 QDs) and zinc sulfide quantum dots (ZnS QDs) and demonstrated a highly efficient green phosphorescent organic light-emitting diode (OLED) with hybrid poly (3,4-ethylenedioxythiophene)/poly (styrenesulfonate) (PEDOT:PSS)/QDs hole injection layer (HIL). The electroluminescent properties of PEDOT:PSS and hybrid HIL based devices were explored. An optimized OLED based on the PEDOT:PSS/MoS_2 QDs HIL exhibited maximum current efficiency (CE) of 72.7 cd A^{-1}, which shows a 28.2% enhancement as compared to counterpart with single PEDOT:PSS HIL. The higher device performance of OLED with hybrid HIL can be attributed to the enhanced hole injection capacity and balanced charge carrier transportation in the OLED devices. The above analysis illustrates an alternative way to fabricate the high efficiency OLEDs with sulfide quantum dots as a HIL.

Keywords: phosphorescent organic light-emitting diodes, metal sulfide QDs, hybrid hole injection layer, PEDOT: PSS, ZnS, MoS_2

OPEN ACCESS

Edited by:
Baiquan Liu,
Sun Yat-Sen University, China

Reviewed by:
Gufeng He,
Shanghai Jiao Tong University, China
Huaibin Shen,
Henan University, China

****Correspondence:***
Wenqing Zhu
wqzhu@shu.edu.cn

Specialty section:
This article was submitted to Nanoscience, a section of the journal Frontiers in Chemistry

Received: *23 January 2021*
Accepted: *15 April 2021*
Published: *29 April 2021*

Citation:
Zhu W, Ding K, Yi C, Chen R, Wei B, Huang L and Li J (2021) Use of Hybrid PEDOT:PSS/Metal Sulfide Quantum Dots for a Hole Injection Layer in Highly Efficient Green Phosphorescent Organic Light-Emitting Diodes. Front. Chem. 9:657557. doi: 10.3389/fchem.2021.657557

INTRODUCTION

New-generation organic light-emitting diodes (OLEDs) have attracted huge research interests due to their unique properties such as high color purity, light weight and flexibility (Liao et al., 2004; Wen et al., 2005; Wang et al., 2018; Wang et al., 2020). One of the most important issue for the OLEDs application in industry is the device efficiency. The effective charge injection and transportation, and exciton confinement in the emitting layer are the key parameters to achieve highly efficient OLEDs (Lee et al., 1999; Wang et al., 2008; Song et al., 2018; Zhao et al., 2020). To date, many research groups have used the solution processed hole injection layer (HIL) to improve the device performance and to decrease the fabrication costs (Li et al., 2018; Hu et al., 2020; Wang et al., 2020). To obtain the highly efficient OLEDs, the overall requirements on solution processed HIL should possess excellent optical and electrical characteristics such as high transparency and conductivity, as well as the low surface roughness (Zhao et al., 2016; McEwan et al., 2018; Feng et al., 2020). Therefore, the synthesis and development of solution processed hole injection materials are very important to achieve high-performance devices.

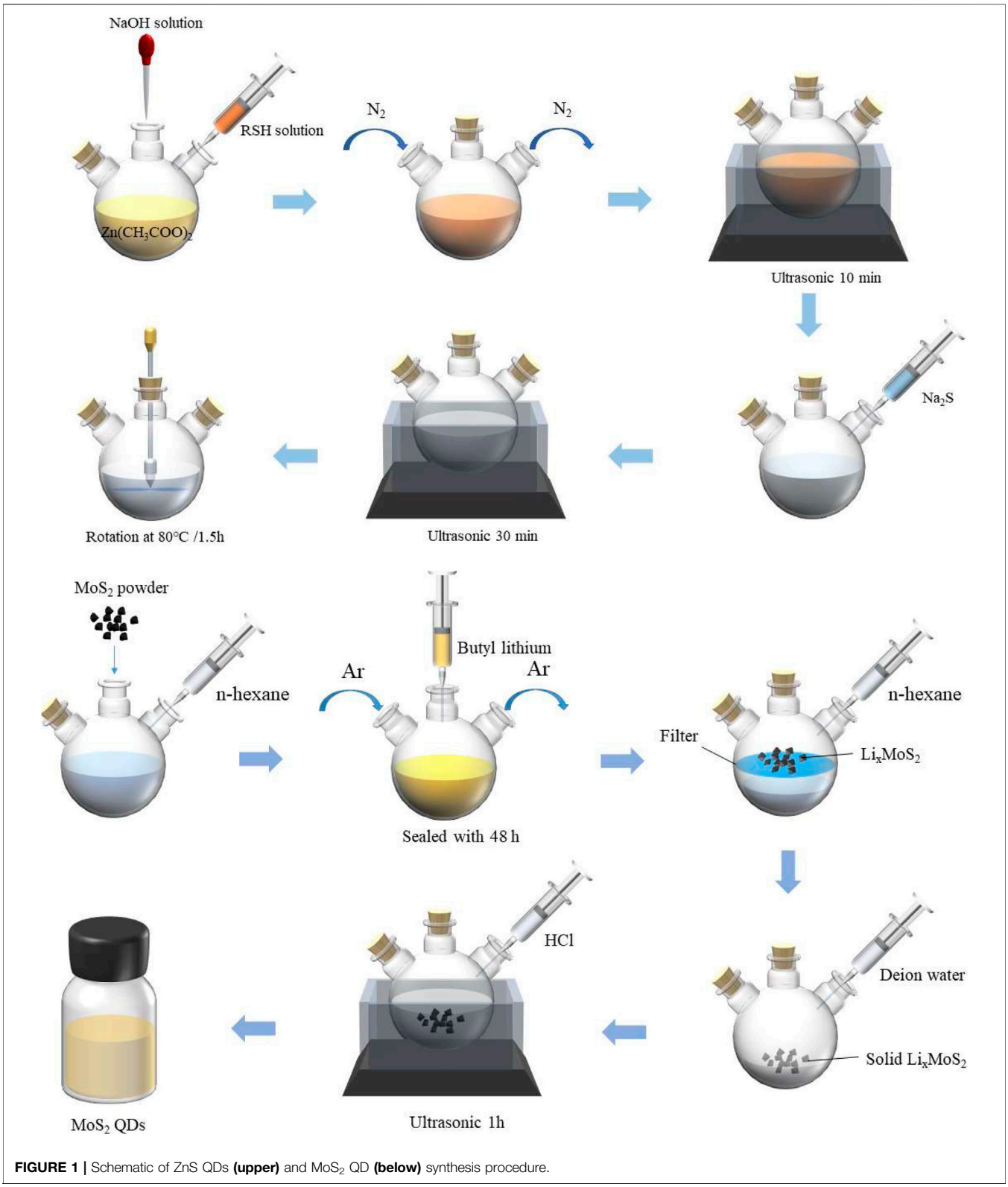

FIGURE 1 | Schematic of ZnS QDs **(upper)** and MoS_2 QD **(below)** synthesis procedure.

The traditional poly (3,4-ethylenedioxythiophene)/poly (styrenesulfonate) (PEDOT:PSS) is widely used as a solution processed HIL in organic electronics (Benor et al., 2010; Salsberg and Aziz, 2019). However, its acidic property and easily absorption for water in the air significantly deteriorate the device performance. The traditional molybdenum oxide

(MoO_x) is also employed in the OLED devices as an effective HIL due to its matched work function with ITO electrode and low surface roughness and high transparency. However, the MoO_x as HIL is normally prepared by using vacuum thermal evaporation method which is not a good candidate for low-cost OLED preparation. More importantly, to date, there is seldom reports related to the solution-processed MoO_x in electronic devices because of the limited solubility. Recently, solution processed sulfide quantum dots (QDs) such as zinc sulfide QDs (Zn QDs), molybdenum sulfide QDs (MoS_2 QDs), and others as HILs/HTLs have been reported as an effective way to increase charge injection due to their unique properties, such as high solubility, tunable work function and low cost, resulting in the enhanced devices performance (Kim et al., 2015; Lenkeviciute et al., 2015; Xie et al., 2019). In our previous work, we have reported a highly efficient inverted OLEDs by using the solution processed ZnS QDs as an electron injection layer due to the excellent optical and electrical properties (Shi et al., 2019).

In this paper, the application of PEDOT:PSS doped with various QDs as the hybrid HIL for high-efficiency green phosphorescent OLED devices have been studied. And the hybrid PEDOT:PSS/QDs HILs were investigated based on their optical and morphological characteristics, as well as the surface energy. We found that the hybrid HIL based device revealed relatively higher device performance with the best current efficiency (CE) of 72.7 cd A^{-1}, which was a 28.2% enhancement as compared to the neat PEDOT:PSS based devices.

EXPERIMENTAL

General Information

The organic functional molecules were obtained from e-Ray Optoelectronics Corp (China). The hole injection material poly (3,4-ethylenedioxythiophene)/poly (styrenesulfonate) (PEDOT: PSS) was purchased from Heraeus, Germany. Indium tin oxide (ITO, 15 Ohm per sheet, 150 nm)-coated glass substrates were ordered from CSG Holding Co. Ltd. (China). All chemicals and reagents in this work were used as received from commercial sources without further purification unless otherwise stated.

Synthesis of Zinc Sulfide Quantum Dots and Molybdenum Sulfide Quantum Dots

ZnS QDs were synthesized using our previously reported method (Shi et al., 2019). As shown in **Figure 1**, in brief, take out 2.4018 g $Na_2S{\cdot}9H_2O$ and put it into a 100 ml volumetric flask. add distilled water to 100 ml scale, mix well and keep well. Then 0.02 mol L^{-1} RSH aqueous solution and 0.1 mol L^{-1} Zn $(CH_3COO)_2$ solution was prepared. The above Na_2S aqueous solution is the same. Add 25 ml of 0.1 mol^{-1} Zn $(CH_3COO)_2$ solution above into a three necked round bottom flask, continue to add 50 ml of 0.02 mol^{-1} ethanoic acid, and then dissolve it with 0.5 mol L^{-1} NaOH. Finally, after ultrasonic treatment for 10 min, the prepared Na_2S aqueous solution was added rapidly to 5 ml, and then the device was ultrasonic treated for 30 min. Finally, ZnS nano quantum dots were prepared by stirring at 80°C for 1 h and 30 min.

For the synthesis of MoS_2 QDs, firstly, taking 1 g of MoS_2 powder into a three-necked round bottom flask, add 12 ml of n-hexane, and passed the protective gas argon into the flask. The three-necked round bottom flask was immediately sealed and allowed to stand for 48 h. The $LixMoS_2$ in the intercalation was vacuum filtered. The product obtained by suction filtration was repeatedly washed with n-hexane solution to remove excess butyl lithium and organic residues. Then quickly took out $LixMoS_2$ on the suction filter membrane and made it react with deionized water. The solution formed by the reaction of $LixMoS_2$ with water was placed in an ultrasonic microwave instrument for auxiliary ultrasound for 1 h. The MoS_2 flakes in the suspension would quickly produce black flocculent precipitates, and then centrifuged with deionized water for several times to adjust the pH of the solution to medium which could remove Li, Cl ions and organic residues and obtain the MoS_2 QD solution.

Device Fabrication

Devices were fabricated with a configuration of ITO/PEDOT: PSS (40 nm)/NPB (30 nm)/TCTA (10 nm)/mCP: 5%Ir $(ppy)_3$ (20 nm)/TPBi (35 nm)/Liq (1 nm)/Al (100 nm), as shown in **Figure 2**, where ITO is the anode; PEDOT: PSS is the hole injection layer; N,N′-bis(naphthalen-1-yl)-N,N′-bis(phenyl)-benzidine (NPB) and 4,4′,4″-tris(carbazol-9-yl)triphenylamine (TCTA) are the hole transporting layer. 1,3-bis(N-carbazolyl) benzene (mCP) is the host for green phosphorescent dopant; tris(2-phenyl-3-methyl-pyridine)iridium (Ir $(ppy)_3$) is the green dopant; 1,3,5-tris(1-phenyl-1H-benzimidazol-2-yl)benzene (TPBi) functions as the electron transporting layer and interlayer; Liq and Al are the electron injection layer and the cathode, respectively. The patterned ITO glass substrates were first cleaned sequentially by using detergent, deionized water, acetone, isopropanol and treated with a UV-ozone environment for about 20 min. Then a 40 nm QDs doped PEDOT:PSS was spin-coated onto the ITO surface under the conditions of rotation speed of 3,000 rpm and spin coating time of 60 s. After the spin coating process was completed, the ITO covering part of the electrode was wiped off with deionized water and being baked at 130°C for 20 min under air conditions. Then the substrates were transferred into a vacuum chamber. Then, organic layers and a metal cathode layer were successively deposited by using shadow masks to finish the device fabrication in a vacuum chamber under a base pressure less than 4×10^{-6} mbar. The deposition rates for the organic layers and Al cathode were typically 2.0 Å s^{-1} and 5.0 Å s^{-1}, respectively. The active area of OLEDs is 2×2 mm^2.

Film and Device Characterization

The transmittance spectra were recorded on a UV-2501PC spectrophotometer at room temperature. Drop shape analysis (Kino optical CA and interface tensiometer) was used to measure the contact angles of deionized (DI) water. The surface morphological images of the various HILs were analyzed in air by using AFM (Bruker, Santa Barbara, CA, USA) in a tapping mode. The EL characteristics were measured using a Keithley 2,400 source meter and a PR650 Spectra Colorimeter. The luminance and spectra of each device were measured in the direction perpendicular to the substrate. All the device characterization steps were carried out at room temperature under ambient laboratory conditions without encapsulation.

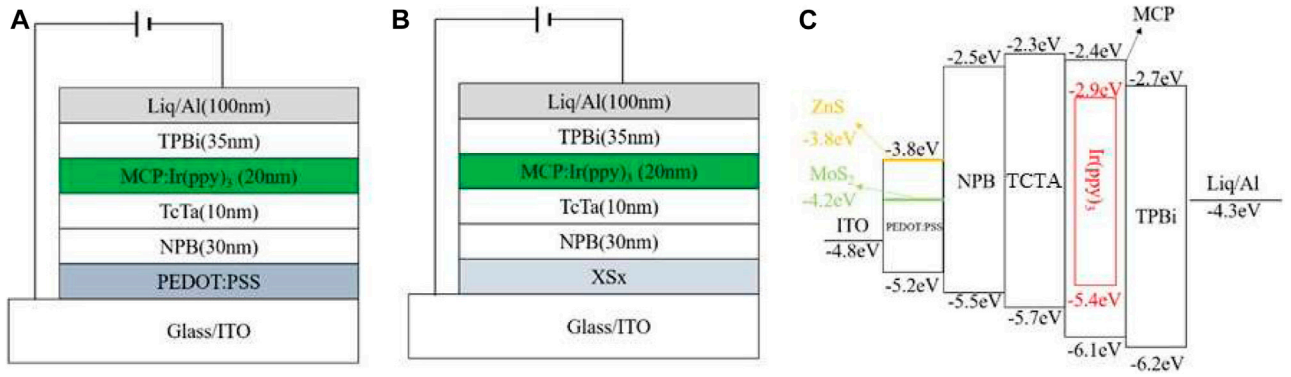

FIGURE 2 | Structure of the green phosphorescent OLEDs with **(A)** neat PEDOT:PSS HIL and **(B)** hybrid HIL. **(C)** The corresponding energy level diagram of the devices.

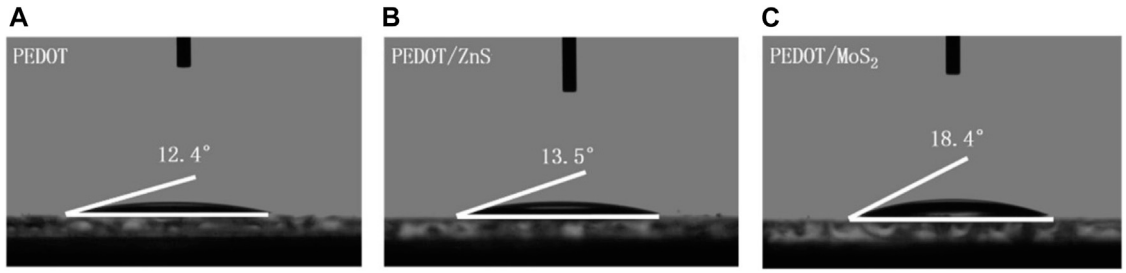

FIGURE 3 | Water contact angle measurements of different HIL of **(A)** PEDOT:PSS, **(B)** PEDOT:PSS/10% ZnS QDs and **(C)** PEDOT:PSS/10% MoS_2 QDs.

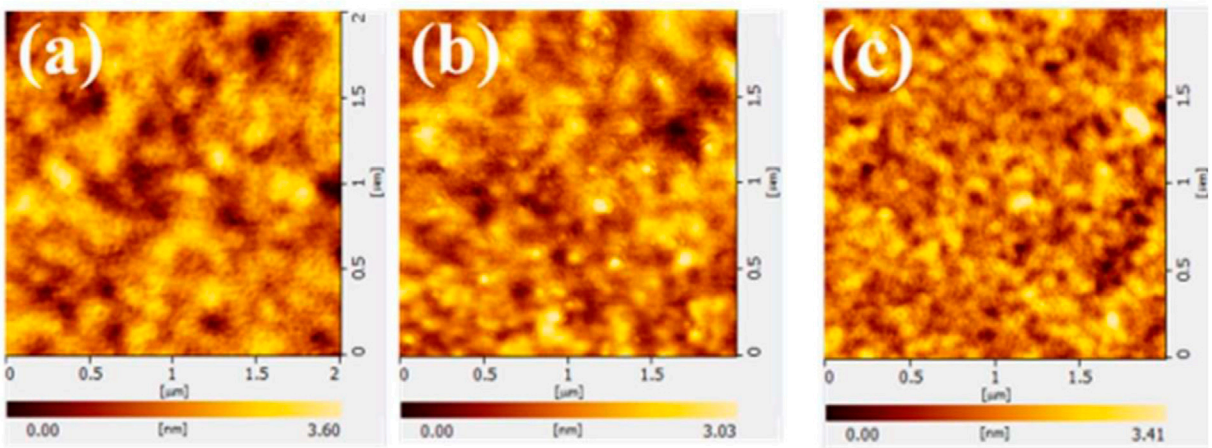

FIGURE 4 | AFM test of HILs of **(A)** PEDOT:PSS, **(B)** PEDOT:PSS/10%ZnS QDs and **(C)** PEDOT:PSS/10% MoS_2 QDs.

RESULTS AND DISCUSSION

Firstly, the water contact angles of neat PEDOT:PSS and hybrid PEDOT:PSS/QDs with the concentration of 10% (v/v) on the glass substrate were measured to identify the hydrophilic and spread-ability of the resulting HILs, which could affect the film-forming property of hole transporting layer (HTL) (Yu et al., 2014; Singh et al., 2014; Huang et al., 2009; Cho et al., 2014). **Figure 3** demonstrate the contact angles of water with PEDOT:PSS and PEDOT:PSS/QDs with different concentration are 12.4°, 13.5° and 18.4°, respectively. The small contact angles reveal that the hybrid PEDOT:PSS/QDs HIL has strong hydrophilic and

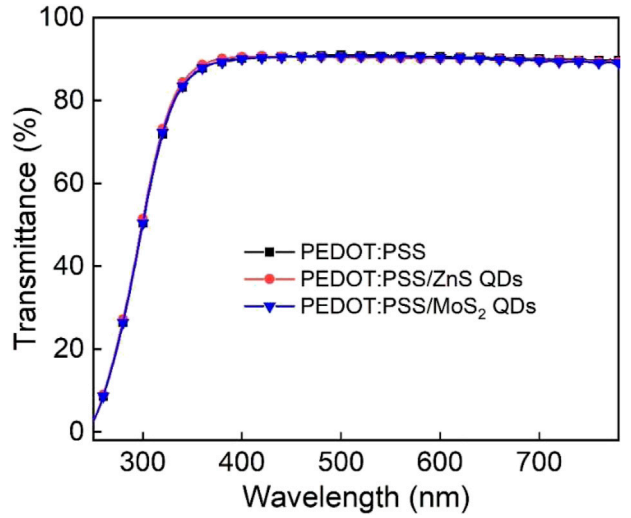

FIGURE 5 | The optical transmittance spectra for neat PEDOT:PSS, PEDOT:PSS/10% ZnS QDs and PEDOT:PSS/10% MoS_2 QDs films.

spread-ability, resulting in a better interface and adhesion between anode and hole transporting layer (Phatak et al., 2012; Tsai et al., 2020).

The OLEDs are multi thin-film structures with the overall device thickness of around 200 nm. Therefore, it is an essential requirement for OLED devices with a smooth surface on the substrate to avoid the trap states such as defects, shorts, and pinholes (Lee et al., 2018; Michels et al., 2021; Lim et al., 2008). **Figure 4** shows the surface morphology profiles of glass/HIL (40 nm) observed by AFM measurements. The values of surface roughness (RMS) of neat PEDOT:PSS, PEDOT:PSS/10%ZnS QDs and PEDOT:PSS/10%MoS_2 QDs film are 0.57, 0.47, and 0.69 nm, respectively. The hybrid HIL films exhibit a low surface roughness, which result in more efficient hole injection and consequently affect the HTL and device performance (Kim et al., 2019; Ma et al., 2019).

Figure 5 shows the ultraviolet visible (UV-Vis) spectra measurement with the wavelength range of 220–800 nm. The transmittances of the resulting film are over 90% in the visible region. Within the green emission spectral range, the glass substrate with hybrid PEDOT:PSS/ZnS QDs and PEDOT:PSS/MoS_2 QDs film with the concentration of 10% yielded a higher transmittance of 93% at 525 nm which is beneficial for enhancing the light extraction in OLED devices with normal configuration (Yang et al., 2014; Chiu and Chuang, 2015). The above results demonstrate the good visible light transmittance property of sulfide QDs-based thin films.

To evaluate the solution-processed hybrid PEDOT:PSS/ZnS QDs and PEDOT:PSS/MoS_2 QDs films as the HIL, the OLED devices with normal configuration were fabricated using the following structure: ITO/HIL (40 nm)/NPB (30 nm)/TCTA (10 nm)/mCP: 5%Ir $(ppy)_3$ (20 nm)/TPBi (35 nm)/Liq (1 nm)/Al (100 nm). Here, the device with neat PEDOT:PSS as HIL was also fabricated as the reference device. The corresponding energy level diagram of OLED devices are also depicted in **Figure 2**. The current density(J)-voltage(V)-brightness(L) properties of the OLEDs are exhibited in **Figure 6** and the main electroluminescent properties are summarized in **Table 1**.

The utilization of PEDOT:PSS/ZnS QDs based HILs significantly improved the device performances. From the J-V characteristics of the devices with various concentrations of QDs based HILs, the current density increased compared with the neat PEDOT:PSS based device. In addition, the device with hybrid PEDOT:PSS/ZnS QDs HILs showed a higher luminance at same current density, as shown in **Figure 6A**. It is also noteworthy that the maximum current efficiency of the device with hybrid PEDOT:PSS/ZnS QDs is higher than that of the device with neat PEDOT:PSS. The PEDOT:PSS/5%ZnS QDs based device showed excellent current efficiency (CE) of 63.8 cd A^{-1}, which is superior to that of device with neat PEDOT:PSS of 55.1 cd A^{-1}. It suggests that the hybrid PEDOT:PSS/ZnS QDs as HIL can significantly enhance hole injection capacity in comparison with the neat PEDOT:PSS HIL. The hybrid PEDOT:PSS/10% ZnS QDs based OLED reaches a maximum luminance of 49,005 cd m^{-2} at 9.5 V, among the other devices. Typical hybrid PEDOT:PSS/ZnS QDs based OLED gives emission with an EL peak of 516 nm, as shown in **Figure 6D**.

Finally, we investigated the device performances based on the hybrid PEDOT:PSS/MoS_2 QDs as the HIL. The results are shown in **Figure 7**, and the performance parameters are also listed in **Table 1**. It should be noted that device with hybrid PEDOT:PSS/10%MoS_2 QDs shows the better performance compared with other devices. The device with the concentration of 10%MoS_2 QDs in PEDOT:PSS exhibited maximum CE of 72.7 cd A^{-1} and maximum luminescence of 46,354 cd m^{-2} with a low turn-on voltage of 3.6 V. We also demonstrate that PEDOT:PSS doped with 10%MoS_2 QDs forms more higher quality film with lower surface roughness, which are beneficial to form a better interface and adhesion between anode and hole transporting layer. (Phatak et al., 2012; Tsai et al., 2020).

To further investigate the mechanisms of the different HILs in the OLED devices, we prepared hole-only devices (HODs) with device structures of ITO/HIL (40 nm)/NPB (100 nm)/Al (100 nm) with various hole injection layers (traditional PEDOT:PSS, PEDOT:PSS/10%ZnS QD, and PEDOT:PSS/10% MoS_2 QD) and the current density-voltage (J-V) characteristics of HODs based on the mixed HILs with the concentration of 10% were compared. The related results are shown in **Figure 8**. The HOD with the mixed PEDOT:PSS/QD HILs showed much higher current density than the devices with the traditional PEDOT:PSS HIL at the same driving voltages, indicating the more efficient hole injection.

The hole mobility based HOD was calculated from space charge limited current method by using the following Mott-Gurney Law equation (Tang et al., 2019):

$$J = \frac{9}{8}\varepsilon\varepsilon_0\mu\frac{V^2}{L^3}\exp\left(\beta\sqrt{\frac{V}{L}}\right),$$

where ε_0 is the vacuum permittivity, ε is the relative dielectric constant, β is the Poole-Frankel factor, and L is the thickness of HIL. The mobility of NPB (1.6×10^{-5} $cm^2/V{\cdot}S^{-1}$) is much lower

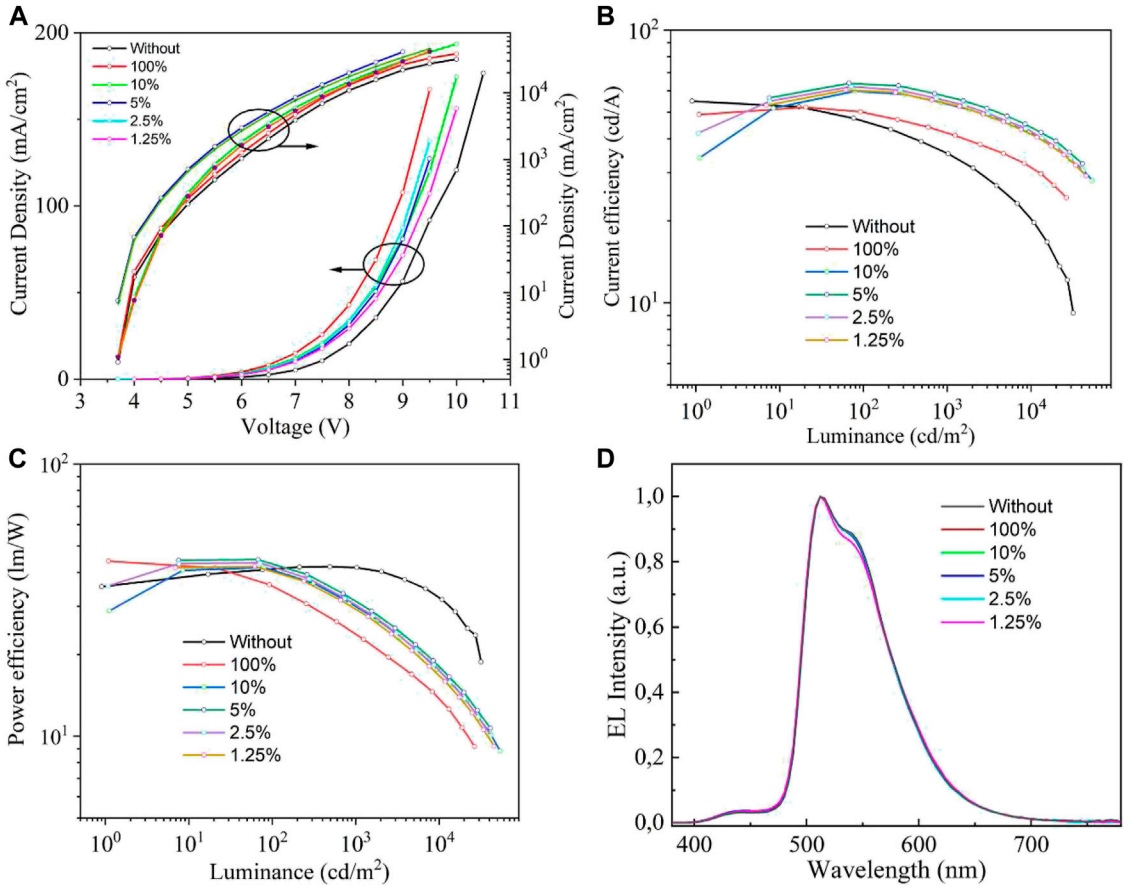

FIGURE 6 | The green phosphorescent OLED device with hybrid PEDOT:PSS/ZnS QDs film as the HIL. **(A)** Current density-voltage-brightness (*J-V-L*), **(B)** Current efficiency-luminance (CE-*L*), **(C)** Power efficiency-current density (PE-*J*) and (d) EL spectra at 6 V of the resulting devices with different concentrations.

TABLE 1 | Performance parameters of the green phosphorescent OLED device with the various HILs.

HIL	V_{on} [V][a]	n_{max} (cd A^{-1})[b]	L_{max} (cd m^{-2})[c]	n_{max} (lm W^{-1})[d]
Neat PEDOT:PSS	4	55.1	35,962	41.9
PEDOT:PSS/100% ZnS	4.2	52.2	46,354	43.9
PEDOT:PSS/10% ZnS	4.3	59.7	49,005	41.6
PEDOT:PSS/5% ZnS	4.3	63.8	41,184	44.5
PEDOT:PSS/2.5% ZnS	4.3	62.1	41,844	43.3
PEDOT:PSS/1.25% ZnS	4.3	60.2	45,705	42.0
PEDOT:PSS/100% MoS_2	3.6	55.8	37,950	40.7
PEDOT:PSS/15% MoS_2	3.8	63.2	45,276	40.2
PEDOT:PSS/10% MoS_2	3.6	72.7	46,354	41.5
PEDOT:PSS/5% MoS_2	3.6	65.3	39,424	45.6
PEDOT:PSS/2.5% MoS_2	3.8	61.1	45,320	38.3
PEDOT:PSS/1.25% MoS_2	3.8	56.7	43,802	39.6

[a]*The operating voltage at a brightness of 1 cd* m^{-2}.
[b]*The maximum CE.*
[c]*The maximum luminance.*
[d]*The maximum PE.*

than that of PEDOT:PSS/QD. (Blom et al., 2005; Zhao et al., 2019) Thus, in the initial SCLC region, the hole mobility of PEDOT:PSS/QD based HODs is limited by the mobility of NPB. The hole mobility of PEDOT:PSS/QD based HOD was evaluated from the linear fitting the SCLC region (based on $\varepsilon = 11.9$, $\varepsilon_0 = 8.85 \times 10^{-12}$ Fm^{-1}, and L = 40 nm), which results in $\mu_1 = 1.748 \times 10^{-4}$ cm^2/

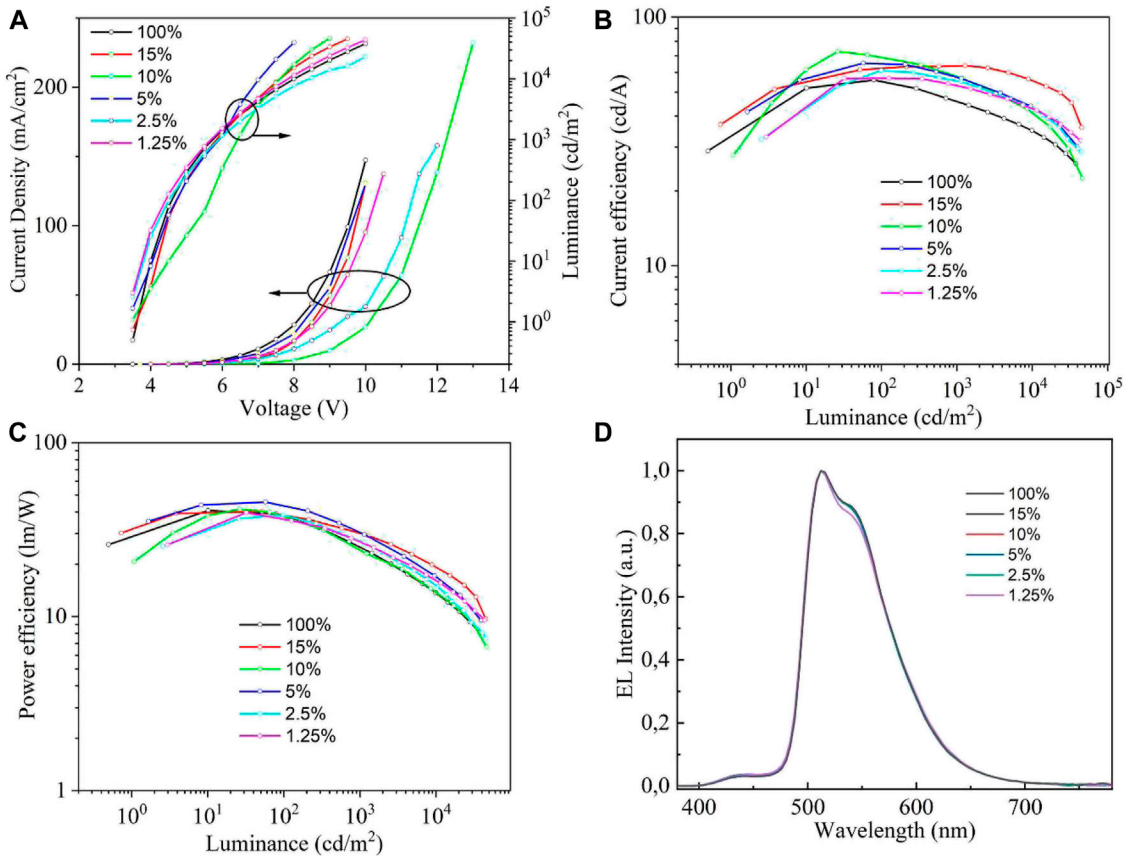

FIGURE 7 | Device performance with hybrid PEDOT:PSS/MoS_2 QDs film as the HIL. **(A)** *J-V-L*, **(B)** CE-*L*, **(C)** PE-*J* and **(D)** EL spectra at 6 V of the resulting devices with different concentrations.

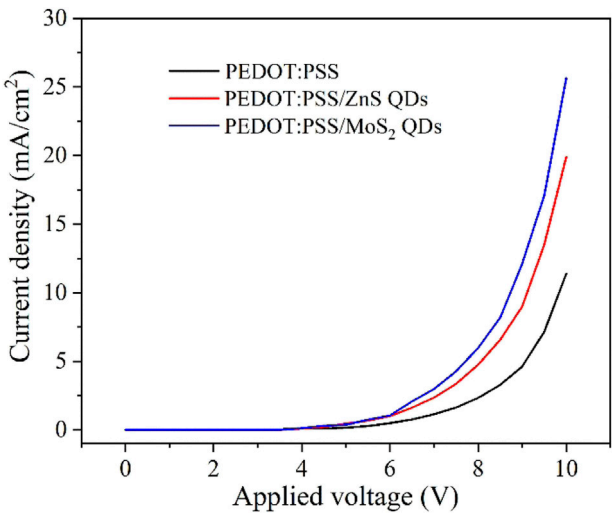

FIGURE 8 | The *J-V* characteristics of hole-only devices of ITO/HIL (40 nm)/NPB (100 nm)/Al (100 nm).

$V{\cdot}S^{-1}$ (PEDOT:PSS), $\mu_2 = 7.67 \times 10^{-4}$ $cm^2/V{\cdot}S^{-1}$ (PEDOT:PSS/ZnS QD), $\mu_3 = 1.464 \times 10^{-3}$ $cm^2/V{\cdot}S^{-1}$ (PEDOT:PSS/MoS_2 QD), indicating that the mixing of QD and PEDOT:PSS can improve the hole mobility compared to PEDOT:PSS based OLED obviously. This result is coincidence with device performance, which is responsible for the improvement of hole injection in OLEDs. Therefore, based on the corresponding energy level diagram of devices and the analytic results of SCLC method of HODs, the enhanced device efficiency with hybrid HILs can be attributed to the reduced hole injection barrier and charge recombination, resulting in the overall performance improvement of the resulting OLEDs. (Li and Marks, 2008; Han et al., 2015; Yadav et al., 2020)

CONCLUSION

In this work, we have systematically investigated the optical and electrical properties of the ZnS and MoS_2 QDs. We have demonstrated that hybrid PEDOT:PSS/QDs film as the HIL in conventional OLED could highly enhance hole injection from anode into organic hole transporting layer, and consequently improves the device efficiency. Furthermore, the device with hybrid HILs shows lower turn-on voltage and higher luminance because of its enhanced hole injection property. Among all the devices with various HILs, the device with hybrid PEDOT:PSS/MoS_2 QDs HIL showed a lowest turn-on voltage of 3.6 V and the highest maximum CE of 72.7 cd A^{-1},

achieving an enhancement of 28.2% than those with neat PEDOT:PSS based devices. We conclude that the improved film morphology of the hybrid HILs, balanced charge carrier injection and recombination are important factors to contribute the high performance of OLEDs.

DATA AVAILABILITY STATEMENT

The raw data supporting the conclusions of this article will be made available by the authors, without undue reservation.

AUTHOR CONTRIBUTIONS

All authors listed have made a substantial, direct, and intellectual contribution to the work and approved it for publication.

FUNDING

This work is financially supported by the National Key Research and Development Program of China (No. 2016YFB0401303).

REFERENCES

Benor, A., Takizawa, S.-y., Pérez-Bolívar, C., and Anzenbacher, P., Jr (2010). Efficiency Improvement of Fluorescent OLEDs by Tuning the Working Function of PEDOT:PSS Using UV-Ozone Exposure. *Org. Electronics* 11 (5), 938–945. doi:10.1016/j.orgel.2010.02.014

Blom, P. W. M., Tanase, C., De Leeuw, D. M., and Coehoorn, R. (2005). Thickness Scaling of the Space-Charge-Limited Current in Poly (P-phenylene Vinylene). *Appl. Phys. Lett.* 86 (9), 092105. doi:10.1063/1.1868865

Chiu, T. L., and Chuang, Y. T. (2015). Spectral Observations of Hole Injection with Transition Metal Oxides for an Efficient Organic Light-Emitting Diode. *J. Phys. D: Appl. Phys.* 48 (7), 075101. doi:10.1088/0022-3727/48/7/075101

Cho, A. R., Kim, S. H., Lee, E.-W., Gwak, G., Jang, J., and Park, L. S. (2014). Flexible OLED Fabricated on Glass Fabric Reinforced Film and Performance. *Mol. Crystals Liquid Crystals* 602 (1), 26–33. doi:10.1080/15421406.2014.944365

Feng, C., Zheng, X., Xu, R., Zhou, Y., Hu, H., Guo, T., and Li, F. (2020). Highly Efficient Inkjet Printed Flexible Organic Light-Emitting Diodes with Hybrid Hole Injection Layer. *Org. Electronics* 85, 105822. doi:10.1016/j.orgel.2020.105822

Han, T.-H., Song, W., and Lee, T.-W. (2015). Elucidating the Crucial Role of Hole Injection Layer in Degradation of Organic Light-Emitting Diodes. *ACS Appl. Mater. Inter.* 7 (5), 3117–3125. doi:10.1021/am5072628

Hu, Y., Song, L., Zhang, S., Lv, Y., Lin, J., Guo, X., et al. (2020). Improving the Efficiency of Multilayer Organic Light-Emitting Transistors by Exploring the Hole Blocking Effect. *Adv. Mater. Inter.* 7 (17), 2000657. doi:10.1002/admi.202000657

Huang, Z. H., Zeng, X. T., Sun, X. Y., Kang, E. T., Fuh, J. Y. H., and Lu, L. (2009). Influence of Electrochemical Treatment of ITO Surface on Nucleation and Growth of OLED Hole Transport Layer. *Thin solid films* 517 (17), 4810–4813. doi:10.1016/j.tsf.2009.03.020

Kim, G.-E., Shin, D.-K., Lee, J.-Y., and Park, J. (2019). Effect of Surface Morphology of Slot-Die Heads on Roll-To-Roll Coatings of Fine PEDOT:PSS Stripes. *Org. Electronics* 66, 116–125. doi:10.1016/j.orgel.2018.12.033

Kim, H. J., Shin, M. H., Hong, H. G., Song, B. S., Kim, S. K., Koo, W. H., and Kim, Y. J. (2015). Enhancement of Optical Efficiency in White OLED Display Using the Patterned Photoresist Film Dispersed with Quantum Dot Nanocrystals. *J. Display Technology* 12 (6), 526–531.

Lee, J., Kim, G., Shin, D.-K., Seo, Y., Kim, K., and Park, J. (2018). Improved Surface Morphology of Crosslinked Hole Transport Films by a Mixture of Polymer for OLEDs. *IEEE Trans. Electron. Devices* 65 (8), 3311–3317. doi:10.1109/ted.2018.2842130

Lee, S. T., Wang, Y. M., Hou, X. Y., and Tang, C. W. (1999). Interfacial Electronic Structures in an Organic Light-Emitting Diode. *Appl. Phys. Lett.* 74 (5), 670–672. doi:10.1063/1.122982

Lenkeviciute, B., Vitkus, M., Juska, G., and Genevicius, K. (2015). Hybrid OLEDs with CdSSe1-/ZnS Core-Shell Quantum Dots: An Investigation of Electroluminescence Properties. *Synth. Met.* 209, 343–347. doi:10.1016/j.synthmet.2015.08.003

Li, B., Gan, L., Cai, X., Li, X.-L., Wang, Z., Gao, K., et al. (2018). An Effective Strategy toward High-Efficiency Fluorescent OLEDs by Radiative Coupling of Spatially Separated Electron-Hole Pairs. *Adv. Mater. Inter.* 5 (10), 1800025. doi:10.1002/admi.201800025

Li, J., and Marks, T. J. (2008). Air-stable, Cross-Linkable, Hole-Injecting/transporting Interlayers for Improved Charge Injection in Organic Light-Emitting Diodes. *Chem. Mater.* 20 (15), 4873–4882. doi:10.1021/cm703689j

Liao, L. S., Klubek, K. P., and Tang, C. W. (2004). High-efficiency Tandem Organic Light-Emitting Diodes. *Appl. Phys. Lett.* 84 (2), 167–169. doi:10.1063/1.1638624

Lim, S. H., Ryu, G. Y., Seo, J. H., Park, J. H., Youn, S. W., Kim, Y. K., et al. (2008). Dependence of Surface Morphology on Molecular Structure and its Influence on the Properties of OLEDs. *Ultramicroscopy* 108 (10), 1251–1255. doi:10.1016/j.ultramic.2008.04.093

Ma, Y.-Y., Hua, X.-C., Zhai, T.-S., Li, Y.-H., Lu, X., Duhm, S., et al. (2019). Doped Copper Phthalocyanine via an Aqueous Solution Process for High-Performance Organic Light-Emitting Diodes. *Org. Electronics* 68, 236–241. doi:10.1016/j.orgel.2019.02.019

McEwan, J. A., Clulow, A. J., Nelson, A., Wang, R., Burn, P. L., and Gentle, I. R. (2018). Influence of Dopant Concentration and Steric Bulk on Interlayer Diffusion in OLEDs. *Adv. Mater. Inter.* 5 (1), 1700872. doi:10.1002/admi.201700872

Michels, J. J., Zhang, K., Wucher, P., Beaujuge, P. M., Pisula, W., and Marszalek, T. (2021). Predictive Modelling of Structure Formation in Semiconductor Films Produced by Meniscus-Guided Coating. *Nat. Mater.* 20 (1), 68–75. doi:10.1038/s41563-020-0760-2

Phatak, R., Tsui, T. Y., and Aziz, H. (2012). Dependence of Dark Spot Growth on Cathode/organic Interfacial Adhesion in Organic Light Emitting Devices. *J. Appl. Phys.* 111 (5), 054512. doi:10.1063/1.3692390

Salsberg, E., and Aziz, H. (2019). Degradation of PEDOT:PSS Hole Injection Layers by Electrons in Organic Light Emitting Devices. *Org. Electronics* 69, 313–319. doi:10.1016/j.orgel.2019.03.009

Shi, G., Zhang, X., Wan, M., Wang, S., Lian, H., Xu, R., et al. (2019). High-performance Inverted Organic Light-Emitting Diodes with Extremely Low Efficiency Roll-Off Using Solution-Processed ZnS Quantum Dots as the Electron Injection Layer. *RSC Adv.* 9 (11), 6042–6047. doi:10.1039/c8ra10290b

Singh, A., Nehm, F., Müller-Meskamp, L., Hoßbach, C., Albert, M., Schroeder, U., et al. (2014). OLED Compatible Water-Based Nanolaminate Encapsulation Systems Using Ozone Based Starting Layer. *Org. Electronics* 15 (10), 2587–2592. doi:10.1016/j.orgel.2014.07.024

Song, C., Hu, Z., Luo, Y., Cun, Y., Wang, L., Ying, L., et al. (2018). Organic/Inorganic Hybrid EIL for All-Solution-Processed OLEDs. *Adv. Electron. Mater.* 4 (2), 1700380. doi:10.1002/aelm.201700380

Tang, X., Xiao, S., Fu, Q., Chen, Y., and Hu, T. (2019). Incorporation of Two Electron Acceptors to Improve the Electron Mobility and Stability of Perovskite Solar Cells. *J. Mater. Chem. C* 7 (27), 8344–8349. doi:10.1039/c9tc02457c

Tsai, C.-T., Gottam, S. R., Kao, P.-C., Perng, D.-C., and Chu, S.-Y. (2020). Improvement of OLED Performances by Applying Annealing and Surface Treatment on Electro-Deposited CuSCN Hole Injection Layer. *Synth. Met.* 269, 116537. doi:10.1016/j.synthmet.2020.116537

Wang, H., Klubek, K. P., and Tang, C. W. (2008). Current Efficiency in Organic Light-Emitting Diodes with a Hole-Injection Layer. *Appl. Phys. Lett.* 93 (9), 325. doi:10.1063/1.2978349

Wang, M., Zhu, W., Yin, Z., Huang, L., and Li, J. (2020). Synergistic Effects of Li-Doped NiO Film Prepared by Low-Temperature Combustion as Hole-Injection Layer for High Performance OLED Devices. *Org. Electronics* 85, 105823. doi:10.1016/j.orgel.2020.105823

Wang, S., Qiao, M., Ye, Z., Dou, D., Chen, M., Peng, Y., and Wong, W. Y. (2018). Efficient Deep-Blue Electrofluorescence with an External Quantum Efficiency beyond 10. *Iscience* 9, 532–541. doi:10.1016/j.isci.2018.10.026

Wang, S., Wu, S., Ling, Z., Chen, H., Lian, H., Portier, X., et al. (2020). Mechanically and Thermally Stable, Transparent Electrodes with Silver Nanowires Encapsulated by Atomic Layer Deposited Aluminium Oxide for Organic Optoelectronic Devices. *Org. Electronics* 78, 105593. doi:10.1016/j.orgel.2019.105593

Wen, S.-W., Lee, M.-T., and Chen, C. H. (2005). Recent Development of Blue Fluorescent OLED Materials and Devices. *J. Display Technol.* 1 (1), 90–99. doi:10.1109/jdt.2005.852802

Xie, J., Wang, X., Wang, S., Ling, Z., Lian, H., Liu, N., et al. (2019). Solution-processed ZnO/MoS2 Quantum Dots Electron Extraction Layer for High Performance Inverted Organic Photovoltaics. *Org. Electronics* 75, 105381. doi:10.1016/j.orgel.2019.105381

Yadav, R. A. K., Dubey, D. K., Chen, S. Z., Liang, T. W., and Jou, J. H. (2020). Role of Molecular Orbital Energy Levels in Oled Performance. *Scientific Rep.* 10 (1), 1–15. doi:10.1038/s41598-020-66946-2

Yang, D. Y., Lee, S.-M., Jang, W. J., and Choi, K. C. (2014). Flexible Organic Light-Emitting Diodes with ZnS/Ag/ZnO/Ag/WO3 Multilayer Electrode as a Transparent Anode. *Org. Electronics* 15 (10), 2468–2475. doi:10.1016/j.orgel.2014.06.021

Yu, S.-Y., Chang, J.-H., Wang, P.-S., Wu, C.-I., and Tao, Y.-T. (2014). Effect of ITO Surface Modification on the OLED Device Lifetime. *Langmuir* 30 (25), 7369–7376. doi:10.1021/la4049659

Zhao, B., Miao, Y., Wang, Z., Wang, K., Wang, H., Hao, Y., et al. (2016). High Efficiency and Low Roll-Off Green OLEDs with Simple Structure by Utilizing Thermally Activated Delayed Fluorescence Material as the Universal Host. *Nanophotonics* 6 (5), 1133–1140. doi:10.1515/nanoph-2016-0177

Zhao, X., Chen, J., and Park, N. G. (2019). Importance of Oxygen Partial Pressure in Annealing NiO Film for High Efficiency Inverted Perovskite Solar Cells. *Sol. RRL* 3 (4), 1800339. doi:10.1002/solr.201800339

Zhao, Y., Wu, S., Ling, Z., Chen, H., Yu, N., Zhou, P., et al. (2020). Systematical Investigation of Ultrathin Doped Emissive Layer Structure: Achieving Highly Efficient and Long-Lifetime Orange Organic Light-Emitting Diodes. *Adv. Mater. Inter.* 7 (2), 1901609. doi:10.1002/admi.201901609

Conflict of Interest: The authors declare that the research was conducted in the absence of any commercial or financial relationships that could be construed as a potential conflict of interest.

frontiers in Chemistry

ORIGINAL RESEARCH
published: 20 May 2021
doi: 10.3389/fchem.2021.691172

Solution-Processed Pure Blue Thermally Activated Delayed Fluorescence Emitter Organic Light-Emitting Diodes With Narrowband Emission

Ting Xu[1,2,3,4]*, *Xiao Liang*[5] *and Guohua Xie*[6]*

[1]Shenzhen Key Laboratory of Polymer Science and Technology, College of Materials Science and Engineering, Shenzhen University, Shenzhen, China, [2]Key Laboratory of Optoelectronic Devices and Systems of Ministry of Education and Guangdong Province, College of Physics and Optoelectronic Engineering, Shenzhen University, Shenzhen, China, [3]State Key Laboratory of Surface Physics and Department of Physics, Fudan University, Shanghai, China, [4]Jiangsu Key Laboratory for Carbon-Based Functional Materials and Devices, Soochow University, Suzhou, China, [5]State Key Laboratory of Coordination Chemistry, Jiangsu Key Laboratory of Advanced Organic Materials, School of Chemistry and Chemical Engineering, Nanjing University, Nanjing, China, [6]Department of Chemistry and Hubei Key Lab on Organic and Polymeric Optoelectronic Materials, Wuhan University, Wuhan, China

OPEN ACCESS

Edited by:
Baiquan Liu,
Sun Yat-Sen University, China

Reviewed by:
Bo Wu,
South China Normal University, China
C Xiang,
Ningbo Institute of Materials Technology and Engineering, CAS, China

***Correspondence:**
Ting Xu
xuting_robin@pku.edu.cn
Guohua Xie
guohua.xie@whu.edu.cn

Specialty section:
This article was submitted to Physical Chemistry and Chemical Physics, a section of the journal Frontiers in Chemistry

Received: 05 April 2021
Accepted: 19 April 2021
Published: 20 May 2021

Citation:
Xu T, Liang X and Xie G (2021) Solution-Processed Pure Blue Thermally Activated Delayed Fluorescence Emitter Organic Light-Emitting Diodes With Narrowband Emission. Front. Chem. 9:691172. doi: 10.3389/fchem.2021.691172

There is a need to satisfy the high color purity requirement of display technology with a simply fabricated process. Herein, solution-processed blue thermally activated delayed fluorescence organic light-emitting diodes (OLEDs) with a narrow spectrum with a full width at half maximum (FWHM) of 32 nm and y color coordinate below 0.2 are demonstrated by employing a molecule containing boron and nitrogen atoms (TBN-TPA) as the guest emitter in the emissive layer. The opposite resonance positions of B-N atoms of TBN-TPA endows a multi-resonance effect, leading to high color purity.

Keywords: organic light-emitting diodes, thermally activated delayed fluorescence, solution process, narrow bandwidth, pure blue

INTRODUCTION

Solution-processed organic light-emitting diodes (s-OLEDs) are regarded as one of the most fascinating and competitive technologies for large-area and low-cost display panels and solid-state lighting sources (Müller et al., 2003; So et al., 2008; Zhu et al., 2011; Sasabe and Kido, 2013; Zheng et al., 2013; Xu et al., 2017a; Xu et al., 2019; Wang et al., 2020; Xu et al., 2021). Modern electronic products can be easily manufactured by ink-jet printing or 'roll-to-roll' coating methods, akin to how newspapers are produced. However, the current state-of-the-art OLEDs rely on physical vapor deposition, which leads to high manufacturing costs and energy consumption (Kololuoma et al., 2004; Mauthner et al., 2008; Sandström et al., 2012; Xu et al., 2016). The invention and application of thermally activated delayed fluorescence (TADF) compounds as the emitters without precious metals (e.g., iridium, platinum, rhenium, etc.), further facilitate more cost-effective OLED technology (Uoyama et al., 2012; Huang et al., 2018; Xu et al., 2018). Blue color plays an important role as one of the three primary colors of OLEDs. A novel concept for multi-resonance TADF (MR-TADF) was proposed by Hatakeyama et al. in 2016. The reported TADF emitters show particular HOMO and LUMO distributions due to the rigid framework of boron and nitrogen (B-N) atoms' array, leading to the MR effect. This MR effect enhances the oscillating strength between S_1 and S_0, generating a narrow full-width-at-half-maximum (FWHM) of 28 nm, showing unexpected high color purity in TADF species (Hatakeyama et al., 2016). Then highly efficient blue MR-

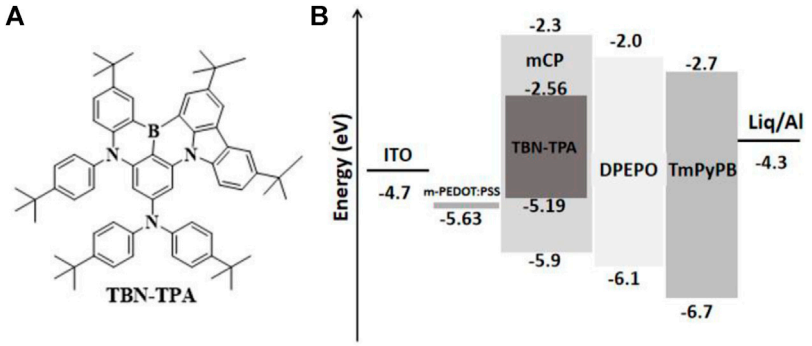

FIGURE 1 | (A) The chemical structure of TBN-TPA. **(B)** Energy level diagrams of the devices.

TADF molecules were developed, showing an extremely high external quantum efficiency (EQE) of up to 34.4% and a narrow FWHM of 14 nm (Kondo et al., 2019). However, blue MR-TADF materials with high color purity are rarely applied in s-OLED. Therefore, it is attractive to investigate blue MR-TADF materials aiming for a solution process.

In this paper, solution-processed blue TADF OLEDs with a narrow bandwidth have been demonstrated by applying a molecule TBN-TPA (Liang et al., 2018) containing boron and nitrogen (B-N) atoms. Our results provided new understanding of the electroluminescence of blue MR-TADF emitter, which would be beneficial to the development of solution-processed OLED technology for high-performance displays.

EXPERIMENT DETAILS

The chemical structures of TBN-TPA and the energy level diagram of the device are exhibited in **Figures 1A,B**, respectively. TBN-TPA was synthesized according to the literature (Liang et al., 2018). 1,3-bis(9H-carbazol-9-yl)benzene (mCP), 8-hydroxyquinolinolatolithium (Liq), bis [2-(diphenyl-phosphino)phenyl]ether oxide (DPEPO), 1,3,5-tri [(3-pyridyl)-phen-3-yl] benzene (TmPyPB), and 8-hydroxyquino -linolatolithium (Liq) were purchased from Xi'an Polymer Light Technology Corporation and used as received.

All the devices were fabricated on the glass substrate patterned with the conducting indium-tin-oxide (ITO) anode with a sheet resistance lower than 20 Ω/square. Acetone and ethanol were consecutively used to clean the ITO substrates in an ultrasonic bath. The substrates were further dried with N_2 flow. After 20 min of ultraviolet light-ozone treatment, a modified PEDOT: PSS (m-PEDOT:PSS) was spin-coated onto the ITO surface at 4,000 rpm (Xiang et al., 2019). Afterward, the substrate was baked at 120°C for 10 min in a glove box. TBN-TPA and mCP, respectively as the guest and host of the emissive material layer (EML), sufficiently dissolved in chlorobenzene solvent. Later, the corresponding EML was spin coated at 1,000 rpm and then accompanied with a 50°C baking process for 10 min. The corresponding functional materials and aluminum cathode were vacuum deposited step by step under 10^{-5} mbar. The actual device area defined by the crossover of the ITO anode and the Al cathode was 2 mm × 2.2 mm.

In this study, the OLEDs using the conventional mCP host were fabricated while TBN-TPA with the B-N core-structure containing a peripheral electron-donating carbazole unit was applied as the blue guest. The structure of the devices is ITO/ m-PEDOT:PSS/TBN-TPA (5 wt%, 10 wt%, and 20 wt%): mCP/ DPEPO (10 nm)/TmPyPB (50 nm)/Liq (1 nm)/Al (100 nm). The energy level diagram of the device is shown in **Figure 1B**. m-PEDOT:PSS acts as the hole injection layer (HIL) (Xiang et al., 2019). DPEPO serves as the exciton blocking layer with a high triplet energy level over 3.0 eV, which helps to confine the excitons in the emitting layer (Xu et al., 2017b). Liq and TmPyPB are used as the electron injection layer (EIL) and electron transporting layer (ETL), respectively.

The current density-voltage-luminance (J-V-L), the current efficiency-luminance -power efficiency (CE-L-PE) characteristics, the color coordinates, and the electroluminescence (EL) spectra of the devices were measured and recorded by a computer-controlled Keithley 2,400 Source Meter Unit and Photo Research PR735 spectrometer. All measurements were carried out at room temperature in ambient air.

RESULTS AND DISCUSSION

The devices A, B, and C were fabricated and tested in one flow doping with different TBN-TPA concentrations i.e., 5 wt%, 10 wt %, and 20 wt%, respectively. The J-V-L and CE-L-PE characteristics are shown in **Figures 2A,B**, respectively. The device performances of the blue TADF OLEDs with different doping concentrations of TBN-TPA are summarized in **Table 1**.

The turn-on voltage of the s-OLED with TBN-TPA depended on the increasing concentration of TBN-TPA. Under the same voltage, the s-OLED with higher concentrations of TBN-TPA as emitter showed lower current density (shown in **Figure 2A**). In contrast, the current efficiency (CE), power efficiency (PE), and EQE increased as the doping concentration increased, shown in **Figure 2B** and **Table 1**. The device with 20 wt% TBN-TPA depicted the maximum EQEs of 1.08% with narrow FWHM of 32 nm. The performances of OLEDs with solution-processed TBN-TPA as blue TADF emitter are much lower than those of the devices with physical vapor deposition, which may be ascribed to the

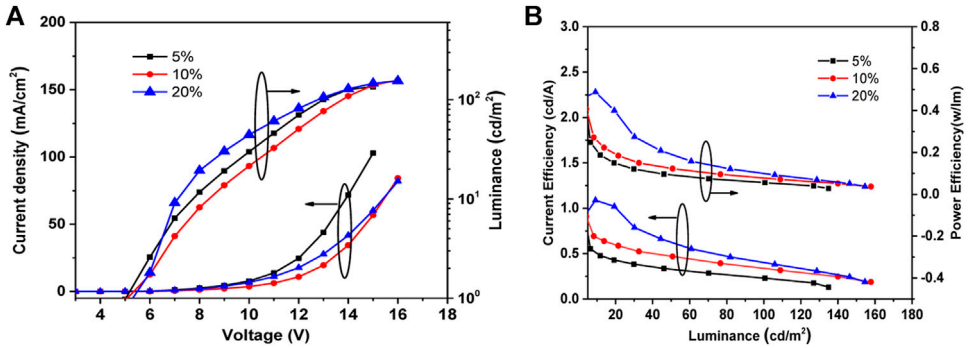

FIGURE 2 | (A) Current density-voltage-luminance and **(B)** current efficiency-luminance-power efficiency characteristics of the devices.

TABLE 1 | The EL characteristics of blue TADF OLEDs.

Device	Processing/ Host	Vo_n[a] [V]	EL_{peak} [nm]	CE_{max}[b] [cd A^{-1}]	FWHM[c] [nm]	PE_{max}[d] [lm W^{-1}]	EQE_{max}[e] [%]	CIE[f] [x, y]
A	Solution/mCP	4.5	464	0.55	32	0.25	0.66	0.19, 0.14
B	Solution/mCP	4.8	464	0.91	32	0.41	1.03	0.19, 0.15
C	Solution/mCP	5.0	464	1.08	32	0.49	1.08	0.19, 0.19

[a]*The turn-on voltage recorded at a brightness of 1 cd m^{-2}.*
[b]*Maximum value [2] of current efficiency.*
[c]*Full-width-at-half-maximum of the EL spectrum.*
[d]*Power efficiency.*
[e]*External quantum efficiency.*
[f]*Commission Internationale de l'Eclairage (CIE) coordinates.*

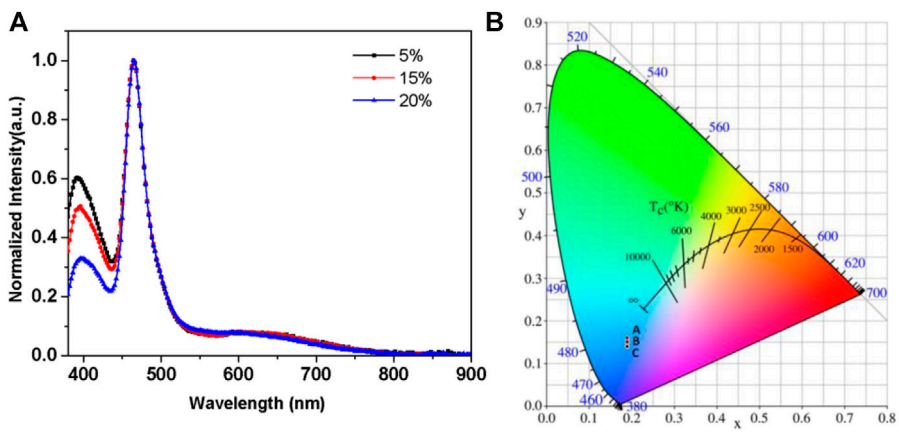

FIGURE 3 | (A) The normalized EL spectra of devices and **(B)** the chromaticity coordinates of devices.

unsatisfactory film quality fabricated by spin-coating (Liang et al., 2018; Tang et al., 2020). Solution-processed organic thin films are generally of a lower quality than those fabricated by physical vapor deposition. More morphological defects could be induced and thus deteriorate charge transport properties and radiative decays in the solution-processed devices. Therefore, it is reasonable that solution-processed OLEDs generally exhibit lower EQEs compared with that of vapor deposition OLEDs using the same emitter despite the simple fabrication processing (Diao et al., 2014). Therefore, more effort should be devoted to device engineering.

The EL spectrum and the chromaticity coordinates of the devices with TBN-TPA are shown in **Figures 3A,B**. The two

peaks of the normalized EL spectra of the devices could be determined, which originated from the blue TADF emitter TBN-TPA and host mCP, respectively, peaking at 464 and 396 nm (shown in **Figure 3A**). This is attributed to the inefficient host-guest energy transfer. As for the chromaticity coordinates of the devices, the CIE (x,y) coordinates were slightly changed with the y value below 0.2 in **Figure 3B**. As the concentration of TBN-TPA increased from 5 to 20%, the residual emission of the host mCP was gradually quenched by TBN-TPA, which resulted in relatively higher EQEs, shown in **Table 1**. Meanwhile, there exists some interfacial exciplex which accounts for the emission band in the region of 600–700 nm.

CONCLUSION

In summary, we succeeded in employing blue TADF dye with the narrow bandwidth in solution-processed OLED as the emitter to realize high color purity. This technical route shows high value in the development of solution-processed OLED display technology.

DATA AVAILABILITY STATEMENT

The raw data supporting the conclusions of this article will be made available by the authors, without undue reservation.

AUTHOR CONTRIBUTIONS

TX conceived, fabricated, and characterized OLED. XL synthesized blue TADF materials. GX directed and supervised the project.

FUNDING

This work was supported by the National Natural Science Foundation of China (No. 51903160, 51803125, and 91833304), China Postdoctoral Science Foundation (2019M663027), Open Project Funding of Jiangsu Key Laboratory for Carbon-Based Functional Materials and Devices, Soochow University, China. (KJS 1908), and Open Project Funding of State Key Laboratory of Surface Physics and Department of Physics, Fudan University, China. (KF2019_13).

ACKNOWLEDGMENTS

The authors would like to express their special gratitude to Prof. Xiaoyuan Hou, Prof. Chuluo Yang, and Prof. Youxuan Zheng for their support and assistance in my research.

REFERENCES

Diao, Y., Shaw, L., Bao, Z., and Mannsfeld, S. C. B. (2014). Morphology Control Strategies for Solution-Processed Organic Semiconductor Thin Films. *Energy Environ. Sci.* 7, 2145–2159. doi:10.1039/c4ee00688g

Hatakeyama, T., Shiren, K., Nakajima, K., Nomura, S., Nakatsuka, S., Kinoshita, K., et al. (2016). Ultrapure Blue Thermally Activated Delayed Fluorescence Molecules: Efficient HOMO-LUMO Separation by the Multiple Resonance Effect. *Adv. Mater.* 28, 2777–2781. doi:10.1002/adma.201505491

Huang, T., Jiang, W., and Duan, L. (2018). Recent Progress in Solution Processable TADF Materials for Organic Light-Emitting Diodes. *J. Mater. Chem. C.* 6, 5577–5596. doi:10.1039/c8tc01139g

Kololuoma, T., Tuomikoski, M., Makela, T., Heilmann, J., Haring, T., Kallioinen, J., et al. (2004). *Towards Roll-To-Roll Fabrication of Electronics, Optics, and Optoelectronics for Smart and Intelligent Packaging*. SPIE. doi:10.1117/12.535456

Kondo, Y., Yoshiura, K., Kitera, S., Nishi, H., Oda, S., Gotoh, H., et al. (2019). Narrowband Deep-Blue Organic Light-Emitting Diode Featuring an Organoboron-Based Emitter. *Nat. Photon.* 13, 678–682. doi:10.1038/s41566-019-0476-5

Liang, X., Yan, Z.-P., Han, H.-B., Wu, Z.-G., Zheng, Y.-X., Meng, H., et al. (2018). Peripheral Amplification of Multi-Resonance Induced Thermally Activated Delayed Fluorescence for Highly Efficient OLEDs. *Angew. Chem. Int. Ed.* 57, 11316–11320. doi:10.1002/anie.201806323

Mauthner, G., Landfester, K., Köck, A., Brückl, H., Kast, M., Stepper, C., et al. (2008). Inkjet Printed Surface Cell Light-Emitting Devices from a Water-Based Polymer Dispersion. *Org. Elect.* 9, 164–170. doi:10.1016/j.orgel.2007.10.007

Müller, C. D., Falcou, A., Reckefuss, N., Rojahn, M., Wiederhirn, V., Rudati, P., et al. (2003). Multi-colour Organic Light-Emitting Displays by Solution Processing. *Nature* 421, 829–833. doi:10.1038/nature01390

Sandström, A., Dam, H. F., Krebs, F. C., and Edman, L. (2012). Ambient Fabrication of Flexible and Large-Area Organic Light-Emitting Devices Using Slot-Die Coating. *Nat. Commun.* 3, 1002. doi:10.1038/ncomms2002

Sasabe, H., and Kido, J. (2013). Development of High Performance OLEDs for General Lighting. *J. Mater. Chem. C.* 1, 1699–1707. doi:10.1039/c2tc00584k

So, F., Kido, J., and Burrows, P. (2008). Organic Light-Emitting Devices for Solid-State Lighting. *MRS Bull.* 33, 663–669. doi:10.1557/mrs2008.137

Tang, Y., Xie, G., Liang, X., Zheng, Y.-X., and Yang, C. (2020). Organic and Quantum-Dot Hybrid White LEDs Using a Narrow Bandwidth Blue TADF Emitter. *J. Mater. Chem. C.* 8, 10831–10836. doi:10.1039/d0tc01942a

Uoyama, H., Goushi, K., Shizu, K., Nomura, H., and Adachi, C. (2012). Highly Efficient Organic Light-Emitting Diodes from Delayed Fluorescence. *Nature* 492, 234–238. doi:10.1038/nature11687

Wang, S., Zhang, H., Zhang, B., Xie, Z., and Wong, W.-Y. (2020). Towards High-Power-Efficiency Solution-Processed OLEDs: Material and Device Perspectives. *Mater. Sci. Eng. R: Rep.* 140, 100547. doi:10.1016/j.mser.2020.100547

Xiang, Y., Xie, G., Li, Q., Xue, L., Xu, Q., Zhu, J., et al. (2019). Feasible Modification of PEDOT:PSS by Poly(4-Styrenesulfonic Acid): A Universal Method to Double the Efficiencies for Solution-Processed Organic Light-Emitting Devices. *ACS Appl. Mater. Inter.* 11, 29105–29112. doi:10.1021/acsami.9b09346

Xu, T., Yan, L., Miao, J., Hu, Z., Shao, S., Li, A., et al. (2016). Unlocking the Potential of Diketopyrrolopyrrole-Based Solar Cells by a Pre-solvent Annealing Method in All-Solution Processing. *RSC Adv.* 6, 53587–53595. doi:10.1039/c6ra09770g

Xu, T., Yi, R., Zhu, C., and Lin, M. (2021). *Simple-Structured OLEDs Incorporating Undoped Phosphorescent Emitters within Non-exciplex Forming Interfaces: Towards Ultraslow Efficiency Roll-Off and Low Driving Voltage for Indoor R/G/B Illumination*, 8. doi:10.3389/fchem.2020.630687

Xu, T., Zhang, Y.-X., Huang, C.-C., Zhou, J.-G., Fung, M.-K., and Meng, H. (2019). Highly Simplified Blue Phosphorescent Organic Light-Emitting Diodes Incorporating Exciplex-Forming Co-host Assisting Energy Transfer. *J. Lumin.* 206, 554–559. doi:10.1016/j.jlumin.2018.10.007

Xu, T., Zhang, Y.-X., Murtaza, I., and Meng, H. (2017a). P-170: Organic Light-Emitting Diodes Incorporating a Novel Exciplex-Forming Host: A Synergistic Strategy to Design Highly Simplified OLEDs for Application. *OLEDs Appl.* 48, 1915–1918. doi:10.1002/sdtp.12004

Xu, T., Zhang, Y.-X., Wang, B., Huang, C.-C., Murtaza, I., Meng, H., et al. (2017b). Highly Simplified Reddish Orange Phosphorescent Organic Light-Emitting Diodes Incorporating a Novel Carrier- and Exciton-Confining Spiro-Exciplex-

Forming Host for Reduced Efficiency Roll-Off. *ACS Appl. Mater. Inter.* 9, 2701–2710. doi:10.1021/acsami.6b13077

Xu, T., Zhou, J.-G., Fung, M.-K., and Meng, H. (2018). Simplified Efficient Warm White Tandem Organic Light-Emitting Devices by Ultrathin Emitters Using Energy Transfer from Exciplexes. *Org. Elect.* 63, 369–375. doi:10.1016/j.orgel.2018.09.026

Zheng, H., Zheng, Y., Liu, N., Ai, N., Wang, Q., Wu, S., et al. (2013). All-solution Processed Polymer Light-Emitting Diode Displays. *Nat. Commun.* 4, 1971. doi:10.1038/ncomms2971

Zhu, X.-H., Peng, J., Cao, Y., and Roncali, J. (2011). Solution-processable Single-Material Molecular Emitters for Organic Light-Emitting Devices. *Chem. Soc. Rev.* 40, 3509–3524. doi:10.1039/c1cs15016b

Conflict of Interest: The authors declare that the research was conducted in the absence of any commercial or financial relationships that could be construed as a potential conflict of interest.

frontiers in Chemistry

ORIGINAL RESEARCH
published: 25 June 2021
doi: 10.3389/fchem.2021.703561

Modification of the SnO_2 Electron Transporting Layer by Using Perylene Diimide Derivative for Efficient Organic Solar Cells

Tianyu Kong, Rui Wang, Ding Zheng and Junsheng Yu**

State Key Laboratory of Electronic Thin Films and Integrated Devices, School of Optoelectronic Science and Engineering, University of Electronic Science and Technology of China (UESTC), Chengdu, China

Recently, tin oxide (SnO_2) nanoparticles (NPs) have attracted considerable attention as the electron transporting layer (ETL) for organic solar cells (OSCs) due to their superior electrical properties, excellent chemical stability, and compatibility with low-temperature solution fabrication. However, the rough surface of SnO_2 NPs may generate numerous defects, which limits the performance of the OSCs. In this study, we introduce a perylene diimide derivative (PDINO) that could passivate the defects between SnO_2 NP ETL and the active layer. Compared with the power conversion efficiency (PCE) of the pristine SnO_2 ETL–based OSCs (12.7%), the PDINO-modified device delivers a significantly increased PCE of 14.9%. Overall, this novel composite ETL exhibits lowered work function, improved electron mobility, and reduced surface defects, thus increasing charge collection efficiency and restraining defect-caused molecular recombination in the OSC. Overall, this work demonstrates a strategy of utilizing the organic–inorganic hybrid ETL that has the potential to overcome the drawbacks of SnO_2 NPs, thereby developing efficient and stable OSCs.

Keywords: organic solar cell, electron transporting layer, perylene diimide derivative, tin oxide, surface defects

OPEN ACCESS

Edited by:
Qifan Xue,
South China University of Technology, China

Reviewed by:
Zhou Yang,
University of Science and Technology Beijing, China
Fei Guo,
Jinan University, China

****Correspondence:***
Ding Zheng
ding_zheng@alu.uestc.edu.cn
Junsheng Yu
jsyu@uestc.edu.cn

Specialty section:
This article was submitted to Nanoscience, a section of the journal Frontiers in Chemistry

Received: *30 April 2021*
Accepted: *10 June 2021*
Published: *25 June 2021*

Citation:
Kong T, Wang R, Zheng D and Yu J (2021) Modification of the SnO_2 Electron Transporting Layer by Using Perylene Diimide Derivative for Efficient Organic Solar Cells. Front. Chem. 9:703561. doi: 10.3389/fchem.2021.703561

INTRODUCTION

Over the past decades, in order to harness clean and abundant solar energy, extensive efforts have been made to develop efficient and affordable photovoltaic cells. Among the numerous candidates, organic solar cell (OSC) has attracted considerable attention of researchers due to its potential of low-cost and large-scale fabrication onto the flexible or stretchable substrate (Thompson and Frechet, 2008; Liang et al., 2010; Li et al., 2012; Hou et al., 2018; Yuan et al., 2019). Owing to the continuous development of organic photoelectric materials in recent years, for the bulk heterojunction (BHJ) OSC device, the power conversion efficiency (PCE) has exceeded 18% (Wang et al., 2020), which paves the way for the future commercialization of OSCs. In addition to the active layer, the charge transporting layer (CTL) also plays a critical role in realizing the high-performance of OSCs (Ma et al., 2010; Yip and Jen, 2012). Being inserted between the electrode and active layer, the CTL can decrease the interfacial barrier and adjust the mismatched energy levels, thus facilitating charge carrier collection and transportation (Hsieh et al., 2010; Li et al., 2010). Currently, an n-type metal oxide, namely, zinc oxide (ZnO), has been widely utilized as the material of the electron transporting layer (ETL) for OSCs because of its matched energy level, good conductivity, high optical transparency, and solution processability (White et al., 2006; Kyaw et al., 2008; Wang et al., 2015; Zhang et al., 2019; Zheng et al., 2019; Fan et al., 2020). However, when placed under ambient

sun illumination, ZnO can absorb a large proportion of ultraviolet light, which brings about the degradation of the organic active layer and thus hampers the performance of OSCs (Jiang et al., 2019).

Tin oxide (SnO_2) is another n-type metal oxide that can be fabricated from pre-dispersed nanoparticle (NP) dispersion annealed at a temperature of less than 150 °C. It has been widely studied as the ETL material in dye-sensitized and perovskite solar cells (Snaith and Ducati, 2010; Jiang et al., 2017). SnO_2 NPs have a wider bandgap, higher conductivity, and less sensitivity to ultraviolet light than the conventional sol-gel ZnO. However, despite the potential to become a superior ETL material for more stable and efficient OSCs, the solution-based fabrication process of the SnO_2 NP ETL inevitably generates a mass of surface defects (Peng et al., 2020). Additionally, the morphology of the active layer may be further affected by the compatibility issue with organic photovoltaic materials and metal oxide NPs (Yin et al., 2016). Given the above, the introduction of the SnO_2 NP ETL could lead to the declines of exciton dissociation and charge extraction efficiencies as well as defect-caused molecular recombination, which significantly limits the performance of OSCs.

Several efforts of surface modification for metal oxide ETLs have been made using various materials, including aluminum (Lin et al., 2016), graphene (Gollu et al., 2016), quantum dot (Zeng et al., 2017), conjugated polyelectrolyte (Kim et al., 2015), and organic small molecule (Song et al., 2013). Among them, perylene diimide (PDI) derivatives, a group of organic small molecule material, have recently drawn lots of research interest due to their excellent stability and the ability to facilitate charge carrier transport by tuning the work function between the active layer and electrodes (Ling et al., 2007; Zhang et al., 2014; Wang et al., 2017). Moreover, the perylene diimide backbone can be easily functionalized by different side chains, thus enabling its water/alcohol processability. A PDI derivative with amine functional groups (PDIN) was utilized as a ZnO ETL modifier, resulting in a near 14% enhanced PCE (Yu et al., 2016). More recently, ($HOOC_5$-triazole) PDIN-hex, a carboxylic acid functionalized PDI, was also successfully adopted. The deposition of functionalized PDI can increase the surface hydrophobicity of the ZnO ETL without causing severe impacts to its optical and photochemical properties, thus accumulating the acceptor component of BHJ at the cathode interface. On account of the enhanced charge carrier concentration, the OSC devices with the modified ZnO ETL exhibited up to 33% improvement in the PCE (Abd-Ellah et al., 2019). Despite these benefits of the PDI derivatives on ZnO, their effects on SnO_2 ETL–based OSCs have not been reported so far.

In this work, a thin layer of perylene diimide derivative with the terminal substituents of amino N-oxide {i.e., 2,9-bis [3-(dimethyloxidoamino) propyl] anthra (2,1,9-def:6,5,10-days'e'f') diisoquinoline-1,3,8,10(2H,9H)-tetrone, (PDINO)} was introduced to modify the SnO_2 NP ETL. This SnO_2/PDINO composite ETL exhibits decent optical transmittance, improved electrical conductivity, and reduced work function (WF). Furthermore, the decline of the surface defects is featured prominently in solution-processed SnO_2 NPs, resulting in an active layer film with more favorable morphology atop the ETL. The poly {[2.6-(4,8-bis(5-(2-ethylhexyl-3-fluoro) thiophen-2-yl)-benzo (1,2-b:4,5-b') dithiophene)]-alt-[5.5-(1′,3′-di-2-thienyl-5′,7′-bis(2-ethylhexyl) benzo (1′,2′-c:4′,5′-c') dithiophene-4,8-dione)]}:2.2'-{(2Z,2′Z)-[(12,13-bis(2-ethylhexyl)-3,9-diundecyl-12,13-dihydro-(1,2,5) thiadiazolo (3,4-e) thieno (2″,3″:4′,5') thieno (2′,3':4.5) pyrrolo (3,2-g) thieno (2′,3':4.5) thieno (3,2-b) indole-2,10-diyl) bis(methanylylidene)] bis (5,6-difluoro-3-oxo-2,3-dihydro-1H-indene-2,1-diylidene)}dimalononitrile (PM6:Y6) OSCs were fabricated with a inverted device structure, and the champion device with SnO_2/PDINO ETLs showed excellent power conversion efficiency (PCE) of 14.9%, which is much higher than that of the control device with the neat SnO_2 ETL (12.7%). The simultaneously enhanced short circuit current (J_{SC}) and fill factor (FF) indicate that modifying the surface of the SnO_2 ETL with PDINO could increase charge collection efficiency and restrain defect-caused molecular recombination in the OSC. The device stability also benefits from the PDINO modification. This novel method provides a promising approach to produce efficient OSCs based on low-temperature fabrication.

MATERIALS AND METHODS

The active layer materials (PM6 and Y6) were purchased from Solarmer, PDINO was obtained from 1-Material, and SnO_2 NPs were obtained from Alfa Aesar. All of these materials were used as received. The molecular structures of PM6, Y6, and PDINO are shown in **Figure 1A**. In addition, chloroform, 1-chloronaphthalene, and other solvents used for device fabrication were purchased from Sigma-Aldrich.

The device structure of the OSCs in this study is ITO/ETLs/PM6:Y6/MoO_3/Ag, as depicted in **Figure 1B**. With the weight ratio of 1:1.2, PM6 and Y6 were stirred in chloroform for 12 h to obtain the BHJ active layer solution. The blend solution has a concentration of 16 mg/ml; 1-chloronaphthalene at a concentration of 0.5% (v/v) was subsequently mixed as solvent additive. The active layer solution was stirred overnight at room temperature. The SnO_2 NP ETL (40 nm) was prepared by spin-coating the pre-dispensed SnO_2 NPs onto cleaned ITO/glass substrates at 5,000 rpm for 45 s and then baked in the air at 120°C for 15 min. For the modified devices, methanol solutions of PDINO at varying concentrations were deposited atop SnO_2 ETLs at 3,000 rpm for 30 s; the concentration of PDINO is 0.5, 1, and 2 mg/ml. The active layers (100 nm) were spin-coated at 2,000 rpm for 60 s atop the ETLs, followed by a 10-min thermal annealing process in nitrogen glove box at 110°C. Finally, the MoO_3 hole transporting layer (15 nm) and Ag electrodes (100 nm) were deposited under a vacuum of 1×10^{-5} Pa. The effective device area is 0.03 cm^2, which is determined by the shadow mask.

RESULTS AND DISCUSSION

The performance of the inverted OSC device is crucially influenced by the optical property of the ETL. Therefore, the

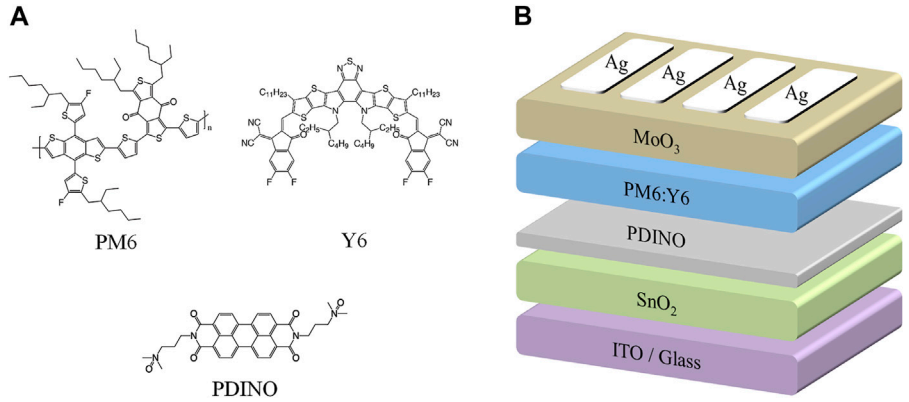

FIGURE 1 | (A) Molecular structures of organic photoelectric materials used in this study. **(B)** Schematic diagram of the OSC device structure.

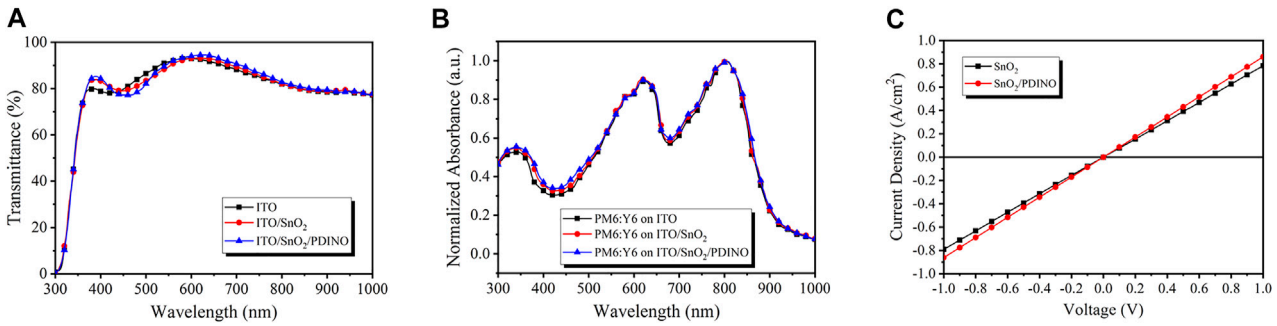

FIGURE 2 | (A) Transmittance spectra of ITO, ITO/SnO_2, and ITO/SnO_2/PDINO. **(B)** Normalized UV–vis absorption spectra of PM6:Y6 on ITO, ITO/SnO_2, and ITO/SnO_2/PDINO. **(C)** *J–V* curves of ETLs with and without PDINO modification.

transmittance spectra of ITO-coated glass, SnO_2, and SnO_2/PDINO ETLs fabricated on ITO/glass were measured and plotted in **Figure 2A**. Compared to the clean ITO/glass, SnO_2 and SnO_2/PDINO ETLs both exhibit enhanced transmittance in the 350–450 nm region that could be beneficial for achieving better absorption of the active layer. SnO_2 covered by the PDINO modification layer has slightly lower transmittance from 450 to 550 nm, which could be attributed to the light absorption of PDINO. Despite this result, the SnO_2/PDINO ETL can still maintain an average transmittance of 87.33% in the 380–780 nm region of visible light, indicating that the PDINO layer will not remarkably impact the light-harvesting ability of the SnO_2 ETL. The normalized ultraviolet–visible (UV-vis) absorption spectra of PM6:Y6 films on different ETLs are displayed in **Figure 2B**. The PM6:Y6 films on ITO/SnO_2 and ITO/SnO_2/PDINO exhibit higher absorbance than those deposited on the ITO substrate in the wavelength of 350–450 nm, which are consistent with the results of the transmittance spectra in **Figure 2A**.

The film conductivities of different ETLs were evaluated to take a glimpse into the effect of the PDINO modification layer. With the ITO/ETL/Ag structure to ensure reliable ohmic contact, the current density–voltage (*J–V*) measurements of SnO_2 and SnO_2/PDINO ETLs are depicted in **Figure 2C**. The conductivity (σ) of the ETLs is defined with **Eq. 1**:

$$\sigma = \frac{Gd}{A} = \frac{Id}{VA} = \frac{Jd}{V}. \quad (1)$$

The conductance (G) is calculated from the slope of the *J–V* lines, where A is the device area, J is the current density, V is the corresponding bias voltage, and d is the thickness of the ETL (d = 40 nm for SnO_2 and d = 50 nm for SnO_2/PDINO). The conductivity of SnO_2 and SnO_2/PDINO ETLs is calculated to be 3.10×10^{-6} and 4.31×10^{-6} S/cm, respectively. The enhanced conductivity of the SnO_2/PDINO ETL suggests that the modified ETL may have fewer surface defects, thus facilitating electronic transmission.

Atomic force microscopy (AFM) was conducted to survey the evolution of surface morphology for the PDINO-modified SnO_2 NP ETL. **Figures 3A,B** display the height images of the SnO_2 ETL and SnO_2/PDINO ETL. The pristine SnO_2 ETL film has a relatively coarse surface, with a 2.71-nm root mean square (RMS) roughness value. For the SnO_2 ETL modified by a PDINO layer, the AFM image exhibits a smoother surface of the ETL, with a significantly decreased RMS roughness value of 1.41 nm. This implies that PDINO could fill the gaps between the

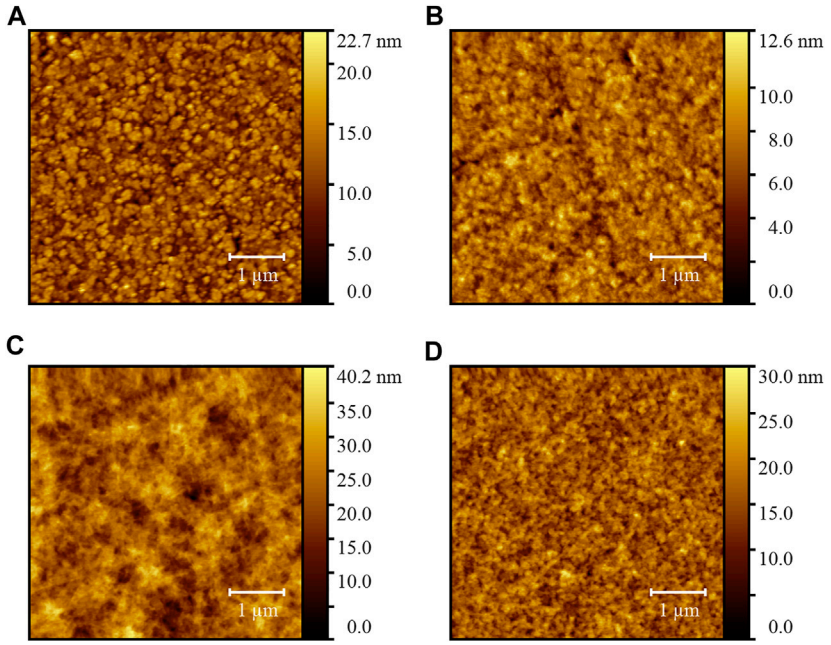

FIGURE 3 | (A) AFM height image of the SnO_2 ETL film. **(B)** AFM height image of the SnO_2/PDINO ETL film. **(C)** AFM height image of the PM6:Y6 blend film on the SnO_2 ETL. **(D)** AFM height image of the PM6:Y6 blend film on the SnO_2/PDINO ETL.

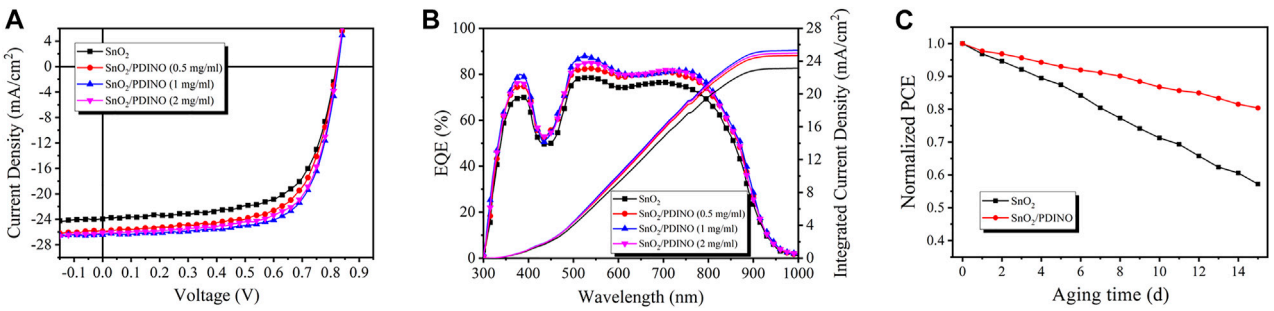

FIGURE 4 | (A) *J–V* curves of OSCs. **(B)** EQE spectra and JEQE curves of OSCs. **(C)** Normalized PCEs of OSCs after 15 days of aging. The devices were stored in the air at room temperature (~20°C) and without encapsulation.

SnO_2 NP aggregates. In order to further elucidate the effects of PDINO modification, the height images of the PM6:Y6 BHJ blend films fabricated atop different ETLs are presented in **Figures 3C,D**. From the images, the BHJ blend film on the SnO_2/PDINO ETL has achieved a more homogeneous surface morphology. The corresponding RMS value is 3.07 nm, which is much lower than that of the BHJ film on the pristine SnO_2 ETL (4.78 nm). Summing up the findings of AFM, it is suggested that the PDINO modification layer effectively reduced the surface defects of SnO_2 NPs. Moreover, as the surface morphology of the ETL plays a crucial role in the formation of the BHJ, the surface morphology of PM6:Y6 blend film is consequently improved after the PDINO modification (Peng et al., 2020).

To verify the effectiveness of PDINO as a SnO_2 ETL modifier, the PM6:Y6 OSCs were fabricated based on the SnO_2 ETL and SnO_2/PDINO ETLs, with the device structure shown in **Figure 1B**. The *J-V* curves are recorded and shown in **Figure 4A**. The performance metrics of the OSCs are summarized in **Table 1**. The unmodified device with pristine SnO_2 NPs as the ETL provides a PCE of 12.73%, with an open circuit voltage (V_{OC}) of 0.820 V, a J_{SC} of 23.95 mA/cm^2, and an FF of 64.82%. With the introduction of the PDINO modification layer, significant device performance improvements are observed. When PDINO concentration is 1 mg/ml, the champion device reaches its maximum PCE value of 14.97%, with an increased V_{OC} of 0.825 V, a J_{SC} of 26.40 mA/cm^2, and an FF of 68.70%. The enhanced parameters could be ascribable to the better qualities of the SnO_2/PDINO ETL film and preferable ETL/active layer interfacial contact. When the concentration of PDINO increases to 2 mg/ml, the denser PDINO layer may have an

TABLE 1 | Photovoltaic performance metrics of OSCs with pristine SnO_2 and different concentrations of PDINO-modified SnO_2 as ETLs. The average PCE (PCEavg) value was obtained form 20 devices fabricated in parallel.

ETL	V_{oc} (V)	J_{sc} (mA/cm^2)	FF (%)	PCE_{max} (%)	PCE_{avg} (%)	J_{EQE} (mA/cm)
SnO_2	0.820	23.95	64.82	12.73	12.59 ± 0.06	23.14
SnO_2/PDINO (0.5 mg/ml)	0.821	25.88	65.43	13.89	13.78 ± 0.11	24.68
SnO_2/PDINO (1 mg/ml)	0.825	26.40	68.70	14.97	14.73 ± 0.24	25.31
SnO_2/PDINO (2 mg/ml)	0.823	26.10	67.94	14.58	14.32 ± 0.16	24.97

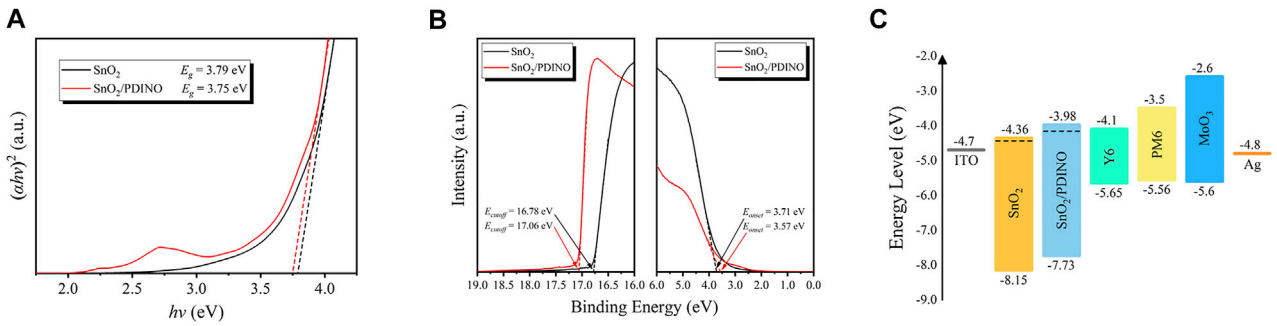

FIGURE 5 | (A) Tauc plots of SnO_2 and SnO_2/PDINO films. **(B)** UPS spectra of SnO_2 and SnO_2/PDINO. **(C)** Schematic diagram of energy levels of OSCs with different ETLs.

adverse effect on charge carrier transportation and further affect the transmittance of the ETL. Therefore, the device suffers from a moderate performance decrease, with a reduced PCE of 14.58%, a V_{OC} of 0.825 V, a J_{SC} of 26.10 mA/cm^2, and an FF of 67.49%.

The measurement of external quantum efficiency (EQE) was also carried out to illustrate the effects of the PDINO modification layer. The EQE spectra are presented in **Figure 4B**. Compared with the pristine SnO_2 ETL device, the EQE values of OSCs with SnO_2/PDINO ETLs notably increased throughout the 350–900 nm wavelength range. For the device with 1 mg/ml PDINO-modified ETL, the maximum EQE value exceeds 85% around the wavelength of 550 nm. The intensified EQE spectra can be ascribed to the combined effects of faster electron transportation and more favorable interfacial contact. From the EQE spectra, the integrated current density (J_{EQE}) curves are plotted in **Figure 4B**, and the J_{EQE} values are listed in **Table 1**. The trend of J_{EQE} makes a good match within less than 5% of the variation of the corresponding J_{SC}.

As an essential parameter for commercialization in the future, the ambient stability of OSCs was tested in the air at room temperature without encapsulation. From **Figure 4C**, after 15 days aging, the pristine SnO_2 NP ETL device exhibited unsatisfying stability, with its PCE dropping to less than 60% of the initial value. In contrast to the control device, the OSC with SnO_2/PDINO ETL successfully maintained up to 81% of its original PCE. It is suggested that by reducing the possible defects of the SnO_2 NP layer, the PDINO layer could strengthen the ETL's oxygen/water shielding effects, thus enhancing the stability of the SnO_2/PDINO ETL OSC.

To investigate the energy level of the SnO_2 NP ETL before and after PDINO modification, in **Figure 5A**, the optical bandgap (E_g) was first determined by Tauc plots derived from the UV–vis absorption spectra. The E_g of the pristine SnO_2 and SnO_2/PDINO are estimated to be 3.79 and 3.75 eV, respectively. The ultraviolet photoelectron spectroscopy (UPS) measurements were subsequently implemented to determine the binding energies of the cutoff region (E_{cutoff}) and onset region (E_{onset}), which are depicted in **Figure 5B**. With the incident photon energy value ($h\nu$) of 21.22 eV (He I), by subtracting the E_{cutoff} from $h\nu$, the WF is estimated to be 4.44 eV for pristine SnO_2 and 4.16 eV for SnO_2/PDINO. The valence band maximum (VBM) level can be calculated with **Eq. 2**:

$$\mathrm{VBM} = h\nu - \left(E_{cutoff} - E_{onset}\right). \tag{2}$$

For the pristine SnO_2 and SnO_2/PDINO, the VBM levels are 8.15 and 7.73 eV, respectively. Considering the E_g of different ETLs, the corresponding conduction band minimum (CBM) levels are 4.36 and 3.98 eV, respectively. From the analyses above, the energy level diagram for the OSC is plotted in **Figure 5C**. The reduced WF and energy level shifts of the modified ETL can benefit both electron extraction and charge collection abilities, contributing to significantly improved J_{SC}, FF, and the slightly increased V_{OC} as summarized in **Table 1** (Guang et al., 2021).

To conduct an in-depth investigation into the performance enhancements after applying the PDINO layer, the electron-only devices were fabricated and the space charge limited current (SCLC) approach was carried out. The corresponding device structure is ITO/ETLs/PM6:Y6/bathophenanthroline/Ag. The *J-V* characteristics are shown in **Figure 6A**. Following the Mott–Gurney law, it can be calculated that the electron

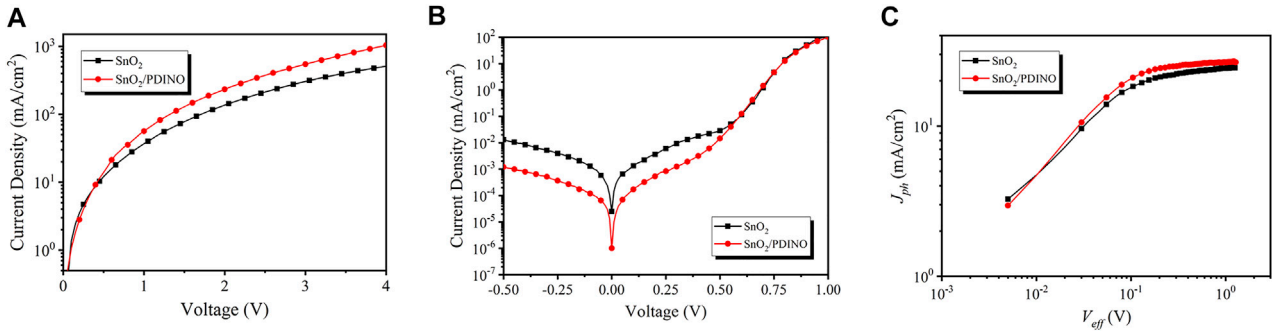

FIGURE 6 | (A) *J–V* curves of electron-only devices. **(B)** *J–V* curves of OSC devices in dark condition. **(C)** Plots of photocurrent (J_{ph}) dependence on effective voltage (V_{eff}).

mobility of devices with the pristine SnO_2 ETL is 1.14×10^{-4} cm^2/Vs. The electron mobility of the modified device notably increases to 1.92×10^{-4} cm^2/Vs after the introduction of PDINO, indicating that the electron transporting ability of the ETL can be improved effectively. The *J-V* curves in the dark condition of OSCs with SnO_2 and SnO_2/PDINO ETLs are displayed in **Figure 6B**. In the applied voltage range of −0.5–0 V, restrained reverse leakage currents were obtained for the SnO_2/PDINO ETL device, which suggested that the PDINO modification layer could suppress the charge carrier recombination. From the dark *J-V* characterization, the photocurrent (J_{ph}) dependence on the effective voltage (V_{eff}) is plotted in **Figure 6C**. J_{ph} is set as $J_{ph} = J_{light} - J_{dark}$, where J_{light} is the illuminated device current density with the irradiance of 100 mW/cm2 and J_{dark} is the current density in the no-light condition. V_{eff} is defined by $V_{eff} = V_0 - V$, where V_0 refers to the compensative voltage where $J_{ph}(V_0) = 0$, and V is the bias voltage. At a large reverse bias voltage, the saturation current density (J_{sat}) will nearly no longer increase and reach a maximum value. The J_{sat} for SnO_2 and SnO_2/PDINO ETL devices are determined with the values being 24.52 and 26.91 mA/cm^2, respectively, where V_{eff} = 1.2 V. The charge collection probability [P(E,T)] can be derived from **Eq. 3** (Kyaw et al., 2013):

$$P(E,T) = \frac{J_{ph}}{J_{sat}}. \tag{3}$$

At the short-circuit ($J_{ph} = J_{SC}$) and the maximum power output ($J_{ph} = J$ (V_{eff} = 0.2 V)) conditions, the P (E,T)s were 0.977/0.857 and 0.981/0.899 for the SnO_2 ETL and SnO_2/PDINO-based devices, respectively. The larger P (E,T) suggests that PDINO modification can promote exciton dissociation and charge extraction of the devices, which is the main responsibility for achieving higher J_{SC} and FF.

Alongside exciton dissociation and charge extraction, the charge recombination behavior also has considerable impacts on the device performance. Therefore, the *J-V* characterizations under different incident light intensities (P_{in}) were performed. The dependence of V_{OC} on the P_{in} in OSCs with and without PDINO-modified ETLs can be deduced from **Eq. 4** (Cowan et al., 2010):

$$V_{OC} \propto n\frac{kT}{q}\ln(P_{in}). \tag{4}$$

The plot of V_{OC} vs. logarithmic P_{in} is displayed in **Figure 7A**. nkT/q is the fitting line slope. k is the Boltzmann constant, T is the thermodynamic temperature, and q is the elementary charge. When the value of n draws closer to 1, it indicates that bimolecular recombination is the dominant recombination process. If the value of n approaches 2, the trap-assisted recombination will govern the recombination mechanism. The pristine SnO_2 ETL device possesses a slope of 1.485 kT/q, suggesting the existence of trap-assisted recombination. After utilizing the PDINO modification layer, the trap-assisted recombination is restricted as the slope of the modified OSC reduces to 1.346 kT/q, which distinctly indicates the optimization of surface defects for the SnO_2 NP ETL (Wu et al., 2019; Yang et al., 2021). To further analyze the bimolecular recombination, the dependence of J_{SC} on the P_{in} was evaluated from **Eq. 5** (Khlyabich et al., 2012):

$$J_{SC} \propto P_{in}^{\alpha}, \tag{5}$$

where α is an exponential factor acquired from the fitting line slope of the J_{SC}–P_{in} double logarithmic plot. Generally, an α value closer to one suggests that there is weaker bimolecular recombination in the OSC. Depicted in **Figure 7B**, the α value of the OSC using the pristine SnO_2 ETL is 0.960, while the SnO_2/PDINO ETL device shows a higher α value of 0.984. The result indicates that the bimolecular recombination of the OSC is remarkably suppressed by PDINO; the increased device FF is explained as well.

Moreover, impedance spectroscopy measurement was implemented to study the electrical contact properties of the OSCs (Tiwana et al., 2011). The Nyquist plots are displayed in **Figure 7C**. In the equivalent circuit of the transmission line model, R_1, R_2, and R_3 correspond to the device series resistance, interfacial resistance, and recombination resistance, respectively (Yang et al., 2017). Derived from the Nyquist plots, the resistance metrics are listed in **Table 2**. The R_1 values of the OSCs based on different ETLs are comparable. For SnO_2/PDINO ETL–based devices, R_2 is smaller than half of the value of a pristine ETL-based device, which suggests the improved charge transportation ability

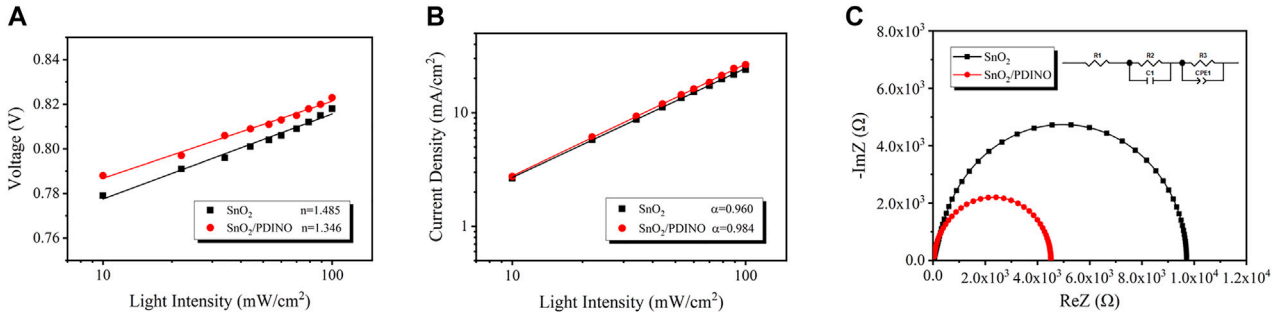

FIGURE 7 | (A) V_{OC} dependence on incident light intensity of the OSCs. **(B)** J_{SC} dependence on incident light intensity of the OSCs. **(C)** Impedance spectra of the OSCs. An inset of the transmission line model equivalent circuit is in the upper right corner.

TABLE 2 | Resistance metrics of the equivalent circuit for OSCs based on different ETLs.

ETL	R_1 (Ω)	R_2 (KΩ)	R_3 (Ω)
SnO_2	48.1	9.4	218.5
SnO_2/PDINO	48.2	4.3	118.7

in the active layer/ETL interface. Meanwhile, given credit to the optimization of PM6:Y6 morphology, the decreased value of R_3 indicates that the charge recombination is effectively suppressed for the active layer deposited upon the SnO_2/PDINO ETL. Conclusively, these above merits lead to improved J_{SC} and FF, which eventually enhance the PCE of the OSC.

CONCLUSION

In conclusion, a facile SnO_2 NP ETL modification strategy by utilizing PDINO has been successfully implemented. The introduction of PDINO as a modifier could reduce the surface defects generated by the solution-based fabricating process of the SnO_2 NP ETL and simultaneously regulate the formation of the active layer's morphology. For the devices based on the PDINO-modified SnO_2 NP ETL, the optimized exciton dissociation, enhanced charge collection efficiency, and suppressed molecular recombination synergistically boost the device performance. With enhanced device stability, the corresponding OSCs exhibit a maximum PCE approaching 14.9%, which improved by 17% from the pristine SnO_2 devices (12.9%). Overall, this work reveals a promising pathway to modify the SnO_2 NP ETL for achieving high-efficiency and stable OSCs.

DATA AVAILABILITY STATEMENT

The original contributions presented in the study are included in the article/Supplementary Material; further inquiries can be directed to the corresponding authors.

AUTHOR CONTRIBUTIONS

TK conceived the idea and wrote the paper. TK, RW, and DZ fabricated and characterized the OSCs. DZ and JY directed and supervised the project. All authors contributed to the article and approved the submitted version.

FUNDING

This work was financially supported by the Foundation of National Natural Science Foundation of China (NSFC) (Grant nos. 61421002, 61675041, and 51703019) and Sichuan Science and Technology Program (Grant nos. 2019YFG0121, 2019YJ0178, 2020YFG0279, and 2020YFG0281). This work was also sponsored by the Sichuan Provincial Key Laboratory of Display Science and Technology.

REFERENCES

Abd-Ellah, M., Cann, J., Dayneko, S. V., Laventure, A., Cieplechowicz, E., and Welch, G. C. (2019). Interfacial ZnO Modification Using a Carboxylic Acid Functionalized N-Annulated Perylene Diimide for Inverted Type Organic Photovoltaics. *ACS Appl. Electron. Mater.* 1 (8), 1590–1596. doi:10.1021/acsaelm.9b00328

Cowan, S. R., Roy, A., and Heeger, A. J. (2010). Recombination in Polymer-Fullerene Bulk Heterojunction Solar Cells. *Phys. Rev. B* 82 (24). doi:10.1103/PhysRevB.82.245207

Fan, P., Zhang, D., Wu, Y., Yu, J., and Russell, T. P. (2020). Polymer-Modified ZnO Nanoparticles as Electron Transport Layer for Polymer-Based Solar Cells. *Adv. Funct. Mater.* 30 (32), 2002932. doi:10.1002/adfm.202002932

Gollu, S. R., Sharma, R., Srinivas, G., Kundu, S., and Gupta, D. (2016). Incorporation of Silver and Gold Nanostructures for Performance Improvement in P3HT: PCBM Inverted Solar Cell with rGO/ZnO Nanocomposite as an Electron Transport Layer. *Org. Electronics* 29, 79–87. doi:10.1016/j.orgel.2015.11.015

Guang, S., Yu, J., Wang, H., Liu, X., Qu, S., Zhu, R., et al. (2021). A Low Temperature Processable Tin Oxide Interlayer via Amine-Modification for

Efficient and Stable Organic Solar Cells. *J. Energ. Chem.* 56, 496–503. doi:10.1016/j.jechem.2020.08.036

Hou, J., Inganäs, O., Friend, R. H., and Gao, F. (2018). Organic Solar Cells Based on Non-fullerene Acceptors. *Nat. Mater.* 17 (2), 119–128. doi:10.1038/nmat5063

Hsieh, C.-H., Cheng, Y.-J., Li, P.-J., Chen, C.-H., Dubosc, M., Liang, R.-M., et al. (2010). Highly Efficient and Stable Inverted Polymer Solar Cells Integrated with a Cross-Linked Fullerene Material as an Interlayer. *J. Am. Chem. Soc.* 132 (13), 4887–4893. doi:10.1021/ja100236b

Jiang, Q., Zhang, L., Wang, H., Yang, X., Meng, J., Liu, H., et al. (2017). Enhanced Electron Extraction Using SnO2 for High-Efficiency Planar-Structure HC(NH2)2PbI3-based Perovskite Solar Cells. *Nat. Energ.* 2 (1), 1–7. doi:10.1038/nenergy.2016.177

Jiang, Y., Sun, L., Jiang, F., Xie, C., Hu, L., Dong, X., et al. (2019). Photocatalytic Effect of ZnO on the Stability of Nonfullerene Acceptors and its Mitigation by SnO2 for Nonfullerene Organic Solar Cells. *Mater. Horiz.* 6 (7), 1438–1443. doi:10.1039/c9mh00379g

Khlyabich, P. P., Burkhart, B., and Thompson, B. C. (2012). Compositional Dependence of the Open-Circuit Voltage in Ternary Blend Bulk Heterojunction Solar Cells Based on Two Donor Polymers. *J. Am. Chem. Soc.* 134 (22), 9074–9077. doi:10.1021/ja302935n

Kim, K., Suh, M., Choi, J., Lee, D., Kim, Y., Cheong, S. H., et al. (2015). Conjugated Polyelectrolyte Hybridized ZnO Nanoparticles as a Cathode Interfacial Layer for Efficient Polymer Light-Emitting Diodes. *Adv. Funct. Mater.* 25 (48), 7450–7456. doi:10.1002/adfm.201502360

Kyaw, A. K. K., Sun, X. W., Jiang, C. Y., Lo, G. Q., Zhao, D. W., and Kwong, D. L. (2008). An Inverted Organic Solar Cell Employing a Sol-Gel Derived ZnO Electron Selective Layer and thermal Evaporated MoO3 Hole Selective Layer. *Appl. Phys. Lett.* 93 (22), 221107. doi:10.1063/1.3039076

Kyaw, A. K. K., Wang, D. H., Gupta, V., Leong, W. L., Ke, L., Bazan, G. C., et al. (2013). Intensity Dependence of Current-Voltage Characteristics and Recombination in High-Efficiency Solution-Processed Small-Molecule Solar Cells. *Acs Nano* 7 (5), 4569–4577. doi:10.1021/nn401267s

Li, G., Zhu, R., and Yang, Y. (2012). Polymer Solar Cells. *Nat. Photon* 6 (3), 153–161. doi:10.1038/nphoton.2012.11

Li, S.-S., Tu, K.-H., Lin, C.-C., Chen, C.-W., and Chhowalla, M. (2010). Solution-Processable Graphene Oxide as an Efficient Hole Transport Layer in Polymer Solar Cells. *Acs Nano* 4 (6), 3169–3174. doi:10.1021/nn100551j

Liang, Y., Xu, Z., Xia, J., Tsai, S. T., Wu, Y., Li, G., et al. (2010). For the Bright Future-Bulk Heterojunction Polymer Solar Cells with Power Conversion Efficiency of 7.4%. *Adv. Mater.* 22 (20), E135–E138. doi:10.1002/adma.200903528

Lin, Z., Chang, J., Zhang, C., Zhang, J., Wu, J., and Hao, Y. (2016). Low Temperature Aqueous Solution-Processed Li Doped ZnO Buffer Layers for High Performance Inverted Organic Solar Cells. *J. Mater. Chem. C* 4 (25), 6169–6175. doi:10.1039/c6tc00760k

Ling, M.-M., Erk, P., Gomez, M., Koenemann, M., Locklin, J., and Bao, Z. (2007). Air-stable N-Channel Organic Semiconductors Based on Perylene Diimide Derivatives without strong Electron Withdrawing Groups. *Adv. Mater.* 19 (8), 1123–1127. doi:10.1002/adma.200601705

Ma, H., Yip, H.-L., Huang, F., and Jen, A. K.-Y. (2010). Interface Engineering for Organic Electronics. *Adv. Funct. Mater.* 20 (9), 1371–1388. doi:10.1002/adfm.200902236

Peng, R., Yan, T., Chen, J., Yang, S., Ge, Z., and Wang, M. (2020). Passivating Surface Defects of N -SnO 2 Electron Transporting Layer by InP/ZnS Quantum Dots: Toward Efficient and Stable Organic Solar Cells. *Adv. Electron. Mater.* 6 (3), 1901245. doi:10.1002/aelm.201901245

Snaith, H. J., and Ducati, C. (2010). SnO2-Based Dye-Sensitized Hybrid Solar Cells Exhibiting Near Unity Absorbed Photon-To-Electron Conversion Efficiency. *Nano Lett.* 10 (4), 1259–1265. doi:10.1021/nl903809r

Song, C. E., Ryu, K. Y., Hong, S.-J., Bathula, C., Lee, S. K., Shin, W. S., et al. (2013). Enhanced Performance in Inverted Polymer Solar Cells with D-π-A-type Molecular Dye Incorporated on ZnO Buffer Layer. *Chemsuschem* 6 (8), 1445–1454. doi:10.1002/cssc.201300240

Thompson, B. C., and Fréchet, J. M. J. (2008). Polymer-Fullerene Composite Solar Cells. *Angew. Chem. Int. Ed.* 47 (1), 58–77. doi:10.1002/anie.200702506

Tiwana, P., Docampo, P., Johnston, M. B., Snaith, H. J., and Herz, L. M. (2011). Electron Mobility and Injection Dynamics in Mesoporous ZnO, SnO2, and TiO2 Films Used in Dye-Sensitized Solar Cells. *Acs Nano* 5 (6), 5158–5166. doi:10.1021/nn201243y

Wang, H., Chen, L., and Xiao, Y. (2017). Perylene Diimide Arrays: Promising Candidates for Non-fullerene Organic Solar Cells. *J. Mater. Chem. C* 5 (48), 12816–12824. doi:10.1039/c7tc04726f

Wang, H., Wang, X., Fan, P., Yang, X., and Yu, J. (2015). Enhanced Power Conversion Efficiency of P3HT : PC71BM Bulk Heterojunction Polymer Solar Cells by Doping a High-Mobility Small Organic Molecule. *Int. J. Photoenergy* 2015, 1–8. doi:10.1155/2015/982064

Wang, Z., Peng, Z., Xiao, Z., Seyitliyev, D., Gundogdu, K., Ding, L., et al. (2020). Thermodynamic Properties and Molecular Packing Explain Performance and Processing Procedures of Three D18:NFA Organic Solar Cells. *Adv. Mater.* 32 (49), 2005386. doi:10.1002/adma.202005386

White, M. S., Olson, D. C., Shaheen, S. E., Kopidakis, N., and Ginley, D. S. (2006). Inverted Bulk-Heterojunction Organic Photovoltaic Device Using a Solution-Derived ZnO Underlayer. *Appl. Phys. Lett.* 89 (14), 143517. doi:10.1063/1.2359579

Wu, Z., Yu, H., Shi, S., and Li, Y. (2019). Bismuth Oxysulfide Modified ZnO Nanorod Arrays as an Efficient Electron Transport Layer for Inverted Polymer Solar Cells. *J. Mater. Chem. A.* 7 (24), 14776–14789. doi:10.1039/c9ta02447f

Yang, L., Wang, J., Lu, X., Lin, H., Du, X., Chen, Z., et al. (2021). Morphology Optimization of Organic Solar Cells Enabled by Interface Engineering of Zinc Oxide Layer with a Conjugated Organic Material. *Org. Electronics* 91, 106065. doi:10.1016/j.orgel.2021.106065

Yang, L., Yan, Y., Cai, F., Li, J., and Wang, T. (2017). Poly(9-vinylcarbazole) as a Hole Transport Material for Efficient and Stable Inverted Planar Heterojunction Perovskite Solar Cells. *Solar Energ. Mater. Solar Cell* 163, 210–217. doi:10.1016/j.solmat.2017.01.040

Yin, Z., Wei, J., and Zheng, Q. (2016). Interfacial Materials for Organic Solar Cells: Recent Advances and Perspectives. *Adv. Sci.* 3 (8), 1500362. doi:10.1002/advs.201500362

Yip, H.-L., and Jen, A. K.-Y. (2012). Recent Advances in Solution-Processed Interfacial Materials for Efficient and Stable Polymer Solar Cells. *Energy Environ. Sci.* 5 (3), 5994–6011. doi:10.1039/c2ee02806a

Yu, J., Xi, Y., Chueh, C.-C., Zhao, D., Lin, F., Pozzo, L. D., et al. (2016). A Room-Temperature Processable PDI-Based Electron-Transporting Layer for Enhanced Performance in PDI-Based Non-fullerene Solar Cells. *Adv. Mater. Inter.* 3 (18), 1600476. doi:10.1002/admi.201600476

Yuan, J., Zhang, Y., Zhou, L., Zhang, G., Yip, H.-L., Lau, T.-K., et al. (2019). Single-Junction Organic Solar Cell with over 15% Efficiency Using Fused-Ring Acceptor with Electron-Deficient Core. *Joule* 3 (4), 1140–1151. doi:10.1016/j.joule.2019.01.004

Zeng, X., Zhou, T., Leng, C., Zang, Z., Wang, M., Hu, W., et al. (2017). Performance Improvement of Perovskite Solar Cells by Employing a CdSe Quantum Dot/PCBM Composite as an Electron Transport Layer. *J. Mater. Chem. A.* 5 (33), 17499–17505. doi:10.1039/c7ta00203c

Zhang, X., Fan, P., Han, Y., and Yu, J. (2019). Effect of Crystallinity Modulation between Electron Transport Layer and Photo-Generation Materials on ZnO-Based Polymer Solar Cells. *Energy Technol.* 7 (2), 263–268. doi:10.1002/ente.201800666

Zhang, Z.-G., Qi, B., Jin, Z., Chi, D., Qi, Z., Li, Y., et al. (2014). Perylene Diimides: a Thickness-Insensitive Cathode Interlayer for High Performance Polymer Solar Cells. *Energ. Environ. Sci.* 7 (6), 1966–1973. doi:10.1039/c4ee00022f

Zheng, D., Wang, G., Huang, W., Wang, B., Ke, W., Logsdon, J. L., et al. (2019). Combustion Synthesized Zinc Oxide Electron-Transport Layers for Efficient and Stable Perovskite Solar Cells. *Adv. Funct. Mater.* 29 (16), 1900265. doi:10.1002/adfm.201900265

Conflict of Interest: The authors declare that the research was conducted in the absence of any commercial or financial relationships that could be construed as a potential conflict of interest.

frontiers in Chemistry

MINI REVIEW
published: 09 July 2021
doi: 10.3389/fchem.2021.724188

Gold Nanomaterials and Bone/Cartilage Tissue Engineering: Biomedical Applications and Molecular Mechanisms

Yifeng Shi[1,2,3†], Xuyao Han[3†], Shuang Pan[2], Yuhao Wu[3], Yuhan Jiang[3], Jinghao Lin[3], Yihuang Chen[2*] and Haiming Jin[1,3*]*

[1]Department of Orthopaedics, The Second Affiliated Hospital and Yuying Children's Hospital of Wenzhou Medical University, Wenzhou, China, [2]College of Chemistry and Materials Engineering, Wenzhou University, Wenzhou, China, [3]The Second School of Medicine, Wenzhou Medical University, Wenzhou, China

OPEN ACCESS

Edited by:
Qifan Xue,
South China University of Technology, China

Reviewed by:
Dezhi Song,
Guangxi Medical University, China
Yuhao Liu,
Guangzhou University of Chinese Medicine, China

***Correspondence:**
Shuang Pan
shuangpan@wzu.edu.cn
Yihuang Chen
yhchen@wzu.edu.cn
Haiming Jin
kkjinhaiming@126.com

[†]These authors have contributed equally to this work and shared first authorship

Specialty section:
This article was submitted to Nanoscience, a section of the journal Frontiers in Chemistry

Received: 12 June 2021
Accepted: 28 June 2021
Published: 09 July 2021

Citation:
Shi Y, Han X, Pan S, Wu Y, Jiang Y, Lin J, Chen Y and Jin H (2021) Gold Nanomaterials and Bone/Cartilage Tissue Engineering: Biomedical Applications and Molecular Mechanisms. Front. Chem. 9:724188. doi: 10.3389/fchem.2021.724188

Recently, as our population increasingly ages with more pressure on bone and cartilage diseases, bone/cartilage tissue engineering (TE) have emerged as a potential alternative therapeutic technique accompanied by the rapid development of materials science and engineering. The key part to fulfill the goal of reconstructing impaired or damaged tissues lies in the rational design and synthesis of therapeutic agents in TE. Gold nanomaterials, especially gold nanoparticles (AuNPs), have shown the fascinating feasibility to treat a wide variety of diseases due to their excellent characteristics such as easy synthesis, controllable size, specific surface plasmon resonance and superior biocompatibility. Therefore, the comprehensive applications of gold nanomaterials in bone and cartilage TE have attracted enormous attention. This review will focus on the biomedical applications and molecular mechanism of gold nanomaterials in bone and cartilage TE. In addition, the types and cellular uptake process of gold nanomaterials are highlighted. Finally, the current challenges and future directions are indicated.

Keywords: gold nanomaterials, bone/cartilage, tissue engineering, molecular mechanism, uptake

INTRODUCTION

Bone and cartilage play a vital role in providing mechanical support, mobility and weight bearing for the body. At present, millions of patients are suffering from bone and cartilage degeneration and diseases, such as fractures, osteoporosis, low back pain and osteoarthritis (Zhang and Jordan, 2010; Agarwal and Garcia, 2015). Bone and cartilage-related medical treatments and costs are rising with the increase in life expectancy of the population. Therefore, tissue engineering (TE) is gradually considered a potential alternative therapeutic technique that could provide regeneration platform for bone and cartilage tissue loss or damage.

Commonly, TE involves the proliferation, stimulation, differentiation, and guidance of cells with the goal of reconstructing impaired or damaged tissues. There are three critical factors in a successful tissue regeneration: cells, scaffolds, and signaling mediators (e.g., growth factors) (Li H. et al., 2020). The repair of bone and cartilage tissue is a complicated event involving cells, signal molecules and suitable scaffolds to prepare new tissue in special environment (Keeney et al., 2011). Furthermore, the rapid development of materials science and engineering has promoted the progress of alternative medical methods for bone and cartilage diseases. Bone and cartilage TE along with modern

nanomaterials science has made a significant contribution to health care and will expand further with the increasing elderly population.

Nanomaterials are tiny particles with size distribution less than 100 nm. In the last decades, various types of nanomaterials have attracted the attention of many researchers in photocatalysis (Pan et al., 2021), electrocatalysis (Zhang et al., 2021a), photoelectrocatalysis (Hu et al., 2020; Zhao et al., 2020; Huang et al., 2021), solar utilization (Jiang et al., 2020), heat management (Zhang et al., 2021b) and other fields because of their unique properties (Wang et al., 2019; He et al., 2020). Among the numerous materials, Au represents one well-studied type (Xu et al., 2016) with tunable shape (Zhu et al., 2015), structure (Ma et al., 2015), and composition (Jiang et al., 2017). For gold nanomaterials, AuNPs, as well as nanoclusters (AuNCs), nanocages, nanorods (AuNRs), nanobelts, nanoplates and so on, are becoming increasingly popular because of their optical nonlinearities (Gao et al., 2015; Huang et al., 2017; Zhang et al., 2018), local surface plasmon resonance (SPR) (Li Q. et al., 2017) and photothermal effect (Jiang et al., 2012). Considering these characteristics, it has been proved that gold nanomaterials can be used in many fields such as chemistry, biomedicine, including the diagnosis and treatment of diseases (Li et al., 2018b), sensor (Li et al., 2015), catalysis (Li et al., 2013), surface-enhanced Raman spectroscopy (Huang et al., 2019), illumination (Zhang et al., 2017b), detector (Du et al., 2018), and therapy (Yeh et al., 2012). The easy of synthesis and the unique properties of gold nanomaterials make them ideal candidates for translation from the laboratory scale into the clinical arena for use in humans.

In recent years, plenty of researchers have reported that various gold nanomaterials could regulate the cell differentiation, maintain tissue stability and promote tissue regeneration in bone and cartilage. The present review focused on the biomedical applications and molecular mechanisms of gold nanomaterials in bone and cartilage TE. We described various kinds of gold nanomaterials and their cellular uptake process, followed by discussion on biomedical applications and molecular mechanisms of gold nanomaterials in bone and cartilage TE. The future work and perspective were also provided.

TYPES OF GOLD NANOMATERIALS

The properties of gold nanomaterials depend sensitively on their size, shape, dimensionality and other properties. The types of gold nanomaterials can be classified according to these properties. Therefore, based on the dimensions of gold nanomaterials, they can be divided into several groups: zero-dimensional (0D), one-dimensional (1D), two-dimensional (2D), and three-dimensional (3D). Gold nanomaterials also can be sorted into various shapes such as gold nanospheres, nanocages, nanorods, nanobelts, nanosheets and so on (Dreaden et al., 2012; Dykman and Khlebtsov, 2012).

AuNPs, mostly referring to spherical gold nanomaterial, represent one type of 0D nanostructure materials possessing unique electrical, magnetic, optical and catalytic properties. AuNPs are widely used in medicine because of their excellent biocompatibility, low toxicity chemical stability and SPR detectability. They are easy to be surface-functionalized, and can be used more widely because of the ability to modify drugs, proteins, peptides and DNA (Mandal et al., 2011). Nanoparticles can easily penetrate the cell membrane and locate in the cytoplasm, thus affecting some cell signal pathways that induce differentiation (Li J. et al., 2017). It has been reported that when thiolated polyethylene glycol was coupled with AuNPs, AuNPs were able to be prevented from being attacked by the intravascular immune system, thus providing a biological basis for their use as drug carriers (Boisselier and Astruc, 2009). Recent studies have shown that AuNPs were closely related to bone and cartilage TE, especially in osteoblasts, osteoclasts, chondrocytes and bone marrow mesenchymal stem cells (BMSCs). Besides AuNPs in 0D nanomaterials, AuNCs and gold nanocages are also usually used in bone and cartilage TE due to their good stability, biocompatibility and two-photon absorption (Ramakrishna et al., 2008; Shiang et al., 2012).

In addition to 0D nanomaterials, AuNRs are an important 1D nanomaterials, that have plasma characteristics, unique optical properties, photoluminescence (Huang et al., 2009). 2D gold nanomaterials mainly include gold nanosheets, gold nanoplates and so on. For gold nanosheets, with thicknesses of single to few atomic layers, they have unique mechanical, electronic, and surface-related properties, which hold good application potential in the fields of photosensitive imaging, biological detection, catalysis and so on (Ye et al., 2019). However, compared to 0D nanomaterials especially AuNPs, the application of 1D and 2D gold nanomaterials in bone and cartilage TE deserves further study.

CELLULAR UPTAKE PROCESS OF GOLD NANOMATERIALS

It is known that gold nanomaterials need to perform their biological function by penetrating the cell membrane. Several uptake mechanisms were proposed and studied for gold nanomaterials. Cellular uptake ways of AuNPs are influenced by many factors, including shape, surface chemistry, functionalization and especially size (Chithrani et al., 2006). Li et al. (Li et al., 2016) suggested that AuNPs were taken in by human mesenchymal stem cells (hMSCs) in a size and shape-dependent manner. And AuNPs can enter into cells by various pathways such as phagocytosis, macropinocytosis, endocytosis and transcellular pathways (Zhao et al., 2011). In bone and cartilage TE, gold nanomaterials enter into cell mostly through endocytosis or transcellular pathway (**Table 1**). From the table, it could be inferred that endocytosis plays the most important role in bone and cartilage-related cellular uptake process of gold nanomaterials with or without functionalization. This effective uptake process keeps cell membrane intact and makes gold nanomaterials play a relatively stable function. Besides, gold nanomaterials are also able to play a role *via* binding to the membrane protein. In consideration of the toxicity and more secure applications, it is necessary to explore the cellular uptake mechanism of gold nanomaterials or the effect mechanism of extracellular gold nanomaterials in further related research.

TABLE 1 | The main cellular uptake processes of gold nanomaterials in bone and cartilage tissue engineering.

Uptake pathways	Au nanomaterials used	TEM size (DLS size)	Cell or tissue used	Function	References
Direct diffusion	Chitosan-conjugated AuNPs	17 nm (40 nm)	hADMSCs	Osteogenic differentiation	Choi et al. (2015)
Endocytosis	AuNPs-loaded hydroxyapatite nanocomposites	4.7 ± 0.7 nm	hMSCs	Osteogenic differentiation	Liang et al. (2019)
Vesicles (endocytosis presumed)	AuNPs	(5, 13, 45 nm)	hPDLPs	Osteogenic differentiation	Zhang et al. (2017a)
Endocytosis	SPIO-Au core-shell NPs	17.3 ± 1.2 nm	Preosteoblast MC3T3-E1 cells	Osteogenic differentiation	Yuan et al. (2017)
Endocytosis	AuNPs	20 nm (20 ± 2 nm)	Mice MSCs	Osteogenic differentiation	Yi et al. (2010)
Endocytosis	AuNPs, bisphosphonate-conjugated AuNPs	20–40 nm (20–49 nm)	BMMs	Inhibition of osteoclast differentiation	Lee et al. (2016)
Endocytosis/activating integrin pathway	AuNPs	20, 40 nm	Primary osteoblasts	Osteogenic differentiation	Zhang et al. (2014)
Endocytosis	Epigallocatechin gallate-functionalized AuNPs	30 nm (35.6 nm)	BMMs	Anti-osteoclastogenesis	Zhu et al. (2019)
Endocytosis	AuNPs, vitamin D-conjugated AuNPs	30–40 nm (36.5 ± 1.1, 60.8 ± 0.3 nm)	hADMSCs	Osteogenic differentiation	Nah et al. (2019)
Endocytosis (author presumed)	Gold nanosphere, nanostar, nanorod	40, 70, 110 nm	hMSCs	Osteogenesis	Li et al. (2016)
Vesicles (endocytosis presumed)	Human β-defensin 3-combined AuNPs	45 nm	hPDLCs	Osteogenic differentiation	Zhou et al. (2018)
Endocytosis	AuNPs	58.71 ± 22.33 nm	hPDLSC	Cell proliferation	Li et al. (2018a)
Endocytosis	AuNPs	13, 50 nm	Joints tissues	Antioxidants for collagen-induced arthritis	Kirdaite et al. (2019)
Endocytosis	Arginine-glycine-aspartate–modified AuNPs	39.4–41.9 nm (55.9–65.4 nm)	hMSCs	Chondrogenic differentiation	Li et al. (2017a)

BMMs, bone marrow-derived macrophages; DLS size, the size of nanomaterials in hydrodynamic form by dynamic light scattering; hADMSCs: human adipose-derived mesenchymal stem cells; hMSCs, human marrow mesenchymal stem cells; hPDLCs, human periodontal ligament cells; hPDLPCs, human periodontal ligament progenitor cells; hPDLSCs, human periodontal ligament stem cell; TEM size, the size of nanomaterials in dried form by transmission electron microscopy.

EFFECT AND MECHANISM OF GOLD NANOMATERIALS IN BONE AND CARTILAGE TISSUE ENGINEERING

Promotion and Regulation of the Differentiation

Bone marrow mesenchymal stem cells (BMSCs) are a heterogeneous population with high replication ability. They are pluripotent stem cells which can differentiate into osteoblasts and chondroblasts and then differentiate into bone or cartilage tissue. As mentioned above, BMSCs, one of three main factors, play a critical role in TE. The proliferation and differentiation of BMSCs can be considered as independent programmable processes, and controlling these processes in a predictable manner is crucial to regeneration of the desired tissue type. It has been reported that gold nanomaterials, mainly AuNPs, promoted osteogenic and chondrogenic differentiation through their effects on BMSCs (Yi et al., 2010; Sansanaphongpricha et al., 2020). The molecular mechanism mainly involved mitogen-activated protein kinase (MAPK), Wnt/β-catenin, and autophagy.

Regulation of Mitogen-Activated Protein Kinase Pathway

There are three parallel pathways of MAPK, including extracellular signal related kinases (ERK1/2), protein kinase 38 (p38), and c-Jun-N-terminal kinases (JNKs) pathways. ERK1/2 are generally referred to as growth factor-related kinases while p38 and JNK are often described as stress-activated protein kinases (SAPK2/p38 and SAPK1/JNK). Studies have indicated that MAPK pathway was involved in the proliferation and differentiation of osteoblasts (Greenblatt et al., 2013).

Extracellular Signal Related Kinases/Mitogen-Activated Protein Kinase Pathway

Among the three pathways, ERK/MAPK pathway is essential for cell growth and differentiation, which is also necessary for osteoblast adhesion, migration and integrin expression. In bone formation, ERK/MAPK pathway can transmit extracellular environmental information into the nucleus, which produces nuclear response to various of signals such as the stimulation of extracellular growth factors, extracellular matrix (ECM) or mechanical load (Ge et al., 2007).

In the study of Zhang el al (Zhang et al., 2014), extracellular AuNPs can activate integrin of primary osteoblasts in answer to the chemical or physical changes in ECM and convert them into intracellular signals for mediating cell behavior. In detail, integrin then activated focal adhesion kinase (FAK) and ERK phosphorylation was enhanced in later, which finally activated ERK/MAPK pathway. Meanwhile, AuNPs also could enter cells via receptor-mediated endocytosis and directly or indirectly activate ERK/MAPK pathway (**Figure 1A**). Runt-related transcription factor-2 (Runx-2) was an vital mediator of MAPK reaction and previous studies indicated Runx-2 was a

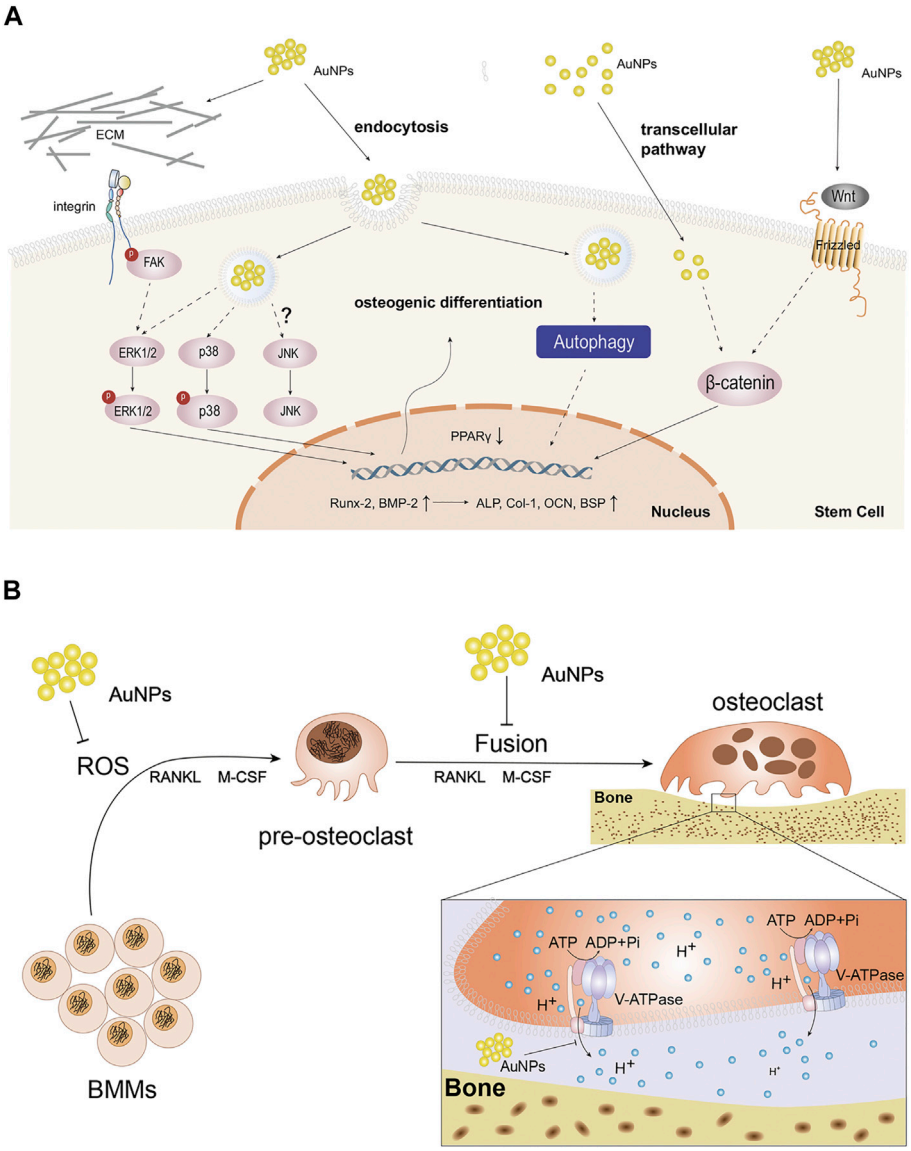

FIGURE 1 | The function and molecular mechanism of AuNPs in cells. **(A)** Schematic diagram of the possible molecular pathways affected by the osteogenic effects of AuNPs. AuNPs activate integrin and Wnt signaling pathway extracellularly or enter cells through endocytosis and transcelluar pathway. AuNPs up-regulate Runx-2, BMP-2, ALP, Col-1, OCN, BSP and reduce PPARγ to enhance osteogenic differentiation via ERK/MAPK, P38/MAPK, Wnt/β-catenin signaling pathways and autophagy in osteogenesis-related cells. JNK/MAPK signaling pathway has been not reported so far. **(B)** Schematic representation of AuNPs disturbing the formation and function of osteoclasts. AuNPs inhibit ROS in BMMs, the fusion of pre-osteoclast cells or the function of V-ATPase in osteoclasts.

key transcription factor regulating the differentiation of BMSCs into osteoblasts due to the function directly regulating the expression of other osteoblastic specific genes including osteocalcin (OCN) and collagen type1 (Col-1), etc (Franceschi et al., 2003). Meanwhile, bone morphogenetic protein-2 (BMP-2) took most responsibility for osteoblasts differentiation (Mahmood et al., 2011) and could enhance the function of Runx-2. In a word, AuNPs activated ERK/MAPK pathway, up-regulated the expression of Runx2, BMP-2, OCN, Col-1 and increased the activity of the early marker for osteoblast differentiation, alkaline phosphatase (ALP) and the number of bone nodules, thus proving that AuNPs stimulate osteoblast proliferation and differentiation indeed through ERK/MAPK pathway.

Protein Kinase 38/Mitogen-Activated Protein Kinase Pathway

Among the three parallel MAPK pathways, p38 is usually called stress-activated protein kinase. Li et al.(Yi et al., 2010) demonstrated that AuNPs could interact with membrane of mesenchymal stem cells (MSCs) and enter into cells through receptor-mediated endocytosis, thus functionalizing as mechanical stimuli. In cells, AuNPs bound to the related-proteins and consequently activated the p38/MAPK signal

pathway (**Figure 1A**). The study of Niu et al. (Niu et al., 2017) also discovered the same phenomenon in human periodontal ligament stem cells (hPDLSCs). Specifically, similar to ERK, AuNPs could up-regulate of osteogenic genes such as BMP-2, Runx-2, OCN, Col-1 and so on through the p38/MAPK signal pathway. In addition, AuNP could also down-regulate adipocyte major transcription factor peroxisome proliferator-activated receptor γ (PPARγ). In summary, AuNPs can produce mechanical stimulation and activate p38/MAPK signal pathway, thus up-regulating the expression of osteogenic genes and down-regulating the adipogenesis specific genes.

Jun-N-terminal kinases/Mitogen-Activated Protein Kinase Pathway

At present, there are no studies on AuNPs promoting osteogenic differentiation by activating JNK/MAPK pathway, but some studies have proved that up-regulating JNK expression and activating MAPK can promote osteogenic differentiation through insulin-like growth factor-1, mineral trioxide and other substances (Zhao et al., 2013; Wang et al., 2014). At the same time, it is not difficult to find that in most studies on JNK/MAPK pathway, JNK and ERK often play a role together (Kim et al., 2015). Whether these two pathways influence each other in the process of promoting osteogenic differentiation is worthy of further study. In addition, some studies have found that ERK, JNK and p38-MAPK were up-regulated under mechanical stimulation (Kyriakis and Avruch, 2001; Zhou et al., 2007). As mentioned above, AuNPs can activate p38/MAPK pathway through mechanical stress to promote osteogenesis, so whether AuNPs have similar effects on JNK pathway is worth exploring. In conclusion, AuNPs of a particular size and concentration could promote osteogenic differentiation in different kind of cells by MAPK pathways.

Regulation of Wnt/β-Catenin Pathway

The Wnt/β-catenin signaling pathway regulates the differentiation of progenitor cells into osteoblasts. Wnts are extracellular proteins that are crucial in multiple cellular functions and many studies have shown that the Wnt pathway was the powerful possible mechanism of AuNPs for promoting cell proliferation (Li et al., 2018a). Wnt signals are regulated by β-catenin that plays an important role in the signaling pathway. In the study of Seon Young choi (Choi et al., 2015), researchers used chitosan as a stabilizer for the reduction of AuNPs, and detected the increased expression of specific markers of osteogenic differentiation, such as OCN, bone sialoprotein (BSP) and ALP, in human adipose-derived mesenchymal stem cells (hADMSCs) co-cultured with chitosan-AuNPs, which confirmed the role of AuNPs in promoting osteogenic differentiation through Wnt/β-catenin pathway (**Figure 1A**). Subsequent study reported by Zhou et al. confirmed the above phenomenon in human periodontal ligament cells as well (Zhou et al., 2018).

Also, several researches suggested that mechanical stimulation enhanced osteogenesis and inhibited adipogenesis through activation of Wnt/β-catenin signaling (Chen et al., 2017). As mentioned earlier, AuNPs can interact with the cell membrane, enter the cell through endocytosis, and combine with proteins in the cytoplasm to produce mechanical stress. This unique mechanical stress activates Wnt/β-catenin pathway similar to the activation of MAPK pathway.

Regulation of Autophagy

Autophagy is a lysosome-based degradative pathway that responds to stress and maintains intracellular homeostasis, which is critical in various physiological and pathological process, including osteogenic differentiation. AuNPs have been shown to be a novel kind of autophagy modulators (Li et al., 2010). Therefore, the mechanism of AuNPs in osteogenic differentiation of MSCs involves autophagy (**Figure 1A**).

In the previous study, Zhang et al. (Zhang et al., 2017a) suggested that the osteogenic differentiation induced by AuNPs depends on the activation of autophagy. The early induction of autophagy is characterized by the accumulation of LC3-II binding to autophagosomes, the up-regulation of autophagy gene Beclin-1 and the decrease of selective autophagy target p62 (Mizushima et al., 2010). It has been proved that AuNPs can up-regulate the mRNA expression of LC3 and Beclin-1, and increase the activity and mineralization rate of ALP, which represented the degree of osteogenic differentiation. The osteogenic differentiation induced by AuNPs has a high similarity with natural osteogenic differentiation, which can play an effective role in bone TE while having little effect on other normal tissues, so they have greater potential in future application.

In addition, autophagy pathway also plays an important role in the differentiation and pathological changes of cartilage tissue. Autophagy has been shown to be related to cartilage formation, and studies have shown that inhibition of autophagy can lead to delayed cartilage development (Wang et al., 2015). However, there are few reports that gold nanomaterials regulate the process of cartilage differentiation by regulating the above pathways or cytokines, and the regulation of cartilage differentiation is mainly regulated by drugs, bioactive factors and so on.

Protection for Bone and Cartilage Tissue

The Protection of Gold Nanoparticles in Bone Tissue

The protective effect of AuNPs in bone tissue is mainly through the inhibition of osteoclast. Osteoclasts, derived from monocyte/macrophage lineage cells, are the main functional cells for bone resorption and play the leading role in the balance between bone resorption and formation. The differentiation and proliferation of osteoclasts directly affect remodeling of bone tissue and hyperactive osteoclasts are the root cause for excessive bone resorption and subsequent osteoporosis. Studies have shown that AuNPs had the ability to inhibit osteoclast and were one of the most effective nanoparticles in the treatment of bone tissue diseases (Lee et al., 2016). Therefore, it is of great significance to clarify the regulatory mechanism of AuNPs on osteoclasts.

Inhibition of Receptor Activator of NF-κB Ligand-Induced Osteoclastogenesis

Receptor activator of NF-κB (nuclear factor-κB) ligand (RANKL) is a key factor motivating the differentiation and activation of

osteoclasts. And RANKL is routinely used in the induction of osteoclast differentiation. Some studied have proved that AuNPs suppressed RANKL-induced osteoclastogenesis mainly by inhibiting reactive oxygen species (ROS) or the fusion of pre-osteoclast cells.

The binding of RANKL to its receptor RANK contributes to the recruitment of tumor necrosis factor receptor-related factor 6 (TRAF6) into the cytoplasmic domain of RANK. RANKL produces ROS that can act as a second messenger in bone marrow-derived macrophages (BMMs), which is involved in TRAF6, NADPH oxidase 1 (Nox1), Nox4 and Rac1. ROS then activate MAPK pathway that required for osteoclast differentiation (Atashi et al., 2015). Therefore, inhibition of ROS helps to inhibit osteoclast differentiation. Sul et al. (Sul et al., 2010) believed AuNPs, an antioxidant, inhibited RANLK-induced osteoclast formation in a dose-dependent manner at 1-2 ug/ml by attenuating ROS production and up-regulating the antioxidant enzyme glutathione peroxidase-1 (Gpx1) which prevented bone resorption (**Figure 1B**). Furthermore, it was believed that excessive ROS significantly restrained osteogenic signaling pathways while promoting adipogenic signaling pathways (Atashi et al., 2015). Therefore, AuNPs not only promotes osteogenesis, but also inhibits osteoclastogenesis through reducing ROS.

On the other hand, it was believed that nanoparticles could weaken RNAKL-induced osteoclastogenesis by suppressing pre-osteoclast fusion, including AuNPs (Zeng et al., 2019) (**Figure 1B**). Osteoclasts are multinuclear terminal cells formed via fusion of monocyte progenitors which is induced by RANKL and macrophage colony-stimulating factor (M-CSF) (Levaot et al., 2015). The fusion process involves three sequential steps. Firstly, BMMs are induced to form pre-osteoclasts possessing the ability to fusion induced by RANKL and M-CSF. Then, these cells migrate, aggregate and adhere to each other with their plasma membranes. Finally, the continuous fusion of pre-osteoclasts forms multinucleated cells, namely osteoclasts. In osteoclastogenesis, cell fusion is a necessary and rate-limiting step in osteoclast development. Li et al. (Zeng et al., 2019) demonstrated that AuNPs suppressed pre-osteoclast migration in a dose-dependent manner and prevented pre-osteoclast fusion by down-regulating expression of fusogenic genes, such as Cx43. In summary, AuNPs can suppress RANKL-induced osteoclastogenesis and they are expected to be a potential target for the treatment of excessive bone resorption.

Regulation of Acidic Microenvironment

AuNPs not only inhibit the generation of osteoclasts, but also disturb the function of osteoclasts. Osteoclasts degrade bone via lysosomal proteases activated in acidic microenvironment which are controlled by vacuolar-type H^+-ATPase (V-ATPase) (Sun-Wada et al., 2003). In osteoclasts, V-ATPase can transfer protons across membranes into extracellular microenvironment and ultimately create an acidic condition. It has been demonstrated that V-ATPase mutations can contribute to paralysis of osteoclasts (Bhargava et al., 2012). In previous studies, AuNPs could prevent V-ATPase binding on the endosome membrane and inhibit the function of V-ATPase, thus alkalifying microenvironment and deactivating osteoclasts (Bai et al., 2018). Further research also suggested that AuNPs can obstruct acidification of osteoclast absorption microenvironment through directly disturbing the partial domain of V-ATPase (Bai et al., 2020) (**Figure 1B**). However, whether the interference of AuNPs on the activity of V-ATP enzyme will cause abnormality of other metabolic processes in osteoclasts and bone tissue, and whether other enzymes similar to V-ATPase structure or function will be inhibited by AuNPs remain to be further explored.

The Protection of Gold Nanoclusters in Bone Tissue

Gold nanoclusters (AuNCs) as emerging fluorescent nanomaterials are smaller than nanoparticles and have better biocompatibility in bone and cartilage. In the study of Kuo Li (Li K. et al., 2020), they constructed AuNCs protected by ultra-small lysozyme (Lys) and found that Lys-AuNCs could not only promote osteogenic differentiation, but also inhibit the formation of osteoclasts. More importantly, the study showed that lysozyme itself had no significant effect on improving the viability of MC3T3E1, important cells for bone tissue regeneration, and the main reason for promoting proliferation rate was the existence of AuNCs. However, except AuNPs and AuNCs, there are few in-depth studies for other types of gold nanomaterials in bone TE and in consideration of their properties, further subsequent studies are needed.

The Protection for Cartilage Tissue

Cartilage tissues with lubrication and cushioning effects are mainly responsible for large mechanical loads (Gilbert and Blain, 2018). As thus, cartilage tissues are easy to be damaged. However, the repair of impaired cartilage is always challenging. The protective function of gold nanomaterials in cartilage tissue has great application prospect, particularly in articular cartilage tissue, including rheumatic arthritis (RA) and OA.

In many studies, it has been demonstrated that AuNPs can inhibit angiogenic activities, suppress inflammation or serve as antioxidant to protect cartilage tissue in arthritis. In the study of Tsai et al. (Tsai et al., 2007), AuNPs have been shown to alleviate collagen-induced arthritis which imitated RA in humans for the first time. They could bound to vascular endothelial growth factor (VEGF), an angiogenic factor, and inhibit endothelial cell proliferation and migration. Another study also indicated that AuNPs in the form of complexes bound to VEGF to treat RA (Lee et al., 2014). Furthermore, AuNPs could down-regulate pro-inflammatory responses and consequently inhibit inflammation both in OA and RA (Gomes et al., 2016; Gul et al., 2018). And the protection of AuNPs for ECM of which the degradation is related to OA and RA have been proved. AuNPs can also quench ROS and prevent the destruction of synovitis in RA (Kirdaite et al., 2019). At the same time, AuNPs as carriers can play a good role in cartilage TE, which will be discussed in the following section.

Similar to AuNPs, gold nanocages are a kind of porous nanogold materials with good biocompatibility to easily use in combination with other materials. And they could reduce

synovial hyperplasia and protect cartilage (Wang et al., 2020). As for AuNRs, it is also easy to modify the surface of their surface. And with the help of other drugs or protein, AuNRs have been shown to promote chondrogenesis (Sansanaphongpricha et al., 2020). As can be seen from the examples above, gold nanomaterials are not only useful as therapeutic agents for cartilage disease but also have enormous potential in cartilage TE.

Carriers in Bone and Cartilage Tissue Engineering

Gold nanomaterials have been widely used in biomedical fields including delivery carriers, because of their adjustable size, optical properties, as well as their biocompatibility (Lopes et al., 2019). Their deliverable application can range from small drug molecules to large biomolecules, such as proteins, DNA or RNA. Among them, AuNPs have become a promising platform for a variety of biomedical applications due to the characteristics of easy synthesis, easy functionalization, stable properties, non-toxic and so on (Boisselier and Astruc, 2009). Similar to AuNPs, AuNRs are also easy for surface modifications and ready to conjugate with functionalized polymers, antibodies and peptides (Huang et al., 2009; Bartczak et al., 2011). Therefore, in bone and cartilage TE, gold nanomaterials could serve as carriers in small molecules and biomacromolecules reputably and need pay more attention to clinic application study.

Small Molecules Delivery

Prior to acting as drug carriers, AuNPs are usually functionalized, which could enhance the stability of AuNPs, increase the circulation time, reduce their side effect, strengthen their interactional ability, improve their biocompatibility and reinforce the regional orientation of drug action. At present, the commonly used functionalization techniques include surface modification via mercaptan, polyethylene glycol (PEG), amino acid (Dykman and Khlebtsov, 2012) and combination of AuNPs with other biocompatible materials (Li H. et al., 2020). With above techniques, it is generally believed that AuNPs have good performance in drug delivery.

Heo et al. (Heo et al., 2014) combined curcumin with AuNPs to prepare cyclodextrin β-cyclodextrin coupled AuNPs, which could significantly restrain the formation of tartrate-resistant acid phosphatase (TRAP)-positive multinucleated cells safely in BMMs. Nah et al. (Nah et al., 2019) used AuNPs to carry vitamin D. The developed AuNPs-vitamin D complex combined well with the mercaptan group between AuNPs and vitamin D. Through the detection of related data, it was confirmed that the complex enhanced osteogenic differentiation. Some researchers also have shown that AuNPs-loaded hydroxyapatite can be internalized into hMSCs and enhance the osteogenic differentiation of hMSCs (Liang et al., 2019). In the above examples, it can be found that AuNPs can carry many types of drugs, which can protect the biological activity of the delivered drugs while improving the bone tissue targeting of the drugs. At the same time, they can play a synergistic effect with the delivered drugs to improve the efficiency of bone TE.

In cartilage tissue, AuNPs can also play the role of drug delivery. Intra-articular injection provides a highly effective and low systemic side effect for the treatment of joint diseases, but it cannot keep the efficacy caused by reduced drug concentration. The application of AuNPs can solve this problem to some extent. Its advantage is that AuNPs can be designed in different sizes and combine with drugs, thus slowing down the clearance of drugs, and when combined with AuNPs, drugs can penetrate ECM or cell barrier (Dwivedi et al., 2015).

The reason that the nano-drug loading system can attract so much attention is mainly due to its unique performance and characteristics in the delivery of drugs for the treatment of diseases. By the way, the use of AuNPs as drug carriers can protect drugs from attacked by the human immune system, and have the characteristics of large drug loading. But at the same time, they are restricted by their limited biodegradability.

Biomacromolecules Delivery

In addition to small molecular drugs, AuNPs can also deliver large biomolecules. In practical work, researchers used a variety of ways to functionalize AuNPs, and utilized functionalized AuNPs to carry the required biological macromolecules. Their adjustable size and function make them a useful scaffold for effective recognition and transmission of biomolecules. At present, it has been proved that AuNPs were successful in the delivery of peptides, proteins or nucleic acids, such as DNA or RNA (Graczyk et al., 2020).

In the field of bone and cartilage TE, it has been reported that AuNPs can deliver siRNA, miRNA and other biomacromolecules with the assistance of various modification (Pan et al., 2016; Wu et al., 2020). AuNPs as effective biomacromolecules delivery carriers provide adequate protection to prevent them from being degraded by enzymes. Certainly, the function of above molecules was enhanced by the carriers. Similarly, AuNRs could serve as delivery carries of BMP-2 and siRNA and ultimately promote osteogenesis and chondrogenesis (Tsai et al., 2007; Zhao et al., 2015; Sansanaphongpricha et al., 2020). In summary, there is massive clinical potential for gold nanomaterials as carrier in bone and cartilage TE.

CONCLUSIONS AND FUTURE PERSPECTIVE

The effective combination of nano-bioengineering and regenerative medicine has become the focus of international research. After establishing interdisciplinary nanotechnology fields, it may be believed that nanomaterials will combine with chemically and clinically applicable fields in the next generation of chemical and medical platforms. Gold nanomaterials, as a new type of medical materials, play a direct role as drug or indirect role as drug carriers. They not only promoted the progress of alternative medical methods, but also provide new ideas and new goals for the clinical treatment for bone and cartilage diseases represented by osteoporosis, bone defect and arthritis. In this review, the majority of biomedical mechanism and applications demonstrated that gold nanomaterials, especially AuNPs, had a

protective effect on bone and cartilage tissue and could be further modified to promote delivery efficiency and loading with other drugs or biomacromolecules. However, it is worth noting that gold nanomaterials need further examination in clinical studies, which may obviously provide help for reducing the medical pressure on bone and cartilage diseases, increasingly with a rapidly aging population.

In spite of the potential therapeutic effectiveness of gold nanomaterials, several limitations and deficiencies of their applications remain. In bone and cartilage TE, the application of gold nanomaterials is mainly limited to 0D AuNPs and 1D AuNRs. However, while 2D gold nanosheets and other hierarchical gold nanomaterials with different and unique physical and chemical properties are well used in different directions, such as tumor treatment, examination, imaging and so on, there are few reports on the application of these materials in bone and cartilage TE. It is thus highly desirable to explore their utilization due to the broad research prospects. In addition, whether naked gold nanomaterials can have a therapeutic effect on chondrocytes and cartilage tissue needs to be further clarified with potential mechanism.

AUTHOR CONTRIBUTIONS

All authors listed have made a substantial, direct and intellectual contribution to the work, and approved it for publication.

FUNDING

The authors would like to thank the financial support from Zhejiang Provincial Natural Science Foundation of China (LQ21B030002, LQ21H060010), Basic Science and Technology Research Project of Wenzhou (G2020007, 2020Y1163), the National College Student Innovation and Entrepreneurship Training Program (202010343028), and Basic research projects of Wenzhou Medical University (KYYW202028).

REFERENCES

Agarwal, R., and García, A. J. (2015). Biomaterial Strategies for Engineering Implants for Enhanced Osseointegration and Bone Repair. *Adv. Drug Deliv. Rev.* 94, 53–62. doi:10.1016/j.addr.2015.03.013

Atashi, F., Modarressi, A., and Pepper, M. S. (2015). The Role of Reactive Oxygen Species in Mesenchymal Stem Cell Adipogenic and Osteogenic Differentiation: a Review. *Stem Cell Develop.* 24 (10), 1150–1163. doi:10.1089/scd.2014.0484

Bai, X., Gao, Y., Zhang, M., Chang, Y.-n., Chen, K., Li, J., et al. (2020). Carboxylated Gold Nanoparticles Inhibit Bone Erosion by Disturbing the Acidification of an Osteoclast Absorption Microenvironment. *Nanoscale* 12 (6), 3871–3878. doi:10.1039/c9nr09698a

Bai, X., Zhang, J., Chang, Y.-N., Gu, W., Lei, R., Qin, Y., et al. (2018). Nanoparticles with High-Surface Negative-Charge Density Disturb the Metabolism of Low-Density Lipoprotein in Cells. *Int J. Mol. Sci* 19 (9), 2790. doi:10.3390/ijms19092790

Bartczak, D., Kanaras, A. G., and Colloids (2011). Preparation of Peptide-Functionalized Gold Nanoparticles Using One Pot EDC/Sulfo-NHS Coupling. *Langmuir* 27 (16), 10119–10123. doi:10.1021/la2022177

Bhargava, A., Voronov, I., Wang, Y., Glogauer, M., Kartner, N., and Manolson, M. F. (2012). Osteopetrosis Mutation R444L Causes Endoplasmic Reticulum Retention and Misprocessing of Vacuolar H+-ATPase A3 Subunit. *J. Biol. Chem.* 287 (32), 26829–26839. doi:10.1074/jbc.M112.345702

Boisselier, E., and Astruc, D. (2009). Gold Nanoparticles in Nanomedicine: Preparations, Imaging, Diagnostics, Therapies and Toxicity. *Chem. Soc. Rev.* 38 (6), 1759–1782. doi:10.1039/b806051g

Chen, X., Guo, J., Yuan, Y., Sun, Z., Chen, B., Tong, X., et al. (2017). Cyclic Compression Stimulates Osteoblast Differentiation via Activation of the Wnt/β-Catenin Signaling Pathway. *Mol. Med. Rep.* 15 (5), 2890–2896. doi:10.3892/mmr.2017.6327

Chithrani, B. D., Ghazani, A. A., and Chan, W. C. W. (2006). Determining the Size and Shape Dependence of Gold Nanoparticle Uptake into Mammalian Cells. *Nano Lett.* 6 (4), 662–668. doi:10.1021/nl052396o

Choi, S. Y., Song, M. S., Ryu, P. D., Lam, A. T., Joo, S. W., and Lee, S. Y. (2015). Gold Nanoparticles Promote Osteogenic Differentiation in Human Adipose-Derived Mesenchymal Stem Cells through the Wnt/β-Catenin Signaling Pathway. *Int. J. Nanomedicine* 10, 4383–4392. doi:10.2147/IJN.S78775

Dreaden, E. C., Alkilany, A. M., Huang, X., Murphy, C. J., and El-Sayed, M. A. (2012). The golden Age: Gold Nanoparticles for Biomedicine. *Chem. Soc. Rev.* 41 (7), 2740–2779. doi:10.1039/c1cs15237h

Du, X., Zhang, X., Jiang, C., Zhang, W., and Yang, L. (2018). The Trace Detection of Nitrite Ions Using Neutral Red Functionalized SH-β-Cyclodextrin @Au Nanoparticles. *Sensors* 18 (3), 681. doi:10.3390/s18030681

Dwivedi, P., Nayak, V., and Kowshik, M. (2015). Role of Gold Nanoparticles as Drug Delivery Vehicles for Chondroitin Sulfate in the Treatment of Osteoarthritis. *Biotechnol. Prog.* 31 (5), 1416–1422. doi:10.1002/btpr.2147

Dykman, L., and Khlebtsov, N. (2012). Gold Nanoparticles in Biomedical Applications: Recent Advances and Perspectives. *Chem. Soc. Rev.* 41 (6), 2256–2282. doi:10.1039/c1cs15166e

Franceschi, R., Xiao, G., Jiang, D., Gopalakrishnan, R., Yang, S., and Reith, E. (2003). Multiple Signaling Pathways Converge on the Cbfa1/Runx2 Transcription Factor to Regulate Osteoblast Differentiation. *Connect. Tissue Res.* 44 (1), 109–116. doi:10.1080/713713603

Gao, H., Xiang, W., Ma, X., Ma, L., Huang, Y., Ni, H., et al. (2015). Sol-gel Synthesis and Third-Order Optical Nonlinearity of Au Nanoparticles Doped Monolithic Glass. *Gold Bull.* 48 (3-4), 153–159. doi:10.1007/s13404-015-0173-1

Ge, C., Xiao, G., Jiang, D., and Franceschi, R. T. (2007). Critical Role of the Extracellular Signal-Regulated Kinase-MAPK Pathway in Osteoblast Differentiation and Skeletal Development. *J. Cel Biol* 176 (5), 709–718. doi:10.1083/jcb.200610046

Gilbert, S. J., and Blain, E. J. (2018). *Cartilage Mechanobiology: How Chondrocytes Respond to Mechanical Load,* London: Academic Press, 99–126. doi:10.1016/b978-0-12-812952-4.00004-0

Gomes, A., Saha, P., Bhowmik, T., Dasgupta, A., and Dasgupta, S. (2016). Protection against Osteoarthritis in Experimental Animals by Nanogold Conjugated Snake Venom Protein Toxin Gold Nanoparticle-Naja Kaouthia Cytotoxin 1. *Indian J. Med. Res.* 144 (6), 910–917. doi:10.4103/ijmr.IJMR_1078_14

Graczyk, A., Pawlowska, R., Jedrzejczyk, D., and Chworos, A. (2020). Gold Nanoparticles in Conjunction with Nucleic Acids as a Modern Molecular System for Cellular Delivery. *Molecules* 25 (1), 204. doi:10.3390/molecules25010204

Greenblatt, M. B., Shim, J.-H., and Glimcher, L. H. (2013). Mitogen-activated Protein Kinase Pathways in Osteoblasts. *Annu. Rev. Cel Dev. Biol.* 29, 63–79. doi:10.1146/annurev-cellbio-101512-122347

Gul, A., Kunwar, B., Mazhar, M., Faizi, S., Ahmed, D., Shah, M. R., et al. (2018). Rutin and Rutin-Conjugated Gold Nanoparticles Ameliorate Collagen-Induced Arthritis in Rats through Inhibition of NF-Kb and iNOS Activation. *Int. Immunopharmacology* 59, 310–317. doi:10.1016/j.intimp.2018.04.017

He, B., Wang, Y., Zhai, Q., Qiu, P., Dong, G., Liu, X., et al. (2020). From Polymeric Carbon Nitride to Carbon Materials: Extended Application to Electrochemical Energy Conversion and Storage. *Nanoscale* 12 (16), 8636–8646. doi:10.1039/d0nr01612h

Heo, D. N., Ko, W.-K., Moon, H.-J., Kim, H.-J., Lee, S. J., Lee, J. B., et al. (2014). Inhibition of Osteoclast Differentiation by Gold Nanoparticles Functionalized with Cyclodextrin Curcumin Complexes. *ACS Nano* 8 (12), 12049–12062. doi:10.1021/nn504329u

Hu, X., Huang, J., Zhao, F., Yi, P., He, B., Wang, Y., et al. (2020). Photothermal Effect of Carbon Quantum Dots Enhanced Photoelectrochemical Water Splitting of Hematite Photoanodes. *J. Mater. Chem. A.* 8 (30), 14915–14920. doi:10.1039/d0ta04144k

Huang, J., Chen, T., Zhao, M., Yi, P., Zhao, F., He, B., et al. (2021). Surface Oxygen Vacancies of TiO2 Nanorods by Electron Beam Irradiation for Efficient Photoelectrochemical Water Splitting. *CrystEngComm* 23 (16), 2952–2960. doi:10.1039/d1ce00205h

Huang, X., Neretina, S., and El-Sayed, M. A. J. A. M. (2009). Gold Nanorods: From Synthesis and Properties to Biological and Biomedical Applications. *Adv. Mater.* 21, 4880–5491. doi:10.1002/adma.200802789

Huang, Y., Lin, D., Li, M., Yin, D., Wang, S., and Wang, J. (2019). Ag@Au Core-Shell Porous Nanocages with Outstanding SERS Activity for Highly Sensitive SERS Immunoassay. *Sensors* 19 (7), 1554. doi:10.3390/s19071554

Huang, Y., Xiang, W., Lin, S., Cao, R., Zhang, Y., Zhong, J., et al. (2017). The Synthesis of Bimetallic Gold Plus Nickel Nanoparticles Dispersed in a Glass Host and Behavior-Enhanced Optical Nonlinearities. *J. Non-Crystalline Sol.* 459, 142–149. doi:10.1016/j.jnoncrysol.2017.01.007

Jiang, B., Xu, L., Chen, W., Zou, C., Yang, Y., Fu, Y., et al. (2017). Ag+-assisted Heterogeneous Growth of Concave Pd@Au Nanocubes for Surface Enhanced Raman Scattering (SERS). *Nano Res.* 10 (10), 3509–3521. doi:10.1007/s12274-017-1562-y

Jiang, K., Wang, J., Wu, F., Xue, Q., Yao, Q., Zhang, J., et al. (2020). Dopant-Free Organic Hole-Transporting Material for Efficient and Stable Inverted All-Inorganic and Hybrid Perovskite Solar Cells. *Adv. Mater.* 32 (16), 1908011. doi:10.1002/adma.201908011

Jiang, X.-M., Wang, L.-M., Wang, J., and Chen, C.-Y. (2012). Gold Nanomaterials: Preparation, Chemical Modification, Biomedical Applications and Potential Risk Assessment. *Appl. Biochem. Biotechnol.* 166 (6), 1533–1551. doi:10.1007/s12010-012-9548-4

Keeney, M., Lai, J. H., and Yang, F. (2011). Recent Progress in Cartilage Tissue Engineering. *Curr. Opin. Biotechnol.* 22 (5), 734–740. doi:10.1016/j.copbio.2011.04.003

Kim, B. S., Kang, H.-J., Park, J.-Y., and Lee, J. (2015). Fucoidan Promotes Osteoblast Differentiation via JNK- and ERK-dependent BMP2-Smad 1/5/8 Signaling in Human Mesenchymal Stem Cells. *Exp. Mol. Med.* 47, e128. doi:10.1038/emm.2014.95

Kirdaite, G., Leonaviciene, L., Bradunaite, R., Vasiliauskas, A., Rudys, R., Ramanaviciene, A., et al. (2019). Antioxidant Effects of Gold Nanoparticles on Early Stage of Collagen-Induced Arthritis in Rats. *Res. Vet. Sci.* 124, 32–37. doi:10.1016/j.rvsc.2019.02.002

Kyriakis, J. M., and Avruch, J. (2001). Mammalian Mitogen-Activated Protein Kinase Signal Transduction Pathways Activated by Stress and Inflammation. *Physiol. Rev.* 81 (2), 807–869. doi:10.1152/physrev.2001.81.2.807

Lee, D., Heo, D. N., Kim, H.-J., Ko, W.-K., Lee, S. J., Heo, M., et al. (2016). Inhibition of Osteoclast Differentiation and Bone Resorption by Bisphosphonate-Conjugated Gold Nanoparticles. *Sci. Rep.* 6, 27336. doi:10.1038/srep27336

Lee, H., Lee, M.-Y., Bhang, S. H., Kim, B.-S., Kim, Y. S., Ju, J. H., et al. (2014). Hyaluronate-gold Nanoparticle/tocilizumab Complex for the Treatment of Rheumatoid Arthritis. *ACS Nano* 8 (5), 4790–4798. doi:10.1021/nn500685h

Levaot, N., Ottolenghi, A., Mann, M., Guterman-Ram, G., Kam, Z., and Geiger, B. (2015). Osteoclast Fusion Is Initiated by a Small Subset of RANKL-Stimulated Monocyte Progenitors, Which Can Fuse to RANKL-Unstimulated Progenitors. *Bone* 79, 21–28. doi:10.1016/j.bone.2015.05.021

Li, C., Li, Z., Zhang, Y., Fathy, A. H., and Zhou, M. (2018a). The Role of the Wnt/β-Catenin Signaling Pathway in the Proliferation of Gold Nanoparticle-Treated Human Periodontal Ligament Stem Cells. *Stem Cel Res Ther* 9 (1), 214. doi:10.1186/s13287-018-0954-6

Li, C., Zhang, Y., Li, Z., Mei, E., Lin, J., Li, F., et al. (2018b). Light-Responsive Biodegradable Nanorattles for Cancer Theranostics. *Adv. Mater.* 30 (8), 1706150. doi:10.1002/adma.201706150

Li, H., Pan, S., Xia, P., Chang, Y., Fu, C., Kong, W., et al. (2020a). Advances in the Application of Gold Nanoparticles in Bone Tissue Engineering. *J. Biol. Eng.* 14 (1). doi:10.1186/s13036-020-00236-3

Li, J. J., Hartono, D., Ong, C.-N., Bay, B.-H., and Yung, L.-Y. L. (2010). Autophagy and Oxidative Stress Associated with Gold Nanoparticles. *Biomaterials* 31 (23), 5996–6003. doi:10.1016/j.biomaterials.2010.04.014

Li, J., Li, J. E. J., Zhang, J., Wang, X., Kawazoe, N., and Chen, G. (2016). Gold Nanoparticle Size and Shape Influence on Osteogenesis of Mesenchymal Stem Cells. *Nanoscale* 8 (15), 7992–8007. doi:10.1039/c5nr08808a

Li, J., Li, X., Zhang, J., Kawazoe, N., and Chen, G. (2017a). Induction of Chondrogenic Differentiation of Human Mesenchymal Stem Cells by Biomimetic Gold Nanoparticles with Tunable RGD Density. *Adv. Healthc. Mater.* 6 (14), 1700317. doi:10.1002/adhm.201700317

Li, K., Zhuang, P., Tao, B., Li, D., Xing, X., and Mei, X. (2020b). Ultra-Small Lysozyme-Protected Gold Nanoclusters as Nanomedicines Inducing Osteogenic Differentiation. *Int. J. Nanomedicine* 15, 4705–4716. doi:10.2147/IJN.S241163

Li, N.-M., Li, K.-M., Wang, S., Yang, K.-Q., Zhang, L.-J., Chen, Q., et al. (2015). Gold Embedded Maghemite Hybrid Nanowires and Their Gas Sensing Properties. *ACS Appl. Mater. Inter.* 7 (19), 10534–10540. doi:10.1021/acsami.5b02087

Li, Q., Wang, F., Bai, Y., Xu, L., Yang, Y., Yan, L., et al. (2017b). Decahedral-shaped Au Nanoparticles as Plasmonic Centers for High Performance Polymer Solar Cells. *Org. Electron.* 43, 33–40. doi:10.1016/j.orgel.2017.01.010

Li, X., Yang, Y., Zhou, G., Han, S., Wang, W., Zhang, L., et al. (2013). The Unusual Effect of AgNO3 on the Growth of Au Nanostructures and Their Catalytic Performance. *Nanoscale* 5 (11), 4976–4985. doi:10.1039/c3nr00603d

Liang, H., Xu, X., Feng, X., Ma, L., Deng, X., Wu, S., et al. (2019). Gold Nanoparticles-Loaded Hydroxyapatite Composites Guide Osteogenic Differentiation of Human Mesenchymal Stem Cells through Wnt/β-Catenin Signaling Pathway. *Int. J. Nanomedicine* 14, 6151–6163. doi:10.2147/IJN.S213889

Lopes, T. S., Alves, G. G., Pereira, M. R., Granjeiro, J. M., and Leite, P. E. C. (2019). Advances and Potential Application of Gold Nanoparticles in Nanomedicine. *J. Cel Biochem* 120 (10), 16370–16378. doi:10.1002/jcb.29044

Ma, Y., Xu, L., Chen, W., Zou, C., Yang, Y., Zhang, L., et al. (2015). Evolution from Small Sized Au Nanoparticles to Hollow Pt/Au Nanostructures with Pt Nanorods and a Mechanistic Study. *RSC Adv.* 5 (126), 103797–103802. doi:10.1039/c5ra21807a

Mahmood, A., Napoli, C., and Aldahmash, A. (2011). In VitroDifferentiation and Maturation of Human Embryonic Stem Cell into Multipotent Cells. *Stem Cell Int.* 2011, 735420. doi:10.4061/2011/735420

Mandal, S., Bakeine, G. J., Krol, S., Ferrari, C., Clerici, A. M., Zonta, C., et al. (2011). Design, Development and Characterization of Multi-Functionalized Gold Nanoparticles for Biodetection and Targeted boron Delivery in BNCT Applications. *Appl. Radiat. Isot.* 69 (12), 1692–1697. doi:10.1016/j.apradiso.2011.05.002

Mizushima, N., Yoshimori, T., and Levine, B. (2010). Methods in Mammalian Autophagy Research. *Cell* 140 (3), 313–326. doi:10.1016/j.cell.2010.01.028

Nah, H., Lee, D., Heo, M., Lee, J. S., Lee, S. J., Heo, D. N., et al. (2019). Vitamin D-Conjugated Gold Nanoparticles as Functional Carriers to Enhancing Osteogenic Differentiation. *Sci. Technol. Adv. Mater.* 20 (1), 826–836. doi:10.1080/14686996.2019.1644193

Niu, C., Yuan, K., Ma, R., Gao, L., Jiang, W., Hu, X., et al. (2017). Gold Nanoparticles Promote Osteogenic Differentiation of Human Periodontal Ligament Stem Cells via the P38 MAPK Signaling Pathway. *Mol. Med. Rep.* 16 (4), 4879–4886. doi:10.3892/mmr.2017.7170

Pan, S., Li, J., Wen, Z., Lu, R., Zhang, Q., Jin, H., et al. (2021). Halide Perovskite Materials for Photo(Electro)Chemical Applications: Dimensionality, Heterojunction, and Performance. *Adv. Energ. Mater.*, 2004002. doi:10.1002/aenm.202004002

Pan, T., Song, W., Gao, H., Li, T., Cao, X., Zhong, S., et al. (2016). miR-29b-Loaded Gold Nanoparticles Targeting to the Endoplasmic Reticulum for Synergistic Promotion of Osteogenic Differentiation. *ACS Appl. Mater. Inter.* 8 (30), 19217–19227. doi:10.1021/acsami.6b02969

Ramakrishna, G., Varnavski, O., Kim, J., Lee, D., and Goodson, T. (2008). Quantum-sized Gold Clusters as Efficient Two-Photon Absorbers. *J. Am. Chem. Soc.* 130 (15), 5032–5033. doi:10.1021/ja800341v

Sansanaphongpricha, K., Sonthithai, P., Kaewkong, P., Thavornyutikarn, B., Bamrungsap, S., Kosorn, W., et al. (2020). Hyaluronic Acid-Coated Gold Nanorods Enhancing BMP-2 Peptide Delivery for Chondrogenesis. *Nanotechnology* 31 (43), 435101. doi:10.1088/1361-6528/aba46d

Shiang, Y.-C., Huang, C.-C., Chen, W.-Y., Chen, P.-C., and Chang, H.-T. (2012). Fluorescent Gold and Silver Nanoclusters for the Analysis of Biopolymers and Cell Imaging. *J. Mater. Chem.* 22 (26), 12972–12982. doi:10.1039/c2jm30563a

Sul, O.-J., Kim, J.-C., Kyung, T.-W., Kim, H.-J., Kim, Y.-Y., Kim, S.-H., et al. (2010). Gold Nanoparticles Inhibited the Receptor Activator of Nuclear Factor-Kb Ligand (RANKL)-Induced Osteoclast Formation by Acting as an Antioxidant. *Biosci. Biotechnol. Biochem.* 74 (11), 2209–2213. doi:10.1271/bbb.100375

Sun-Wada, G.-H., Wada, Y., and Futai, M. (2003). Vacuolar H+ Pumping ATPases in Luminal Acidic Organelles and Extracellular Compartments: Common Rotational Mechanism and Diverse Physiological Roles. *J. Bioenerg. biomembranes* 35 (4), 347–358. doi:10.1023/a:1025780932403

Tsai, C.-Y., Shiau, A.-L., Chen, S.-Y., Chen, Y.-H., Cheng, P.-C., Chang, M.-Y., et al. (2007). Amelioration of Collagen-Induced Arthritis in Rats by Nanogold. *Arthritis Rheum.* 56 (2), 544–554. doi:10.1002/art.22401

Wang, B., Iocozzia, J., Zhang, M., Ye, M., Yan, S., Jin, H., et al. (2019). The Charge Carrier Dynamics, Efficiency and Stability of Two-Dimensional Material-Based Perovskite Solar Cells. *Chem. Soc. Rev.* 48 (18), 4854–4891. doi:10.1039/c9cs00254e

Wang, X., Qi, H., Wang, Q., Zhu, Y., Wang, X., Jin, M., et al. (2015). FGFR3/fibroblast Growth Factor Receptor 3 Inhibits Autophagy through Decreasing the ATG12–ATG5 Conjugate, Leading to the Delay of Cartilage Development in Achondroplasia. *Autophagy* 11 (11), 1998–2013. doi:10.1080/15548627.2015.1091551

Wang, Y., Li, J., Song, W., and Yu, J. (2014). Mineral Trioxide Aggregate Upregulates Odonto/osteogenic Capacity of Bone Marrow Stromal Cells from Craniofacial bonesviaJNK and ERK MAPK Signalling Pathways. *Cell Prolif.* 47 (3), 241–248. doi:10.1111/cpr.12099

Wang, Z., Yang, J., Yang, Y., Pu, X., Zhao, J., and Zhang, N. (2020). Targeted and Combined TPCA-1-Gold Nanocage Therapy for *In Vivo* Treatment of Inflammatory Arthritis. *AAPS PharmSciTech* 21 (8), 298. doi:10.1208/s12249-020-01856-0

Wu, Q., Wang, K., Wang, X., Liang, G., and Li, J. (2020). Delivering siRNA to Control Osteogenic Differentiation and Real-Time Detection of Cell Differentiation in Human Mesenchymal Stem Cells Using Multifunctional Gold Nanoparticles. *J. Mater. Chem. B* 8 (15), 3016–3027. doi:10.1039/c9tb02899d

Xu, L., Wang, K., Jiang, B., Chen, W., Liu, F., Hao, H., et al. (2016). Competitive Effect in the Growth of Pd-Au-Pd Segmental Nanorods. *Chem. Mater.* 28 (20), 7394–7403. doi:10.1021/acs.chemmater.6b02871

Ye, S., Brown, A. P., Stammers, A. C., Thomson, N. H., Wen, J., Roach, L., et al. (2019). Sub-Nanometer Thick Gold Nanosheets as Highly Efficient Catalysts. *Adv. Sci.* 6 (21), 1900911. doi:10.1002/advs.201900911

Yeh, Y.-C., Creran, B., and Rotello, V. M. (2012). Gold Nanoparticles: Preparation, Properties, and Applications in Bionanotechnology. *Nanoscale* 4 (6), 1871–1880. doi:10.1039/c1nr11188d

Yi, C., Liu, D., Fong, C.-C., Zhang, J., and Yang, M. (2010). Gold Nanoparticles Promote Osteogenic Differentiation of Mesenchymal Stem Cells through P38 MAPK Pathway. *ACS Nano* 4 (11), 6439–6448. doi:10.1021/nn101373r

Yuan, M., Wang, Y., and Qin, Y. X. (2017). SPIO-Au Core-Shell Nanoparticles for Promoting Osteogenic Differentiation of MC3T3-E1 Cells: Concentration-dependence Study. *J. Biomed. Mater. Res.* 105 (12), 3350–3359. doi:10.1002/jbm.a.36200

Zeng, L., Geng, H., Gu, W., Ma, S., Qin, Y., Xia, S., et al. (2019). Au Nanoparticles Attenuate RANKL-Induced Osteoclastogenesis by Suppressing Pre-Osteoclast Fusion. *J. Nanosci Nanotechnol* 19 (4), 2166–2173. doi:10.1166/jnn.2019.15764

Zhang, D., Liu, D., Zhang, J., Fong, C., and Yang, M. (2014). Gold Nanoparticles Stimulate Differentiation and Mineralization of Primary Osteoblasts through the ERK/MAPK Signaling Pathway. *Mater. Sci. Eng. C* 42, 70–77. doi:10.1016/j.msec.2014.04.042

Zhang, X., Pan, S., Song, H., Guo, W., Gu, F., Yan, C., et al. (2021a). Photothermal Effect Enables Markedly Enhanced Oxygen Reduction and Evolution Activities for High-Performance Zn-Air Batteries. *J. Mater. Chem. A*. doi:10.1039/D1TA03652A

Zhang, X., Pan, S., Song, H., Guo, W., Zhao, S., Chen, G., et al. (2021b). Polymer-Inorganic Thermoelectric Nanomaterials: Electrical Properties, Interfacial Chemistry Engineering, and Devices. *Front. Chem.* 9, 677821. doi:10.3389/fchem.2021.677821

Zhang, Y., Jin, Y., He, M., Zhou, L., Xu, T., Yuan, R., et al. (2018). Optical Properties of Bimetallic Au-Cu Nanocrystals Embedded in Glass. *Mater. Res. Bull.* 98, 94–102. doi:10.1016/j.materresbull.2017.10.009

Zhang, Y., and Jordan, J. M. (2010). Epidemiology of Osteoarthritis. *Clin. Geriatr. Med.* 26 (3), 355–369. doi:10.1016/j.cger.2010.03.001

Zhang, Y., Kong, N., Zhang, Y., Yang, W., and Yan, F. (2017a). Size-dependent Effects of Gold Nanoparticles on Osteogenic Differentiation of Human Periodontal Ligament Progenitor Cells. *Theranostics* 7 (5), 1214–1224. doi:10.7150/thno.17252

Zhang, Y., Zhang, J., Zhang, J., Lin, S., Huang, Y., Yuan, R., et al. (2017b). Intense Enhancement of Yellow Luminescent Carbon Dots Coupled with Gold Nanoparticles toward white LED. *Dyes Pigm.* 140, 122–130. doi:10.1016/j.dyepig.2017.01.043

Zhao, F., Zhao, Y., Liu, Y., Chang, X., Chen, C., and Zhao, Y. (2011). Cellular Uptake, Intracellular Trafficking, and Cytotoxicity of Nanomaterials. *Small* 7 (10), 1322–1337. doi:10.1002/smll.201100001

Zhao, M., Chen, T., He, B., Hu, X., Huang, J., Yi, P., et al. (2020). Photothermal Effect-Enhanced Photoelectrochemical Water Splitting of a BiVO4 Photoanode Modified with Dual-Functional Polyaniline. *J. Mater. Chem. A.* 8 (31), 15976–15983. doi:10.1039/d0ta03698f

Zhao, X., Huang, Q., and Jin, Y. (2015). Gold Nanorod Delivery of LSD1 siRNA Induces Human Mesenchymal Stem Cell Differentiation. *Mater. Sci. Eng. C* 54, 142–149. doi:10.1016/j.msec.2015.05.013

Zhao, Y.-F., Zeng, D.-L., Xia, L.-G., Zhang, S.-M., Xu, L.-Y., Jiang, X.-Q., et al. (2013). Osteogenic Potential of Bone Marrow Stromal Cells Derived from Streptozotocin-Induced Diabetic Rats. *Int. J. Mol. Med.* 31 (3), 614–620. doi:10.3892/ijmm.2013.1227

Zhou, J., Zhang, Y., Li, L., Fu, H., Yang, W., and Yan, F. (2018). Human β-defensin 3-combined Gold Nanoparticles for Enhancement of Osteogenic Differentiation of Human Periodontal Ligament Cells in Inflammatory Microenvironments. *Int J. Nanomedicine.* 13, 555–567. doi:10.2147/IJN.S150897

Zhou, Y., Millward-Sadler, S. J., Lin, H., Robinson, H., Goldring, M., Salter, D. M., et al. (2007). Evidence for JNK-dependent Up-Regulation of Proteoglycan Synthesis and for Activation of JNK1 Following Cyclical Mechanical Stimulation in a Human Chondrocyte Culture Model. *Osteoarthritis and Cartilage* 15 (8), 884–893. doi:10.1016/j.joca.2007.02.001

Zhu, J., Lu, N., Chen, W., Kong, L., Yang, Y., Ma, D., et al. (2015). Influence of Au Nanoparticle Shape on Au@Cu2O Heterostructures. *J. Nanomater.* 2015, 389790. doi:10.1155/2015/389790

Zhu, S., Zhu, L., Yu, J., Wang, Y., and Peng, B. (2019). Anti-osteoclastogenic Effect of Epigallocatechin Gallate-Functionalized Gold Nanoparticles *In Vitro* and *In Vivo*. *Int J. Nanomedicine.* 14, 5017–5032. doi:10.2147/IJN.S204628

Conflict of Interest: The authors declare that the research was conducted in the absence of any commercial or financial relationships that could be construed as a potential conflict of interest.

Advantages of publishing in Frontiers

OPEN ACCESS
Articles are free to read for greatest visibility and readership

FAST PUBLICATION
Around 90 days from submission to decision

HIGH QUALITY PEER-REVIEW
Rigorous, collaborative, and constructive peer-review

TRANSPARENT PEER-REVIEW
Editors and reviewers acknowledged by name on published articles

Frontiers
Avenue du Tribunal-Fédéral 34
1005 Lausanne | Switzerland

Visit us: www.frontiersin.org
Contact us: frontiersin.org/about/contact

REPRODUCIBILITY OF RESEARCH
Support open data and methods to enhance research reproducibility

DIGITAL PUBLISHING
Articles designed for optimal readership across devices

FOLLOW US
@frontiersin

IMPACT METRICS
Advanced article metrics track visibility across digital media

EXTENSIVE PROMOTION
Marketing and promotion of impactful research

LOOP RESEARCH NETWORK
Our network increases your article's readership